THE UNIVERSITY of ADELAIDE

Unsteady Separation Control on Wind Turbine Blades

Amanullah Choudhry

School of Mechanical Engineering

The University of Adelaide

South Australia 5005

Australia

A thesis submitted in fulfillments of
the requirements for the degree of
Doctor of Philosophy in October, 2014

Dedicated to my parents

Dr. Sanaullah Choudhry and Mrs. Tahira K. Choudhry

For their unbounded support and love

SUMMARY

Dynamic stall is one of the primary causes of unsteady loads on wind turbine blades. The process can be instigated by a multitude of factors, common in wind turbine operating environments, such as inflow turbulence, wind gusts and sustained yaw misalignment. The unsteady separation due to dynamic stall can lead to excessive loads, much larger than the design loads for the turbine, and vibrations in the blade, leading to fatigue damage. Furthermore, massive flow separations can lead to performance losses for the turbines. Therefore, it is of utmost importance to devise methods to control the unsteady separation on wind turbines and to reduce its impact on the performance and structural integrity of the system.

Dynamic stall on wind turbine blades is initiated by a rapid variation in wind speed and direction. However, no viable methods are available that could reliably predict the occurrence of unsteady separation for wind turbines. Therefore, in the present research, an analytical method has been developed and validated against well-known test cases to quickly and reliably deduce the variations in the sectional angles of attack, based on the variability of wind speed and direction of the oncoming flow. The concept of limiting reduced frequency as a precursor for unsteady separation is proposed in this initial study. Furthermore, it is illustrated, using high-quality wind data, that unsteady separation principally exists near the root regions of turbine blades where thick airfoil sections are generally used.

Further research was conducted to determine the effects of wakes on the occurrence of dynamic stall. For this study, the mean and turbulent wind conditions in the wake were acquired through Large Eddy Simulation of a wind turbine wake performed at the University of Adelaide. The data was used to determine the influence of wakes on the occurrence of dynamic stall on wind turbines operating in the wake of an upstream turbine. It was shown that the primary cause of large unsteady loads on downstream wind turbines is the rapid variation in the wind direction. It is emphasized that the model can be used during wind turbine design phase to determine the regions of the blade where the dynamic stall control is necessary.

After determining the occurrence of dynamic stall on the turbine blades under normal operating conditions, the second objective of the present research was to gain a deeper insight into the dynamic stall process, particularly the lift characteristics of thick airfoils under unsteady separation. Experiments were conducted to understand the non-linear lift behavior of the airfoil during dynamic stall at constant pitch rates. It was shown that the thickening of the boundary layer during pitch-up resulted in an apparent increase in the thickness and camber of the airfoil. It is, furthermore, proposed that the primary dynamic stall vortex also increases the effective camber of the airfoil. This results in the sudden increase in the lift-slope when the vortex is formed. This effect was further demonstrated using numerical simulations of the thick NACA 0021 airfoil at low turbulence levels. During steady-state operation, a long separation bubble on the airfoil surface was found to be responsible for the increased lift-slope, greater than the theoretical maximum, and the abrupt stalling behavior of the foil. It was proposed that this long separation bubble was responsible for an apparent increase in the airfoil's camber. Furthermore, removing the bubble, through an artificial increase in turbulence, degraded the lift-to-drag

ratio of the airfoil. However, due to the absence of the bubble, the steady-state stall angle of attack was significantly increased. This study, therefore, illustrated that apparent changes in thickness and camber of the airfoil during dynamic stall process are principally responsible for the non-linear lift behavior.

It was observed, in the experiments, that an increase in the reduced frequency or the Reynolds number resulted in the increase in the strength of the primary dynamic stall vortex. It was also observed that the stall intensity of the airfoil undergoing unsteady separation is also dictated by the primary vortex. Therefore, an increase in the reduced frequency or the Reynolds number resulted in increased stall intensity. Hence, in order to improve the post-stall lift behavior of the airfoil, it is necessary to modify the primary dynamic stall vortex. This can be accomplished by reducing the strength of the vortex and delaying its formation on the airfoil by minimizing the reversed flow accumulation that leads to the formation of the vortex. In order to propose appropriate control methodologies for dynamic stall on wind turbine blades, literature survey illustrated that the required control would need to be implemented passively, near the leading edge of the airfoil. It was, furthermore, observed that the control methodologies need to be deployed before the formation of the dynamic stall vortex in order to affect the post-stall behavior of the foil. Finally, the required control needs to influence the flow field to a large extent to diminish the effects of the vortex. Therefore, three different methods were proposed to control the dynamic stall process. These included streamwise vortices generated using leading edge vortex generators, spanwise-vortices generated using a novel concept of a thin elevated wire affixed at the leading edge, and a cavity on the upper surface of the airfoil. It is demonstrated through experiment that all three methods influence the formation of the dynamic stall vortex during unsteady separation. However, the methods

that promoted enhanced mixing, namely the vortex generators and the elevated wire, were observed to favorably reduce the excessive lift associated with the primary vortex structure. It was also observed that the stall intensity was significantly reduced for these methods since the strength of the primary dynamic stall vortex was significantly reduced. It was, furthermore, illustrated that these methods aid in the lift recovery after separation, leading to reduced stall intensity and post-stall load fluctuations. On the other hand, the cavity was observed to consistently delay the unsteady separation. However, the primary vortex structure was not affected to large degree and, therefore, the stall intensity was similar to the baseline airfoil. Out of these three methods, it is proposed that the vortex generators and the novel elevated wire concept can be used to control the process of dynamic stall on wind turbine blades. These methods are not only easier to implement on existing blades, but also improve the steady-state performance of the airfoil through sustained lift and reduced drag, even at high angles of attack.

The research presented in this thesis aims to improve the unsteady stalling conditions of wind turbine blades. This is accomplished by minimizing the primary dynamic stall vortex lift generated during pitch-up and reducing the abrupt lift-decay after separation. The thesis presents a comprehensive review of dynamic stall on wind turbine blades as well as investigates previous attempts in controlling the unsteady separation. The new research conducted in the thesis has been presented in the form of journal manuscripts, arranged in an order that will assist the development of ideas. The research as a whole provides renewed insight into dynamic stall control on wind turbine blades.

DECLARATION

I certify that this work contains no material which has been accepted for the award of any other degree or diploma in my name, in any university or other tertiary institution and, to the best of my knowledge and belief, contains no material previously published or written by another person, except where due reference has been made in the text. In addition, I certify that no part of this work will, in the future, be used in a submission in my name, for any other degree or diploma in any university or other tertiary institution without the prior approval of the University of Adelaide and where applicable, any partner institution responsible for the joint-award of this degree.

I give consent to this copy of my thesis when deposited in the University Library, being made available for loan and photocopying, subject to the provisions of the Copyright Act 1968. The author acknowledges that copyright of published works contained within this thesis resides with the copyright holder(s) of those works.

I also give permission for the digital version of my thesis to be made available on the web, via the University's digital research repository, the Library Search and also through web search engines, unless permission has been granted by the University to restrict access for a period of time.

_____ _____

Amanullah Choudhry Date

ACKNOWLEDGMENTS

All knowledge belongs to Him, the Creator of all things, and that is why all the beginnings, and all the ends, and everything between leads one to acknowledge that the universe, with all its secrets, is the creation of a Mastermind, a Scientist unlike any other. Hence, I begin by thanking God the Almighty for guiding me throughout this journey and inspiring me for seeking knowledge.

I would like to express my utmost gratitude to my supervisors, Dr. Maziar Arjomandi and A/Prof. Richard Kelso. Without your help, guidance and patience throughout, this undertaking would have been impossible for me. Thank you for teaching me so much through these four long years and guiding me through the rough terrains of academic research.

I would also like to thank the Mechanical Engineering Workshop staff, especially Garry Clarke, and Ryan Leknys for assisting me with the design of my experimental rig. Also, I would like to thank the staff of Electronics and Instrumentation workshop for helping me with the instrumentation of my equipment. I would also like to thank William Constantine for his help in arranging for appropriate computing resources for the research.

To my father, Dr. Sanaullah Choudhry, I reserve the deepest gratitude for believing in me and for being there whenever I needed you and for constantly supporting me and guiding me. And to my mother, Mrs. Tahira K. Choudhry, thank you for all the midnight prayers that you sent, and keep sending, my way and for all the love and support. I would

not have been able to do this without you two. Thank you for all your support and love throughout this journey and throughout my life.

I would also like to thank all six of my brothers for helping me in different ways throughout this journey, especially my elder brother Omer Choudhry. You were always there for me, to inspire me and guide me and share with me in all my worries, thank you so much for being there.

In the end, I would like to thank my wife, Sara Mansoor. Without you, I would not be here. Thank you for all your patience, love and care during this undertaking, for always being there for me and for always reaffirming my faith. Words cannot express my appreciation and thanks for the love and kindness you have shown me.

CONTENTS

CHAPTER 1

INTRODUCTION

1.1 Motivation and Perspective

Energy and global warming are two of the most important challenges that we are facing in the current century. With the ever-increasing rise of worldwide energy consumption, most electricity today is being generated by burning limited fossil fuel reserves, such as coal and natural gas. However, this results in the degradation of the environmental conditions of our planet, due to increased emissions and rapid accumulation of greenhouse gases in the atmosphere. The buildup of these greenhouse gases in the atmosphere has resulted in a global temperature rise of 1^{o} Celsius, over the last century [1]. Due to this increase in the global temperature levels, catastrophic climate changes are being observed, worldwide. These include an increase in the global rainfall, resulting in floods and droughts, and an increase in the global sea levels by 100-

200mm due to melting of polar ice caps over the past century [2]. With the rapidly dwindling reserves of fossil fuel, and in an attempt to reduce the greenhouse gas emissions, an international collaborative effort is now being directed towards clean and renewable energy sources. The Kyoto Protocol is an international agreement, chartered under the United Nations Framework Convention on Climate Change [3], that commits the partner nations to decrease their national emission levels. Since wind energy itself does not lead to any detrimental emissions, and is readily available, most governments are using it as a means to reduce their national emission levels, as well as to meet their respective energy demands. Several countries, around the globe, have approved plans for development of their individual wind sectors and have set goals, and provided subsidies, towards the development of the industry. This has resulted in a large and rapid growth of the wind energy sector globally and it is currently the fastest growing renewable energy source is the world. Global wind generation capacity is now approaching 320 Gigawatts at the end of 2013, according to the World Wind Energy Association [4]. On the other hand, estimates indicate that the overall global potential for onshore wind energy is between 20×10^9 to 50×10^9 Megawatt-hours, which is substantially larger than the current electricity needs of the entire world [5]. Therefore, the global wind energy resources have the potential to provide for all the energy demands of the world as well as improve the environmental conditions, by reducing the greenhouse gas emission levels.

The growth of the wind industry primarily stems from the fact that wind turbines are the lowest-cost renewable source in the world that are capable of being deployed at a large scale to meet the ever-increasing global electricity demands [6]. However, a major barrier towards the growth of the industry in the future is the severe competition it has to

face with conventional energy sources [6]. Despite the recent progress made in deploying wind energy on a global scale, the sector still has a long way to go to become the energy source of choice. In fact, according to the International Energy Agency, long-term research and development needs to be undertaken for the wind energy sector to maintain its economic benefit in the future [7]. According to an estimate, cost reductions of approximately 30% are required if wind energy is to provide 10% of world electricity by the year 2020 [7]. Further to this, government incentives need to be maintained for the sector to further flourish.

One of the earlier methods to improve the cost-effectiveness of wind turbines resulted in a rapid increase in the rotor size [8]. Since wind turbines 'capture' the wind, a larger rotor size implied more energy production. In fact, the largest turbines being designed now reach an approximate capacity of 5 Megawatts, with rotor diameter exceeding 120 meters [9]. This rapid increase in the size of wind turbines is motivated to decrease the Cost of Energy (COE) of the turbine [10]. The COE is a simple concept and is governed by three independent variables; the capital cost of deployment, the operations and maintenance (O&M) costs, and the lifetime energy capture of the turbine. One approach to decrease the COE is to locate turbines in locally concentrated groups, called wind farms, to take benefit of geographically-limited and profitable wind resources. Such an arrangement not only results in improving the lifetime energy capture of the turbines, but also results in the reduction of O&M costs, due to a concentration of the maintenance equipment and spare parts on the site [11]. Reductions in COE are also possible by improving the manufacturing practices for the turbines, in order to reduce the capital costs associated with the deployment of turbines. Further reductions can be attained by improving the reliability of

turbines, in order to avoid any downtime; thereby, further improving the lifetime energy capture and reducing the O&M costs.

However, there are several issues associated with the operating conditions of wind turbines that hinder improvements in turbine reliability. First, and foremost, is that wind turbines inherently operate in the lowest parts of the atmosphere, typically called the Atmospheric Boundary Layer (ABL). The ABL is an important concept and plays a vital role not only in the design of wind turbines but also in the design of multistory building, towers and bridges. It is a turbulent boundary layer, that envelopes the planet, with the turbulent intensity decreasing and the wind speed increasing with the height [11]. These factors are the prime motivations of the large tower heights that are commonly seen for commercial wind turbines nowadays. Hence, the ABL directly determines the wind turbine performance at a particular height above the surface. On the other hand, it also influences the fatigue life of the wind turbine, due to varying wind speeds with height as well as the turbulent fluctuations in the wind speed and direction. Operation in the ABL therefore effects the power production and fatigue life of wind turbines, due to flow separation and time-varying loads, respectively.

Secondly, due to the often compact arrangement of commercial wind turbines, most turbines regularly operate in the wakes of other wind turbines. The wake behind a wind turbine has been identified as a system of complex turbulent flows with rotational motion being imparted by the turbine blades [12-15]. Two major issues have been found to be associated with operation of a turbine in the wake. The first is the significant increase in the turbulence intensity in the wake which results in increased unsteady loads on downstream wind turbines operating therein. The second is the velocity deficit produced by the upstream wind

turbine, through energy extraction from the wind, which results in reduced power productions for the downstream wind turbines. All these factors contribute to the increase in the COE of wind turbines by increasing the O&M costs and decreasing the lifetime energy capture of the turbines. Therefore, in order to improve the economic viability of the wind energy sector, these issues need to be further studied.

Towards this end, the present thesis focusses on one of these issues, namely the reduction of the unsteady loads on wind turbine blades. A major source of such unsteady loads is due to the phenomenon of dynamic stall, sometimes referred to as the 'unsteady separation' [16]. Dynamic stall is generally considered as the delay in conventional flow separation due to rapid changes in the sectional angle of attack of the blades [17]. The process is generally characterized by the formation of a large leading edge vortex structure on the upper surface of the blade section, called the dynamic stall vortex (DSV). The vortex is considered to be the cause of the undesirably high increase in lift and drag that is generally observed during the unsteady separation. This large increase in the forces can cause excessive bending loads on the turbine blades. As soon as the vortex convects downstream over the surface of the blade, and sheds into the wake, the airfoil goes into a state of abrupt stall. The ensuing rapid lift decay results in blade vibrations and, therefore, causes fatigue damage and performance loss of the turbine. The flow afterwards reattaches only when the angle of attack is brought down to a small enough value, which is generally not possible due to the blade twist.

Industrial wind turbine designs do not cater for the unsteady effects associated with dynamic stall [6]. Surmounting evidence now exists indicating that the dynamic loads on wind turbine blades need to be adequately understood and predicted in order to improve the energy

yield and fatigue life of wind turbines [18]. Dynamic stall in wind turbines can be caused by time-varying inflow, yaw misalignment between the rotor-axis and the oncoming flow, tower shadow, vertical wind shear and even small-scale turbulence [19]. In fact, according to a conservative estimate, it was found that for a yawed horizontal axis wind turbine under steady inflow, dynamic stall occurred for over 50% of the recorded cycles [20]. The process can result in extremely large loads that, in some cases, are even capable of breaking the blades [21]. Furthermore, the deep stall that is established after the primary dynamic stall vortex is shed and the subsequent process of vortex shedding, can lead to vibrations of the blade, adversely affecting the fatigue life of the turbine. It has, furthermore, been speculated that the interaction between the blades of a wind turbine and the DSV can lead to excessive noise production, posing a significant health risk to nearby residents [22]. Therefore, the primary motivation of the research presented in this thesis is the reduction of unsteady loads generated on wind turbine blades. This research aims not only to improve the energy production of wind farms in general but also to improve the lifespan of wind turbines.

1.2 Objectives of the Research

The primary objective of the research presented in this thesis is to develop understanding and knowledge regarding dynamic stall on wind turbine blades and investigate methods to mitigate the negative effects of unsteady separation on the blades. In order to accomplish this ambitious task, it is, first of all, important to understand the occurrence of dynamic stall on wind turbine blades. Such an understanding will aid in better determining the severity and incidence of the unsteady separation process on wind turbine blades operating in freestream conditions. Since wind turbines seldom operate in isolation, it is also

important to understand the effects of wake on dynamic stall occurrence on wind turbines operating in tandem to each other. The research will, therefore, not only enhance the understanding of the causes of unsteady separation for wind turbine applications, but also aid in determining the appropriate locations along the turbine blade where control might be necessary to mitigate the effects of the unsteady separation.

In order to develop control methodologies pertaining to the mitigation of unsteady separation on wind turbine blades, it is vital to gain a deeper understanding of the process itself. Even though extensive studies into the process of dynamic stall have already been conducted in the past, several avenues of further research exist. In particular, the causes of unsteady lift generation during the process of dynamic stall are not well-understood. Moreover, a limited insight is available for the post-stall behavior of airfoils undergoing dynamic stall. This is primarily because most studies have focused on the dynamic stall process for sinusoidally pitching airfoils, a type that is generally encountered on retreating helicopter blades [23, 24]. In this case, the blade returns to the initial angles of the cycle and, therefore, does not operate in the post-stall conditions for extended amounts of time. On the other hand, it is convenient to study the post-stall variation in loads when the airfoils are pitched to a predetermined maximum angle of attack and allowed to undergo separation. Such an unsteady separation can be encountered on wind turbine blades due to prolonged gusts of large length scale or persistent wind direction changes. Even though the differences between the two cases are subtle, a deeper understanding of the lift characteristics during the dynamic stall process is still necessary at both pre- and post-stall conditions.

The final objective of this research is to investigate dynamic stall control methodologies that are suitable for wind turbine applications. It

is desirable to improve the unsteady post-stall conditions of wind turbine blades since this can aid in improving the performance and fatigue life of the blades. The control methods should therefore be selected based firstly on their effectiveness and secondly on the ease with which they can be implemented on currently operational wind turbines.

1.3 Chronology of the Thesis

A brief chronology of the thesis is presented in the current section. The thesis is a collection of manuscripts that have been published, accepted for publication or are currently undergoing the review process for publication in international peer-reviewed journals. These manuscripts constitute the chapters of the thesis and cover the progress made during the course of the current study. This includes the development, validation and implementation of an analytical method to determine the occurrence of dynamic stall on wind turbine blades. Next, a detailed investigation into the effects of wakes on downstream wind turbines and the occurrence of unsteady separation is presented. Following this, the lift characteristics during steady and unsteady separation processes, particularly the effects of prominent flow features, are discussed in detail. Finally, based on an improved understanding of the unsteady separation, three passive flow control techniques are evaluated, specifically for wind turbine applications. Following is brief outline of the current thesis.

In Chapter 2 of the thesis, a detailed framework for the present study has been established, based on review of seminal studies that have been conducted in the past. The chapter provides the basics of wind turbine aerodynamics and explores the flow field in the vicinity of the turbine blade. In addition, the operating conditions of the wind

turbines have been explored and the effects of changing wind conditions on wind turbine blades have been discussed. Finally, a detailed description of the dynamic stall process is presented, as well as an extensive and critical review of the different control methodologies.

Chapter 3 presents the concepts relating ambient wind conditions to the occurrence of dynamic stall on wind turbine blades. An analytical model has been developed and is presented in the article that constitutes the chapter. The model computes the rate at which angle of attack changes due to the changes in wind speed and direction. It, furthermore, takes into account rotor parameters such as the type of foil used, the height of the rotor hub above the ground and the rotational speed of the rotor. Using ambient wind conditions as an input to the model, the occurrence of dynamic stall on wind turbines operating in freestream has been determined. The chapter introduces the important concept of limiting reduced frequency that can be used as a precursor to dynamic stall occurrence.

In Chapter 4, the effects of wake on downstream wind turbines are discussed. For this study, the wake properties, acquired through numerical analysis [14, 15], are used to determine the occurrence of dynamic stall on downstream wind turbines. These studies have been conducted primarily to quantify the occurrence of unsteady separation on wind turbine blades as well as to determine the primary causes of unsteady separation on the blades of turbines operating in the wake of upstream turbines. These results can also be used in the design phase of wind farms to accurately map-out the regions of the blade where control is likely to be necessary.

Chapter 5 of the thesis focusses on the process of steady–state separation observed on thick airfoil sections. In the article that

constitutes this chapter, a detailed numerical investigation of steady-state operation and stalling behaviour of the NACA 0021 airfoil is presented. This study was principally motivated from earlier wind tunnel experiments on the same airfoil where peculiar aerodynamic features such as increased lift-slope as well as an abrupt leading edge stall were observed. It is conventionally understood that thick airfoil sections undergo a smooth stall, where flow separation initiates at the trailing edge of the airfoil and gradually moves upstream. However, during experiments, a rapid loss of lift was observed on the thick airfoil, similar to that observed on thin airfoils [25]. Therefore, in this chapter, numerical studies are presented to explain this aspect of the thick airfoil sections. It was observed that a long separation bubble on the upper surface of the foil leads to an apparent camber effect that modifies the lifting characteristics of the airfoil section. Furthermore, the bursting of this long separation bubble leads to the sharp fall in lift that was observed during previous experimental studies. An insight into these characteristics, and the influence of such flow features, can aid in better understanding the lift behaviour of an airfoil undergoing dynamic stall. The camber effect associated with the separation bubble can, therefore, be translated to an increased camber effect due to the formation of the dynamic stall vortex.

In Chapter 6, a detailed account of the dynamic stall process is presented. The study aims to improve the current understanding of the unsteady separation process, particularly the lift behaviour, in order to propose appropriate control methods for its mitigation on wind turbine blades. The analysis is based on the review of seminal studies in the field and experiments, involving pressure measurements and flow visualization of airfoils undergoing dynamic stall. An in-depth insight into the non-linear lift behaviour of the NACA 0021 airfoil during the

unsteady stall process is discussed in detail. The lift curve is subdivided into smaller segments and each segment is analysed separately to gain a deeper understanding of the dynamic stall process.

Chapter 7 of the thesis consists of an article that discusses the dynamic stall control objectives, specifically for the wind turbine industry. It furthermore illustrates the primary control requirements necessary for the appropriate mitigation of the negative effects of the unsteady separation process on thick airfoil sections. After establishing the control objectives and requirements, the article then discusses the use of three different passive control methodologies that can be used to improve the unsteady stalling behaviour of thick airfoils and, in extension, the wind turbine blades. These methods have been selected based on their ease of implementation on wind turbine blades as well as due their effects on the dynamic stall process.

The final chapter of the thesis, Chapter 8, summarizes the significant findings and the chief conclusions of the works undertaken during the course of this research. In addition to this, several avenues of further research into the subject are proposed.

1.4 Publications arising from the Research

The research discussed in the present thesis has resulted in publications and articles, including publications in peer-reviewed conference proceedings and international journals. These manuscripts are closely related to the topic of the research presented in the current thesis. Following is the list of manuscripts, published and otherwise, that have been produced as part of this research:

1.4.1 Published Journal Articles:

1) **Choudhry, A.**, Arjomandi, M., & Kelso, R. (2013). Horizontal axis wind turbine dynamic stall predictions based on wind speed and direction variability. Proceedings of the Institution of Mechanical Engineers, Part A: Journal of Power and Energy, 227(3), 338-351.
2) **Choudhry, A.**, Leknys, R., Arjomandi, M., & Kelso, R. An Insight into the Dynamic Stall Lift Characteristics. Experimental Thermal and Fluid Science, DOI: http://dx.doi.org/10.1016/j.expthermflusci.2012.07.006.
3) **Choudhry, A.**, Mo, J. O., Arjomandi, M and Kelso, R. (2014). Effects of Wake Interaction on Downstream Wind Turbines. Wind Engineering, 38(5), 535-548.
4) **Choudhry, A.**, Arjomandi, M., & Kelso, R. (2014). A study of long separation bubble on thick airfoils and its consequent effects. International Journal of Heat and Fluid Flow, 52, 84-96.

1.4.2 Submitted Journal Articles:

5) **Choudhry, A.**, Arjomandi, M., & Kelso, R. (2014). Methods to Control Dynamic Stall for Wind Turbine Applications.

1.4.3 Refereed Conference Articles:

1) **Choudhry, A.**, Mo, J. O., Arjomandi, M., & Kelso, R. M. (2012). Effects of spacing between wind turbines on blade dynamic stall. In Australasian Fluid Mechanics Conference (18th: 2012: Launceston, Tasmania).
2) **Choudhry, A.**, Arjomandi, M., & Kelso, R. M. (2012). Estimation of dynamic stall on wind turbine blades using an analytical model. In Australasian Fluid Mechanics Conference (18th: 2012: Launceston, Tasmania).

3) **Choudhry, A.**, Mo, J. O., Arjomandi, M., & Lee, Y. H. (2012). Turbulent wake study of NREL phase VI wind turbine in a virtual wind tunnel using Large Eddy Simulation. In Proceedings: the 7th Australasian Congress on Applied Mechanics (ACAM 7), 9-12 December 2012, the University of Adelaide, North Terrace Campus/National Committee on Applied Mechanics of Engineers Australia (p. 837). Engineers Australia.
4) Hansen, K.L., Kelso, R. M., **Choudhry, A.** & Arjomandi, M. (2014). Laminar Separation Bubble Effect on Lift Curve Slope of an Airfoil. In Australasian Fluid Mechanics Conference (19th: 2014: Melbourne, Victoria).
5) **Choudhry, A.**, Arjomandi, M., & Kelso, R. M. (2014). Lift curve breakdown for airfoil undergoing dynamic stall. In Australasian Fluid Mechanics Conference (19th: 2014: Melbourne, Victoria).

In addition, the author of the present thesis was closely involved in studies related to the development of wake behind a wind turbine using numerical techniques. This study was used to understand the effects of turbine wakes on the occurrence of dynamic stall on downstream wind turbines. The articles produced as part of this work are not included in this thesis. However, these are listed as follows:

1) Mo, J. O., **Choudhry, A.**, Arjomandi, M., & Lee, Y. H. (2013). Large eddy simulation of the wind turbine wake characteristics in the numerical wind tunnel model. Journal of Wind Engineering and Industrial Aerodynamics, 112, 11-24.
2) Mo, J. O., **Choudhry, A.**, Arjomandi, M., Kelso, R., & Lee, Y. H. (2013). Effects of wind speed changes on wake instability of a wind turbine in a virtual wind tunnel using large eddy simulation. Journal of Wind Engineering and Industrial Aerodynamics, 117, 38-56.

1.5 Thesis format

The thesis has been submitted as a collection of the above manuscripts according to the formatting requirements of the University of Adelaide. The printed and online versions of the thesis are completely identical in all regards. The online version of the thesis is available as a PDF file on the University of Adelaide Library Website and can be viewed in its correct intended fashion using Adobe Reader 9.

1.6 References for Chapter 1

[1] US-EPA, Climate Change Indicators in the United States, 2006.

[2] E. Denny, A Cost Benefit Analysis of Wind Power, University College Dublin, Ireland, 2007.

[3] Kyoto-Protocol, United Nations Framework Convention on Climate Change. Available: www.unfccc.int, 1992

[4] Half-year Report - 2013, The World Wind Energy Association, 2013.

[5] G.M. Joselin Herbert, S. Iniyan, E. Sreevalsan, S. Rajapandian, A review of wind energy technologies, Renewable and Sustainable Energy Reviews, 11(6) (2007) 1117-1145.

[6] S. Tonio, Improving BEM-based Aerodynamic Models in Wind Turbine Design Codes, Dutch: Delft University of Tecnology, (2007).

[7] S.E. Thor, P. Weis-Taylor, Long-term research and development needs for wind energy for the time frame 2000–2020, Wind Energy, 5(1) (2002) 73-75.

[8] V. Maldonado, J. Farnsworth, W. Gressick, M. Amitay, Active control of flow separation and structural vibrations of wind turbine blades, Wind Energy, 13(2 3) (2010) 221-237.

[9] J.M. Jonkman, S. Butterfield, W. Musial, G. Scott, Definition of a 5-MW reference wind turbine for offshore system development, National Renewable Energy Laboratory Golden, CO, 2009.

[10] S.J. Johnson, C. Van Dam, D.E. Berg, Active load control techniques for wind turbines, SAND2008-4809, Sandia National Laboratories, Albuquerque, NM, (2008).

[11] J.F. Manwell, J.G. McGowan, A.L. Rogers, Wind energy explained, Wiley Online Library, 2002.

[12] S. Wagner, R. Bareiss, G. Guidati, Wind turbine noise, Springer-Verlag, Berlin/Heidelberg, Germany, 1996.

[13] J.O. Mo, Y.H. Lee, Numerical simulation for prediction of aerodynamic noise characteristics on a HAWT of NREL phase VI, Journal of Mechanical Science and Technology, 25(5) (2011) 1341-1349.

[14] J.O. Mo, A. Choudhry, M. Arjomandi, Y.-H. Lee, Large eddy simulation of the wind turbine wake characteristics in the numerical wind tunnel model, Journal of Wind Engineering and Industrial Aerodynamics, 112 (2013) 11-24.

[15] J.O. Mo, A. Choudhry, M. Arjomandi, R. Kelso, Y.-H. Lee, Effects of wind speed changes on wake instability of a wind turbine in a virtual wind tunnel using large eddy simulation, Journal of Wind Engineering and Industrial Aerodynamics, 117 (2013) 38-56.

[16] C.P. Butterfield, D. Simms, G. Scott, A. Hansen, Dynamic stall on wind turbine blades, National Renewable Energy Lab., Golden, CO (United States), 1991.

[17] L.W. Carr, M. Chandrasekhara, Compressibility effects on dynamic stall, Progress in Aerospace Sciences, 32(6) (1996) 523-573.

[18] A. Hansen, C. Butterfield, X. Cui, Yaw loads and motions of a horizontal axis wind turbine, Journal of Solar Energy Engineering, 112(4) (1990) 310-314.

[19] J.W. Larsen, S.R.K. Nielsen, S. Krenk, Dynamic stall model for wind turbine airfoils, Journal of Fluids and Structures, 23(7) (2007) 959-982.

[20] D.E. Shipley, M.S. Miller, M.C. Robinson, Dynamic stall occurrence on a horizontal axis wind turbine blade, National Renewable Energy Lab., Golden, CO (United States), 1995.

[21] M. Sun, S. Sheikh, Dynamic stall suppression on an oscillating airfoil by steady and unsteady tangential blowing, Aerospace Science and Technology, 3(6) (1999) 355-366.

[22] A. Laratro, M. Arjomandi, R. Kelso, B. Cazzolato, A discussion of wind turbine interaction and stall contributions to wind farm noise, Journal of Wind Engineering and Industrial Aerodynamics, 127 (2014) 1-10.

[23] F.D. Harris, R.R. Pruyn, Blade StallHalf Fact, Half Fiction, Journal of the American Helicopter Society, 13(2) (1968) 27-48.

[24] N.D. Ham, M.S. Garelick, Dynamic stall considerations in helicopter rotors, Journal of the American Helicopter Society, 13(2) (1968) 49-55.

[25] K.L. Hansen, Effect of leading edge tubercles on airfoil performance, Ph.D Thesis, University of Adelaide, (2012).

CHAPTER 2

RESEARCH BACKGROUND

2.1 Wind Turbine Operation

Wind turbines are the devices that extract the kinetic energy of the wind and convert this to electrical energy. When deployed on a large scale, wind turbines are a viable and commercial source of electricity production. Even at a small scale, with rotor diameters of only a several meters, wind turbines can be utilized to provide decentralized energy supply for rural and urban environments. Therefore, turbines can be classified according to their size as small- and large-scale, based on their intended purpose [1, 2]. Further, classifications can be based on orientation of the rotor axis with respect to ground, such as vertical or horizontal axis wind turbines [3, 4]. Categorizations can also be based on the primary force driving the turbine rotor, such as drag- and lift-type turbines [5]. Moreover, horizontal-axis turbines can be further

categorized based on the rotor orientation relative to the tower as upwind or downwind [6]. Most wind turbines used commercially today are generally of a large scale, comprising a rotor axis that is aligned with the oncoming wind, with an upwind rotor configuration, and using the lift force as the primary driving mechanism for the rotor. Generally abbreviated as HAWT, for horizontal axis wind turbine, such turbines are the topic of the current thesis.

2.1.1 Components of a Turbine

A horizontal axis wind turbine generally comprises of several subparts that convert the wind power to electricity. The primary subparts of a HAWT are schematically illustrated in Figure 2.1. The most fundamental of these is the rotor, consisting conventionally of 3 blades, which is based on a 'propeller-like' design [4]. The design aids the control of rotor speed and power output by allowing the blades to pitch about their longitudinal axes. The implementation of this mechanism is necessary for large scale wind turbines to optimize the power production. However, for small scale wind turbines, this method is not cost effective and, therefore, not employed [7]. Instead, most small scale wind turbines are stall-controlled at higher wind speeds. The rotor blades are connected to the hub which also houses the blade pitch control mechanism, if applicable. These parts are, in turn, connected to the nacelle of the turbine. The nacelle houses the gearbox, generator and the rotor brakes as well as mechanisms for yaw control and other switchboards and control systems. This entire system is then mounted on a tower structure. Generally, for large scale wind turbines, the power cables and the transformers are placed within the tower. The tower is then placed in a deep foundation to reduce the vibrations in the tower, caused by flow-tower interaction.

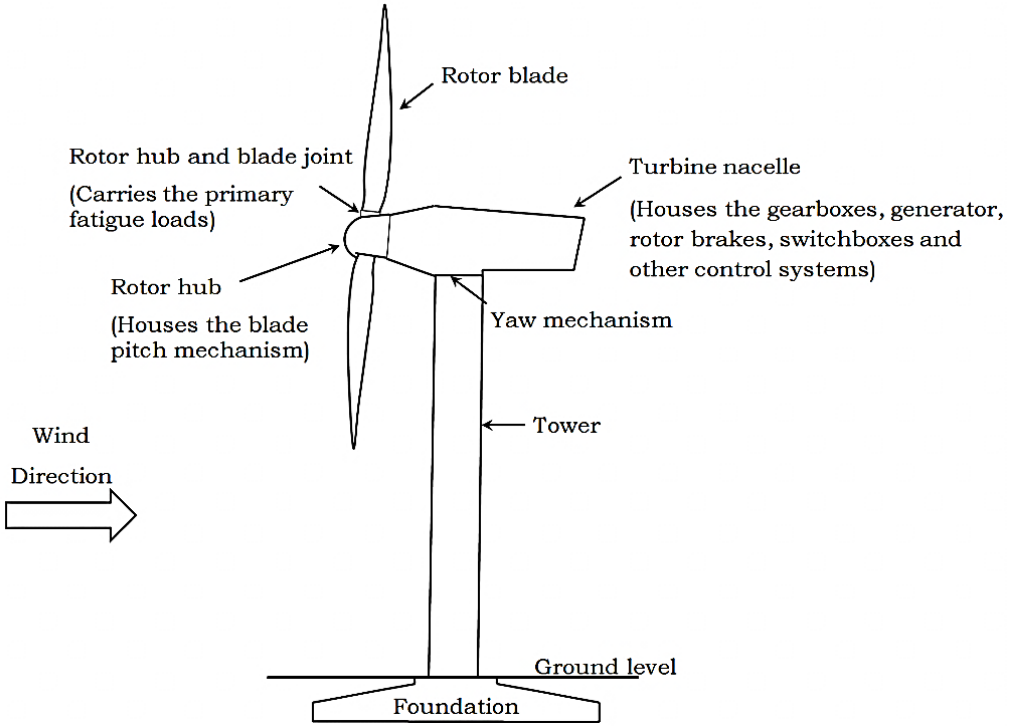

Figure 2.1 - Primary subparts of a horizontal axis wind turbine.

Most modern wind turbine blades are designed using airfoil families that have been tested and validated in reliable wind tunnel experiments. The blade tip is designed using a thin airfoil section, for larger lift-to-drag ratios (L/D), whereas, the root region is designed using a thicker version of, generally, an airfoil from the same family, for higher structural strength. Catalogues of 2D airfoils, such as those produced by Miley [8] and Bertagnolio *et al.* [9], are used by designers of wind turbines. Earlier, in the 1970s and 80s, the NACA series airfoils were used to design turbine blades, similar to helicopter rotor blades. However, recently, foils tailored specifically for wind turbine applications are being designed and used [10-17]. The general design objective of wind turbine airfoils is a high L/D ratio and less susceptibility to leading edge roughness effects [18-20]. It is also desirable for the airfoils of a wind turbine to have appropriate stalling characteristics. This is a

primary requirement for most stall-regulated wind turbines but recently is also a necessity for large-scale turbine rotors. Poor stalling characteristics, such as a sharp decrease in the lift after flow separation, may lead to fatigue damage in the rotor-hub joint and undesirable fluctuations in the power output.

2.1.2 Principles of Turbine Aerodynamics

Being the primary component of a wind turbine, and the first element in the chain of functional components, the rotor plays a critical role in determining the performance and system dynamics of the entire wind turbine [21]. Furthermore, it constitutes one of the most fundamental aspects of a wind turbine design process and acutely influences the cost effectiveness of the entire system [13, 22]. Therefore, it is of vital importance to understand the flow field in the vicinity of a turbine blade, for accurate predictions of the turbine performance.

The flow approaching a wind turbine can be considered as a streamtube, where the mass flow rate at each cross-section of the tube can be assumed constant. As the flow nears the turbine, it slows down, due to the presence of the turbine, resulting in an expansion of the streamtube [7]. Each rotor blade of the turbine may be considered as a wing, with each section comprising of an airfoil. As illustrated in Figure 2.2, in the blade cross-sectional view, the resultant velocity experienced by a turbine blade (V_R) is constituted by the wind velocity vector (V_W) and the head wind. The magnitude of the head wind depends on the rotational speed of the rotor (ω) and the distance from the hub (r). Consequently, the angle between the resultant velocity vector, as well its magnitude, and the airfoil is governed by the magnitude of the wind speed, its orientation with respect to the turbine rotor and the rotational speed of the rotor. The air flowing around the blade, due to the bound

vortex circulation, results in the production of lift and drag forces, as shown in Figure 2.2. The combined action of these forces results in the torque output, which leads to the rotation of the turbine blades, and the thrust force, in the direction of the oncoming wind. The rotation is transmitted to the generator, through a series of gears, and results in the sustained power production of the turbine.

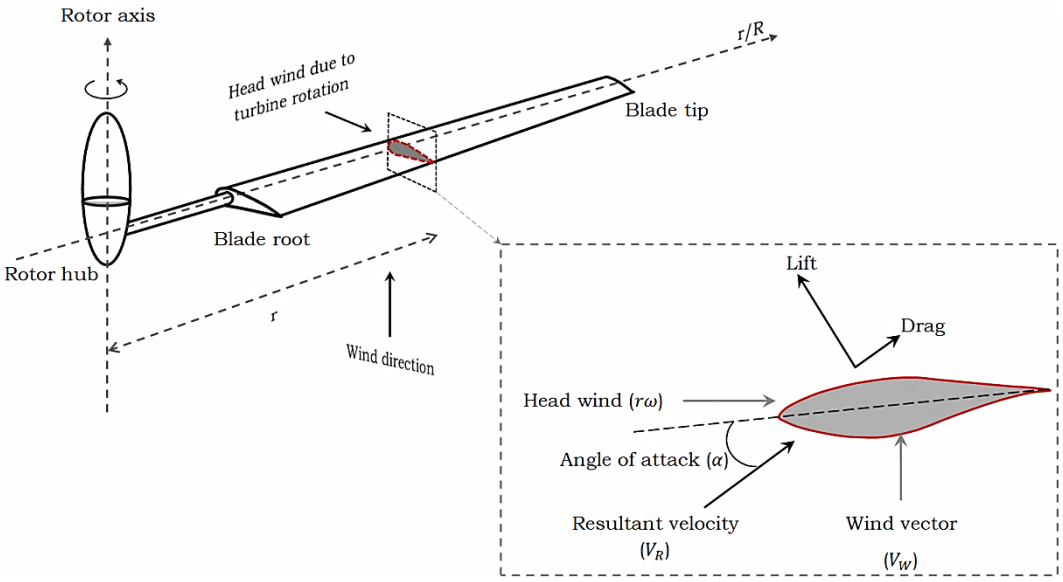

Figure 2.2 - A sketch of blade interaction with oncoming wind.

It can be seen from Figure 2.2 that the angle of attack along a turbine blade varies, resulting in a multitude of different flow scenarios along the blade length. A wind turbine designer needs to be aware of these flow features along the blade and select the appropriate airfoil for each section of the blade. However, even with the dedicated methods to design suitable sectional profiles, such as the Eppler code [23], the design methodologies employed for the entire rotor are still lacking [24]. The basic methodology used for the design of turbine rotors, the Blade Element Momentum (BEM) approach, assumes that the velocity component along the turbine span is comparatively smaller, in

magnitude, compared to the chordwise component and, therefore, it can be ignored. The consequence of this assumption is that the flow can be treated primarily as two dimensional at each cross-section of the blade and can be modeled as such [25]. However, it well known that the BEM approach does not take into account the unsteady loads that can be encountered during routine turbine operation [22]. Furthermore, it undermines the flow interaction along a blade length leading to under-predictions of both the power produced and the blade loading. This has been observed in a blind comparison study, organized by the National Renewable Energy Laboratories (NREL) in the year 2000 [26], where large inconsistencies were observed in the prediction capabilities of different codes used for turbine modelling and design [27]. This primarily stems from a lack of understanding of certain aerodynamic features on the turbine blade in relation to wind turbines [28].

2.1.3 Prominent Flow Features on a Turbine Blade

2.1.3.1 Delayed Stall

Due to the rotation, a delayed stall effect is observed on the blades, particularly at inboard stations. It is believed that this delayed stall is caused by a spanwise flow that results in a Coriolis acceleration [29]. This leads to favorable chordwise pressure gradients, resulting in increased lift production and delayed flow separation [27, 30-36]. A streamline pattern, indicating the spanwise migration of flow, on the blade of the NREL phase VI wind turbine [37] is shown in Figure 2.3 at two different wind speeds. The flow was modelled using the $\gamma - Re_\theta$ transition model [38-40] using constant inflow velocities and turbulence levels, similar to the experiments [27, 41]. It can be observed that at the smaller velocity of 7m/s, the flow along the majority of the length of the blade is attached, apart from slight separation at the blade root, near the

trailing edge of the blade. The streamlines here can be seen to curl outwards, away from the hub, as indicated by the arrow heads. This attached flow, here, results from the smaller angles due to the smaller inflow velocity. However, as the angle of attack of the blade section increases due to an increase in the wind speed, the flow will start to separate, starting at the inboard stations. The flow separation will then progressively move towards the outboard stations of the turbine, as the wind speed increases. In Figure 2.3, the flow separation has spread along the entire length of the blade due to the high inflow velocity of 20 m/s. The low momentum separated flow is influenced by the centrifugal pumping effect due to the blade rotation, and extends radially outwards towards the outboard stations of the turbine. As can be observed, the effects of this spanwise migration are aggravated when large scale, albeit steady, flow separation occurs on the turbine blade at larger wind speeds. Similar observations were made by Xu and Sankar [42] using a hybrid method to study the three-dimensional flow field around NREL phase II and III rotors. The phase II rotor consisted of a rectangular planform wing with no twist and taper, whereas the phase III rotor employed the same wing with a non-linear twist distribution [43]. It was observed that during steady inflow, with no misalignment between the rotor and oncoming flow, the centrifugal pumping effect was pronounced at higher wind speeds due to increased flow separation.

Generally, empirical corrections, such as those due to Viterna and Corrigan [44], are applied to estimate the effects of delayed stall to some extent. However, as shown by Breton *et al.* [45], even these methods are susceptible to inaccuracies, in certain situations, in their prediction of three-dimensional flow effects on a turbine blade.

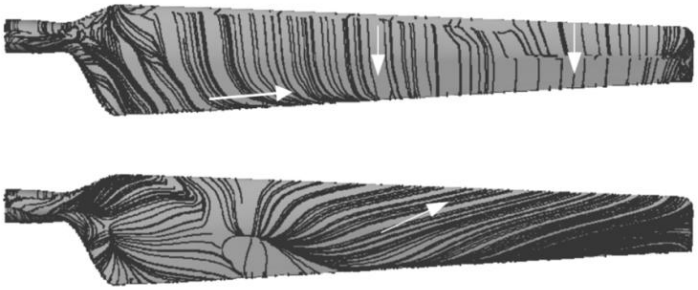

Figure 2.3 – Streamline curvature on the upper low pressure surface of the NREL phase VI wind turbine indicating the centrifugal pumping effect caused by the turbine rotation. The top is for the turbine operating at a wind speed of 7m/s whereas the bottom is for wind speed of 20m/s. The arrow heads indicate the primary direction of the streamlines. Extracted from [37].

2.1.3.2 Tip Vortex

Tip vortices are an important aerodynamic aspect of any finite-span wing. For wind turbines, the tip vortices play a significant role in the wake development and progression behind the turbine [46, 47]. These vortices are produced due to the pressure differential that exists between the upper and lower surfaces of the blade. The vortex grows quickly on the upper surface of the tip, due to flow leakage from the lower surface, as the blade starts moving. The low pressure cores of the helical tip vortex results in flow acceleration at the blade tip [48]. The core development, flow acceleration and entrainment of the adjacent flow are indicated in the velocity magnitude contours of the wing tip vortex structure in Figure 2.4, extracted from [49]. The primary contribution of the wing tip vortex is decreased angle of attack at the tip of the blade, due to a downwash effect [50]. The entrainment by the vortex structure and the reduced attack angles results in completely attached flow in this region of the blade. As will be seen in the later sections, the tip vortex principally governs the wake development behind a wind turbine.

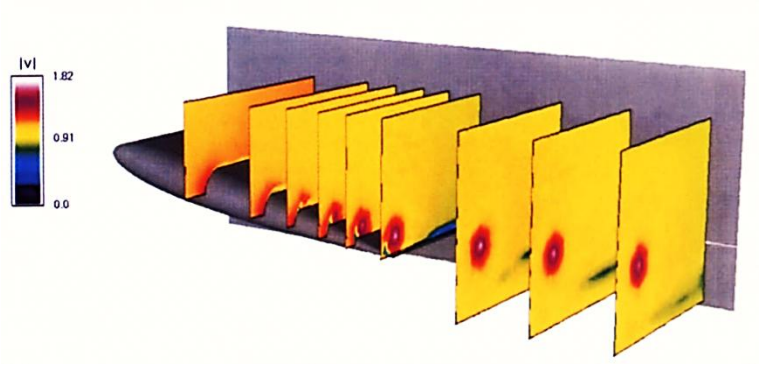

Figure 2.4 - Contours of experimentally-measured velocity magnitudes indicating the tip vortex structure on a finite wing [49].

2.1.3.3 Unsteady Flow Features

The final flow feature on turbine blades can be attributed to the unsteady environment, influenced by ground effects, with fluctuating wind speed and direction. For instance, it has been observed that yawed operation is one of the fundamental operating modes of a wind turbine and poses severe limitations on the performance and structural integrity of a turbine [51]. It is estimated that turbines can be exposed to up to ±30 degs of flow misalignment for a duration of several minutes [6]. In addition, the effects of yawed flow such as increased loading on the blades and skewed wake effects are not taken into account in commercial design codes [52, 53]. The primary effect of a yawed inflow, as well as other forms of turbulence, is the dynamic variation of the sectional angle of attack of the turbine blade. The sudden change in the sectional angle of attack results in the formation of a leading edge vortex that leads to increased loads on the turbine blades [54, 55]. These unsteady effects are more pronounced at the inboard stations of a wind turbine blade, due to larger angles of attack, as a consequence of blade twist, and smaller rotational speeds. The increased loads observed during this unsteady process can not only lead to fatigue damage on the

blade but can also cause performance inadequacies due to large flow separations.

2.1.4 Section Summary

The aerodynamics of wind turbine blades is largely different from fixed-winged vehicles. In fixed-wing vehicles, flow separation is avoided at all costs; whereas, in the case of wind turbines, separation is an intrinsic part of the turbine operation. The primary differences result from the variation of sectional angles of attack along the turbine blade, due to turbine rotation, as well as the uncertainty in atmospheric wind conditions. Therefore, higher aerodynamic lift, encountered due to the centrifugal pumping effects, is common on wind turbine blades, as is the flow influenced by tip vortices. Furthermore, turbines are subjected to atmospheric turbulence, such as wind shear due to ground effects and prolonged variations in wind direction, as well as the wakes of neighboring turbines. These factors can lead to unsteady effects, particularly at the inboard stations of the turbine blade. Therefore, in general, the flow field in the vicinity of the turbine can be broadly categorized into four main features, as shown in Figure 2.5, for turbines operating in atmospheric conditions:

1. Attached flow – Generally encountered at the mid-span of the blade and extending towards the tip locations, the attached flow is encountered on the turbine blade where the angles are not sufficiently large to cause flow separation and the rotor speeds are large enough to mitigate the unsteady effects due to inflow turbulence or other parameters. The attached flow region is primarily responsible for the sustained power productions of a wind turbine.
2. Tip flow – Encountered at the tip regions of the turbine blades, the flow is influenced due to the presence of the tip vortices that originate

as a result of the pressure differential on either sides of the blade. The tip vortices reduce the angle of attack near the tip, resulting in attached flow.

3. Centrifugal flow – Separated low momentum flow that is influenced by the centrifugal pumping effects due to turbine rotation, leading to favorable pressure distribution and higher lift, is generally observed at the inboard to mid-span of turbines. The centrifugal pumping effects are more pronounced when steady-state flow separation is encountered on a turbine blade during low turbulence conditions. However, the effects are less pronounced and shifted further towards the mid-span of the blade during normal operating conditions.
4. Unsteady flow - Primarily encountered at the inboard regions of turbine blades and can extend to mid-span locations due to increased levels of turbulence, the unsteady flow is characterized by large scale vortical structures near the leading edge of the blade. The vortex structures can result in increased lift. Furthermore, the process of vortex shedding can disrupt the power production as well as cause vibrations in the blade.

Therefore, a wind turbine blade is subjected to tip-vortex effects, an attached flow region, spanwise flow migration and unsteady effects at the same instant. The extent of each feature depends on the freestream wind conditions. It is important to consider these effects, and their dependence on freestream conditions, for efficient design of blades.

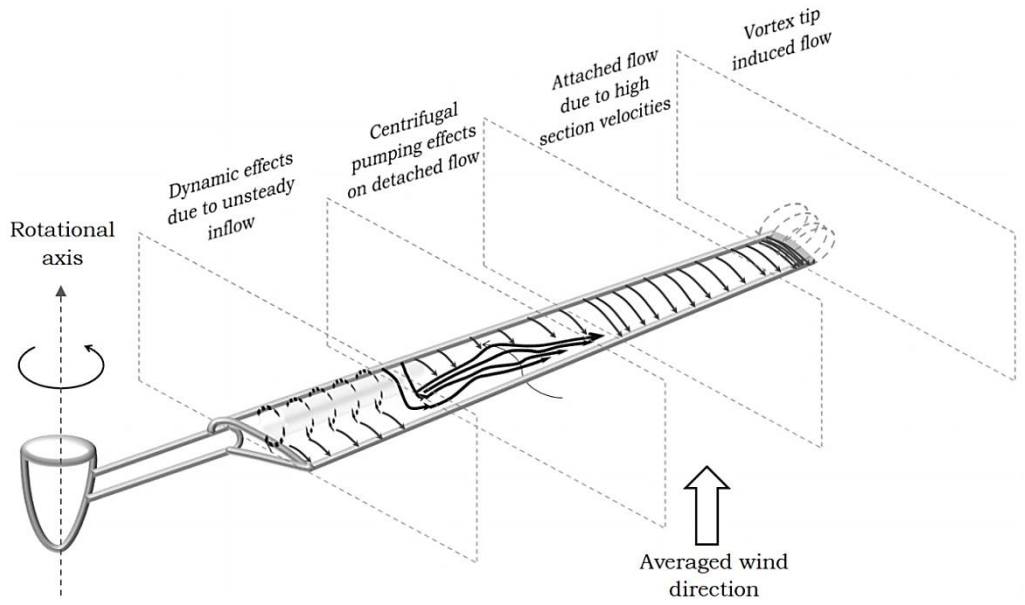

Figure 2.5 - A schematic illustration of the flow field patterns on a wind turbine blade. The diagram shows the four prominent flow features observed on a turbine blade. These include: the tip region, attached flow region, centrifugal flow region and unsteady flow region.

2.2 Turbine Operating Conditions

The unsteady flow field on a wind turbine blade can extend to a rather large portion of the blade, depending on the freestream conditions, and can therefore influence the forces and dynamics of the blade to a significant degree. The extent of unsteady flow can sometimes cover the entire blade during gust events or yaw-misalignment, due to increased variations in the sectional angles of attack. Therefore, it is prudent to understand the occurrence of the unsteady flow on wind turbine blades, and its dependence on the operating conditions of a turbine, to mitigate its detrimental effects on the performance and structural integrity of the blade. Therefore, in this section, a discussion regarding the operating conditions of a wind turbine is presented, including the atmospheric boundary layer and the wakes of upstream turbines.

2.2.1 The Atmospheric Boundary Layer

The atmospheric boundary layer, commonly abbreviated as ABL, is the lowest 1-2 kilometers of the atmosphere enveloping the planet [56]. It is region most influenced by the exchange of momentum, heat and water vapor. Turbulent motions that primarily exist in this region, transport atmospheric properties both horizontally and vertically, and can be of time scales exceeding one hour. The turbulent nature of ABL is fundamentally different from that observed in most wind tunnel studies [57]. However, the basic structure of the ABL is similar to a two dimensional turbulent boundary layer observed in wind tunnel experiments. Both have a distinct inner and outer region, where the outer region is mostly independent of the surface effects. For the ABL, the Coriolis force, due to earth's rotation, is important in the outer layer, known as the Ekman layer. In contrast, the flow in the inner layer, termed as the surface layer, is mainly dependent on the surface characteristics and is less affected by the rotation of the planet. The surface layer generally extends between 50 to 100 meters above the ground level. The mean properties of the flow such as wind speed, temperature and humidity experience their sharpest gradients in the surface layer. The structure of the ABL is shown in Figure 2.6, where it can be observed that the turbulence is superimposed on the mean wind profile [58]. The surface layer, as can be observed, is severely influenced by the surface roughness. These surface roughness elements can induce severe fluctuations in the wind speed at smaller heights, as well as increase the velocity gradient of the mean wind profile. However, as the height is increased, these turbulent fluctuations become smaller, especially in the Ekman layer.

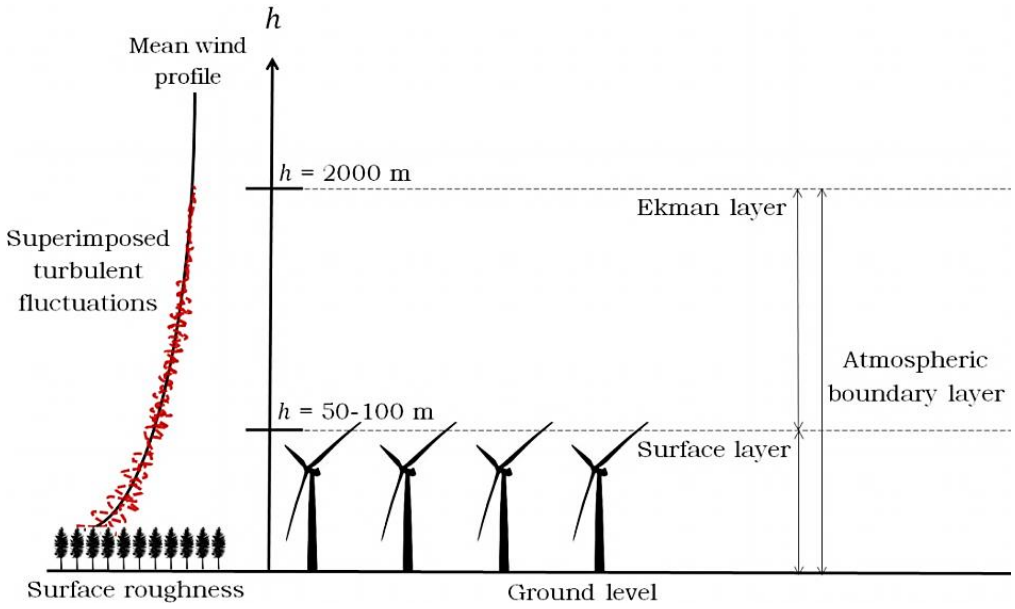

Figure 2.6 – The structure of the atmospheric boundary layer.

Wind turbines usually have tower heights ranging from 20-120m above the ground [59] and, therefore, operate consistently in the turbulent surface layer. The ABL, therefore, directly determines the performance of a turbine at a specific height. Furthermore, it determines the fatigue life of a turbine due to increasing wind speeds with height as well as the turbulent fluctuations in wind speed and direction. The increase in wind speed with height is referred to as the 'vertical profile of wind speed' or the 'vertical wind shear' [13]. It is, therefore, important to predict the variation in wind speeds with height above the surface for the design of wind turbines [60]. Generally, two models have been used extensively for prediction of wind vertical velocity profile: the log law and the power law. Both methods have uncertainties associated with them due to the turbulent nature of the wind [61], but they do provide the designer with the initial estimates of the vertical wind profile at the selected sites, necessary for the design process. The accuracy and validity of both laws was tested by Kircsi & Tar [62], in Hungary, for

three different locations. Wind measurements were taken using SODAR (Sonic-Detection-And-Ranging), a method that uses sound waves to non-intrusively measure the wind speed. The measured data was compared with the power law and log law approximations for three different locations. It was found that the log law was more accurate for two of the locations, whereas the power law was found more accurate for the location with a higher gradient in the wind profile. For engineering purpose, generally, the power law is mostly used for its simplicity and is given by the following expression:

$$\frac{V_W\,(h)}{V_W(h_r)} = \left[\frac{h}{h_r}\right]^e$$

Here, $V_W\,(h)$ is the wind velocity at height h, $V_W(h_r)$ is the reference wind velocity at reference height h_r generally taken as 10 meters, and e is the power law exponent or the Hellman's exponent. Therefore, the method requires measurements of wind velocity at the reference height, which are readily available to the designer for planned wind turbine sites. The Hellman exponent is a function of surface roughness lengths and heights, as well as the thermal stability of the atmospheric boundary layer [63, 64]. Typical values of the exponent are presented in Table 2.1. Note that for most wind turbine sites, the value of the Hellman's exponent is generally 0.1 [64, 65].

Table 2.1 - Values for Hellman's exponent for different terrains [64].

Terrain	Hellman's exponent
Open water surfaces	0.06 – 0.27
Flat open lands	0.11 – 0.40
Cities, villages	0.27 – 0.60

In addition to the mean velocity profiles, the turbulence in the ABL also needs to be characterized. The turbulence can be considered as being superimposed on the mean wind and can be visualized as a system of irregular eddies of different length scales [58]. Generally, it is measured as the standard deviation in the mean velocity measurements [64]. Much of the turbulence in the ABL is generated due to interaction with ground obstacles, such as trees and buildings, and thermal forcing due to solar heating, resulting in vertical convections of large air parcels. Much like the mean wind profile, semi-empirical expressions are available for the variation in turbulence intensity with height. For surface layers, Panofsky [66] proposed that the streamwise turbulence intensity can be predicted based on the following expression:

$$I_x\,(h) = \frac{0.88}{\ln(h/h_o)}$$

Here, $I_x\,(h)$ is the streamwise component of turbulence intensity and h_o is the surface roughness height. According to ESDU [67], the h_o value corresponding to the Hellman's exponent of 0.1 is 10^{-4} m for wind turbine applications. Turbulence intensity predictions, based on this method, are according to the Danish standards for safety of wind turbines [68].

In addition to the small-scale turbulence superimposed on the mean wind speed, it is often useful to know the gust behavior at a given site [69]. Gusts are often classified as small-scale turbulence [70]; however, here, it is treated as a separate class for analysis purposes. Such a classification is illustrated in Figure 2.7 for a wind measurement over an interval of one minute. The data were recorded at a height of 3m at the Surface Layer Turbulence and Environmental Science Test (SLTEST) facility, in the western salt flats of Utah, using 3D sonic

anemometers at a rate of 20Hz [71]. As can be observed, the gust behavior of the wind speed is masked by the small-scale turbulence. Furthermore, gusts can have sustained time-scales of up to several seconds and, therefore, length scales of several tens of meters. Such sustained gust events can easily cover the entire chordwise and spanwise extent of the turbine blade and lead to considerable unsteady loads [72].

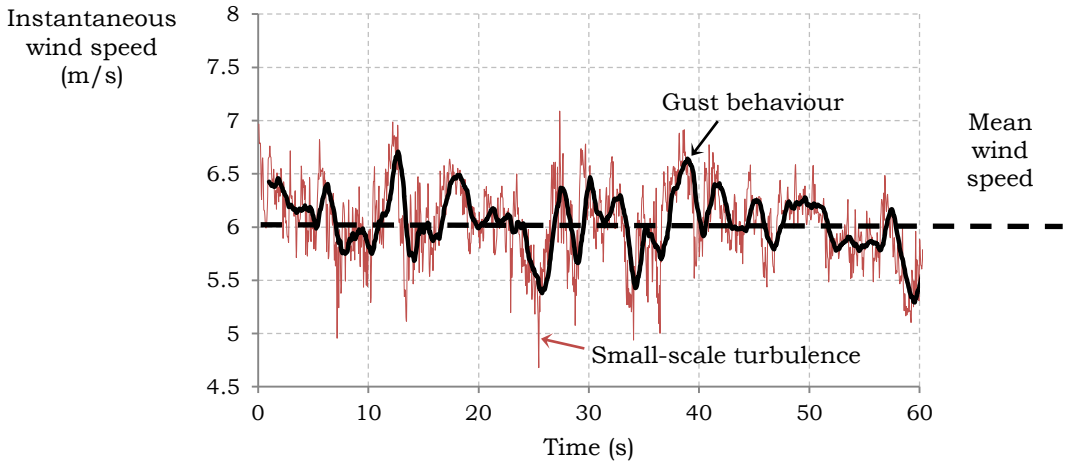

Figure 2.7 - Classification of short term wind measurements. Data extracted from Hutchins and Marusic [71].

Several methods exist that can be used to estimate the value of the peak gust. According to Davis & Newstein [73], for a specific height, the peak gust bears a linear relationship with the average wind speed. Deacon [74] proposed that the power law can be used to predict the magnitude of the peak gusts using smaller values for Hellman's exponent (0.03-0.06). Melbourne [75], through careful recordings and observations, proposed that the peak gust can be related to the turbulence intensity at a specific height and the mean wind speed at that height using the following expression:

$$V_G = \bar{V}_W \, (1 + 3.5 \, I_x)$$

Here, V_G is the magnitude of the peak gust, $\bar{V}_W$ is the averaged wind speed and I_x is the streamwise turbulence intensity in the wind over the averaging period. Therefore, using this expression, the gust behavior at a particular site can be established for the design of wind turbines.

The final component of the ABL that influences the operation of wind turbines is the wind direction. Similar to the mean wind speed profile, the mean wind direction profile can also be considered as being superimposed by a turbulent component. The turbulent fluctuations in wind direction can be as large as ±20-30 degs [6]. The mean wind direction, on the other hand, remains essentially constant as the height above the ground level is increased [76, 77]. Wind turbines are designed to align themselves with the averaged wind direction through an inbuilt yaw control mechanism. Since this repositioning of large rotors can lead to excessive gyroscopic loads on the entire structure of the turbine [78], generally the directional averaging is performed over the duration of several minutes. Therefore, the turbulent fluctuations in wind direction are not taken into account. The large variations in the wind direction can lead to sustained operation at yaw for the turbine, resulting in performance losses and structural damage.

2.2.2 The Wake behind a Turbine

Most wind turbines are clustered in groups, known as wind farms, to take advantage of geographically-limited wind resources and to reduce the installation and maintenance costs [13, 79]. However, interference between the wakes and downstream turbines leads to reduced total power output, as compared to an equal number of stand-alone systems [80, 81]. Using multiple LiDAR (Light Detection And Ranging) measurements, Iungo and Porté-Agel [82] illustrated that the power

production of downstream wind turbines is severely degraded due to the cumulative wake produced by the upstream turbines. Similarly, using satellite Synthetic Aperture Radar (SAR), it was shown that the cumulative velocity deficit in large wind farms can exceed 8-9% and recovery is achieved to within 2% of the freestream wind velocity at distances as large as 20 km [83]. Estimates have further indicated that velocity deficits in excess of 20% are present in the wake of individual turbines [84]. The other significant problem associated with the wakes of turbines is the large increase in the turbulence levels in the wake [85]. The increase in the turbulence negatively affects the dynamic loading on downstream wind turbines and influences the fatigue life of a turbine operating in the wake [86]. The turbulence levels between turbines are aggravated due to the additive nature of the parameter through mixing with surrounding wakes. The cumulative wake of the turbines at the Horns Rev wind farm in Denmark is shown in Figure 2.8 and clearly depicts the gravity of the situation.

Figure 2.8 - The cumulative wake at the Horns Rev 1 in Denmark, illustrating the severity of conditions at a typical wind farm (Owned by Vattenfall. Photo rights owned by Christian Steiness).

Due to these issues, wind turbine wakes have been the subject of extensive research over the past few decades. Several reviews, such as those by Snel [87], Crespo et al. [88] and Vermeer et al. [89], are available and provide a valuable source of information in the subject matter. It is well-understood that the wake behind a wind turbine is created due to momentum extraction from the oncoming stream by the rotor. The rotor, furthermore, imparts a spin on the wake, the direction of which is opposite to the torque applied to the rotor. Therefore, the wake created by the turbine consists of continuous vortex sheets shed from the trailing edge of the blade. These vortex sheets immediately roll-up in the wake, forming the blade tip and root vortices [22, 88].

The wake behind a wind turbine is illustrated as a simple schematic in Figure 2.9, showing some of the salient features of the wake. The flow approaching the turbine, generally assumed constant with height for such analyses, slows down due to the presence of the turbine and results in smaller velocities than the freestream velocities. This causes the slight expansion of streamtube, depicted in Figure 2.9, as the flow approaches the turbine. The wake behind a turbine expands further due to the flow retardation, caused by energy extraction. In order to accommodate the slower moving flow in the wake, expansion occurs. As can be observed in the schematic illustration, two prominent flow structures are present in the immediate wake behind the turbine: the tip vortices, originating from the tip, mark the periphery of the streamtube; and the root vortices, distorted due to their close proximity to the hub. The basic dynamics of these vortex structures determines the characteristics of the wake. These will be discussed further in this section.

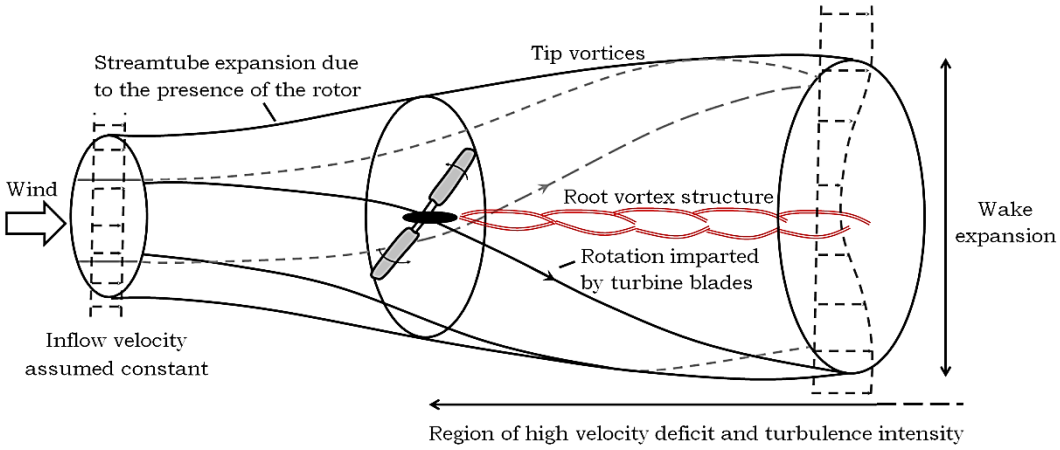

Figure 2.9 – Wake development behind a wind turbine indicating the velocity deficits and the rotation of the wake structure.

The wake behind a wind turbine is generally divided into near- and far-wake regions [90]. This classification is mainly used for wind farm design purposes, in order to determine the distance between two consecutive turbines. Several different definitions of these regions are present in the literature. For instance, Vermeer *et al.* [89] described the near-wake as the region where the effects of the rotor are still visible on the turbine wake, approximately one rotor diameter downstream. The far-wake, in contrast, is simply the region beyond the near wake. Crespo *et al.* [88], on the other hand, marked the near wake as the region where the shear-layer between the flow inside and outside the wake reaches the turbine central axis. This distance ranges between 2 and 5 rotor diameters downstream from a turbine, depending on the ambient conditions. However, both of these approaches require visual inspection of the wake and, therefore, cannot be directly used for design purposes. Note that wake studies related to wind turbines are limited to the near-wake region, due to difficulties in instrumentation of tunnels as well as limitations in the tunnel lengths [91-93]. On the other hand, due to the vast computational resources required to model the flow around the

turbine blades and in the wake, most CFD studies either rely on Reynolds-Averaged Navier-Stokes (RANS) simulations of the flow in the near-wake [94-96] or apply the actuator line/disc methods, without the rotor blades, to predict the velocity recoveries in the wake [97, 98]. However, recently, Mo *et al.* [47] proposed an improved definition of the near- and far-wakes, using a high resolution numerical analysis, employing Large Eddy Simulation (LES), to capture the flow details in the wake of the NREL Phase VI wind turbine, operating inside a virtual wind tunnel. These wake studies were not restricted to small distances behind the turbine. Furthermore, due to operation in the virtual tunnel, the wake propagation was not influenced by the ambient wind conditions that are commonly observed in field experiments. Using this numerical analysis, the authors were able to demonstrate that the wake of a wind turbine is constituted and governed by the tip and root (central) vortices shed from the blade and the rotor hub, as shown in Figure 2.10. In the figure, instantaneous vorticity contours clearly mark out these vortical structures at different locations downstream from the turbine. As can be observed, as the vortices propagate downstream, wake instabilities result in the eventual breakdown of the primary tip vortices. The breakdown of these vortices was observed to coincide with a rapid fall in the average turbulence intensity. Mo *et al.* defined the region prior to this breakdown as the near-wake. In this region, the root and tip vortices are distinct and therefore cause the excessive increase in the turbulence intensity and hinder the velocity recovery. However, beyond this region, in the far-wake, the turbulence intensity and the velocity deficits were observed to decrease rapidly. However, even at distances as large as 20 rotor diameters downstream in the wake, the turbulence levels were still observed to be approximately ten times larger the freestream conditions in this study. Further studies by the authors demonstrated that the wake instability and the location of breakdown of the primary vortex

structure in the wake is a function of the freestream wind speed for a given turbine design [46]. As the wind speed increased, the length of the near-wake region increased, approximately linearly. From a wind farm design point of view, it is important to locate the downstream turbine in the far-wake to ensure better performance and structural integrity.

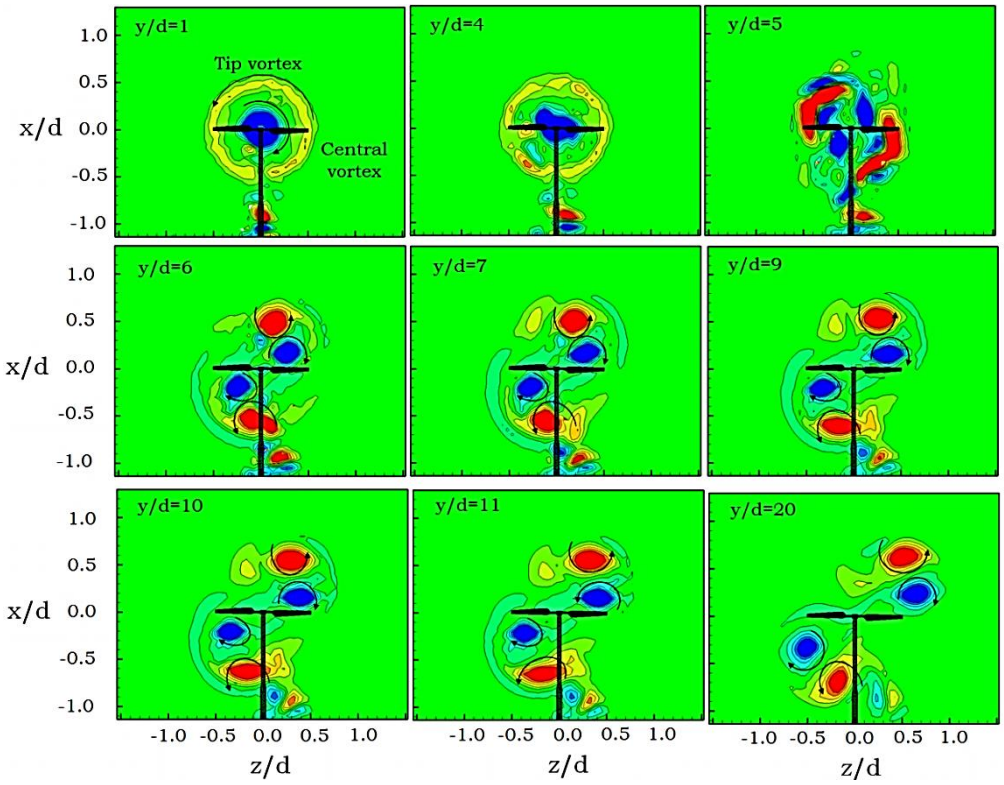

Figure 2.10 – Instantaneous vorticity contours in the wake of NREL phase VI wind turbine in a virtual wind tunnel, depicting the evolution of the wake up to distances as large as 20 rotor diameters [47].

Generally, semi-empirical approaches are used to situate wind turbines in arrays and to determine the distance between the turbines. For instance, in order to estimate the velocity recovery in the wake of a turbine, the simple wake model proposed by Jensen [99] is employed. This method is based on a linear expansion of the wake downstream of turbine, and, due to its simplicity, is widely used in the turbine industry

[100]. Using this model, the velocity deficit in the wake at a particular station y_i (V_{y_i}/V_W) is the function of the turbine thrust coefficient (C_T), the rotor size in terms of its diameter (d) and a wake decay factor (k_{wake}), with values ranging from 0.05-0.075 for offshore/onshore wind turbines, and is given by the following expression:

$$V_{y_i}/V_W = \left[1 - (1 - \sqrt{1 - C_T}) \left(\frac{d}{d + 2(k_{wake})y_i}\right)^2\right]$$

Similarly, the decay of average turbulence in the wakes of turbines with the downstream distance is also given by semi-empirical relationships. Described by Hansen [101], and summarized here, the turbulence in the wake (I_{wake}) is defined in terms of added turbulence (I_+) and ambient turbulence intensity (I_O) as:

$$I_{wake} = \sqrt{{I_O}^2 + {I_+}^2}$$

Here, I_+, which is the turbulence generated by the rotating blades, can be determined empirically using the following expression [102]:

$$I_+ = 5.7 {C_T}^{0.7} {I_O}^{0.68} \left(\frac{y}{y_n}\right)^{-0.96}$$

In the above equation, y is the downstream distance behind the wind turbine and y_n is the length of the near-wake region, determined according to Vermeulen [103]. The length of the near-wake is dependent on the rotor radius and the wake growth rate. A detailed explanation and implementation of the model are available in Hansen [101].

2.2.3 Effects of Atmospheric Turbulence

Wind turbine aerodynamics and loads are largely governed by the turbulent environments in which the turbine operates. The effects of

such turbulent conditions are illustrated schematically in Figure 2.11. The nomenclature used in this diagram is similar to that employed earlier for Figure 2.2. Note that the turbulence in the wind can be classified simply as a change in wind speed, a change in wind direction or a combination of both. Therefore, in the schematic illustration, in Figure 2.11, the increase in wind speed and the changes in wind direction have been presented separately and are represented as dotted lines. From the diagram, it can be observed that the increase in wind speed or a change in its direction leads to a variation in the resultant velocity magnitude and direction, represented by V_{R_2} and $\Delta\alpha$ respectively in Figure 2.11. The change in the magnitude, in this case, is of little significance since it only leads to slight variations in the Reynolds numbers of the blade section. However, the variation in the sectional angle of attack of the airfoil can lead to unsteady loads on the turbine blade, similar to those discussed in Section 2.1.3.

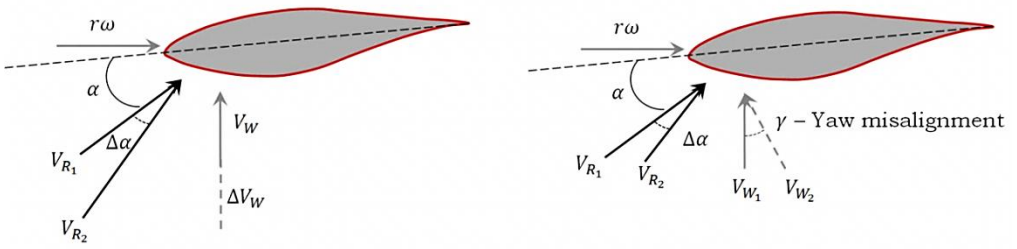

(a) Wind speed changes **(b) Wind direction changes**

Figure 2.11 – A schematic illustration of the wind speed and direction changes on the sectional angle of attack of a wind turbine blade.

2.3 The Process of Dynamic Stall

The unsteady process associated with the large increase in the angle of attack of an airfoil was first observed by Kramer [104] in 1932. In this early study, Kramer observed the effects of vertical wind gusts on small

aspect ratio wings with symmetrical (Gottingen 459 airfoil) and cambered (Gottingen 298) profiles. It was observed that the gust leads to an increase in the angle of attack of the wing sections and a sudden rise in the lift generated by the airfoil. However, after this initial observation, due to a limited perceived applicability at the time, little attention was given to the problem for over three decades. Then, in the late 1960s, the process of dynamic stall was identified on the retreating blades of helicopters in forward flight [105, 106]. The process has been observed to impose severe restrictions on the performance of the vehicle as well as resulted in high demands on material selection for the blade to withstand the large loads. Therefore, considerable research has been conducted to understand the dynamic stall process on helicopter blades, principally to avoid its negative effects [107-116].

The dynamic stall process, as observed on the NACA 0015 airfoil, is illustrated in Figure 2.12. The flow patterns illustrated in the figure were simulated by the Wind Energy and Atmospheric Physics Department of the Risø National Laboratory within the EC project VISCWIND [117, 118]. As can be observed in Figure 2.12(a), the process begins with the formation of a leading edge vortex structure due to a shear layer roll-up at the leading edge. As this vortex structure, called the dynamic stall vortex, continues to buildup due to momentum from the freestream, the lift and drag generated by the airfoil continue to increase (Figure 2.12(b)). Finally, due to formation of a secondary vortex at the leading edge, the primary dynamic stall vortex is pushed away from the airfoil, as shown in Figure 2.12(c), resulting in an abrupt loss of lift and an increase in the drag force. As can be observed, the extent of the primary dynamic stall vortex is similar to that of the airfoil and therefore its presence and eventual departure have significant effects on the performance of the airfoil.

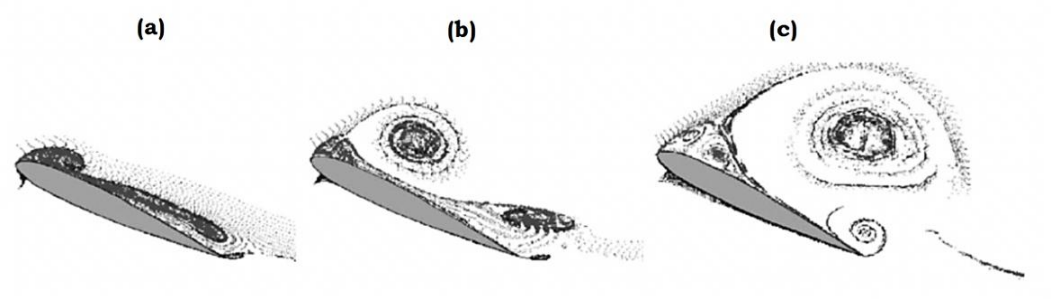

Figure 2.12 – Flow visualizations of a CFD simulation of NACA 0015 airfoil undergoing dynamic stall. (a) Initiation of leading edge separation (b) Dynamic stall vortex formation (c) Detachment of dynamic stall vortex. Images from VISCWIND [117]

Due to the complex nature of the problem, several theories exist regarding the source of excessive lift generated during the dynamic stall process. Early research into the unsteady process has indicated the primary dynamic stall vortex as the main source of additional lift generated by the airfoil during the process [119-122]. However, Albertson *et al.* [123], on the other hand, indicated that the vortex comes into play much later in the cycle and showed that the majority of lift produced, approximately 91% of it, occurs prior to any observation of a vortex structure above the airfoil. Such lack of consensus still persists today and indicates a lack of understanding of the lift behavior during the unsteady separation process. Some prominent characteristics of the lift generated during the dynamic stall process on an airfoil undergoing constant pitch motion are illustrated in Figure 2.13. As can be observed, several of the unsteady lift characteristics are significantly different from the steady-state counterpart. For instance, starting at the onset of rotation, the lift produced by a rotating airfoil is larger than that observed on the same airfoil during steady-state operation [124, 125]. Afterwards, a curvature in the unsteady lift-curve slope is observed during the so-called 'linear-regime'. The causes of this non-linear lift behavior during the airfoil pitch-up are still unknown and largely

ignored. After this, a sharp plateau-effect can be noted in the lift-curve [126, 127]. The causes of this sudden leveling-off of the lift-curve are also unknown. This plateau is, however, considered to be the precursor of the dynamic stall vortex. Once the dynamic stall vortex is formed, the unsteady lift-curve slope increases significantly. As long as the vortex remains in the vicinity of the foil, the lift force is sustained [123]. It is believed that the vortex structure has a low pressure core that affects the lift generated by the airfoil [128, 129]. Afterwards, due to the vortex departure, the airfoil goes into a state of abrupt stall. The flow separation results in a sudden loss of lift on the airfoil. However, it is important to note that the 'intensity' of this stall, in terms of loss of lift, and its dependence on airfoil profile are not available in literature. During the post-stall conditions, additional secondary or sometimes even tertiary vortices can be formed on the airfoil surface. These vortex structures, though of lesser strength compared to the primary dynamic stall vortex, can induce significant fluctuations in the lift generated by the airfoil.

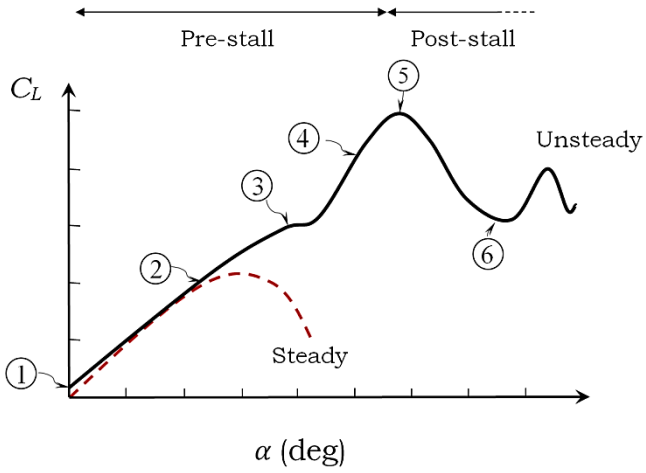

1	Slightly increased lift
2	Curvature in the lift curve
3	Distinct plateau
4	Increased lift-curve slope
5	Abrupt fall of lift
6	Post-stall lift variation

Figure 2.13 – Schematic representation of the lift curve characteristics of an airfoil undergoing constant pitch dynamic stall.

It should be pointed out that the process of dynamic stall, as it occurs on helicopter rotors, is believed to be different from that observed on wind turbine blades due to gusts or sustained yawed operation. The principal difference lies in the angle of attack histories of the blades of the respective rotors. For helicopter blades in forward flight or wind turbine blades operating in the atmospheric boundary layer with vertical wind shear, a cyclic variation in the angle of attack is observed. This variation has been replicated in a large number of wind tunnel experiments through sinusoidally pitching an airfoil at a fixed axis. However, on wind turbines, during gusts or changes in wind direction, the blade undergoes a sustained increase in the sectional angle of attack beyond the steady-state stall angle of attack. Depending on the length and time scale of the gust event or the time it takes for the turbine yaw-axis to align with the oncoming flow, the blade might operate under unsteady post-stall conditions for extended periods of time. Regardless of these distinctions, it is important to note that there are distinct similarities between the two cases, such as large overshoots in lift and drag beyond the steady-state stall angle of attack and the formation of a leading edge vortex. Therefore, an insight into one 'type' of dynamic stall should aid in the understanding of the unsteady separation process in more detail. In the current thesis, particular focus is given to the dynamic stall during constant-pitch motions, due to its significant impact on the aerodynamic loading of wind turbine blades.

In the following discussion, a detailed account is presented of several parameters influencing the unsteady separation process. Several pivotal sources have been verified to illustrate the effects, without regard to the type of motion resulting in the unsteady separation. However, where possible, a distinction has been made between the sinusoidal cases and the constant pitch rate cases. The primary interest in the

thesis is the post-stall behavior of an airfoil undergoing dynamic stall. Therefore, the focus of the section is to study the effects of pitch rate, Reynolds number and airfoil profiles on the lifting characteristics of a pitching airfoil.

2.3.1 Effects of Pitch Rate

The parameter used to describe the unsteadiness imposed on an airfoil through its motion is the reduced frequency [130]. Simply, it can be defined as the ratio of the airfoil leading edge velocity to the freestream velocity. For an airfoil with chord length of c, pitching about the mid-chord at a pitch rate of $\dot{\alpha}$ (rad/s) with a freestream flow velocity U, the reduced frequency (κ) is given as:

$$\kappa = \frac{\dot{\alpha}c}{2U}$$

In the equation, if $\dot{\alpha}$ is constant, the effects due to the resulting motion are termed as constant-pitch dynamic stall or ramp-style dynamic stall. However, if $\dot{\alpha}$ is a sinusoidal function of time, the resulting motion is sinusoidal.

From the expression of reduced frequency, it is clear that when κ approaches unity, the convective and unsteady time scales are of the same order of magnitude and the flow can be considered as unsteady [131]. However, it has been observed that significant differences from steady-state behavior are present for reduced frequencies even as low as 0.05 [132]. Digavalli [131] proposed that the unsteady effects become dominant when the ratio of viscous diffusion length-scales to the airfoil motion length-scale ($\kappa\sqrt{R_{e_c}}$) exceeds unity. Therefore, even with smaller reduced frequencies, the chord Reynolds number of the flow (R_{e_c}) might be large enough to confer unsteady effects on an airfoil. This, furthermore, illustrates that an increase in Reynolds number might

result in the decrease of the unsteadiness required to cause dynamic stall on an airfoil, although no direct studies have illustrated this effect.

The effects of reduced frequency on the lift generated by an airfoil undergoing dynamic stall are illustrated in Figure 2.14, extracted from [124] and [107] for constant pitch rate and sinusoidal cases respectively. As can be observed from Figure 2.14(a), for an airfoil undergoing constant pitch rate motions, an increase in the reduced frequency results in the delay of dynamic stall to higher angles as well as a significant increase in the maximum lift coefficient (C_L). These observations have been made by several researchers over the past few decades [133, 134]. Sheng *et al.* [135], furthermore, illustrated that the delay in the dynamic stall angle of attack varies linearly with the reduced frequency. However, no such trends have been noted for the maximum lift generated by the airfoil. Similarly, no measure of the intensity of stall after unsteady separation and its relation with the reduced frequency is available in the current literature.

For the sinusoidal case, on the other hand, an increase in the reduced frequency results in the increase in the dynamic lift generated by an airfoil and the hysteresis in the lift force that is observed during the return cycle [136-138]. This is illustrated in Figure 2.14(b), where the airfoil is rotating with a mean angle of attack of 15^{o} and amplitude of 10^{o}. Based on the observation of the primary dynamic stall vortex on sinusoidally oscillating airfoils, McCroskey *et al.* [120] proposed to classify the stalling behavior of the airfoil as either light stall or deep stall. The light-stall regime is defined when the downstroke motion of the airfoil begins prior to the formation of the dynamic stall vortex; whereas, deep-stall occurs when the dynamic stall vortex, and the consequent lift overshoot, are observed prior to the downstroke [139]. Therefore, in Figure 2.14(b), it can be observed that an increase in the reduced

frequency results in the transition of stalling behavior of the airfoil from light to deep dynamic stall. It is important to note that the amplitude of the oscillation and the mean angle of attack also determine the stalling behavior of a sinusoidally oscillating airfoil [107]. Generally, deep-stall conditions persist at larger amplitudes or mean angles beyond the steady-state stall angle of attack [111, 136, 140, 141].

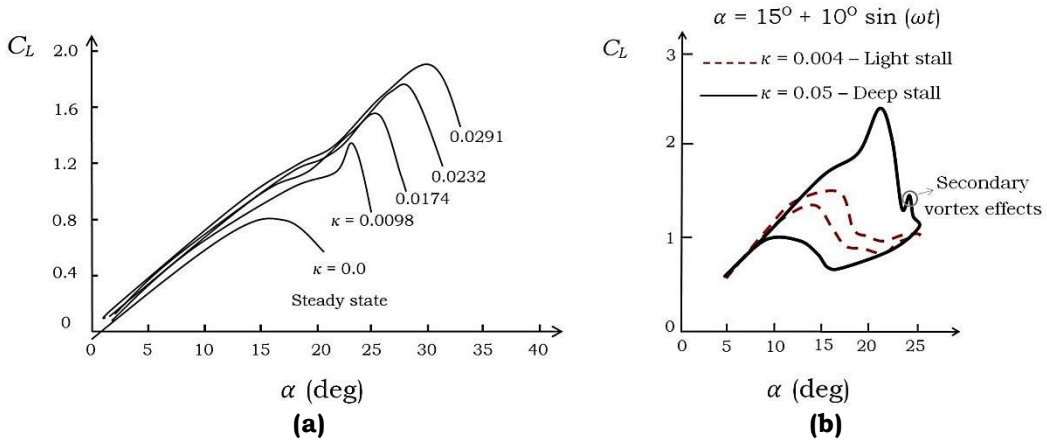

Figure 2.14 – Effects of increasing reduced frequency on the lifting characteristics of an airfoil undergoing (a) constant pitch rate motion [124] and (b) sinusoidal motion [107].

Here, a small comment can be made regarding the similarity of the two different 'types' of unsteady separations. As can be observed in Figure 2.14(b) for the deep stall case, a slight plateau effect is visible in the lift-curve prior to the formation of the dynamic stall vortex. This is similar to the plateau effect that was highlighted for the constant pitch dynamic stall case in Figure 2.13. Furthermore, the prominent increase in the lift-curve slope is apparent for the deep stall case and is caused by the suction peaks created by the low-pressure core of the dynamic stall vortex. Similarly, just before the commencement of the downstroke motion, a secondary vortex structure also influences the lift curve slightly, similar to post-stall conditions during constant pitch dynamic stall. Therefore, it can be argued that the primary difference between the

two cases is simply that during sinusoidal oscillations, the airfoil is allowed to return to its initial state whereas for the constant pitch rate case the airfoil is kept in the unsteady stall condition for extended periods of time. This observation is significant since results are transferrable from one type to another, as will be demonstrated in the next section of this chapter.

2.3.2 Effects of Reynolds number

The Reynolds number is defined based on the freestream velocity (U), the chord length of the airfoil (c) and the fluid properties of density (ρ) and dynamic viscosity (μ), as:

$$Re_c = \frac{\rho U c}{\mu}$$

The effects of Reynolds number on an airfoil undergoing unsteady separation have been investigated by several researchers in the past using force and surface pressure distributions [111, 142-146]. Studies have generally concluded that the Reynolds number plays no significant role in the dynamic stall process as a whole. However, there are several ambiguities in literature that encourage further research. For instance, Robinson and Wissler [142], through direct surface pressure measurements, concluded that an increase in the Reynolds number had no significant effect on the stall process as a whole. However, they also stated that as the Reynolds number increases, the low-pressure peaks near the leading edge were observed to increase in magnitude. Although not mentioned in their article, this is indicative of increased vortex strength. Similarly, Choudhuri and Knight [143] showed that increasing the Reynolds number from 10^4 to 10^5 resulted in the decrease of the length scales associated with the flow structures, indicating compact vortices. However, the overall effects were still deemed insignificant. For

Reynolds numbers applicable to an industrial scale, the NREL conducted a series of experiments on several airfoil sections undergoing unsteady separation due to sinusoidal motions [132, 147-149]. A sample test result for the well-known S809 airfoil [150, 151], from one of these studies, is illustrated in Figure 2.15. The airfoil in the presented cases has a smooth surface finish and was tested at different mean angles of attack at the indicated Reynolds numbers. As can be observed, for the light-stall case (left plot in Figure 2.15), the characteristic hysteresis is similar at both reduced frequencies. The flow is primarily attached in this case, as can be observed from the maximum angle of attack of the oscillation cycle (15^{o}), being less than the steady-state stall angle of attack of the airfoil, and the hysteresis occurs simply due to the lag of flow response time to the moving airfoil. Similarly, it can be argued that the hysteresis is similar for the deep-stall case as well (right plot in Figure 2.15) and the slightly larger lift peak for the smaller Reynolds number case can be attributed to the slightly larger reduced frequency at this Reynolds number.

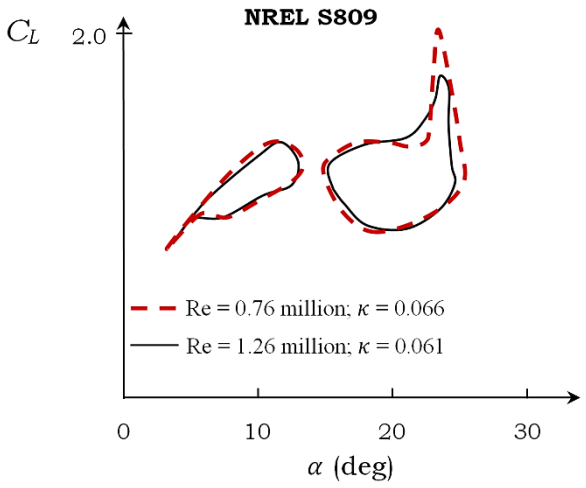

Figure 2.15 – Comparison of the lift curves of a smooth airfoil undergoing sinusoidal motion at different Reynolds numbers. Plots reproduced from [132].

On the other hand, several recent studies indicate that the effects of Reynolds number cannot simply be ignored during analysis. For instance, Zhang and Schlüter [152], showed that for very small Reynolds numbers, typically less than 10,000, the maximum lift coefficient of a flat plate undergoing dynamic stall exhibits a non-linear behavior. A similar non-linear behavior in the lift force for a harmonically pitching NACA 0012 airfoil was noted by Amiralaei et al. [153]. Furthermore, as discussed earlier in Section 2.3.1, the unsteady effects are dependent on a coupled forcing of reduced frequency and Reynolds number [131] and, therefore, it is incorrect to consider that the Reynolds number has no significant effect during the process of dynamic stall.

It is believed that the Reynolds number ranges in most works are too limited to produce a justifiable claim regarding the effects of Reynolds number on the dynamic stall process. For instance, in the NREL work [132], illustrated above, the flow around the airfoil, at such high Reynolds number, would mostly be turbulent. In contrast, most other works, being performed in conventional wind tunnels, are limited to a smaller Reynolds number range where the flow can primarily be considered as laminar. Due to this, the effects of Reynolds number on the dynamic stall process have remained concealed. Research needs to be undertaken for both these regimes for a particular airfoil and the effects should be compared. The transitional Reynolds number regime, where the boundary layer transitions from laminar to turbulent, can also be used for this purpose. During this regime, the boundary layer characteristics are extremely sensitive to the Reynolds number and, therefore, the location of transition and the extent of turbulent flow can be varied on the airfoil simply by varying the freestream velocity. Such a study would clearly distinguish the effects of Reynolds number and the state of the boundary layer on the dynamic stall process.

2.3.3 Effects of Airfoil Profile

The effects of the airfoil profile shape on the unsteady separation process are generally considered to be dictated by the steady-state stalling behavior of the airfoil. It has been concluded that the airfoils with better steady-state stall characteristics have better dynamic stall behavior, in terms of stall delay and the maximum lift coefficients [120, 154]. McCroskey *et al.* [120] performed the seminal comparison of eight different airfoil profiles undergoing sinusoidal pitch oscillations. It was concluded that during light-stall conditions, the airfoil profile has a significant effect on the dynamic stall process. However, during deep-stall conditions, the profile shape showed no significant consequence on the unsteady separation process.

A comparison of two different airfoils, NLR-1 and NLR-7301, from the study by McCroskey *et al.* [120] operating at both the light- and deep-stall conditions is presented in Figure 2.16. The profiles of the airfoils are also illustrated in the figure for comparison. The NLR-1 is a comparatively thinner airfoil section, with a sharper leading edge. On the other hand, the NLR-7301 airfoil is a thicker version, of the same family, with a much more rounded leading edge. The comparison of the two airfoils during the light-stall conditions indicates that the thicker airfoil has a considerably better performance during oscillations compared to the thinner airfoil. Apart from the increased maximum lift coefficient, it is also important to note the smaller hysteresis in the lift force for the thicker airfoil, since the hysteresis is an indication of the loss of lift during the cyclic changes in the angle of attack and directly represents the amount of fatigue for a blade section.

Similarly, for deep-stall conditions, it can be observed that for NLR-1 airfoil a peak in the lift force is observed, slightly after a plateau

in the lift curve during the upstroke motion. This peak is indicative of the formation of the dynamic stall vortex. After the peak, the airfoil goes into a state of abrupt stall, even though the foil is still in the upstroke motion. Afterwards, the presence of a secondary vortex structure is also apparent in the lift force, just prior to the downstroke motion, and indicates that the flow is principally separated from the airfoil. On the other hand, no such peaks are observed for the thicker NLR-7301 airfoil, indicating that the formation of the vortex is delayed, principally due to the airfoil profile. The loss in lift is encountered in this case once the NLR-7301 airfoil begins its downstroke motion. Therefore, based on this discussion, it can be argued that the airfoil profile has a significant effect on the unsteady process. A thicker profile, with a rounded leading edge, can not only lead to a smaller hysteresis in the lift force but also a considerable delay in the dynamic stall onset.

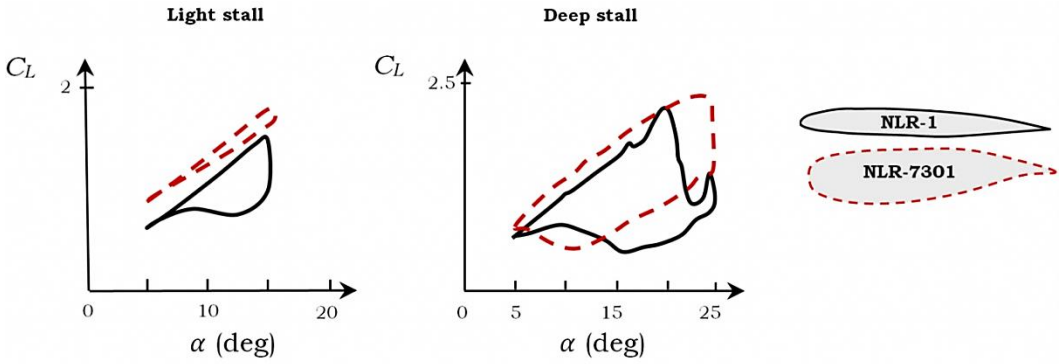

Figure 2.16 – Effects of profile on the unsteady separation process during sinusoidal motion. Extracted from McCroskey *et al.* [120].

Apart from this early study by McCroskey *et al.* [120], no direct comparisons of the airfoil profile on the dynamic stall process are available in the literature. Difficulty arises in making comparisons between different sources, primarily due to the dissimilar operating conditions between them. This problem is further exacerbated by a lack

of specific parameters or methods that can be used to compare airfoil performance during unsteady operation. Since it is not always feasible to visually compare the lift hysteresis of different airfoils, an earlier parameter, known as the Liiva criterion [155], can be used for dynamic stall due to sinusoidal motions. The criterion can be estimated by calculating the area enclosed by the curve and, therefore, is applicable for cases where the forces and moments exhibit a closed-loop behavior. For airfoils undergoing dynamic stall due to constant pitch rate motions, no such parameter is available to compare the post-stall characteristics of different airfoils.

2.3.4 Dynamic Stall on Wind Turbine Blades

It is interesting that before 1988 dynamic stall was not considered to affect the performance and loads of a wind turbine. An early analytical study by Hibbs [156] actually demonstrated that the dynamic stall could be ignored during the design of a wind turbine since it was deemed to have a minimal effect on the performance of the turbine. However, soon after, Butterfield [157] was able to experimentally quantify the effects of dynamic stall on a wind turbine. It was illustrated, through wind tunnel experiments on an actual turbine, that dynamic stall can occur on a wind turbine blade due to yawed flow, inflow turbulence and tower shadow. It is now widely known that the problem of dynamic stall not only persists during the 'normal' operating conditions of a turbine but also determines the structural loads and power production in a highly transient time frame [158]. Therefore, efforts are being directed towards efficient modelling of dynamic stall process on wind turbine blades to account for the large loads produced during the process [110, 130, 159].

The occurrence of dynamic stall on a wind turbine blade can be clearly seen in Figure 2.17. The figure was extracted and reproduced

from the seminal work of Butterfield *et al.* [160], where a downwind wind turbine was tested under conditions of yawed-inflow. The three-bladed turbine was constituted from the basic S809 airfoil due to the large number of reliable wind tunnel data available for the airfoil. The primary attribute of this airfoil is decreased roughness sensitivity and a sustained maximum lift coefficient of 0.95 over a range of angle of attacks prior to stall [161, 162]. One of the blades of the turbine was instrumented with pressure sensors at selected spanwise locations to study the variation of the forces during the turbine rotation under yaw-misalignment of 0^{o} and 30^{o}. Furthermore, a flow angle probe was used in the experiment to determine the exact angle of attack at the selected spanwise locations. The azimuth-averaged results at 47% and 80% span locations, illustrated in Figure 2.17, were acquired over a total of 25 revolutions of the blades.

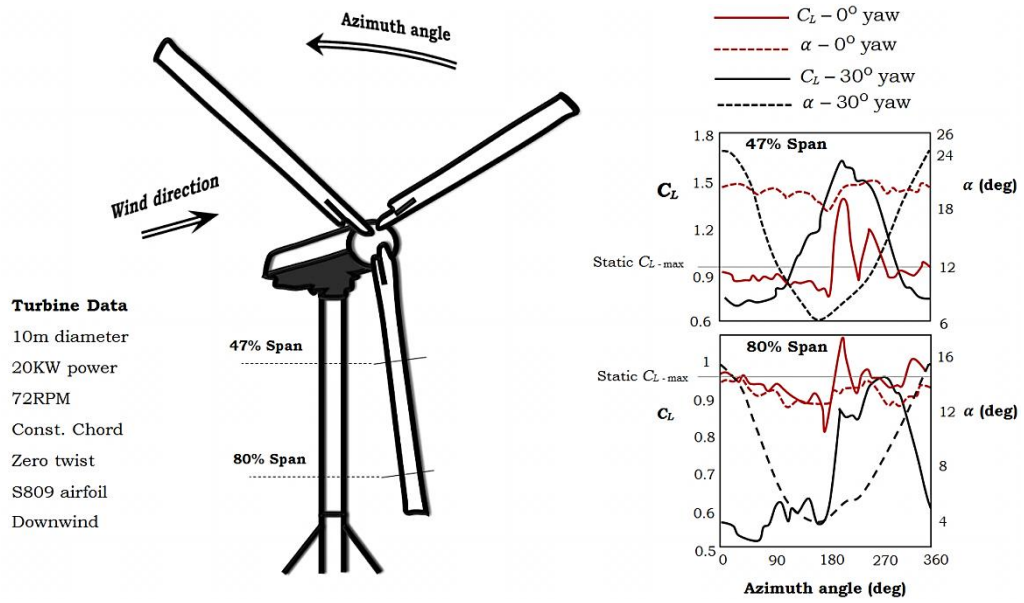

Figure 2.17 – Comparison of lift and angle of attack histories on a turbine blade at selected spanwise locations during rotation at yawed inflow of 30^{o} and with no yaw misalignment. The plots clearly depict the occurrence of dynamic stall at the inboard stations of the turbine blades. Reproduced from [160].

It can be observed from the plots that the angle of attack variation under yawed flow condition is significantly higher compared to the case with zero yaw-misalignment, where large variations are only observed due to the tower shadow at an azimuth angle of 180^{O}. Due to these rapid variations, it can be observed that the lift coefficient at inboard station, 47% span, considerably exceeds the steady-state maximum lift coefficient of the S809 airfoil. This is a clear indication of dynamic stall occurrence on the turbine blade. At zero yaw-misalignment, the sectional lift coefficient only exceeds the steady-state maximum under the influence of the tower shadow, at an azimuth of 180^{O}. On the other hand, due to the high rotational speeds at the outboard station, 80% span, the sectional angle of attack at this location does not exceed the steady-state stall angle of the airfoil. Therefore, the lift coefficients do not exceed the maximum steady-state lift of the airfoil. There is a prominent increase in the lift, particularly for the zero-yaw misalignment case when the blade passes behind the tower of the turbine. From this study, therefore, it was clear that the tower shadow and yaw-misalignment can lead to such large excursions in sectional angles of attack that dynamic stall is an inevitable outcome. A similar study by Shipley *et al.* [54] in fact estimated that dynamic stall occurred during more than 50% of recorded cycles for both upwind and downwind wind turbine configurations, due to yaw-misalignment. Such studies have led to the abolition of downwind turbine configurations due to excessive cyclic loading that is observed as the blade passed through the wake of the tower. Therefore, most turbines used today have an upwind configuration.

For a two-bladed upwind rotor-configuration with taper and blade twist, Schreck *et al.* [163] demonstrated, through surface pressure measurements, that dynamic stall occurs periodically on wind turbine

blades under yawed inflow. It was shown that the dynamic stall vortex kinematics is largely influenced by three-dimensional effects due to the rotation of the turbine blade. Recording the pressure signature of the dynamic stall vortex, the study demonstrated that once the vortex is formed, the dynamics of the blade are governed by it due to its large extent and the extended periods it stays in the vicinity of the blade. One such case study is presented in Figure 2.18 for the turbine operating at an inflow velocity of 13m/s and a yaw misalignment of 40^{o}. The pressure signatures of the vortex were used to map out the chordwise position of the vortex as a function of time. As can be observed, the vortex is first developed at the leading edge of the inboard station of the turbine blade, at 30% span (0.30R). At this inboard station, vortex convection velocities are comparatively smaller compared to the other sections and, therefore, the vortex stays in the vicinity of the section for longer periods of time. Note that the timeframe depicted in the plot represents approximately half of the time the blade takes to complete one revolution. Therefore, at the inboard stations of the blade during yawed inflow, the dynamic stall occurrences are excessive and prolonged. On the other hand, for the outermost parts of the blade, such as at 80% span, the vortex is first observed at 0.2% chord. Furthermore, the vortex convection velocities are significantly larger in this case and so the vortex swiftly convects over the blade. Similar observations were made for a rectangular, twisted blade with no taper [164]. Therefore, due to the extended periods of vortex-residence near the blade of the turbine, the turbine performance and structural loads are severely affected by it.

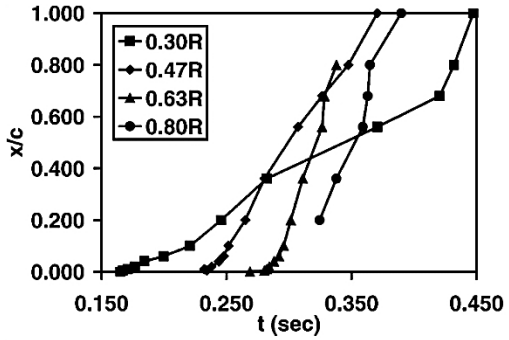

Figure 2.18 - Dynamic stall vortex convection histories on a wind turbine blade at different spanwise sections [163]

2.4 Dynamic Stall Control

The process of dynamic stall can be initiated by a number of phenomena, as discussed in this chapter, such as inflow turbulence in wind speed and direction, tower shadow effects, gusts and sustained yawed-operation as well as operation in the wake of an upstream wind turbine. Therefore, in order to improve the operation of the turbines and further enhance its efficiency, it is important to determine methods for controlling the process of dynamic stall. In this section, therefore, the various techniques that have been utilized in recent research to limit the effects of dynamic stall are presented. In particular, we are interested in the effects of different control methods on the lift produced by the dynamic stall vortex, since a large increase in the lift force can lead to large bending loads on the blade and the blade-hub joint. Furthermore, the dynamic stall vortex can also cause large negative pitching moments that can increase torsional loads on turbine blades. The sudden loss of lift, after flow separation, leads to vibrations in the blades. This flow separation and the ensuing vibrations can affect the performance of the turbine and, furthermore, degrade the fatigue life of turbine blades. The two different types of dynamic stall presented in this chapter, sinusoidal

and constant pitch, pose very similar control challenges. The control objectives for dynamic stall lift, under different operating conditions, are illustrated in Figure 2.19, and summarized as follows:

- Reduced hysteresis - For an airfoil in sinusoidal motion, it is desirable to reduce the hysteresis in the lift force. This is somewhat equivalent to the required control objective of smoother lift decay when an airfoil undergoes constant-pitch rate motion. For both cases, it implies that the control methodology aids in the lift-recovery process after separation.
- Reduced dynamic stall lift - It is desirable to reduce the lift associated with the primary dynamic stall vortex. This objective ensures that the bending loads created due to a sudden increase in the lift are minimized. It, furthermore, ensures that the loss of lift after vortex separation is less abrupt, thus ensuring a smoother lift decay. Moreover, the negative pitching moment excursions that are associated with the dynamic stall vortex can be significantly reduced if the vortex structure is completely avoided or delayed during the pitch-up motion of the airfoil.
- Delay in dynamic stall - It is desirable to delay the onset of dynamic stall for both cases. In terms of wind turbine operation, this implies a greater resistance to unsteady separation and, therefore, improves the reliability of the turbines. With delayed dynamic stall, the turbines can then be placed at locations with higher levels of average turbulence in the wind or can be packed closer together for improved wind farm performance. Again, it is difficult to observe this effect for light-stall regime during sinusoidal motion.

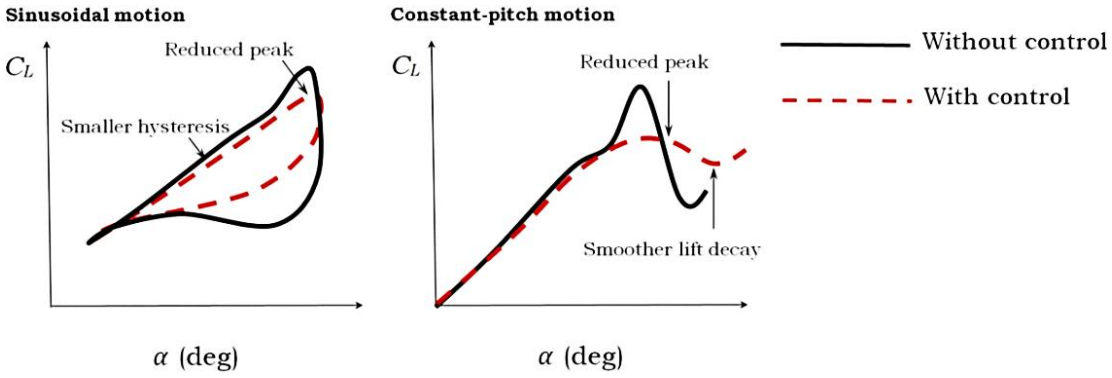

Figure 2.19 Desired lift behavior of an airfoil undergoing dynamic stall for different types of motions. Both desired lift behaviors would yield appreciable improvement in the performance and fatigue life of the device.

It should be noted that most research into dynamic stall control has been motivated principally by helicopter blades and, therefore, is often limited to sinusoidal motions of the airfoils. However, the effects of the control on the dynamic stall process during sinusoidal variations of angle of attack are interpretable and transferrable, to a certain degree, to the constant-pitch cases, as discussed. The objective of this section is therefore to review different flow control techniques that have been used to suppress dynamic stall effects, regardless of the type of motion that is causing the separation. The section has been categorized according the type of flow control technique; for instance, the subsection regarding leading edge modifications includes discussions for both the use of slats as well as drooped leading edges. However, leading edge perturbations have been grouped with vortex generators, since both methods produce streamwise-oriented vortices. Therefore, some of the methods can be categorized in other subsections as well, or form their own category. However, for the purpose of present discussion, this classification method is used.

2.4.1 Effects of Fluid Injection and Removal

The use of high-momentum fluid injection into or low-momentum fluid extraction from the boundary layer to improve the boundary layer stability and resistance to separation has been investigated by several researchers [165-167]. For steady-state operation it has been observed that such boundary layer control methodologies can delay the flow separation by several degrees, as well as result in an increase of steady-state maximum lift of the airfoil.

For unsteady airfoils, Gardner *et al.* [168] numerically studied the influence of jets of various configurations, with significant mass flow injection, on the performance of a sinusoidally pitching OA209 airfoil. The jets were positioned on the airfoil at $0.1c$ such that the fluid injection was tangential to the airfoil surface and minimized the possibility of boundary layer separation of bubble formation to the mass flow from the jet. Several different configurations of the jets were investigated in the research, using three dimensional RANS simulations. It was observed that the effect of tangential jets, used for the Coanda effect, is to shift the entire vortex structure towards the trailing edge of the airfoil. It was observed that the resultant vortex structure was smaller in size compared to that observed on the clean airfoil section. This results in a significant reduction in the maximum lift produced by the airfoil, as shown in Figure 2.20 (a). As can be observed, the lift-hysteresis, after the vortex convection, is also significantly smaller compared to the clean airfoil. This indicates that the tangential fluidic injection also aids in the lift-recovery process during the downstroke motion of the airfoil. However, the loss of lift, though initially smooth, is rather sudden as the airfoil approaches the angles at which the primary dynamic stall vortex (DSV) is observed on the clean airfoil. Similar effects were observed for thick airfoil sections principally used in the wind

turbine industry [169]. Further to this, Gardner *et al.* [168] also investigated the effects of inclined and skewed jets for dynamic stall control. It was believed that such a configuration could lead to splitting of the primary DSV into smaller vortices of reduced strength and extent. However, due to the limited domain of the analysis, this effect was not observed. As can be observed in Figure 2.20 (b), this method leads to a reduction in the vortex strength and, therefore, the lift peak is levelled off for the controlled case. However, the hysteresis is still significantly large and flow reattachment is considerably delayed compared to the clean case. This indicates that inclined and skewed fluidic injection does not aid in lift-recovery during the unsteady separation process. The final method investigated in the work was vertical fluidic injection. It was observed that flow injection normal to the airfoil surface leads to the creation of a stable separation bubble, anchored by the jets. The DSV formed in this case was also shifted towards the trailing edge of the airfoil and was of significantly reduced size and strength. This resulted in the smaller contribution to the lift generated by the airfoil, as shown in Figure 2.20 (c). The hysteresis in the lift is also somewhat reduced initially; however, the vertical fluidic injection can be observed to hinder flow recovery.

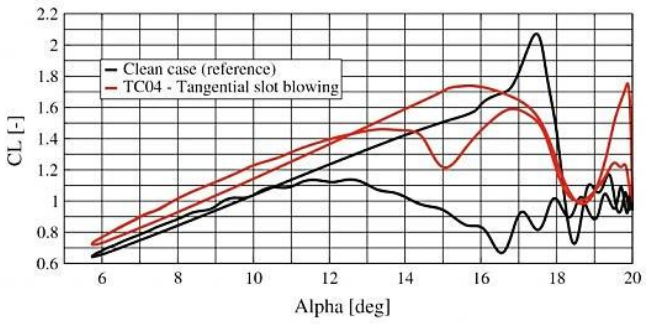

(a) Tangential fluidic injection

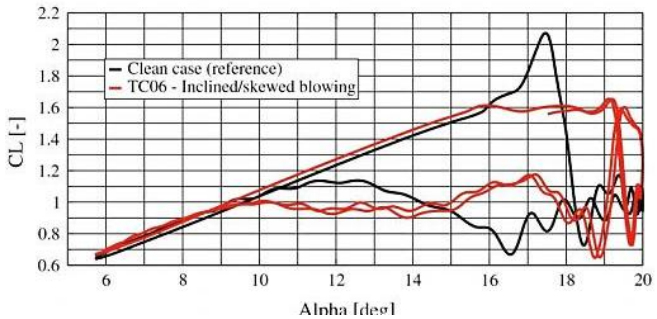

(b) Inclined and skewed fluidic injection

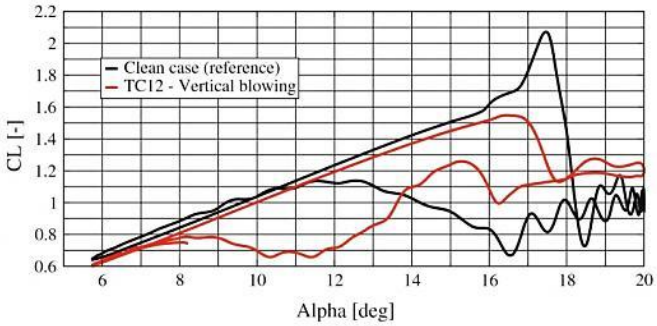

(c) Vertical fluidic injection

Figure 2.20 – Effects of different fluidic injection methods and configurations (red) on the dynamic stall process of OA2019 airfoil [168].

Similarly, the effects of fluid removal during the dynamic stall process were investigated in detail by Karim and Acharya [170] using flow visualization. It was indicated that reverse flow accumulation near the leading edge of the airfoil was primarily responsible for the formation of the dynamic stall vortex. This reverse flow can be removed from the leading edge of the airfoil using suction to delay the dynamic stall process. The flow suction was applied near the leading edge of the NACA 0012 airfoil and the slot location was varied between 0.2*c* and 0.5*c*. It was observed that for sufficient flow removal the dynamic stall vortex could be avoided altogether on the airfoil. This can be observed in the flow visualization of the airfoil, undergoing constant-pitch rate motion at a reduced frequency of 0.15, as presented in Figure 2.21. The

visualizations are provided for different Reynolds numbers, as indicated in the image, and at an angle of attack of 35°. As can be observed, the DSV is completely suppressed due to the flow removal near the leading edge of the airfoil. From the flow state illustrated in Figure 2.21, it can be argued that the increased lift created due to the vortex will completely vanish. Furthermore, the abrupt loss of lift might also be avoided in this case due to partially attached flow.

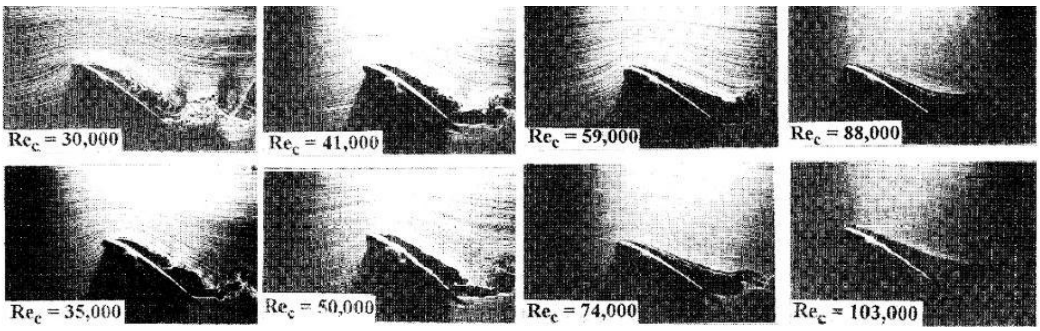

Figure 2.21 - State of flow field on the NACA 0012 airfoil at an angle of attack of 35°, pitching at a reduced frequency of 0.15 at different Reynolds numbers [170].

Periodic excitation has also been investigated for dynamic stall control of airfoils. For steady-state operation, it has generally been observed that excitation of the flow through periodic fluid addition is more effective compared to the traditional methods of continuous removal or addition of high momentum fluid [171, 172]. This has also been demonstrated for the dynamic stall case. However, the mechanisms involved in improved control are unknown. It can be postulated that through periodic excitation, vortices are created that entrain the fluid and enhance mixing. However, further investigations are required to definitively understand the mechanisms involved. Greenblatt *et al.* [173, 174] illustrated through experiments that periodic excitation could lead to a significantly reduced hysteresis in the lift force, compared to the

continuous fluidic injection mechanism. This is demonstrated in Figure 2.22 for the NACA 0015 airfoil operating at a reduced frequency of 0.1. Note that for periodic excitation, the reduced excitation frequency, given as the ratio of the product of the excitation frequency and the distance between the slot and the trailing edge to the freestream velocity, is 0.6. It was observed that the periodic excitation leads to a significantly diminished hysteresis in the lift compared to the continuous injection method at similar flow injection rates.

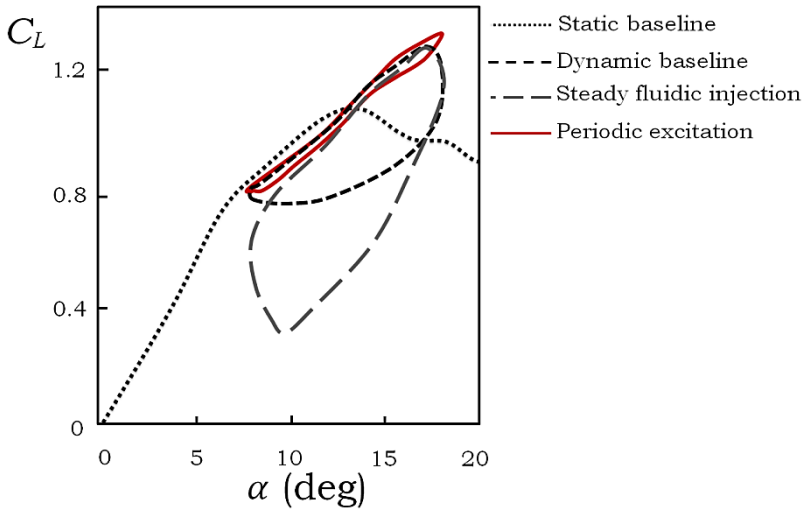

Figure 2.22 - Comparison of periodic and continuous fluidic injection on the dynamic stall process of a NACA 0015 airfoil. Reproduced from [173].

Note that the airfoil in Figure 2.22 is examined at light-stall conditions. Therefore, the DSV is not formed in this case. Consequently, at present, no suggestions can be made for the effectiveness of this method in reducing the strength of the primary DSV or in reducing the stall intensity after the primary DSV convects.

2.4.2 Effects of Streamwise Vortices

The control of flow separation through streamwise-oriented vortices, generated by simple vane-type vortex generators (VGs), was first

introduced in 1947 by Taylor [175]. Vortex generators are small vanes that are mounted normal to a surface at a certain angle to the freestream. These VGs are able to produce high-energy streamwise vortices that allow enhanced mixing between the high-momentum external-flow and the boundary layer. The longitudinal streamwise vortices are created due to the flow past the tips of the VGs. Generally mounted slightly before the point of separation, the VGs can enhance the aerodynamic performance by eradicating flow separation due to adverse pressure gradients. In terms of wind turbines, this manifests as a higher torque and power generation by the turbine [176]. Performance enhancements for wind turbines using vortex generators have been demonstrated through field studies as well [177].

An exhaustive amount of effort and research has been conducted to understand the flow physics of the vortex generators as well as in optimizing different aspect of the flow generators for different applications [178-181]. However, most of these research and optimization efforts are principally focused on steady-state separation control. Only recently, efforts have been diverted to understanding the effects of VGs during the process of dynamic stall. To this end, Pape *et al.* [182] studied the effects of increasing heights of the vortex generator on the dynamic stall process of the OA209 airfoil. As can be observed in Figure 2.23, an increase in the height of the vortex generator results in a systematic reduction of the lift-hysteresis and indicates that the vortex generators assist in the flow reattachment process. However, due to the small range of angles and consequently operation in light-stall regime, the effects of VGs on the dynamic stall vortex cannot be described using the plot. Similarly, the effects of different shaped VGs were investigated by Heine *et al.* [183]. It was observed in the study that VG shapes promoting counter-rotating spanwise-oriented vortices showed slightly

better hysteresis behavior to the configurations that produced co-rotating streamwise-oriented vortices. It was, furthermore, observed that a larger spacing between each pair of counter-rotating streamwise vortices resulted in a larger lift during the dynamic stall process. Therefore, a more compact arrangement of VGs can alleviate the effects of the dynamic stall vortex.

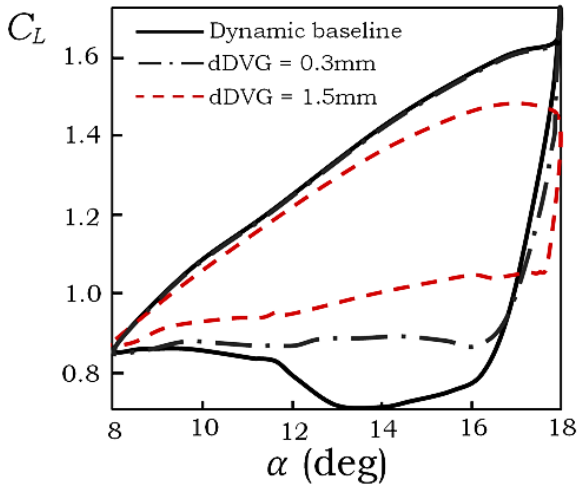

Figure 2.23 - Effect of vortex generator height (hDVG) on the dynamic stall process of an OA209 airfoil. Reproduced from [182].

Mai *et al.* [184] proposed a unique arrangement of VGs in order to reduce the higher drag produced by the VGs during steady-state operation. In the study, the vortex generators were placed at the underside of the airfoil, near the stagnation point location at moderate angles of attack, as illustrated in Figure 2.24. This arrangement was found to be beneficial since the VGs did not influence the steady-state behavior of the airfoil up to moderate angles of attack. At the higher angles, the VGs would start to interact with the flow and improve the steady-state post-stall lift, as can be observed in Figure 2.24. For the unsteady case, as the angle of attack increased, the VGs were found to still reduce the lift hysteresis during the unsteady process. However,

since the VGs do not influence the flow state earlier, the abrupt loss of lift is still governed by the primary DSV and is found to be similar to the clean airfoil. Therefore, the VGs were observed to improve the lift-recovery after unsteady separation but did not influence the DSV. From this observation, it is clear that the control methodology needs to be applied prior to DSV formation in order to affect the abrupt loss of lift during unsteady separation.

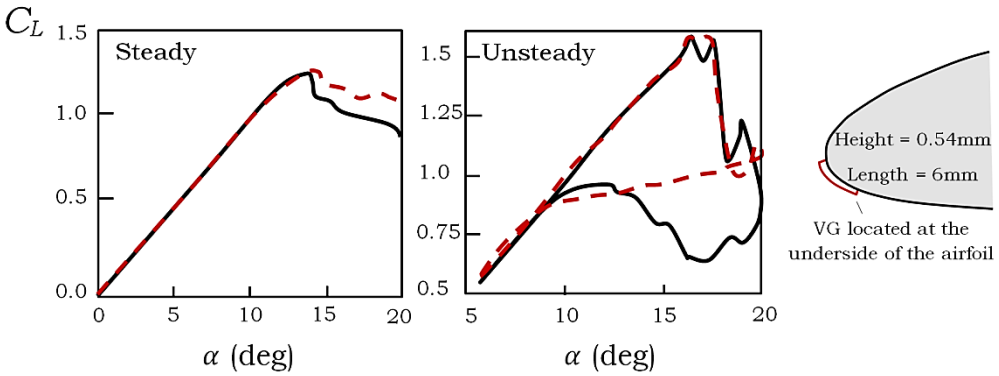

Figure 2.24 – Effects of VGs (dashed lines) placed on the underside of an airfoil on the steady and unsteady performance. Reproduced from [184].

Similar to VGs, leading edge perturbations, such as tubercles or sinusoidal leading edges, have also been observed to produce streamwise vortices. Substantial effort has been devoted to understanding the effects of such leading edge modifications by various researchers [185-188] in order to gain a deeper insight into the underwater maneuverability of fish and aquatic mammals. It has generally been observed that such protuberances at the leading edge can lead to delay in flow separation and an increased lift after steady-state flow separation [189, 190]. The improvements in airfoil performance are associated with counter-rotating streamwise-oriented vortices that entrain the fast-moving flow outside the boundary layer and increase the resistance of boundary layer separation at higher angles of attacks [191], similar to VGs. However, most studies related to such leading edge perturbations are primarily

performed on stationary airfoils and wings. Therefore, it is important to understand the degree to which unsteady motion can influence the flow structures. Ozen and Rockwell [192] found that the use of sinusoidal perturbations at the leading edge of a flat flapping plate resulted in sustained flow attachment due to the formation of counter-rotating streamwise vortices at the leading edge. Further investigations by Fassmann & Thomson [193], using PIV, indicated that these streamwise vortices inhibit spanwise flow during the flapping process. This is illustrated in the vorticity contours presented in Figure 2.25 for a flat plate flapping at a reduced frequency of 0.35. Note that no dynamic stall vortex was observed in these cases.

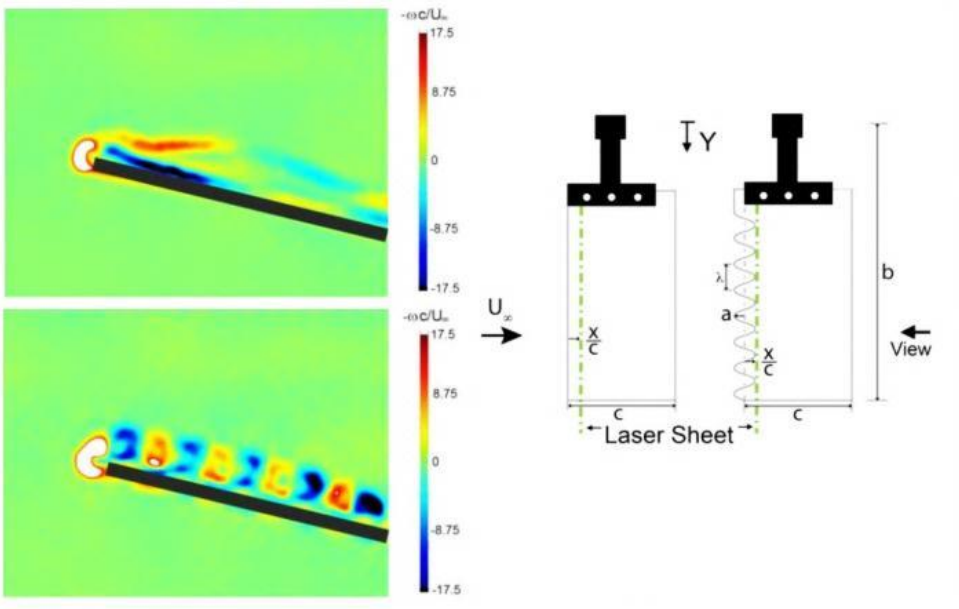

Figure 2.25 - Vorticity contours of a flapping plate with leading edge perturbations indicating the streamwise-oriented vortices [193].

Borg [194] examined the effects of sinusoidal leading edge perturbations on the performance of a pitching NACA 0021. It was stated that the sinusoidal profile improved the performance of the airfoil in terms of the maximum lift generated as well as reducing the size of the

hysteresis during the downstroke motion of the airfoil. It was, furthermore, shown that an increase in the spacing between peaks leads to an increased maximum lift and a larger hysteresis during the dynamic stall process. This observation is similar to the case of VGs, discussed earlier. Therefore, closely packed streamwise vortices, generated by closely spaced leading edge perturbations or VGs, is effective for dynamic stall control. This is advantageous since such an arrangement was also observed to improve the steady-state maximum lift as well the stall angle of attack of the NACA 0021 airfoil. It has furthermore been demonstrated, using numerical analysis, that such leading edge modifications can improve the performance of wind turbine blades at higher wind speeds [195].

Using leading edge perturbations for dynamic stall control is, therefore, similar to the use of vortex generators near the leading edge of the airfoil. It is, though, worth noting that leading edge perturbations do not affect the steady-state drag to a large extent as compared to the vortex generators. Nevertheless, implementation of leading edge perturbations on practical wind turbines would require changes in the design process of the blades and, therefore, would affect the current manufacturing practices. On the other hand, VGs can be implemented on currently operational turbines. However, further research is required to understand the effects of VGs on the dynamic stall process during deep-stall conditions. Such an analysis is necessary in order to better perceive the influence of the VGs on the primary dynamic stall vortex and the associated large increases in lift and drag.

2.4.3 Effects of Spanwise Vortices

Similar to streamwise-oriented vortices, vortices with an axis-orientation normal to the oncoming flow can also be used to increase flow

entrainment and reduce the extent of flow separation. However, unlike the extensive research into methods used to generate streamwise vortices, a rather limited amount of work has been done to understand the effects of spanwise-oriented vortical structures. An investigation by Neumann and Wengle [196] illustrates the effectiveness of such vortices on separation control. In the study, surface-mounted fences were used to generate spanwise-oriented vortices that would enhance mixing and lead to a reduction of the size separation zone behind a backward facing step. Due to increased entrainment of ambient flow, it was observed that a 13% reduction of the mean reattachment length was obtained using surface-mounted fences. The mechanisms involved in such flow, perceived by the author of the thesis, are illustrated schematically in Figure 2.26. It is believed that high entrainment of ambient flow, caused by spanwise-oriented vortices, is primarily responsible for the decrease in the separation zone behind a backward facing step.

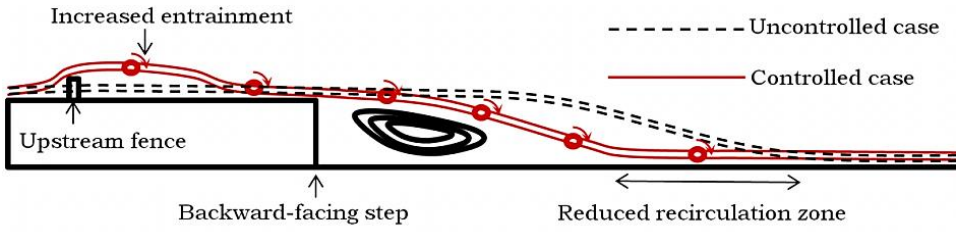

Figure 2.26 - A conceptual illustration of the workings of a surface-mounted fence and its effects on the reattachment extent behind a backward facing step.

Other than this particular study, no practical implementation of fences, for the purpose of airfoil stall control, was found. It is believed that such a control would yield similar effects on the airfoil performance to vortex generators. It has been argued that using two fences in close proximity along with a small amount of suction can lead to a captured vortex structure that can increase the bound circulation on an airfoil

and the lift generated [197, 198]. However, such methods are difficult to implement in real life. Similarly, no particular studies have focused on exploring the effects of spanwise vortices on dynamic stall. However, some inferences can be obtained from the published work. For instance, plasma actuators can be used to create spanwise vortices as illustrated by Post and Corke [199]. Although the actuators are a zero net-mass flux method and can be used to modify the boundary layer profile and postpone separation [200-202], periodic switching can lead to the creation of spanwise vortices. Unsteady excitation, at lower forcing frequencies, for the NACA 0015 airfoil [199] was observed to give rise to a train of spanwise periodic vortices, as shown in Figure 2.27. These periodic spanwise vortices cause the flow to reattach more quickly, compared to the unactuated case, and also interfere with the DSV formation. However, it can be observed that these vortex structures are significantly weaker compared to the streamwise vortices generated by vortex generators.

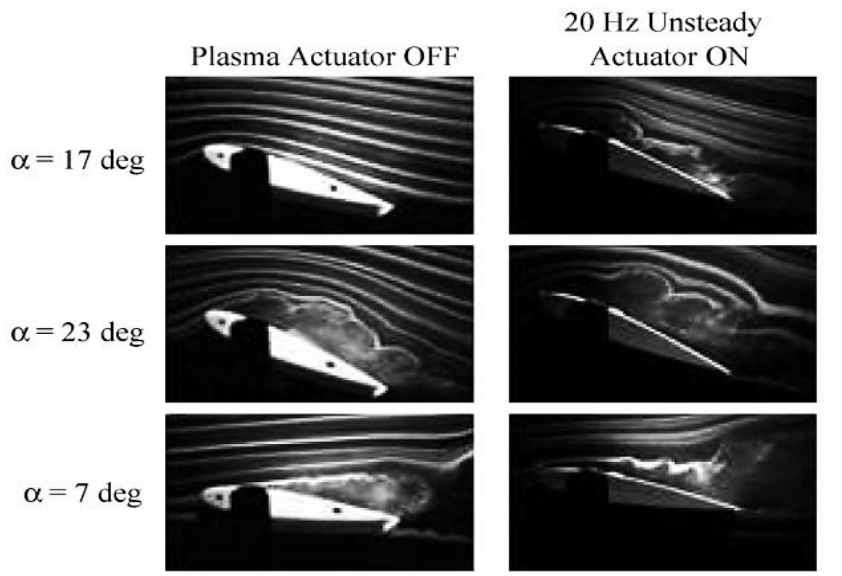

Figure 2.27 – Spanwise oriented vortices generated using plasma actuators through unsteady actuation on the NACA 0015 airfoil undergoing dynamic stall [199].

The effects of the spanwise vortices, produced from unsteady actuation, on the process of dynamic separation can be observed clearly from the lift plots presented in Figure 2.28. As can be observed during steady actuation, the lift produced by the airfoil during sinusoidal pitching is largely unaffected, except near the peak lift. The steady actuation does not aid in lift-recovery or reduce the vortex lift. However, through unsteady actuation, the peak vortex lift is reduced. It can, furthermore, be observed that the hysteresis in the lift force is slightly smaller compared to the unactuated case. This effect is caused by the spanwise-oriented vortical structures that are produced through unsteady actuation of the plasma actuators.

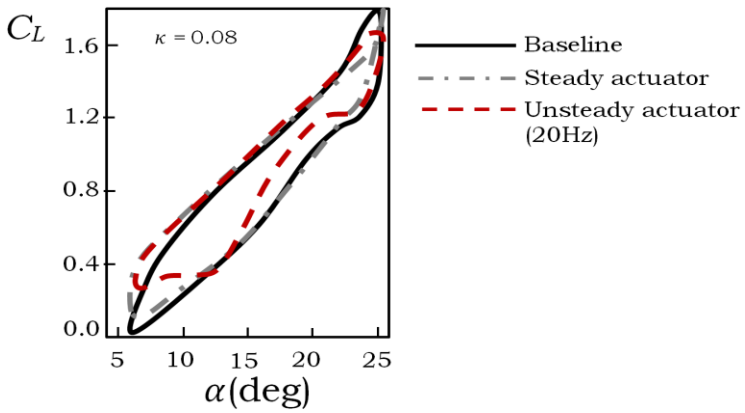

Figure 2.28 – Effects of plasma actuator on dynamic stall of NACA 0015 airfoil. Reproduced from [199].

As can be observed in the flow visualization (Figure 2.27), the spanwise vortices created using unsteady actuation of plasma actuators are considerably weaker and further apart. Therefore, other methods need to be investigated for the creation of stronger and more compact spanwise-oriented vortices. Local surface buzzing is one such approach, where high frequency surface vibrations can lead to the creation of spanwise-oriented vortices. This method was investigated by Park *et al.* [203] to control the flow separation at high angles of attack on the NACA

0012 airfoil. The method has been demonstrated to reduce the abrupt flow separation of thin airfoils during steady state operation at high angles of attack. It was shown that at an angle of attack of 14°, the flow separation on the upper surface of the NACA 0012 airfoil is delayed and the separation region is forced towards the trailing edge of the airfoil. This effect can be attributed to the spanwise-oriented vortices created by the buzzing process, as illustrated in the oil-surface flow visualizations presented in Figure 2.29. However, note that the vortices are not coherent at inception, and in fact take form much later on the airfoil compared to the location of the buzzing, which is at the leading edge of the airfoil. The buzzing process, therefore, might produce shear layer oscillations in the detached flow at the leading edge that ultimately rollup at reattachment to form the spanwise vortex structures illustrated in Figure 2.29. It is also important to note that the mechanisms involved in creating this local buzzing effect are difficult to implement in practical conditions.

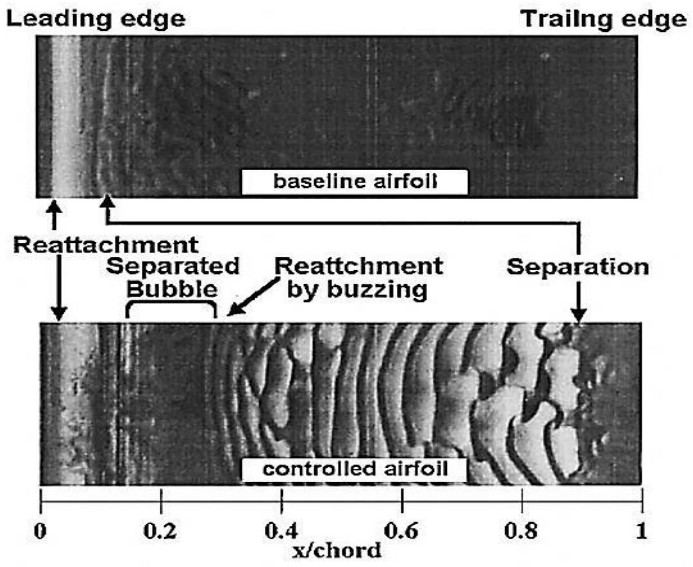

Figure 2.29 – Surface flow visualizations of the 'buzzing' effect on the NACA 0012 airfoil at an angle of attack of 14° [203].

Furthermore, recent investigations into self-excited Helmholtz resonators, with a square exit, have shown similar shear layer oscillations as those observed for the buzzing method [204-206]. These shear layer oscillations can lead to roll-up, resulting in the formation of spanwise oriented vortices. This is indicated in the streamwise velocity contours over the resonator, acquired using LES of the flow, in Figure 2.30. The spanwise vortices created using this method have been used for laminar flow control on flat surfaces. However, notice that the spanwise extent of the vortices is very limited and, therefore, the effect is very local. This can be remedied, though, using a distribution of several such resonators over the wing surface. The novel concept has an added benefit that no moving parts are involved in the flow control and, hence, the shear layer instability is caused by the self-excitation of the pressure within the resonator. Further research into this method is essential before implementation.

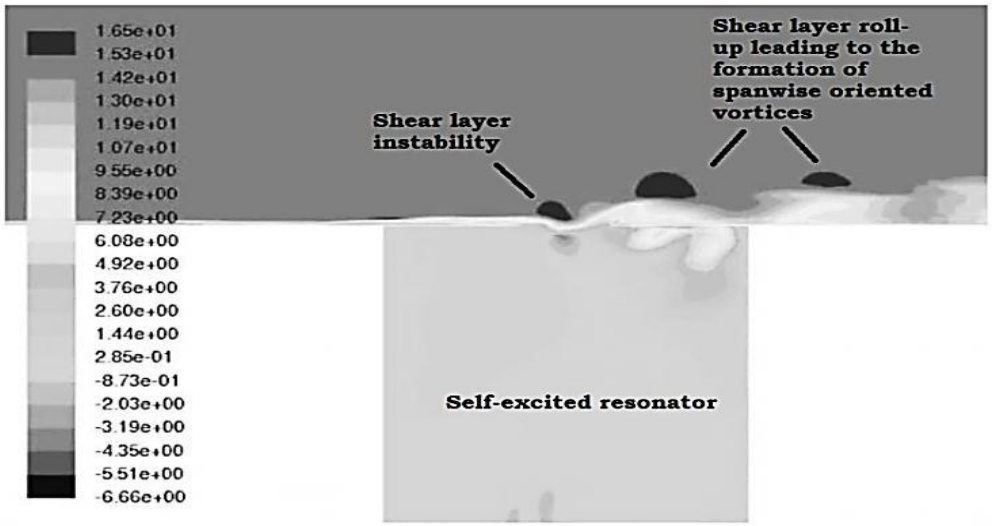

Figure 2.30 – Streamwise velocity contours for flow in the vicinity of a self-excited Helmholtz resonator, indicating the shear layer instability and eventual roll-up to produce spanwise-oriented vortices [205].

It is interesting to note that although spanwise-oriented vortices might constitute a similar or perhaps better effect than the streamwise-oriented vortices, no significant research has been conducted to understand the effects of such vortices on the performance of airfoils used in wind turbine industry. Particularly, the effects of abrupt lift decay during unsteady separation are unknown and cannot be inferred from the light-stall cases presented in this section. It is also interesting to note that most of these methods have a zero net-mass flux, implying that no additional fluid is injected in the flow to actuate the effects. However, the drawback of such methods is that they require ambient fluid to be present in the vicinity of the control to influence the flow to a large degree. Therefore, after separation, such favorable conditions are generally not available and the methods would lose their potency to control flow separation. Furthermore, a pair of counter-rotating spanwise vortices might be even more effective. However, no method has been investigated to create such vortical patterns.

2.4.4 Effects of Ring-Type Vortices

Synthetic jets have been known to produce ring-type vortices that can deform and influence the flow field in the vicinity of the jets. Classified as a zero net-mass flux method, synthetic jets can be used to improve the static or steady-state performance of airfoils, through delayed stall and decreased drag [207, 208]. These have, furthermore, been predicted to improve the structural stability of a wind turbine blade through reduced vibrations [209, 210]. The jets are formed entirely by ambient fluid in the vicinity of the body, through the motion of a piston or diaphragm enclosed inside a cavity [211]. Therefore, the zero-net mass flux property of this method obviates the need for complex plumbing and reservoirs required for consistent, or even periodic, flow injection or removal, similar to self-excited resonators discussed in the previous section.

Synthetic jets have also been examined for dynamic stall control. For a thick NACA 0020 airfoil, it was demonstrated that the hysteresis in the forces observed during the dynamic stall process is significantly reduced and the use of synthetic jets improves the performance of a vertical axis wind turbine [212]. It has, furthermore, been illustrated that use of directed synthetic jets can increase the dynamic stall angle of attack and improve the post-stall lift behavior of an airfoil considerably [213]. The process through which synthetic jets obtain this control is illustrated in Figure 2.31, using instantaneous contours of vorticity magnitude in the wake of a jet at selected spanwise locations. These images were obtained through Direct Numerical Simulation (DNS) of the flow field in the vicinity of a jet [214]. Note that a vortex line that passes through the center of the vortex cores is also depicted in the diagram. As can be observed, the jets expel a ring-shaped vortex structure that travels downstream under the influence of the flow. Though, not strictly a spanwise- or streamwise-oriented vortex, the ring vortex structure also serves to entrain the ambient fluid to yield a similar effect. However, it has been shown that the structure is very unstable and usually constitutes a local effect, depending on the actuation frequency and the Reynolds number [215].

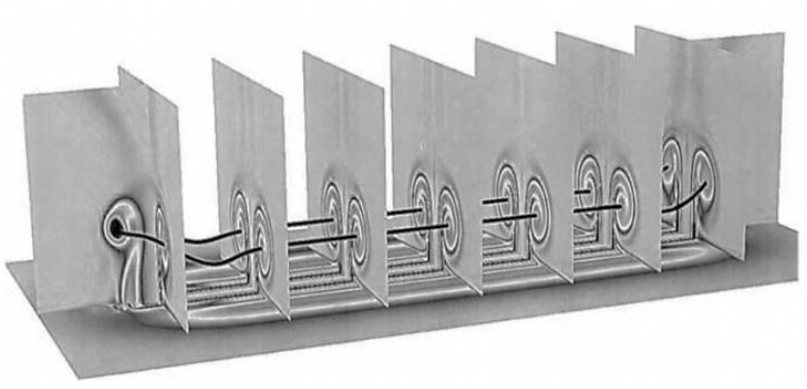

Figure 2.31 – Flow field in the wake of a synthetic jet [214]

The concept of using synthetic jets for dynamic stall control is still in its infancy. Further experimental evidence needs to be produced in order to better understand the effects and mechanisms involved. The effects of an airfoil motion on the vortex rings created by the jets should also be investigated. There are several drawbacks associated with the use of synthetic jets that need to be addressed as well, prior to its implementation for dynamic stall control. For instance, the moving diaphragm of a synthetic jet would pose difficulties in maintenance. This problem is further exacerbated since the jets need to be placed within the wing itself, near the leading edge. Moreover, the small openings of jets are prone to dust and water accumulation that will negatively influence the performance of the control.

2.4.5 Effects of Leading edge Modifications

Several leading edge modifications have been used previously to control dynamic stall, specifically for helicopter applications. For instance, leading edge slots, or retractable leading edge slats, have been investigated for this purpose. Slats are commonly used in modern aircraft during landing and takeoff. These have been found to increase the steady-state maximum lift generated by the airfoil as well as the stall angle of attack [216, 217]. The principal mechanism of the slats is that they increase the area of the wing during extension and the camber of the wing due to pivoting. Furthermore, the high momentum fluid from the lower side of the wing is discharged through the opening of the slat elements, increasing the boundary layer momentum and making it less prone to adverse pressure gradients at higher angles. A drawback of this method is the increased drag that is observed during deployment.

Numerous studies have demonstrated the capability of slots and retractable slats during the process of dynamic stall [218, 219]. Studies

by Carr and McAlister [219] have indicated that a fixed leading edge slot, optimized for steady-state lift for a VR-7 airfoil, can lead to a delay in the primary DSV formation on the airfoil during unsteady operation. This suppression of the DSV can lead to reduced peak lift and moment as well as a reduction in the lift hysteresis. An increased distance between the slat element and the airfoil leads to a further delay in the dynamic stall process. A similar suppression was observed for the VR-12 airfoil, as illustrated in Figure 2.32. The plots indicate that there is slight delay in the dynamic separation for the slatted airfoil since the lift peak due to the vortex structure is not yet fully realized. Furthermore, the slat also assists in the lift-recovery process during the downstroke motion.

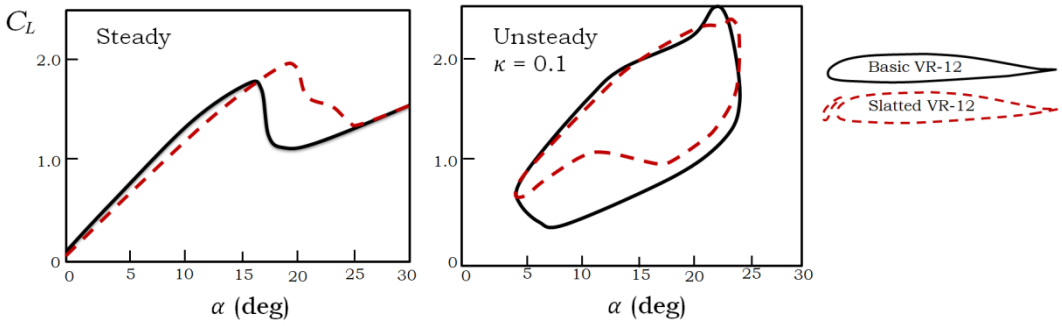

Figure 2.32 - The effects of a leading edge slat on the steady and unsteady performance of the VR-12 airfoil. Reproduced from [220].

In addition to the high momentum fluid injection at the leading edge, the effects of the slat on an airfoil can also be attributed to the change in camber. The effects of changing camber on the dynamic stall process have been examined further through the concept of drooping leading edges [221, 222]. Dynamically-drooped leading edges have been shown through numerical studies to reduce the large scale flow separation and the DSV size during unsteady separation [223]. A Variable-Droop Leading Edge (VDLE) was studied experimentally for dynamic stall control on the VR-12 airfoil by Chandrasekhara *et al.*

[224]. The leading 25% of a VR-12 airfoil was drooped during the sinusoidal pitch oscillations. The VDLE concept was obtained simply by fixing the leading edge with respect to the laboratory coordinate system while rotating the airfoil. The concept aimed to lower the leading edge of the airfoil to reduce the angle of attack at the leading edge, promoting favorable pressure gradients and resistance to flow separation there. The application of the VDLE concept resulted in reduced vortex strength, as shown in Figure 2.33 through unsteady surface pressure measurements. Furthermore, it can be observed that the VDLE delayed the onset of dynamic stall.

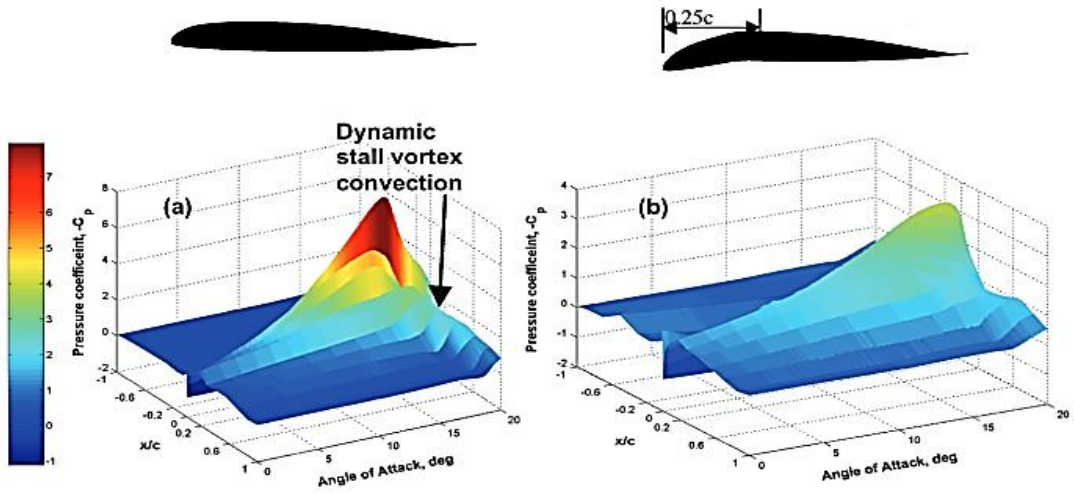

Figure 2.33 – Pressure distribution contours for the (a) uncontrolled and (b) controlled dynamic stall process on the VR-12 airfoil. The pressure signature of the dynamic stall vortex is clearly visible for the uncontrolled case, as is the reduced vortex strength for the controlled case [224].

The effects of variable droop on the performance of the airfoil lift during dynamic stall are illustrated in Figure 2.34. As can be observed, the reduced vortex strength, due to the leading edge droop, results in a significantly smaller peak lift during the pitch-up. Furthermore, for the smaller reduced frequency of 0.05, it can be observed that after the

vortex separation, the airfoil with a variable-droop leading edge has a smoother lift decay compared to an abrupt loss of lift for the simple airfoil. However, the hysteresis in the lift is significantly more pronounced compared to the clean airfoil, indicating that the lift-recovery process during the pitch-down motion is hindered by the leading edge droop. This observation can also be made in the numerical work discussed in references [222, 223]. A similar, yet less pronounced, behavior is observed at the higher reduced frequency. Therefore, an airfoil with a larger camber near the leading edge can promote an improved dynamic stall behavior, such as a decrease in vortex strength and a delay in its inception compared to the un-cambered airfoils, albeit at the expense of greater hysteresis.

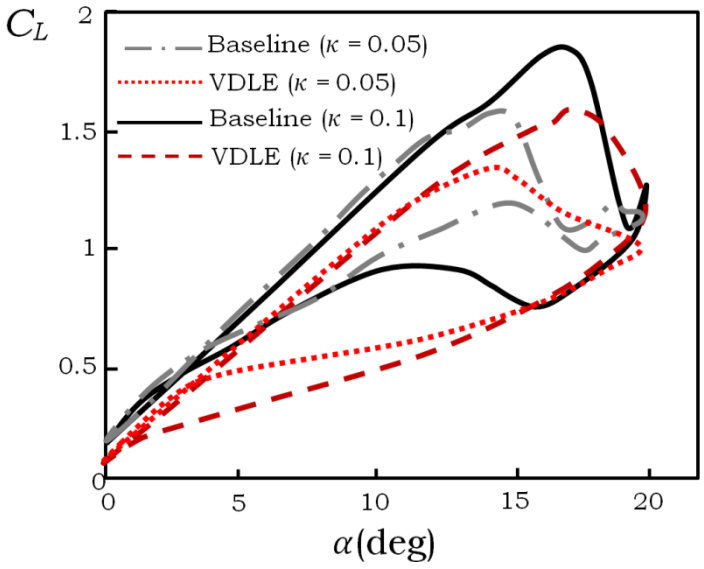

Figure 2.34 – Effects of VDLE on the lift generated during sinusoidal dynamic stall at different reduced frequencies. Reproduced from [224].

2.4.6 Effects of Trailing edge Modifications

Similar to leading edge modifications, several trailing edge alterations, conventionally used for steady-state improvements in performance of airfoils, have been investigated for dynamic stall cases. For instance,

trailing edge flaps have been investigated for dynamic stall control. Operating on a similar principle to the leading edge droop, the trailing edge flap also modifies the camber of the airfoil section. Davis *et al.* [225] used a discrete vortex method to numerically simulate dynamic stall control using a trailing edge flap. The base airfoil was a NACA 0012 airfoil pitched about a mean angle of attack of 15^{o} at an amplitude of 10^{o}. The flap was deflected upwards using a brief sinusoidal pulse signal. It was observed that only an upward flap deflection could yield any benefit in controlling the peak moments. The flap deflection, however, had a minimal effect on the dynamic stall vortex development. The effects of an upward flap deflection of 20^{o} are illustrated in Figure 2.35. As can be observed, deflecting the flap during the last third quarter of the dynamic stall process reduces the strength of the DSV slightly. The effects of induced camber in this manner are less beneficial, since the actuation takes place at the trailing edge of the airfoil. Further to this, the lift decay is also quite significant during the downstroke motion, resulting in a much larger hysteresis of the forces. The trailing edge flap deflection, therefore, considerably aggravates the lift-recovery process. Similar effects were observed for other airfoils using trailing edge flaps for dynamic stall control [226, 227].

Note that a similar, but less pronounced effect was observed for the leading edge droop study presented in the previous section. This confirms the observation presented earlier that the camber of the airfoil can lead to a larger hysteresis in the lift force. Furthermore, in order to affect the dynamic stall vortex, leading edge modifications are more effective compared to trailing edge modifications.

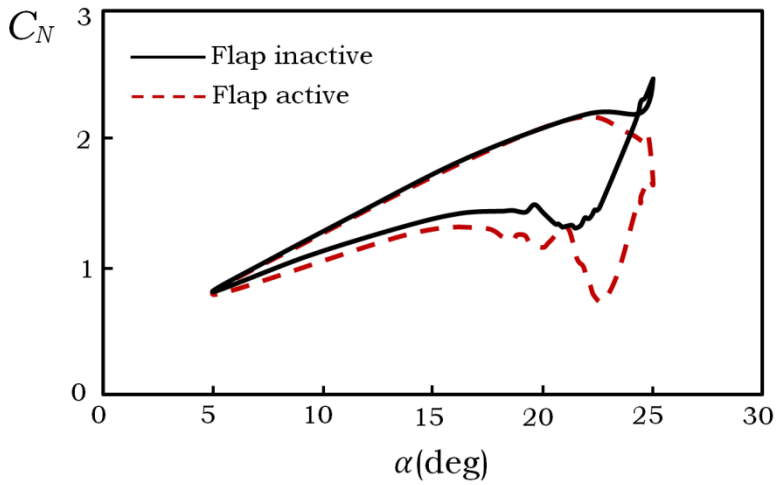

Figure 2.35 - Effects of a trailing edge flap on the dynamic stall process of NACA 0012. Reproduced from [225].

Trailing edge flaps require a very large control area in order to affect the flow conditions on the airfoil. For example, in the experiments and numerical work discussed here, up to 25% of the airfoil trailing edge was used as the flap. In recent studies, similar changes in camber have been proposed using Gurney flaps or other modifications. The Gurney flap is a simple device placed at the trailing edge of the airfoil to increase the aerodynamic lift [228]. The flap has been shown experimentally to improve the lift produced by the airfoil during steady operation [229, 230]. A deployed Gurney flap has been observed to shift the entire lift curve upwards, similar to the effects of increasing camber on an airfoil [231]. For dynamic stall control, the flap is, however, seldom used as a stand-alone control and is often employed with other methods to improve the lift characteristics during unsteady separation. For instance, with the VDLE, the Gurney flap can be used to shift the entire lift curve upwards [232]. However, it was also observed that the hysteresis in the lift force was significantly larger compared to the clean airfoil (VR-12) used in the study.

Similar to a Gurney flap, miniature trailing edge effectors (MiTEs) increase the associated camber of the airfoil and therefore result in a similar jump in the lift curve [233]. However, the overall drag is also increased. The MiTEs are, however, not placed exactly at the trailing edge and are generally designed so that they can be deployed on either side of the airfoil. Therefore, it can be proposed that the increased hysteresis, due to the increased camber, can be negated using the MiTEs by deploying on the upper side of airfoil.

Generally, compared to the leading edge methods, the trailing edge methods have a limited efficacy, primarily due to the nature of the dynamic stall process. The process is instigated due to the formation of the primary DSV structure at the leading edge of the airfoil. This primary DSV is responsible for the sudden increase in lift, drag and moments during the later stages of the pitching cycle. Furthermore, as the vortex structure convects, large flow separation follows. Therefore, dynamic stall control strategies need to focus on modifying the core vortex behavior. This can only be obtained using methods that interfere with the vortex formation and development early on during the pitching process. Hence, trailing edge methods are not effective strategies to control the vortex lift, the abrupt flow separation and the lift hysteresis.

2.4.7 Effects of airfoil deformation

Similar to the methods that have been used to change the apparent camber of the airfoil, such as the VDLE concept, other methods have been proposed to increase the leading edge radius of airfoils during the dynamic stall process. This has been acquired through the Dynamically Deforming Leading edge (DDLE) concept [234]. It has been observed that the leading edge curvature of the airfoil can be deformed dramatically in real time through small chordwise movements of the leading edge [235].

The primary objective of this approach was to reduce the local Mach number in compressible flow conditions and favorably alter the leading edge pressures by re-shaping the airfoil nose. This would allow possible delays in the dynamic stall onset and would reduce the effects of the separation on the airfoil. Using the NACA 0012 airfoil as the base case (shape 0), it was illustrated that leading edge curvature could be changed by up to 320%, resulting in a different leading edge profile at each change in curvature. The modifications in the airfoil leading edge were made possible through very slight deformations of a thick carbon-fiber composite skin, making up the first 20% of the airfoil. Linear translation of a truss system placed inside the airfoil resulted in large leading edge deformations.

The method was tested at real helicopter operating conditions, between Mach numbers of 0.3 and 0.4. The airfoil was oscillated at a reduced frequency of 0.05 and Point Diffraction Interferometry (PDI) measurements were used to acquire detailed and instantaneous flow field density information that could be used to derive both surface and global pressure distributions. Keeping the deformation constant as the airfoil was pitched, the effects of DDLE on the dynamic stall process were investigated using the pressure signature of the primary DSV. It was observed that increasing the leading edge radius resulted in the delay of dynamic stall onset to higher angles. Furthermore, at the largest leading edge radius, it was illustrated that the loss of peak suction pressure was gradual, indicating a less abrupt flow separation. It is important to note that the rate at which the shape is changed in DDLE is not as significant as the shape itself. Therefore, a permanent modification can also improve the dynamic stall characteristics [236]. This further implies that a rounder leading edge, with smaller pressure gradients, can improve the dynamic stall characteristics of an airfoil.

2.4.8 Hybrid Schemes

Apart from stand-alone control systems, hybrid schemes have also been investigated for dynamic stall control. The hybrid schemes comprise of two or more control methods applied simultaneously to result in an additive effect on the dynamic stall process. For instance, earlier it was discussed that the VDLE concept has been used with Gurney flaps to improve the lift characteristics of the airfoil [232, 237]. Similarly, other hybrid schemes such as combinations of plasma actuators/Gurney flaps [238], trailing edge flaps/Gurney flaps [239], leading- and trailing edge flaps [240] and even schemes involving three separate control methods (VGs, VDLE and Gurney flap) [241] have been used for dynamic stall control. However, it is important to note that, generally, implementing even a single control methodology on actual blades and wings requires significant modification of the blade structure. Even though the effects of different control methodologies can be combined to yield desirable outcomes, practical applications of such hybrid schemes are generally limited to relatively simple control techniques.

2.4.9 Summary of Control Techniques

The process of dynamic stall has been controlled using various flow control methodologies, as shown in this section. Several of these methods have been shown to provide varying degrees of effect on the process. A summary of all the methods reviewed in this chapter is given in Table 2.2. The table outlines the methods, their primary effect on the flow and the degrees by which these methods affect the dynamic stall lift.

Several important observations for control requirements have been made during this review process. These are highlighted as follow:

- **Modification of primary DSV:** The primary vortex structure during dynamic stall results in an abrupt increase in the lift and moment during the process. Modifying or reducing the vortex strength is, therefore, a vital part of dynamic stall control. It is important for a control scheme to be active prior to the formation of the dynamic stall vortex. It has been observed that delayed interference in the unsteady separation process yields small benefits.
- **Abrupt stall:** Once the primary DSV separates from the airfoil, large scale flow separation is observed. This results in an abrupt loss of lift after separation. Therefore, reduced vortex strength can lead to smoother lift decay.
- **Lift recovery:** The lift hysteresis during sinusoidal oscillations is also an indication of the extent of flow separation during the unsteady case. A control method that reduces the hysteresis, therefore, assists in flow recovery as the angle of attack is lowered. This can be translated for the constant pitch case as smoother lift decay after primary DSV separation.
- **Leading edge control:** It has been observed that trailing edge flow control has a very limited effect on the dynamic stall process. Since the unsteady separation process instigates at the leading edge of an airfoil, it is necessary for the control to be applied in this region.
- **Active and passive flow control:** Active flow control is generally favored under steady operating conditions since the precursors for such separations are widely understood. This is primary due to the fact that the control is applied only when needed and, therefore, does not modify the flow behavior unnecessarily. However, for dynamic stall control such methods are generally not applicable since a significantly robust actuation is required. Furthermore, issues pertaining to sensor location and selection, determination of suitable

precursors to unsteady separation and appropriate control algorithms further restrict the applicability of active control methods for dynamic stall control. Therefore, it is more suitable to look into passive control methodologies when dealing with dynamic stall control. Such control methodologies do not require any sensors and are deployed continuously to affect the flow. However, due to continuous deployment, passive flow control methods can degrade the steady-state performance of airfoils.

Therefore, for dynamic stall control on wind turbine blades, a passive flow control methodology that does not degrade the steady-state behavior to a large extent, needs to be implemented at the leading edges of the blades, near the root locations where the problem predominantly exists. Such a control strategy would considerably improve the unsteady performance of the turbine blades by reducing the stall intensity and the ensuing vibrations in the blade.

Table 2.2 – Summary of flow control methods and effects on the lift generated during dynamic stall process.

Method (Active/Passive)	Effect	Reduced vortex strength	Delay in stall onset	Reduced stall intensity	Aid in lift recovery	Comments
Fluidic injection (Active)	Improves BL stability and resistance to separation.	High	Minimal	Minimal	Minimal	Requires complex plumbing and reservoirs of high pressure fluid.
Fluid removal (Active)	Improves BL stability due to removal of low-momentum or reversed flow.	High	-	-	-	Requires complex plumbing and reservoirs. Only flow visualization results available. Further testing required.
Periodic excitation (Active)	Periodic fluidic injection. Might create spanwise-orientated vortices.	-	Minimal	High	High	Requires complex plumbing and reservoirs of high pressure fluid. Only light-stall cases investigated. Further testing required.
Vortex generators (Active/Passive)	Streamwise vortices to increase fluid entrainment and enhance mixing.	-	High	-	High	Further optimization studies required. Effects of counter-rotating streamwise vortices unknown.

Vortex generators (Passive - deployment on pressure side)	Streamwise vortices created at high angles of attack. Reduced influence on steady-state drag.	Minimal	Minimal	Minimal	High	The generators do not influence the DSV formation during early stages of development.
Leading edge perturbations (Passive)	Streamwise vortices to increase fluid entrainment and improve stall behavior.	Moderate	Minimal	-	Moderate	Further testing for dynamic stall control still required for deep-stall case.
Surface-mounted fences (Passive)	Creation of co-rotating spanwise oriented vortices to improve reattachment.	-	-	-	-	No testing for dynamic stall cases available.
Plasma actuators - Steady actuation (Active)	Modifies BL profile and postpones separation through flow acceleration.	Minimal	Minimal	-	Minimal	No significant effect on the dynamic stall process was observed.
Plasma actuators - Unsteady actuation (Active)	Creation of spanwise-oriented vortices for improved flow entrainment.	Moderate	Moderate	-	Moderate	Vortices generated are of reduced strength. Methods need to investigated to create stronger spanwise vortex structures

Local surface buzzing (Active)	Creates spanwise vortices through shear layer instability for increased flow entrainment and separation delay.	-	-	-	-	No testing for dynamic stall cases available.
Self-excited Helmholtz resonator with square outlet (Passive)	Creates spanwise vortices through shear layer instability for increased flow entrainment and separation delay.	-	-	-	-	Limited extent of control in the immediate vicinity of the resonator. No testing for dynamic stall cases available.
Synthetic jets (Active)	Ring-type vortices can lead to high entrainment. Results in delayed stall and decreased drag.	-	Moderate	-	Moderate	Needs further work particularly for deep-stall cases. Mechanisms involved need to be studied under dynamic stall conditions.
Slots/Slats (Active/Passive)	Increased airfoil area and camber. High momentum fluid from pressure side spilled through the slot opening on the low-pressure upper side.	Minimal	Moderate	-	Moderate	Increased drag due to the slot element needs to be reduced. Further research into deep-stall cases required.

Variable Droop Leading edge (Active)	Changes camber of airfoil. Promotes favorable pressure distribution near the LE.	High	Minimal	Moderate	Degrading	Requires a large control length and complex mechanisms for deployment to affect the dynamic stall lift. Increased hysteresis in lift observed. Further testing required for deep-stall case.
Trailing edge flap (Active)	Modified camber of the airfoil.	Moderate	-	-	Degrading	Requires a large control length to be effective. Significantly degrades the lift-recovery process. Not suitable for dynamic stall control.
Gurney flap (Passive)	Modified camber. Needs to be deployed from the onset of rotation.	Degrading	-	-	-	Increases the lift generated from the onset. Not observed to modify other factors.
Miniature Trailing edge Effectors (Active)	Modified camber. Can be deployed on either side of airfoil.	-	-	-	-	No testing for dynamic stall cases available.
Leading edge deformation (Active)	Modifies leading edge radius for favorable pressure gradient.	Minimal	Moderate	-	Moderate	Requires complex mechanisms near the leading edge. Further testing required for deep dynamic stall cases.

2.5 Concluding Remarks

The purpose of this literature review is to clearly elaborate that the problem of dynamic stall widely occurs on wind turbine blades at normal operating conditions. It is well understood that the unsteady separation on wind turbine blades can be caused by a multitude of factors such as turbulent inflow, gusts, tower shadow effects and persistent wind direction changes. When turbines are packed closely together in wind farms, the problem is aggravated due to operation in the wakes of upstream turbines. Large-scale wind tunnel experiments by the NREL have given a considerable insight into the process on wind turbine blades. These experiments have shown that dynamic stall generally persists near the inboard sections of a turbine rotor, under low-turbulence conditions, when the turbine is operating at a persistent yaw misalignment with the inflow. However, it was also observed that, other than direct experimental observation, no methods are available to compute the rapid changes in angle of attack on a blade section that can lead to occurrence of dynamic stall in general operating conditions.

After establishing that dynamic stall persists on wind turbine blades, a detailed investigation of the dynamic stall process illustrated that the primary mechanisms involved in the increased lift are still disputed. Similarly, other than the effects of increasing pitch rates, the effects of several other parameters are largely uncertain. It was also shown that the lift-curve behavior of the different types of dynamic stall processes, such as dynamic stall due to sinusoidal and constant pitch motions, are principally similar. This facilitated the comparison of different methods that have been used for dynamic stall control on sinusoidally pitching airfoils. It was found that the control methodologies, most suited for wind turbine applications, need to be

implemented passively at the leading edge of the blades to influence the dynamic stall vortex development from the very onset.

In light of the literature review, the primary objective of this research can be highlighted as follows:

- To develop a better understanding of the occurrence of dynamic stall on wind turbine blades in real environments and devise methods to predict its occurrence. This research objective also helps to develop suitable precursors for dynamic stall control based on incoming wind speed and direction. Furthermore, it allows appropriate location of the control methodology on wind turbine blades near inboard stations in order to minimize the influence of the control at the outer regions of the blade.
- To understand the unsteady lift generated during the dynamic stall process. A deeper insight into the mechanisms involved would aid in developing appropriate control techniques for dynamic stall vortex suppression.
- Devise and test different passive flow control methods on thick airfoil sections to determine the effectiveness of these control techniques for wind turbine applications. It is, furthermore, desirable to test control techniques that can be implemented on currently-operational wind turbines with relative ease.

Towards these objectives, **Chapter 3** of the thesis presents an analytical model that predicts the occurrence of dynamic stall on wind turbine blades based on wind speed and direction variability. The model has been validated against previously-published experimental work and gives an insight into the causes of dynamic stall on wind turbine blades. Further to this, in **Chapter 4**, the effects of wakes on downstream wind turbines are presented. For this study, numerical analysis [46, 47] was

used to determine the wake characteristics. These wake characteristics were then employed to determine the occurrence and causes of dynamic stall on wind turbines operating in the wake. This research provides information regarding suitable location of required passive control devices along the blade length. **Chapter 5** of the thesis investigates the separation process of thick airfoil sections under steady-state conditions. Previous research [190] indicated larger lift-curve slopes, greater than the theoretical maximum, for the thick airfoil section at transitional Reynolds numbers and an abrupt loss in lift after flow separation. Since a large increase in the lift curve slope is also observed for the dynamic stall case, further investigations into this steady-state behavior of the airfoils were conducted in chapter 5 to better understand the lifting behavior during the dynamic case. For the unsteady process, an experimental campaign was undertaken to better understand the effects of differing parameters during dynamic stall. This study is presented in **Chapter 6** of the thesis. **Chapter 7** of the thesis discusses the control requirements and objectives for dynamic stall on wind turbine blades. Following this, three different passive flow control mechanisms were investigated for dynamic stall control. The methods were selected based on an improved understanding of the unsteady process and the detailed review of the control methods presented in this chapter. Two of these methods were based on improving flow entrainment and resistance of the boundary layer to reverse flow during the airfoil pitch-up. These methods included the use of counter-rotating streamwise vortices generated using vane-type delta vortex generators and counter-rotating spanwise vortices generated using an elevated wire. The final control method consisted of a cavity on the upper side of the airfoil to act as a reservoir for the reverse flow during pitch-up. Finally, **Chapter 8** of the thesis outlines the significant findings of the research and presents further avenues of research in the subject.

2.6 References for Chapter 2

[1] P. Gipe, Wind energy basics: a guide to small and micro wind systems, Chelsea Green publishing company, 1999.

[2] A. Peacock, D. Jenkins, M. Ahadzi, A. Berry, S. Turan, Micro wind turbines in the UK domestic sector, Energy and Buildings, 40(7) (2008) 1324-1333.

[3] Y. Kato, K. Seki, Y. Shimizu, Vertical axis wind turbine, US patent number US4247526A, 27 Jan 1981.

[4] E. Hau, H. Von Renouard, Wind turbines: fundamentals, technologies, application, economics, Springer, 2013.

[5] G. Müller, M.F. Jentsch, E. Stoddart, Vertical axis resistance type wind turbines for use in buildings, Renewable Energy, 34(5) (2009) 1407-1412.

[6] A.C. Hansen, C.P. Butterfield, Aerodynamics of Horizontal-Axis Wind Turbines, Annual Review of Fluid Mechanics, 25(1) (1993) 115-149.

[7] T. Burton, N. Jenkins, D. Sharpe, E. Bossanyi, Wind energy handbook, John Wiley & Sons, 2011.

[8] S.J. Miley, A catalog of low Reynolds number airfoil data for wind turbine applications, US Department of Energy, Wind Energy Technology Division, Contract No. DE-AC04-76DP0.3533, 1982.

[9] F. Bertagnolio, N.N. Sørensen, J. Johansen, P. Fuglsang, Wind turbine airfoil catalogue, Report Risø-R-1280(EN), Risø National Laboratory, Roskilde, Denmark, 2001.

[10] R.K. Singh, M.R. Ahmed, M.A. Zullah, Y.-H. Lee, Design of a low Reynolds number airfoil for small horizontal axis wind turbines, Renewable energy, 42 (2012) 66-76.

[11] D.M. Somers, The S809 through S813 Airfoils. Airfoils Inc, 1988. [Proprietary of NREL].

[12] W. Timmer, R. van Rooij, Summary of the Delft University wind turbine dedicated airfoils, Journal of solar energy engineering, 125 (2003) 488.

[13] J.F. Manwell, J.G. McGowan, A.L. Rogers, Wind energy explained, Wiley Online Library, 2002.

[14] P. Fuglsang, C. Bak, Development of the Risø wind turbine airfoils, Wind Energy, 7(2) (2004) 145-162.

[15] P. Fuglsang, C. Bak, M. Gaunaa, I. Antoniou, Design and verification of the Risø-B1 airfoil family for wind turbines, Journal of solar energy engineering, 126(4) (2004) 1002-1010.

[16] F. Grasso, Usage of numerical optimization in wind turbine airfoil design, Journal of Aircraft, 48(1) (2011) 248-255.

[17] J.L. Tangler, D.M. Somers, NREL airfoil families for HAWTs, National Renewable Energy Laboratory, 1995.

[18] R. Clark, R. Davis, Performance changes caused by rotor blade surface debris, American Wind Energy Association, Windpower '91, Palm Springs, CA, (1991).

[19] D.M. Eggleston, Wind turbine bug roughness sampling and power degradation, American Wind Energy Association, Windpower '91, Palm Springs, CA, (1991).

[20] W.D. Musial, C.P. Butterfield, M. Jenks, A comparison of two-and three-dimensional S809 airfoil properties for rough and smooth HAWT rotor operation, Solar Energy Research Institute, 1990.

[21] E. Hau, Wind turbines: fundamentals, technologies, application, economics, Springer Verlag, 2006.

[22] S. Tonio, Improving BEM-based Aerodynamic Models in Wind Turbine Design Codes, PhD Thesis, Delft University of Tecnology, (2007).

[23] R. Eppler, Airfoil design and data, Springer Berlin etc, 1990.

[24] T. Sant, G. van Kuik, G. Van Bussel, Estimating the angle of attack from blade pressure measurements on the NREL phase VI rotor using a free wake vortex model: Axial conditions, Wind Energy, 9(6) (2006) 549-577.

[25] M.O. Hansen, Aerodynamics of wind turbines, Routledge, 2013.

[26] S. Schreck, The NREL full-scale wind tunnel experiment Introduction to the special issue, Wind Energy, 5(2-3) (2002) 77-84.

[27] D.A. Simms, S. Schreck, M. Hand, L. Fingersh, NREL unsteady aerodynamics experiment in the NASA-Ames wind tunnel: a comparison of predictions to measurements, National Renewable Energy Laboratory Colorado, USA, 2001.

[28] J.G. Leishman, Challenges in modelling the unsteady aerodynamics of wind turbines, Wind energy, 5(2-3) (2002) 85-132.

[29] W. Banks, G. Gadd, Delaying effect of rotation on laminar separation, AIAA journal, 1(4) (1963) 941-941.

[30] S. Schreck, M. Robinson, Rotational augmentation of horizontal axis wind turbine blade aerodynamic response, Wind Energy, 5(2-3) (2002) 133-150.

[31] G. Ronsten, Static pressure measurements on a rotating and a non-rotating 2.375 m wind turbine blade. Comparison with 2D calculations, Journal of Wind Engineering and Industrial Aerodynamics, 39(1) (1992) 105-118.

[32] S. Schreck, M. Robinson, Structures and interactions underlying rotational augmentation of blade aerodynamic response, in: ASME 2003 Wind Energy Symposium, American Society of Mechanical Engineers, 2003, pp. 104-114.

[33] S. Schreck, M. Robinson, Competing Local and Global Influences on Rotationally Augmented HAWT Blade Aerodynamics, in: Proceedings of the Special Topic Conference: The Science of Making Torque from Wind, EWEA, 2004.

[34] H. Snel, R. Houwink, J. Bosschers, Sectional prediction of lift coefficients on rotating wind turbine blades in stall, Netherlands Energy Research Foundation, 1994.

[35] N.N. Sørensen, J. Michelsen, S. Schreck, Navier–Stokes predictions of the NREL phase VI rotor in the NASA Ames 80 ft× 120 ft wind tunnel, Wind Energy, 5(2-3) (2002) 151-169.

[36] D. Wood, A three-dimensional analysis of stall-delay on a horizontal-axis wind turbine, Journal of Wind Engineering and Industrial Aerodynamics, 37(1) (1991) 1-14.

[37] R. Langtry, J. Gola, F. Menter, Predicting 2D airfoil and 3D wind turbine rotor performance using a transition model for general CFD codes, in: 44th AIAA Aerospace Sciences Meeting and Exhibit, Reno, NV, 2006.

[38] R. Langtry, F. Menter, Transition modeling for general CFD applications in aeronautics, AIAA paper, 522 (2005) 2005.

[39] R.B. Langtry, F. Menter, S. Likki, Y. Suzen, P. Huang, S. Völker, A correlation-based transition model using local variables-Part II: Test cases and industrial applications, Journal of Turbomachinery, 128(3) (2006) 423-434.

[40] F. Menter, R. Langtry, S. Likki, Y. Suzen, P. Huang, S. Völker, A correlation-based transition model using local variables-Part I: model formulation, Journal of Turbomachinery, 128(3) (2006) 413-422.

[41] L.J. Fingersh, Unsteady aerodynamics experiment, Journal of solar energy engineering, 123 (2001) 267.

[42] G. Xu, L.N. Sankar, Computational study of horizontal axis wind turbines, Journal of solar energy engineering, 122 (2000) 35.

[43] D. Simms, M. Robinson, M. Hand, L. Fingersh, Characterization and Comparison of Baseline Aerodynamic Performance of Optimally-Twisted Versus Non-Twisted HAWT Blades, in: Prepared for 15th ASME Wind Energy Symposium, 1996.

[44] L.A. Viterna, R.D. Corigan, Fixed pitch rotor performance oflarge HAWTs, DOE/NASA Workshop on Large HAWTs, Cleveland, Ohio, USA, 1980..

[45] S.P. Breton, F.N. Coton, G. Moe, A study on rotational effects and different stall delay models using a prescribed wake vortex scheme and NREL phase VI experiment data, Wind Energy, 11(5) (2008) 459-482.

[46] J.O. Mo, A. Choudhry, M. Arjomandi, R. Kelso, Y.-H. Lee, Effects of wind speed changes on wake instability of a wind turbine in a virtual wind tunnel using large eddy simulation, Journal of Wind Engineering and Industrial Aerodynamics, 117 (2013) 38-56.

[47] J.O. Mo, A. Choudhry, M. Arjomandi, Y.-H. Lee, Large eddy simulation of the wind turbine wake characteristics in the numerical wind tunnel model, Journal of Wind Engineering and Industrial Aerodynamics, 112 (2013) 11-24.

[48] W.J. Devenport, M.C. Rife, S.I. Liapis, G.J. Follin, The structure and development of a wing-tip vortex, Journal of Fluid Mechanics, 312 (1996) 67-106.

[49] J. Dacles-Mariani, G.G. Zilliac, J.S. Chow, P. Bradshaw, Numerical/experimental study of a wingtip vortex in the near field, AIAA Journal, 33(9) (1995) 1561-1568.

[50] J.D. Anderson, Fundamentals of aerodynamics, McGraw-Hill New York, 2001.

[51] R. Lynette, K. Conover, J. Young, Experiences with Commercial Wind Turbine Design: Main report, Electric Power Research Institute, 1989.

[52] H.A. Madsen, N.N. Sorensen, S. Schreck, Yaw aerodynamics analyzed with three codes in comparison with experiment, in: ASME 2003 Wind Energy Symposium, American Society of Mechanical Engineers, 2003, pp. 94-103.

[53] S. Benjanirat, L.N. Sankar, Recent improvements to a combined Navier-Stokes full potential methodology for modeling horizontal axis wind turbines, AIAA Paper, 830 (2004) 2004.

[54] D.E. Shipley, M.S. Miller, M.C. Robinson, Dynamic stall occurrence on a horizontal axis wind turbine blade, National Renewable Energy Lab., Golden, CO (United States), 1995.

[55] C.P. Butterfield, Aerodynamic pressure and flow-visualization measurement from a rotating wind turbine blade, Solar Energy Research Inst., Golden, CO (USA), 1988.

[56] J.C. Kaimal, J.J. Finnigan, Atmospheric boundary layer flows: their structure and measurement, (1994).

[57] J.R. Garratt, The atmospheric boundary layer, Cambridge University Press, 1994.

[58] R.B. Stull, An introduction to boundary layer meteorology, Springer, 1988.

[59] T.-H. Yeh, L. Wang, A study on generator capacity for wind turbines under various tower heights and rated wind speeds using Weibull distribution, Energy Conversion, IEEE Transactions on, 23(2) (2008) 592-602.

[60] N. Dimitrov, A. Natarajan, M. Kelly, Model of wind shear conditional on turbulence and its impact on wind turbine loads, Wind Energy, (2014).

[61] T. Hiester, W. Pennell, Meteorological aspects of siting large wind turbines, Battelle Pacific Northwest Labs., Richland, WA (USA), 1981.

[62] A. Kircsi, K. Tar, Profile tests to optimize the utilization of wind energy, Acta Silvatica et Lignaria Hungarica, 4 (2008) 107–123.

[63] M. Kaltschmitt, W. Streicher, A. Wiese, Renewable energy: technology, economics, and environment, Springer Verlag, 2007.

[64] J.D. Holmes, Wind loading of structures, CRC Press, 2001.

[65] N. Zoumakis, The dependence of the power-law exponent on surface roughness and stability in a neutrally and stably stratified surface boundary layer, Atmosfera, 6(1) (1993).

[66] H. Panofsky, A survey of current throught on wind properties relevant for diffusion in the lowest 100 m, in 'Symp, Atm. Turb. Diffusion', Sandia Laboratories, Albuquerque, NM, (1967) 47-58.

[67] ESDU-72026, Characteristics of wind speed in the lower layers of the atmosphere near the ground: strong winds (nuetral atmosphere), Engineering Sciences Data Unit, 1972.

[68] DS472, Code of practice for loads and safety of wind turbine constructions., Danish Society of Engineers and the Federation of Engineers,, Copenhagen:, 1992.

[69] F. Verheij, Development of a gust model for the design of large wind turbines, Journal of Wind Engineering and Industrial Aerodynamics, 27(1) (1988) 89-102.

[70] D. Walshaw, C.W. Anderson, A model for extreme wind gusts, Journal of the Royal Statistical Society: Series C (Applied Statistics), 49(4) (2000) 499-508.

[71] N. Hutchins, I. Marusic, Evidence of very long meandering features in the logarithmic region of turbulent boundary layers, Journal of Fluid Mechanics, 579 (2007) 1-28.

[72] W. Bierbooms, P.-W. Cheng, Stochastic gust model for design calculations of wind turbines, Journal of Wind Engineering and Industrial Aerodynamics, 90(11) (2002) 1237-1251.

[73] F.K. Davis, H. Newstein, The Variation of Gust Factors with Mean Wind Speed and with Height, Journal of Applied Meteorology, 7 (1968) 372-378.

[74] E. Deacon, Gust variation with height up to 150 m, Quarterly Journal of the Royal Meteorological Society, 81(350) (1955) 562-573.

[75] W. Melbourne, Criteria for environmental wind conditions, Journal of Wind Engineering and Industrial Aerodynamics, 3(2) (1978) 241-249.

[76] J. Kaimal, J. Wyngaard, D. Haugen, O. Coté, Y. Izumi, S. Caughey, C. Readings, Turbulence structure in the convective boundary layer, Journal of the Atmospheric Sciences, 33(11) (1976) 2152-2169.

[77] R. Harris, The nature of the wind, Modern design of wind sensitive structures, Proc. Seminar at Institute of Civil Engineers (1970).

[78] A. Hansen, Yaw dynamics of horizontal axis wind turbines, NASA STI/Recon Technical Report N, 92 (1992) 30837.

[79] J.N. Sørensen, Aerodynamic Aspects of Wind Energy Conversion, Annual Review of Fluid Mechanics, 43(1) (2011) 427-448.

[80] S. Grassi, S. Junghans, M. Raubal, Assessment of the wake effect on the energy production of onshore wind farms using GIS, Applied Energy, (2014).

[81] C.-R. Chu, P.-H. Chiang, Turbulence effects on the wake flow and power production of a horizontal-axis wind turbine, Journal of Wind Engineering and Industrial Aerodynamics, 124 (2014) 82-89.

[82] G.V. Iungo, F. Porté-Agel, Multiple-LiDAR measurements of wind turbine wakes: effect of the atmospheric stability, in: European Geosciences Union, 2013.

[83] M.B. Christiansen, C.B. Hasager, Wake effects of large offshore wind farms identified from satellite SAR, Remote Sensing of Environment, 98(2) (2005) 251-268.

[84] M.B. Christiansen, C.B. Hasager, Using airborne and satellite SAR for wake mapping offshore, Wind Energy, 9(5) (2006) 437-455.

[85] B. Sanderse, Aerodynamics of wind turbine wakes, Energy research Centre of the Netherlands, ECN-E-09-016, (2009).

[86] J.F. Ainslie, Calculating the flowfield in the wake of wind turbines, Journal of Wind Engineering and Industrial Aerodynamics, 27(1) (1988) 213-224.

[87] H. Snel, Review of the present status of rotor aerodynamics, Wind Energy, 1(s 1) (1998) 46-69.

[88] A. Crespo, J. Hernandez, S. Frandsen, Survey of modelling methods for wind turbine wakes and wind farms, Wind Energy, 2(1) (1999) 1-24.

[89] L. Vermeer, J.N. Sørensen, A. Crespo, Wind turbine wake aerodynamics, Progress in Aerospace Sciences, 39(6-7) (2003) 467-510.

[90] S. Voutsinas, K. Rados, A. Zervos, On the analysis of wake effects in wind parks, Wind Engineering, 14 (1990) 204-219.

[91] L.P. Chamorro, F. Porté-Agel, A wind-tunnel investigation of wind-turbine wakes: boundary-layer turbulence effects, Boundary-layer meteorology, 132(1) (2009) 129-149.

[92] C.J. Fisichella, An improved prescribed wake analysis for wind turbine rotors, 2001.

[93] Y. Shimizu, Y. Kamada, Studies on a horizontal axis wind turbine with passive pitch-flap mechanism (performance and flow analysis around wind turbine), Journal of fluids engineering, 123(3) (2001) 516-522.

[94] M.A. Potsdam, D.J. Mavriplis, Unstructured mesh CFD aerodynamic analysis of the NREL Phase VI rotor, AIAA paper, 1221 (2009) 2009.

[95] M. Harrison, W. Batten, L. Myers, A. Bahaj, Comparison between CFD simulations and experiments for predicting the far wake of horizontal axis tidal turbines, IET Renewable Power Generation, 4(6) (2010) 613-627.

[96] J. Johansen, N.N. Sørensen, Aerofoil characteristics from 3D CFD rotor computations, Wind Energy, 7(4) (2004) 283-294.

[97] Y.T. Wu, F. Porté-Agel, Large-eddy simulation of wind-turbine wakes: evaluation of turbine parametrisations, Boundary-layer meteorology, 138(3) (2011) 345-366.

[98] N. Troldborg, J.N. Sørensen, R. Mikkelsen, Numerical simulations of wake characteristics of a wind turbine in uniform inflow, Wind Energy, 13(1) (2010) 86-99.

[99] N.O. Jensen, A note on wind generator interaction, Risø National Laboratory, Roskilde, Denmark, 1983.

[100] I. Katic, J. Højstrup, N. Jensen, A simple model for cluster efficiency, Palz W, Sesto E, editor. Proceedings of EWEC, Rome, Italy, (1986).

[101] M.O.L. Hansen, Aerodynamics of wind turbines, Earthscan/James & James, 2008.

[102] U. Hassan, A wind tunnel investigation of the wake structure within small wind turbine farms, (1993).

[103] P. Vermeulen, An experimental analysis of wind turbine wakes, in, 1980, pp. 431-450.

[104] M. Kramer, Increase in the maximum lift of an airfoil due to a sudden increase in its effective angle of attack resulting from a gust, NASA TM-678, (1932).

[105] F.D. Harris, R.R. Pruyn, Blade StallHalf Fact, Half Fiction, Journal of the american helicopter society, 13(2) (1968) 27-48.

[106] N.D. Ham, M.S. Garelick, Dynamic stall considerations in helicopter rotors, Journal of the american helicopter society, 13(2) (1968) 49-55.

[107] L.W. Carr, Progress in analysis and prediction of dynamic stall, Journal of Aircraft, 25 (1988) 6-17.

[108] J.A. Ekaterinaris, M.F. Platzer, Computational prediction of airfoil dynamic stall, Progress in Aerospace Sciences, 33(11-12) (1998) 759-846.

[109] W. McCroskey, The phenomenon of dynamic stall, DTIC Document, 1981.

[110] J. Leishman, T. Beddoes, A semi-empirical model for dynamic stall, Journal of the american helicopter society, 34(3) (1989) 3-17.

[111] W.J. McCroskey, Unsteady Airfoils, Annu. Rev. Fluid Mech., 14 (1982) 285-311.

[112] A. Krzysiak, Improvement of helicopter performance using self-supplying air jet vortex generators, Journal of KONES Powertrain and Transport, 20(2) (2013).

[113] K. Mulleners, M. Raffel, Dynamic stall development, Experiments in Fluids, 54(2) (2013) 1-9.

[114] H. Mueller-Vahl, C. Strangfeld, C.N. Nayeri, C.O. Paschereit, D. Greenblatt, Thick Airfoil Deep Dynamic Stall, in: Wind Energy-Impact of Turbulence, Springer, 2014, pp. 35-40.

[115] K. Gharali, D.A. Johnson, Numerical modeling of an S809 airfoil under dynamic stall, erosion and high reduced frequencies, Applied Energy, 93 (2012) 45-52.

[116] K. Gharali, D.A. Johnson, PIV-based load investigation in dynamic stall for different reduced frequencies, Experiments in Fluids, 55(8) (2014) 1-12.

[117] VISCWIND, Viscous effects on wind turbine blades, final report on the JOR3-CT95-0007, Joule III project, Technical Report ET-AFM-9902, Technical University of Denmark, Denmark, 1999.

[118] J.W. Larsen, S.R.K. Nielsen, S. Krenk, Dynamic stall model for wind turbine airfoils, Journal of Fluids and Structures, 23(7) (2007) 959-982.

[119] L. Ericsson, J. Reding, Fluid mechanics of dynamic stall part I. Unsteady flow concepts, Journal of Fluids and Structures, 2(1) (1988) 1-33.

[120] W. McCroskey, K. McAlister, L. Carr, S. Pucci, O. Lambert, R. Indergrand, Dynamic stall on advanced airfoil sections, Journal of the American Helicopter Society, 26(3) (1981) 40-50.

[121] J. Walker, H. Helin, J. Strickland, An experimental investigation of an airfoil undergoing large-amplitude pitching motions, AIAA journal, 23(8) (1985) 1141-1142.

[122] J. Walker, H. Helin, D. Chou, Unsteady surface pressure measurements on a pitching airfoil, DTIC Document, 1985.

[123] J. Albertson, T. Troutt, W. Siuru, J. Walker, Dynamic stall vortex development and the surface pressure field of a pitching airfoil, DTIC Document, 1987.

[124] E. Jumper, S. Schreck, R. Dimmick, Lift-curve characteristics for an airfoil pitching at constant rate, Journal of Aircraft, 24 (1987) 680-687.

[125] E. Jumper, J. Hitchcock, R. Docken, Investigating dynamic stall using a modified momentum-integral method, in: AIAA, Aerospace Sciences Meeting, 25th, Reno, NV, 1987.

[126] M.S. Francis, J. Keesee, J.P.J. Retelle, An investigation of airfoil dynamic stall with large amplitude motion, F.J. Seiler Research Laboratory, U.S. Air Force Academy, CO, 1983.

[127] M. Francis, J. Keesee, Airfoil dynamic stall performance with large-amplitude motions, AIAA journal, 23(11) (1985) 1653-1659.

[128] S. Wang, D.B. Ingham, L. Ma, M. Pourkashanian, Z. Tao, Turbulence modeling of deep dynamic stall at relatively low Reynolds number, Journal of Fluids and Structures, 33 (2012) 191-209.

[129] K. Gharali, D.A. Johnson, Dynamic stall simulation of a pitching airfoil under unsteady freestream velocity, Journal of Fluids and Structures, (2013).

[130] S. Gupta, J.G. Leishman, Dynamic stall modelling of the S809 aerofoil and comparison with experiments, Wind Energy, 9(6) (2006) 521-547.

[131] S.K. Digavalli, Dynamic Stall of a NACA 0012 Airfoil in Laminar Flow, Ph.D Thesis, Massachussetts Institute of Tecnology (1994).

[132] H.M.J. Ramsay R. R. , Gregorek G. M, Effects of Grit Roughness and Pitch Oscillations on the S809 Airfoil, NREL/TP-442-7817, National Renewable Energy Laboratory, Golden, CO, 1995.

[133] S.J. Schreck, Unsteady vortex dynamics and surface pressure topologies on a finite pitching wing, DTIC Document, 1994.

[134] D. Rival, C. Tropea, Characteristics of pitching and plunging airfoils under dynamic-stall conditions, Journal of Aircraft, 47(1) (2010) 80-86.

[135] W. Sheng, R.M. Galbraith, F. Coton, A modified dynamic stall model for low Mach numbers, Journal of Solar Energy Engineering, 130(3) (2008) 31013.

[136] W. McCroskey, K.W. McAlister, L. Carr, S. Pucci, An Experimental Study of Dynamic Stall on Advanced Airfoil Sections. Volume 1. Summary of the Experiment, DTIC Document, 1982.

[137] K.W. McAlister, L.W. Carr, W.J. McCroskey, Dynamic stall experiments on the NACA 0012 airfoil, NASA TP 1100 (1978).

[138] W.J. McCroskey, The phenomenon of dynamic stall, DTIC Document, 1981.

[139] K. Mulleners, M. Raffel, The onset of dynamic stall revisited, Experiments in fluids, 52(3) (2012) 779-793.

[140] W.J. McCroskey, K.W. McAlister, L.W. Carr, S.L. Pucci, O. Lambert, R.F. Indergrand, Dynamic stall on advanced airfoil sections, Journal of the american helicopter society, 26(3) (1981) 40-50.

[141] W.J. McCroskey, L.W. Carr, K.W. McAlister, Dynamic stall experiments on oscillating airfoils, AIAA journal, 14(1) (1976) 57-63.

[142] M. Robinson, J. Wissler, Pitch rate and Reynolds number effects on a pitching rectangular wing, in: 6th Applied Aerodynamics Conference, AIAA, Williamsburg, United States of America, 1988, pp. pp. 428-440.

[143] P.G. Choudhuri, D. Knight, Effects of compressibility, pitch rate, and Reynolds number on unsteady incipient leading edge boundary layer separation over a pitching airfoil, Journal of Fluid Mechanics, 308 (1996) 195-218.

[144] M.V. Ol, L. Bernal, C.-K. Kang, W. Shyy, Shallow and deep dynamic stall for flapping low Reynolds number airfoils, in: Animal Locomotion, Springer, 2010, pp. 321-339.

[145] M.V. Ol, L. Bernal, C.K. Kang, W. Shyy, Shallow and deep dynamic stall for flapping low Reynolds number airfoils, Experiments in Fluids, 46(5) (2009) 883-901.

[146] C.-k. Kang, Y.S. Baik, L. Bernal, M.V. Ol, W. Shyy, Fluid dynamics of pitching and plunging airfoils of Reynolds number between 1×10^4 and 6×10^4, AIAA Paper, 536 (2009).

[147] R.R. Ramsay, M.J. Hoffmann, G.M. Gregorek, Effects of Grit Roughness and Pitch Oscillations on the S801 Airfoil: Airfoil Performance Report, National Renewable Energy Laboratory, Golden, CO, 1999.

[148] R. Ramsay R, J. Hoffmann M, M. Gregorek G, Effects of Grit Roughness and Pitch Oscillations on the S809 Airfoil, NREL/TP-442-7817, National Renewable Energy Laboratory, Golden, CO, 1995.

[149] R.R. Ramsay, G.M. Gregorek, Effects of Grit Roughness and Pitch Oscillations on the S813 Airfoil: Airfoil Performance Report, National Renewable Energy Laboratory, Golden, CO, 1999.

[150] D.A. Simms, NREL unsteady aerodynamics experiment in the NASA-Ames wind tunnel: A comparison of predictions to measurements, National Renewable Energy Laboratory, 2001.

[151] M. Hand, D. Simms, Unsteady Aerodynamics Experiment, (2001).

[152] X. Zhang, J.U. Schlüter, Numerical study of the influence of the Reynolds-number on the lift created by a leading edge vortex, Physics of Fluids, 24 (2012) 065102.

[153] M. Amiralaei, H. Alighanbari, S. Hashemi, An investigation into the effects of unsteady parameters on the aerodynamics of a low Reynolds number pitching airfoil, Journal of Fluids and Structures, 26(6) (2010) 979-993.

[154] J.G. Leishman, Principles of helicopter aerodynamics, Cambridge University Press, 2006.

[155] J. Liiva, Unsteady aerodynamic and stall effects on helicopter rotor blade airfoil sections, Journal of Aircraft, 6(1) (1969) 46-51.

[156] B. Hibbs, HAWT performance with dynamic stall, NASA STI/Recon Technical Report N, 87 (1986) 17402.

[157] C.P. Butterfield, Three-dimensional airfoil performance measurements on a rotating wing, Solar Energy Research Institute, 1989.

[158] D.E. Shipley, M. Miller, M. Robinson, M. Luttges, D. Simms, Evidence that aerodynamic effects, including dynamic stall, dictate HAWT structural loads and power generation in highly transient time frames, National Renewable Energy Lab., Golden, CO (United States), 1994.

[159] J. Dai, Y. Hu, D. Liu, X. Long, Aerodynamic loads calculation and analysis for large scale wind turbine based on combining BEM modified theory with dynamic stall model, Renewable Energy, 36(3) (2011) 1095-1104.

[160] C.P. Butterfield, D. Simms, G. Scott, A. Hansen, Dynamic stall on wind turbine blades, National Renewable Energy Lab., Golden, CO (United States), 1991.

[161] J.L. Tangler, D.M. Somers, Status of the special-purpose airfoil families, in: Presented at Windpower'87, San Francisco, Calif., 5 Oct. 1987, 1987.

[162] D. Somers, Design and experimental results for the S809 airfoil NREL, sr-440-6918. Tech. rep., NREL, 1997.

[163] S.J. Schreck, M.C. Robinson, M.M. Hand, D.A. Simms, Blade dynamic stall vortex kinematics for a horizontal axis wind turbine in yawed conditions, Journal of Solar Energy Engineering, 123 (2001) 272.

[164] S. Schreck, M. Robinson, M. Hand, D. Simms, HAWT dynamic stall response asymmetries under yawed flow conditions, Wind Energy, 3(4) (2000) 215-232.

[165] L. Huang, P. Huang, R. LeBeau, T. Hauser, Numerical study of blowing and suction control mechanism on NACA0012 airfoil, Journal of Aircraft, 41(5) (2004) 1005-1013.

[166] D. McCormick, Boundary layer separation control with directed synthetic jets, AIAA paper, 519 (2000).

[167] J.F. Donovan, L.D. Kral, A.W. Cary, Active flow control applied to an airfoil, AIAA paper, 210 (1998).

[168] A. Gardner, K. Richter, H. Rosemann, Numerical investigation of air jets for dynamic stall control on the OA209 airfoil, CEAS Aeronautical Journal, 1(1-4) (2011) 69-82.

[169] H. Mueller-Vahl, C. Strangfeld, C. Nayeri, C. Paschereit, D. Greenblatt, Thick Airfoil Deep Dynamic Stall and its Control, in: 51st AIAA Aerospace Sciences Meeting including the New Horizons Forum and Aerospace Exposition, 2013.

[170] M. Karim, M. Acharya, Suppression of dynamic-stall vortices over pitching airfoils by leading edge suction, AIAA journal, 32(8) (1994) 1647-1655.

[171] A. Seifert, A. Darabi, I. Wyganski, Delay of airfoil stall by periodic excitation, Journal of Aircraft, 33(4) (1996) 691-698.

[172] A. Seifert, T. Bachar, D. Koss, M. Shepshelovich, I. Wygnanskil, Oscillatory blowing: a tool to delay boundary-layer separation, AIAA journal, 31(11) (1993) 2052-2060.

[173] D. Greenblatt, I. Wygnanski, Dynamic stall control by periodic excitation, Part 1: NACA 0015 parametric study, Journal of Aircraft, 38(3) (2001) 430-438.

[174] D. Greenblatt, B. Nishri, A. Darabi, I. Wygnanski, Dynamic stall control by periodic excitation, part 2: Mechanisms, Journal of Aircraft, 38(3) (2001) 439-447.

[175] H. Taylor, The elimination of diffuser separation by vortex generators, United Aircraft Corp, (1947).

[176] S. Xue, B. Johnson, D. Chao, A. Sareen, C. Westergaard, Advanced aerodynamic modeling of vortex generators for wind turbine applications, in: Proceddings of EWEC European Wind Energy Conference, Warsaw, 2010.

[177] S. Øye, The effect of vortex generators on the performance of the ELKRAFT 1000 kW turbine, 9th IEA Symposium on Aerodynamics of Wind Turbines, Stockholm, ISSN 0590-8809, (1995).

[178] J.C. Lin, Control of turbulent boundary-layer separation using micro-vortex generators, AIAA paper, (99-3404) (1999).

[179] C.M. Velte, M.O.L. Hansen, D. Cavar, Flow analysis of vortex generators on wing sections by stereoscopic particle image velocimetry measurements, Environmental Research Letters, 3(1) (2008) 015006.

[180] G. Godard, M. Stanislas, Control of a decelerating boundary layer. Part 1: Optimization of passive vortex generators, Aerospace Science and Technology, 10(3) (2006) 181-191.

[181] K. Angele, Experimental studies of turbulent boundary layer separation and control, (2003).

[182] A.L. Pape, M. Costes, G. Joubert, F. David, J.-M. Deluc, Dynamic Stall Control Using Deployable Leading edge Vortex Generators, AIAA journal, 50(10) (2012) 2135-2145.

[183] B. Heine, K. Mulleners, G. Joubert, M. Raffel, Dynamic stall control by passive disturbance generators, AIAA journal, 51(9) (2013) 2086-2097.

[184] H. Mai, G. Dietz, W. Geißler, K. Richter, J. Bosbach, H. Richard, K. de Groot, Dynamic stall control by leading edge vortex generators, Journal of the American Helicopter Society, 53(1) (2008) 26-36.

[185] F. Fish, G. Lauder, Passive and active flow control by swimming fishes and mammals, Annu. Rev. Fluid Mech., 38 (2006) 193-224.

[186] F.E. Fish, L.E. Howle, M.M. Murray, Hydrodynamic flow control in marine mammals, Integrative and Comparative Biology, 48(6) (2008) 788-800.

[187] D.S. Miklosovic, M.M. Murray, L.E. Howle, Experimental evaluation of sinusoidal leading edges, Journal of Aircraft, 44(4) (2007) 1404-1408.

[188] K.L. Hansen, R.M. Kelso, B.B. Dally, Performance variations of leading edge tubercles for distinct airfoil profiles, AIAA journal, 49(1) (2011) 185-194.

[189] H. Johari, C.W. Henoch, D. Custodio, A. Levshin, Effects of leading edge protuberances on airfoil performance, AIAA journal, 45(11) (2007) 2634-2642.

[190] K.L. Hansen, Effect of leading edge tubercles on airfoil performance, (2012).

[191] N. Rostamzadeh, R. Kelso, B. Dally, K. Hansen, The effect of undulating leading edge modifications on NACA 0021 airfoil characteristics, Physics of Fluids (1994-present), 25(11) (2013) 117101.

[192] C. Ozen, D. Rockwell, Control of vortical structures on a flapping wing via a sinusoidal leading edge, Physics of Fluids (1994-present), 22(2) (2010) 021701.

[193] W. Fassmann, S. Thomson, Effect of Flapping Frequency and Leading Edge Profile on Airfoil Leading Edge Vortical Structures, Utah Space Grant Consortium, (2014).

[194] J. Borg, The effect of leading edge serrations on dynamic stall, M.S. Thesis, University of Southampton, 2012.

[195] R.K. Zhang, V.D.J.Z. Wu, Aerodynamic characteristics of wind turbine blades with a sinusoidal leading edge, Wind Energy, 15(3) (2012) 407-424.

[196] J. Neumann, H. Wengle, DNS and LES of passively controlled turbulent backward-facing step flow, Flow, Turbulence and Combustion, 71(1-4) (2003) 297-310.

[197] V.J. Rossow, Two-fence concept for efficient trapping of vortices on airfoils, Journal of Aircraft, 29(5) (1992) 847-855.

[198] V.J. Rossow, Aerodynamics of airfoils with vortex trapped by two spanwise fences, Journal of Aircraft, 31(1) (1994) 146-153.

[199] M.L. Post, T.C. Corke, Separation control using plasma actuators: dynamic stall vortex control on oscillating airfoil, AIAA Journal, 44(12) (2006) 3125-3135.

[200] T.C. Corke, E.J. Jumper, M.L. Post, D. Orlov, T.E. McLaughlin, Application of weakly-ionized plasmas as wing flow-control devices, AIAA paper, 350 (2002).

[201] J. Huang, T.C. Corke, F.O. Thomas, Plasma actuators for separation control of low-pressure turbine blades, AIAA Journal, 44(1) (2006) 51-57.

[202] M.L. Post, T.C. Corke, Separation control on high angle of attack airfoil using plasma actuators, AIAA Journal, 42(11) (2004) 2177-2184.

[203] Y. Park, S.-G. Lee, D.-H. Lee, S. Hong, Stall control with local surface buzzing on a NACA 0012 airfoil, AIAA Journal, 39(7) (2001) 1400-1402.

[204] F. Ghanadi, M. Arjomandi, B.C. Zander, Interaction of a flow-excited Helmholtz resonator with a grazing turbulent boundary layer, Experimental Thermal and Fluid Science, (2014).

[205] F. Ghanadi, M. Arjomandi, A.C. Zander, B.S. Cazzolato, Numerical simulation of grazing flow over a self-excited Helmholtz resonator, Engineering Letters, 21(3) (2013) 137-142.

[206] F. Ghanadi, M. Arjomandi, B. Cazzolato, A. Zander, Understanding of the flow behaviour on a Helmholtz resonator excited by grazing flow, International Journal of Computational Fluid Dynamics, (ahead-of-print) (2014) 1-13.

[207] W. Siauw, J.-P. Bonnet, J. Tensi, L. Cordier, B. Noack, L. Cattafesta, Transient dynamics of the flow around a NACA 0015 airfoil using fluidic vortex generators, International Journal of Heat and Fluid Flow, 31(3) (2010) 450-459.

[208] J. Tensi, S. Bourgois, J. Bonnet, W. Siauw, J. Breux, Airfoil Performance enhancement using fluidic actuators, in: 2nd European Conference for Aero-Space Sciences, Brussels, Belgium, July 1-6, 2007.

[209] O. Stalnov, A. Kribus, A. Seifert, Evaluation of active flow control applied to wind turbine blade section, Journal of Renewable and Sustainable Energy, 2(6) (2010) 063101.

[210] V. Maldonado, J. Farnsworth, W. Gressick, M. Amitay, Active control of flow separation and structural vibrations of wind turbine blades, Wind Energy, 13(2-3) (2010) 221-237.

[211] A. Glezer, V. Kibens, D. Parekh, M. Amitay, A. FAQs, F. by Institutions, The dynamics of flow reattachment over a thick airfoil controlled by synthetic jet actuators, in: 37th Aerospace Sciences Meeting and Exhibit, Reno, NV, AIAA, 1999, pp. 99-1001.

[212] J. Yen, N.A. Ahmed, Enhancing vertical axis wind turbine by dynamic stall control using synthetic jets, Journal of Wind Engineering and Industrial Aerodynamics, 114 (2013) 12-17.

[213] P. Lorber, D. McCormick, T. Anderson, B. Wake, D. MacMartin, M. Pollack, T. Corke, K. Breuer, P.F. Lorber, D.C. Mccormick, Rotorcraft retreating blade stall control, AIAA paper 2000-2475, (2000).

[214] D.P. Rizzetta, M.R. Visbal, M.J. Stanek, Numerical investigation of synthetic-jet flowfields, AIAA Journal, 37(8) (1999) 919-927.

[215] A. Glezer, M. Amitay, Synthetic jets, Annual Review of Fluid Mechanics, 34(1) (2002) 503-529.

[216] M.P. Patel, Z.H. Sowle, T.C. Corke, C. He, Autonomous sensing and control of wing stall using a smart plasma slat, Journal of Aircraft, 44(2) (2007) 516-527.

[217] T. Wang, Aircraft wing stall control device and method, U.S. Patent No. 4702441, 27th Oct 1987.

[218] L. Carr, M. Chandrasekhara, M. Wilder, K. Noonan, Effect of compressibility on suppression of dynamic stall using a slotted airfoil, Journal of Aircraft, 38(2) (2001) 296-309.

[219] L. Carr, K. McAlister, The effect of a leading edge slat on the dynamic stall of an oscillating airfoil, AIAA paper, 2533 (1983) 1983.

[220] Y.H. Yu, S. Lee, K.W. McAlister, C. Tung, C.M. Wang, Dynamic stall control for advanced rotorcraft application, AIAA Journal, 33(2) (1995) 289-295.

[221] W. Geissler, M. Raffel, Dynamic stall control by airfoil deformation, in: European Rotorcraft Forum, 19th, Como, Italy, 1993.

[222] M.F. Kerho, Adaptive airfoil dynamic stall control, Journal of Aircraft, 44(4) (2007) 1350-1360.

[223] J. Reuster, J. Baeder, Leading edge deformation for dynamic stall control, Leading Edge, AIAA paper 2001-0120 (2001).

[224] M. Chandrasekhara, P.B. Martin, C. Tung, Compressible dynamic stall control using a variable droop leading edge airfoil, Journal of Aircraft, 41(4) (2004) 862-869.

[225] G. Davis, D. Feszty, F. Nitzsche, Trailing edge flow control for the mitigation of dynamic stall effects, in: 31st European Rotorcraft Forum, European Rotorcraft Forum, Florence, Italy, 2005.

[226] T. Lee, P. Gerontakos, Dynamic stall flow control via a trailing edge flap, AIAA Journal, 44(3) (2006) 469-480.

[227] R. Rennie, E.J. Jumper, Experimental measurements of dynamic control surface effectiveness, Journal of Aircraft, 33(5) (1996) 880-887.

[228] R.H. Liebeck, Design of subsonic airfoils for high lift, Journal of Aircraft, 15(9) (1978) 547-561.

[229] P. Gigu-ccedil, re, G. Dumas, J. Lemay, Gurney flap scaling for optimum lift-to-drag ratio, AIAA Journal, 35(12) (1997) 1888-1890.

[230] D. Jeffrey, D. Hurst, Aerodynamics of the Gurney flap, in: 14th Applied Aerodynamics Conference, 1996.

[231] D. Jeffrey, X. Zhang, D.W. Hurst, Aerodynamics of Gurney flaps on a single-element high-lift wing, Journal of Aircraft, 37(2) (2000) 295-301.

[232] M. Chandrasekhara, Optimum Gurney flap height determination for “lost-lift” recovery in compressible dynamic stall control, Aerospace Science and Technology, 14(8) (2010) 551-556.

[233] J.G. Coder, M.D. Maughmer, P.B. Martin, CFD Investigation of Unsteady Rotorcraft Airfoil Aerodynamics: MiTEs and Dynamic Stall, in: 49th AIAA Aerospace Sciences Meeting including the New Horizons Forum and Aerospace Exposition, 2011.

[234] M. Chandrasekhara, M. Wilder, L. Carr, Unsteady stall control using dynamically deforming airfoils, AIAA Journal, 36(10) (1998) 1792-1800.

[235] M. Chandrasekhara, M. Wilder, L. Carr, Control of flow separation using adaptive airfoils, Defense Technical Information Center, 1997.

[236] M. Sahin, L.N. Sankar, M. Chandrasekhara, C. Tung, Dynamic stall alleviation using a deformable leading edge concept-a numerical study, Journal of Jircraft, 40(1) (2003) 77-85.

[237] W. Joo, B.-S. Lee, K. Yee, D.-h. Lee, Combining passive control method for dynamic stall control, Journal of Aircraft, 43(4) (2006) 1120-1128.

[238] L.-H. Feng, T.N. Jukes, K.-S. Choi, J.-J. Wang, Flow control over a NACA 0012 airfoil using dielectric-barrier-discharge plasma actuator with a Gurney flap, Experiments in Fluids, 52(6) (2012) 1533-1546.

[239] T. Lee, Y. Su, Pitching Airfoil with Combined Gurney Flap and Unsteady Trailing edge Flap Deflection, AIAA Journal, 50(2) (2012) 503-507.

[240] T. Lee, P. Gerontakos, Unsteady airfoil with dynamic leading-and trailing edge flaps, Journal of Aircraft, 46(3) (2009) 1076-1081.

[241] M. Mumtaz, A. Shahzad, H. Hamdani, K. Parvez, Dynamic Stall Control through Passive Devices in Hybrid Configuration, in: 51st Aerospace Sciences Meeting, Grapevine, Texas, 2013.

CHAPTER 3

DYNAMIC STALL PREDICTIONS ON WIND TURBINES

3.1 Chapter Overview

This chapter discusses the occurrence of dynamic stall on wind turbine blades in relation to the ambient wind conditions. An analytical model was developed to relate the wind speed and direction variability with the onset of dynamic stall on the turbine blades. The model has been validated against the well-known wind turbine experiments conducted by the National Renewable Energy Laboratories. Furthermore, using high quality wind data, the model was further extended to the actual wind conditions that a turbine would experience. The article, furthermore, introduces the concept of limiting reduced frequency as the precursor to

dynamic stall. This concept is further explored in Chapter 6 where dynamic stall experiments for a thick airfoil are presented.

The details of the model, its validation and implementation are presented in the next section of this chapter as an article published in the Proceedings of the Institution of Mechanical Engineers, Part A: Journal of Power and Energy. Permission to reproduce the article in the thesis has been provided by the relevant publishing authority.

3.2 Relation of Ambient Conditions to Dynamic Stall

Statement of Authorship

Title of Paper	Horizontal axis wind turbine dynamic stall predictions based on wind speed and direction variability.
Publication Status	⊙ Published, ○ Accepted for Publication, ○ Submitted for Publication, ○ Publication style
Publication Details	Choudhry, A., Arjomandi, M., & Kelso, R. (2013). Horizontal axis wind turbine dynamic stall predictions based on wind speed and direction variability. Proceedings of the Institution of Mechanical Engineers, Part A: Journal of Power and Energy, 227(3), 338-351.

Author Contributions

By signing the Statement of Authorship, each author certifies that their stated contribution to the publication is accurate and that permission is granted for the publication to be included in the candidate's thesis.

Name of Principal Author (Candidate)	Amanullah Choudhry		
Contribution to the Paper	Developed ideas and the model, performed the calculations, interpreted data, wrote the manuscript, acted as corresponding author, wrote the rebuttal		
Signature		Date	

Name of Co-Author	Maziar Arjomandi		
Contribution to the Paper	Supervised the work, helped in developing ideas, manuscript evaluation		
Signature		Date	

Name of Co-Author	Richard Kelso		
Contribution to the Paper	Supervised the work, helped in developing ideas, manuscript evaluation		
Signature		Date	

Name of Co-Author			
Contribution to the Paper			
Signature		Date	

Choudhry, A., Arjomandi, M., & Kelso, R. (2013). Horizontal axis wind turbine dynamic stall predictions based on wind speed and direction variability. *Proceedings of the Institution of Mechanical Engineers, Part A: Journal of Power and Energy, 227*(3), 338-351.

CHAPTER 4

EFFECTS OF WAKE ON DYNAMIC STALL

4.1 Chapter Overview

This chapter presents numerical wake studies conducted at the University of Adelaide and discusses the impact of the wake on a downstream wind turbine. The wake data was acquired using Large Eddy Simulation and was then used in conjunction with the model discussed in Chapter 3 to predict the occurrence of dynamic stall on downstream wind turbines operating in the wake. An important observation regarding wind turbine wakes is first presented in the article that primarily constitutes this chapter. This is followed by a brief comparison of the LES wake data with the current empirical methods used to estimate the wake characteristics. Through this comparison, it is illustrated that the empirical models agree well with the numerical work, at least in the far-wake, and therefore can be used to estimate the turbulence intensity and velocity deficits in the wake. However, it is

found that the primary cause of dynamic stall for turbines operating in the wake is the rapid variation in wind direction. For this parameter, no empirical model exists.

In the following section, the article published in Wind Engineering is presented. Note that further details of the LES simulation, including detailed model setup and validations, have been presented in Appendix A of the thesis as a conference article published in the 7th Australasian Congress on Applied Mechanics.

4.2 Dynamic Stall on Downstream Wind Turbines

Statement of Authorship

Title of Paper	Effects of wake interaction on downstream wind turbines
Publication Status	⦿ Published, ○ Accepted for Publication, ○ Submitted for Publication, ○ Publication style
Publication Details	Choudhry, A., Mo, J. O., Arjomandi, M., & Kelso, R. (2014). Effects of Wake Interaction on Downstream Wind Turbines. Wind Engineering, 38(5), 535-548.

Author Contributions

By signing the Statement of Authorship, each author certifies that their stated contribution to the publication is accurate and that permission is granted for the publication to be included in the candidate's thesis.

Name of Principal Author (Candidate)	Amanullah Choudhry		
Contribution to the Paper	Developed and applied model, interpreted data, wrote the manuscript, wrote the rebuttal, acted as the corresponding author		
Signature		Date	

Name of Co-Author	Jang-Oh Mo		
Contribution to the Paper	Helped in developing ideas, manuscript evaluation		
Signature		Date	

Name of Co-Author	Maziar Arjomandi		
Contribution to the Paper	Supervised the work, helped in developing ideas, manuscript evaluation		
Signature		Date	

Name of Co-Author	Richard Kelso		
Contribution to the Paper	Supervised the work, helped in developing ideas, manuscript evaluation		
Signature		Date	

WIND ENGINEERING Volume 38, No. 5, 2014 PP 535–548 535

Effects of Wake Interaction on Downstream Wind Turbines

Amanullah Choudhry[1*], Jang-Oh Mo[1], Maziar Arjomandi[1] and Richard Kelso[1]
[1]*School of Mechanical Engineering, The University of Adelaide, South Australia 5005, Australia*

Received 12/04/2013; Revised 01/04/2014; Accepted 07/27/2014

ABSTRACT
The present article revisits the wake studies behind the NREL (National Renewable Energy Laboratory) Phase VI wind turbine inside a virtual wind tunnel that were recently performed at the University of Adelaide using Large Eddy Simulation (LES). A notable observation has been made in the current article, through comparisons of instantaneous contours of vorticity, velocity and turbulence intensity, that the regions of velocity deficits and high turbulence intensities in the wake are restricted to the regions of high vorticity. Therefore, for a downstream wind turbine, the smaller power production, the increased unsteady loads and the noise produced can directly be associated with the turbine blades passing through the streamwise vortices generated by the upstream wind turbine. In addition, a comparative analysis has been performed between the LES and semi-empirical models, used in the industry, to better understand the development of the wake inside the wind tunnel model. Finally, in order to illustrate the effects of wake on downstream wind turbines, a dynamic stall prediction model was used to determine the regions of the turbine blade affected by dynamic stall as a function of spacing between the turbines.

Keywords: Wind turbine wake, large eddy simulation, flow structures, turbulence intensity, velocity deficit, noise

1. INTRODUCTION

Wind turbines operate in locally concentrated groups that take benefit of geographically limited and profitable wind resources. Clustered arrangements have also been observed to reduce the overall cost associated with the operation of the turbines due to concentration of maintenance equipment and spare parts on the site [1]. However, despite the commercial benefits of locally-clustered turbines and the advancements in design and manufacturing, several drawbacks associated with the wakes of the wind turbines cannot be overlooked. These are summarized as follows:

1. The velocity deficits produced by the extraction of kinetic energy from the wind by an upstream wind turbine results in reduced power productions for the downstream wind turbines.
2. The phenomenal increase in turbulence intensity in the wake results in large unsteady loads on the wind turbines operating downstream, and hence reduces the lifetime of the turbines due to increased fatigue loads.
3. The increased noise emission levels observed from downstream wind turbines operating in the wake of other turbines is considered to be one of the biggest social problems restricting the growth of onshore windfarms.

*Corresponding author: Amanullah Choudhry, School of Mechanical Engineering, The University of Adelaide, SA 5005, Adelaide, Email address: amanullah.choudhry@adelaide.edu.au, Phone number: 0061413032885

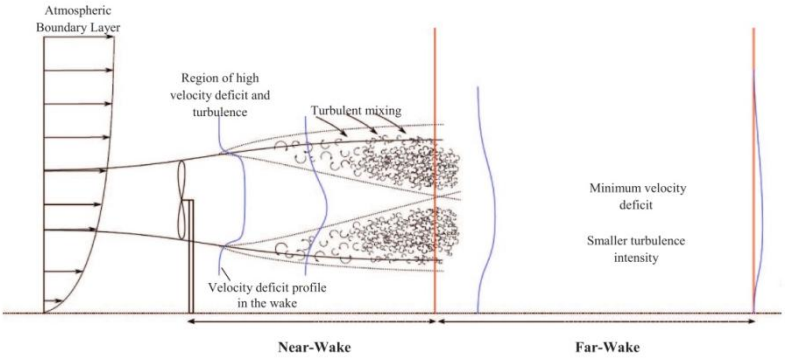

Figure 1. Schematic illustration of the wake behind a wind turbine indicating the near- and far-wakeas well as the process of velocity recovery [5].

Wind turbine wakes have, therefore, been the subject of extensive studies, using both experimental and numerical methods, as reviewed by Snel [2], Crespo *et al.,* [3] Vermeer *et al.* [4] and Sanderse [5]. The wake behind a wind turbine can be divided into two regions: the near-wake and the far-wake [4]. It has been observed that the difference in velocities between the air inside and outside of the wake results in the formation of a shear layer that increases in thickness as the distance behind the turbine increases and ultimately reaches the wake axis. According to Crespo *et al.,* [3] this marks the end of the near-wake and lies approximately 2–5 rotor diameters downstream of the turbine. Recently Mo *et al.* [6] have refined the definition of near-wake as the region where a tightly wound helical vortex structure, originating from the blade tips, is the dominant flow feature. On the other hand, the far-wake is the region where this structure has broken down due to wake-instability.

The significance of identifying these zones is due to the high velocity deficits and the turbulence intensities in the near-wake as compared to the far-wake (Figure 1.). As the kinetic energy from the wind is extracted by the turbine, a large region of high velocity deficit and turbulence intensity is generated in the wake. However, as the distance behind the turbine increases, the velocity deficits are eventually recovered primarily due to turbulent mixing with the flow outside the wake. Investigation into these zones and their clear distinction can, therefore, lead to efficient wind farm designs, through optimizing the space between the turbines, resulting in increased power output from the downstream turbines, less noise irritants and reduced maintenance costs.

However, most of the studies have been limited to understanding the near-wake characteristics behind a turbine [7–10]. Therefore, in the current article, the evolution and eventual breakdown of the wake behind a wind turbine has been simulated using Large Eddy Simulation (LES). The wake structure has been related to the velocity and turbulence intensity fields in the wake. An in-depth analysis has yielded some very interesting observations that have not been previously reported regarding wind turbine wakes. In addition, a comparative analysis has been presented in the current article between the mean flow parameters computed using LES and those determined using semi-empirical models. The comparison assists us in better understanding the development of the wake inside the wind tunnel model. Finally, the wake data from the LES have been utilized to determine unsteady excursions in the apparent angle of attack along the turbine blades operating in the wake. Through the use of an analytical model [11], the large excursions in the angle of attack are related to the occurrence of dynamic stall on downstream wind turbines. The study performed supplements the wake discussions presented in the article and shows the effect of spacing on dynamic stall occurrence on downstream wind turbine blades.

2. NUMERICAL ANALYSIS

Large Eddy Simulation of the NREL Phase VI wind turbine inside a numerical wind tunnel was performed for distances as far as twenty rotor diameters downstream of the turbine [6, 12]. The test section dimensions of the numerical wind tunnel were similar to the NASA Ames 24.4 m × 36.6 m

WIND ENGINEERING Volume 38, No. 5, 2014 PP 535–548 537

wind tunnel that was used in the original experiments [13–14]. The schematic of the computational domain is shown in Figure 2. The numerical setup has been presented here in brevity for quick reference.

The turbine was placed approximately in the middle of the test section at a distance of 2 d from the upwind boundary, d being the diameter of the turbine rotor. The computational domain consisted of two parts: the moving part surrounding the turbine blade and the stationary part. The moving interface, shown in Figure 2, consisted of a cylindrical zone that was modelled using the sliding mesh technique. The flow around the blades was captured using 20 inflation layers composed of hexahedral elements with a growth ratio of 1.1. Care was taken to ensure that the y^+ value was less than one for all wall-bounded flow regions. A total of 3.6×10^6 cells were used in the simulation.

The wind turbine blades were set to operate at uniform flow conditions, as in the experiment, with a velocity of 7 m/s and turbulence intensity of 0.2% applied as the inlet boundary condition. Spectral synthesizing technique [15–16] was employed to model the turbulent inflow. The ambient domain condition was selected for the outlet. The turbine was set to rotate at a fixed angular velocity of 71.6 rpm with a yaw misalignment of zero degrees. Wall condition was applied at the walls of the tunnel, the ground and the turbine itself. The coupled implicit solver was used in the present work to speed up the convergence. The simulation was carried out in ANSYS® Fluent, *Release 13.0* which is a general-purpose CFD code that solves the governing equations using cell-centred control volume space discretization approach.

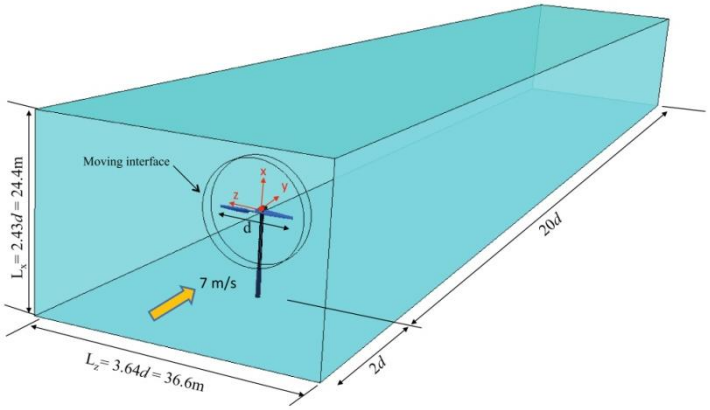

Figure 2. Schematic diagram of the computational domain used for the LES.

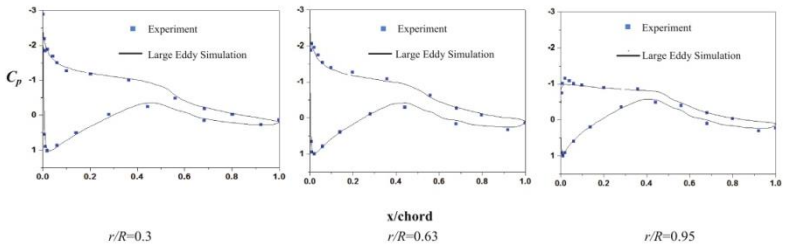

Figure 3. Comparison of experimental and numerical chordwise time-averaged pressure coefficients at selected spanwise sections along the blade.

The simulation was validated by comparing the power output of the turbine as well as the chordwise time-averaged pressure coefficients at selected spanwise sections along the turbine blade with the experimental results. A slight under-prediction of approximately 3% was observed in the computed power output. Moreover, the computed pressures agreed very well with the experimental results except for a minor discrepancy near the leading edge of the tip region as shown in Figure 3. Therefore, the LES results were found to be in excellent agreement with the experiments. Consequently, the subsequent wake analysis presented in the article can be considered to be of sufficient accuracy. Further information regarding the simulation can be found in the articles by Mo *et al*. [6, 12].

3. DISCUSSION

3.1. Wake propagation

The flow structures in the wake of the turbine can most conveniently be analysed using the instantaneous y-vorticity contours at selected streamwise stations (y/d = 1, 4, 8, 12, 16, 20) presented in Figure 4. The figure shows the complex flow field in the wake of a turbine and depicts the evolution, deformation and eventual breakdown of the prominent flow structures in the wake.

As can be observed, at y/d = 1, immediately behind the turbine, tip vortices originating from the blade form a tightly wound helical vortex structure, that persists until y/d = 4. The tip vortices manifest as the ring of high vorticity in the periphery, as indicated in Figure 4. A central vortex structure, originating from the blade roots and the nacelle, is also visible in the vorticity fields as a tightly wound streamwise vortex concentrated in the centre. Similar helical vortex structures in the near-wake were observed by Yang *et al*. [17] in a small scale experiment performed inside a wind tunnel using a high resolution Particle Image Velocimetry (PIV) system. They were able to show the distinct evolution of the wake vortex structures in the near-wake and observed the formation of a similar helical vortex structure originating at the tips.

From Figure 4, it can be observed that as the distance behind the turbine is increased, at y/d = 4, the vortex structures in the wake tend to become unstable due to wake instability. The instability seems to originate due to wake expansion and interaction of the two helical vortex structures originating from the blade tips and roots. At this station, the tip vortices begin to manifest themselves as an uneven vorticity distribution around the vortex tip wake; whereas, the streamwise root vortex also starts to unwind. Downstream, the tip and the root vortices completely breakdown resulting in the formation of two distinct counter-rotating vortex pairs, visible at y/d = 8. The counter-rotating vortices tend to gradually move away from the turbine axis and are observed to undergo very little rotation and can, therefore, be considered axially-aligned downstream from this point. It can be argued, however, that the rotation of the counter-rotating vortex pairs is hindered

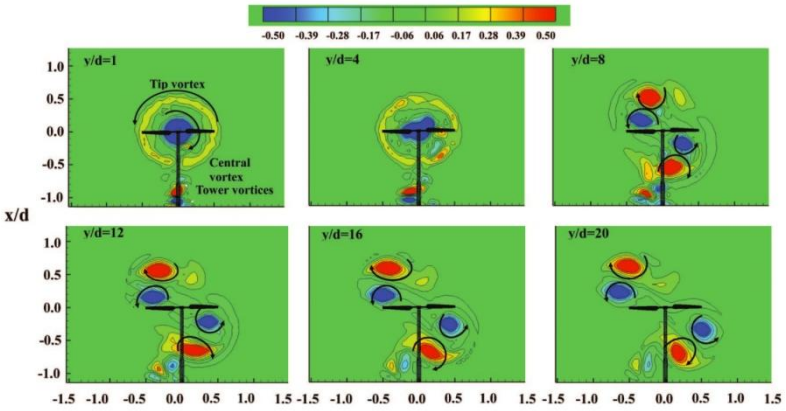

Figure 4. Instantaneous vorticity contours, extracted from Mo *et al.,* [6], indicating the unstable tip vortex and the resulting counter-rotating vortex pairs respectively in the wake of the NREL Phase wind turbine.

WIND ENGINEERING Volume 38, No. 5, 2014 PP 535–548 539

due to the growing boundary layer on the tunnel walls and its interaction with the flow in the far-wake. Other flow features, visible in the contours, are the tower vortices originating at the base of the circular tower. The tower vortices, as the downstream distance increases, seem to interact with the tip vortices; however, they do not appear to alter the overall flow field to a great degree.

It is interesting to note that the velocity deficits in the wake observe a close relationship with the vortical structures and flow fields that have been described. The instantaneous dimensionless velocity contours in the wake of the turbine are presented in Figure 5. The process of momentum extraction from the oncoming freestream by the turbine and the gradual recovery in the wake are clearly evident from the contours. It can be observed that a large area of velocity deficit exists immediately downstream of the wind turbine at $y/d = 1$. This region of velocity deficit slowly, but surely, deforms as the distance behind the turbine is increased. It is interesting to note that these velocity deficit zones are closely related to the vortical structures in the wake. The deformation and breakdown of the large scale vorticity in the near-wake of the turbine ($y/d = 4$) into the counter-rotating vortex pairs in the far-wake ($y/d = 20$) can also be observed from the instantaneous dimensionless velocity contours presented in Figure 5. It can be observed that the regions of velocity deficits in the wake are completely contained inside the regions of high vorticity. This can clearly be observed by comparing Figure 4 and Figure 5. Immediately outside of the vortices, the velocities are larger than the freestream, primarily due to the presence of the tunnel walls. Therefore, it can be inferred that the smaller power production of the downstream turbines operating in the far-wake is caused when the blades pass through these vortices of high velocity deficits.

In the same manner, the contours of instantaneous axial turbulence intensity, presented in Figure 6, indicate a similar relationship with the vortical structures. It can be observed from the contours that a large increase in the turbulence intensity occurs immediately behind the turbine at $y/d = 1$. Interestingly, as the distance increases, the turbulence does not decay immediately but tends to increase in the near-wake till $y/d = 4$ due to the tip vortices. However, due to wake breakdown, the diffusion of turbulence is clearly evident from the contours beyond this station. It is interesting to note that, much like the previous case of velocity deficits, the turbulence field in the wake also bears a close relationship with the flow structures. It can be observed, through a simple comparison of Figure 4 and Figure 6, that the increased turbulence intensity zones are primarily restricted to the

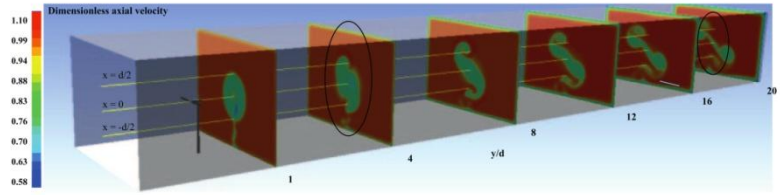

Figure 5. Instantaneous dimensionless velocity contours in the wake of the NREL Phase VI wind turbine enclosed inside a virtual wind at selected streamwise stations.

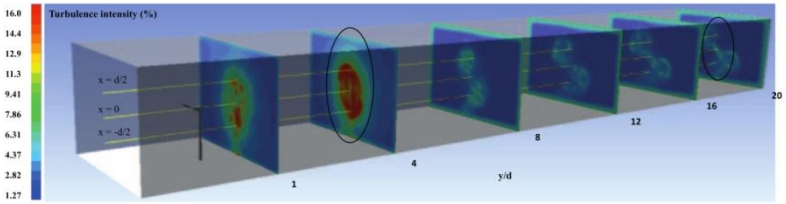

Figure 6. Instantaneous contours of turbulence intensity in the wake of the NREL Phase VI wind turbine at selected streamwise stations.

regions of high vorticity in the wake, primarily due to the strong coupling between vorticity and turbulence kinetic energy. Immediately outside these zones, the turbulence intensity is comparatively very small. It can be deduced from this observation that the primary cause of unsteady loads on the downstream wind turbines is when the blades pass through these vortex structures of high turbulence intensity.

Finally, the present discussion can be concluded with a small note on the noise generated by wind turbines. Wind turbine noise can be broadly classified as tonal, broadband and impulsive types [18]. The tonal noise generated by wind turbine components, such as holes or slits, and the broad band noise caused by interaction of flow with the blades are observed for all classes of wind turbines (upwind and downwind). The broadband noise is considered to be the prominent source since it drowns out the noise generated by the mechanical components. On the other hand, the impulsive noise, generally attributed to blade-tower interaction in downwind turbines, has been observed intermittently in wind farms composed entirely of upwind turbines [19]; however the cause is not well understood [20–21]. It has been speculated that such noise can be generated due to the flow perturbation upstream of the tower [22] but the intermittent and non-periodic nature of the noise leads us to consider other mechanisms. From the observations made so far, regarding the regions of velocity deficits and high turbulence intensities being restricted to regions of high vorticity, the authors of the present article believe that the impulsive noise in wind farms is primarily caused when a downstream wind turbine blade passes through the regions of high vorticity generated by the upstream wind turbines. Therefore, the impulsive noise can be classified as a wake-induced noise.

3.2. Mean flow parameters from LES and comparison with empirical approximations

The variation of the averaged flow parameters such as the mean velocities, mean turbulence intensity and the mean wind direction parameters, with downstream distance are presented in the current section and compared with the currently-used empirical models (where applicable). The objectives of the present section are to obtain a better understanding of the variation of the mean flow parameters and to highlight the differences between LES averages and those obtained using the semi-empirical methods. A better understanding of the mean momentum recovery and turbulence intensity decay can help wind farm designers to improve the energy yield of the farm and to reduce the unsteady loads experienced by turbines.

3.2.1. Variation of mean velocity

The mean velocities at selected streamwise stations downstream of the wind turbine are compared with the empirically determined velocities in Figure 7. The empirical approximations were based on the wake model used in Wind Atlas Analysis and Application Program (WAsP) [23–24] employed in the European Wind Atlas [25]. WAsP contains a simple wake model, proposed by Jensen [26], which is based on the linear expansion of the wake downstream of the turbine. The model is widely used in the industry for estimations of velocity recovery in the wake due to its simple implementation and reduced requirements for user input [27]. The velocity deficit is calculated using the following expression:

$$\frac{V_{yi}}{V_w} = \left[1 - \left(1 - \sqrt{1 - C_T} \right) \left(\frac{d}{d + 2(y_{wake})_i} \right)^2 \right]$$

Here (V_{y_i}/V_W) is the velocity deficit at station i, C_T is the experimental thrust coefficient, d is the rotor diameter and k_{wake} is the wake decay factor. The wake decay factor for onshore cases is suggested to be 0.075. It is important to note that the model is applicable for distances in excess of three rotor diameters [28] but in the following has been evaluated for the entire range.

The comparison of velocity deficits in the wake calculated using the WAsP model and those obtained through the LES is presented in Figure 7. It can be observed that as soon as the flow passes through the turbine, a clear evidence of momentum extraction is apparent in the wake as seen by the large deficit at $y/d = 1$ from both LES and WAsP. Afterwards, the WAsP model predicts a continuous parabolic recovery of the velocity in the wake and estimates that the wake velocity recovers to approximately 90% of the freestream at $y/d = 6$. Subsequently, the velocity deficit gradually asymptotes towards the freestream velocity but a complete recovery is not observed for distances as large as twenty rotor diameters in the far-wake.

WIND ENGINEERING Volume 38, No. 5, 2014 PP 535–548 541

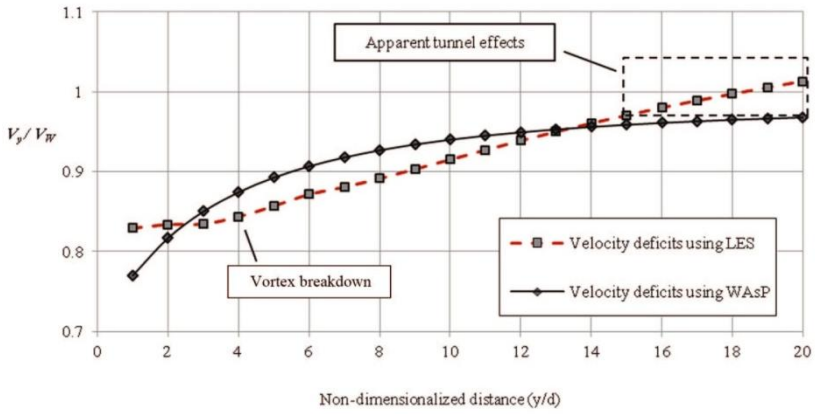

Figure 7. Comparison of average velocity deficits in the wake of the NREL Phase VI wind turbine determined using LES and WAsP.

On the other hand, the LES predicts that approximately no velocity recovery takes place in the near-wake where the dominant flow structures are still comprised of the helical vortex from the tips and the streamwise vortex from the roots. Only after the vortex breakdown at $y/d = 4$, an approximate linear recovery of mean velocity is observed. The LES predicts that approximately 90% of the velocity recovery takes place at around $y/d = 9$ and complete recovery is observed at $y/d = 18$. In the far-wake, it is clear that the effects of the tunnel influence the velocity recovery quite significantly, as marked out in Figure 7. The presence of the walls tends to accelerate the recovery process and after $y/d = 18$ the velocities exceed the freestream value.

Therefore, it can be concluded that two models agree to some extent in their predictions. The discrepancies observed are primarily due to the limitation of the numerical work being influenced by the tunnel walls and the WAsP model being inadequate for near-wake regions. The authors believe that in the near-wake ($y/d \leq 5$), the LES predictions are superior to WAsP predictions since here the influence of the walls is negligible. Hence, in the near-wake, the average velocities should remain largely similar.

3.2.2. Variation of mean turbulence intensity

In this section, the decay of average turbulence intensity in the wake as calculated from the LES has been presented. Furthermore, in order to gain a deeper understanding of the average turbulence intensity characteristics in the wake, the LES results are compared with a semi-empirical model, described by Hansen [29], and reproduced here in brevity. Empirically, the turbulence in the wake (I_{wake}) is defined in terms of added turbulence (I_+) and ambient turbulence intensity (I_0) as:

$$I_{wake} = \sqrt{I_0^2 + I_+^2}$$

Here, I_+ can be determined empirically using the following expression [30]:

$$I_+ = 0.7\, C_T^{0.7}\, I_0^{0.68} \left(\frac{y}{y_n}\right)^{-0.96}$$

In the equation, C_T is the experimental thrust coefficient of the turbine, y is the downstream distance behind the wind turbine and y_n is the length of the near-wake region, determined according to Vermeulen [31]. The length of the near-wake is dependent on the rotor radius and the wake growth rate. A detailed explanation and implementation of the model are available in Hansen [29].

The variation of average axial turbulence intensity with downstream distance, calculated using the LES, is compared with the semi-empirical model in Figure 8. It can be observed that immediately behind the wind turbine, at $y/d = 0.03$, both the LES and the empirical model predict a very large increase in the turbulence intensity. Afterward, a sudden drop in the turbulence intensity

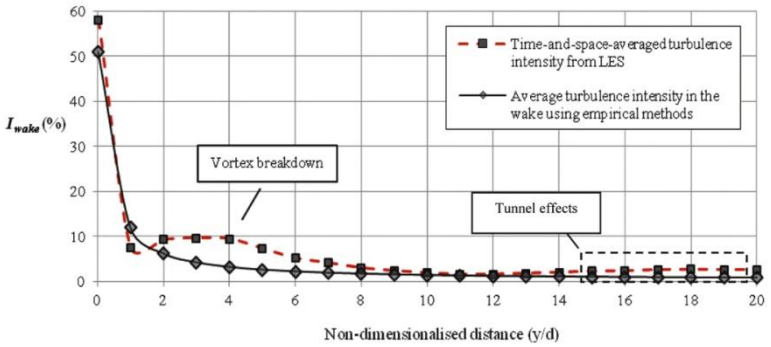

Figure 8. Comparison of the empirically-determined turbulence intensities in the wake of a wind turbine, with those determined using LES at selected downstream locations

is observed at $y/d = 1$. The semi-empirical model predicts a parabolic decline of average turbulence intensity in the wake, as shown in Figure 8, that asymptotes towards the ambient turbulence intensity (I_0). The turbulence intensity in the wake as predicted by the model reaches approximately 0.22% at $y/d = 20$. On the other hand, the LES predicts that after the first initial decrease, between $y/d = 0.03$ and 1, the wake turbulence intensity starts to rise again. This is primarily due to the turbulence generated at the tips and the roots of the turbine blades. However, as the vortices become unstable and finally collapse, the average turbulence intensity in the wake also falls as indicated in Figure 8 ($y/d = 4$). Subsequently, the average turbulence intensity calculated using the LES closely follows the predicted turbulence intensity from the semi-empirical model. Interestingly, here as well, the effects of the tunnel walls are somewhat present in the far-wake. It can be observed that, due to the presence of the walls, the turbulence intensity starts to increase again in the far-wake. This results in the average turbulence intensity, calculated using the LES, to be approximately 11 times higher at $y/d = 20$ as compared to the freestream turbulence intensity.

Hence, the comparison between the two methods indicates the overall behaviour of the average turbulence intensity in the wake of the turbine and its decay with the downstream distance. The discrepancy observed in the near-wake is due to the presence of the large scale vortical structures in the wake. The semi-empirical model does not take into account the presence of these vortices and, therefore, predicts a quicker decay in the near-wake. However, in the far-wake the LES results can be seen to be affected by the tunnel walls. The present results, therefore, indicate a need for further research to be conducted in the wake of the turbines that are not restricted by the tunnel walls. It furthermore illustrates the need for improvement in the current semi-empirical models for better predictions in the near-wake.

3.2.3. Variation of wind direction

The variation of wind directionin the wake is generally overlooked when wake characteristics of wind turbines are analysed. However, wind direction and its rapid variation can significantly increase the unsteady loads experienced by a turbine blade [11]. The blades of most modern wind turbines, due to their large inertia, cannot cope with the rapid changes in the wind direction. Hence modern wind turbines are designed to align themselves with the most prevalent wind direction in order to minimize the yaw misalignment and increase the overall power production. The variation in the wind direction, much like the turbulent fluctuations in the wind speed, tends to increase the unsteady loads experienced by the turbine blades due to rapid variations of blade angle of attack. Hence, it is important to estimate the trends of wind direction in the wake of a turbine.

The variation of mean yaw misalignment experienced by a downstream wind turbine in the wake is shown in Figure 9 using the data generated from the LES. It is assumed that the rotational axis of the downstream rotor is permanently aligned with that of the upstream rotor. The mean yaw misalignment at each station was then calculated using the average wind speed in the axial (y) and lateral (z) directions at the corresponding station. Similarly, the standard deviation in wind direction

WIND ENGINEERING Volume 38, No. 5, 2014 PP 535–548 543

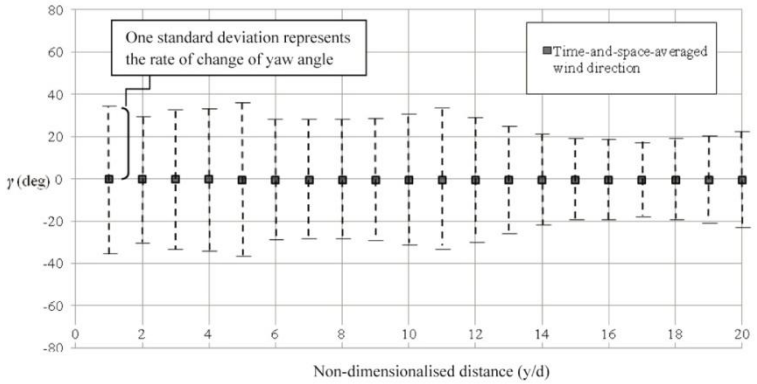

Figure 9. Wind direction variation as experienced by a downstream wind turbine operating in the wake of the upstream turbine. The dotted lines represent the standard deviation in yaw angle and are indicative of the turbulent fluctuations in wind direction in the wake.

was estimated using the turbulent fluctuations in wind speed in both the axial and the lateral direction at each downwind station. The standard deviation in the wind speed is indicative of the time rate of change of wind direction as proposed by Melbourne [32]. The standard deviation is also indicated in Figure 9 as dashed lines and represents the extents of wind direction fluctuations at each downstream station.

It can be observed from Figure 9 that the mean yaw angle experienced by a downstream wind turbine remains essentially zero, regardless of the downstream distance. This indicates that the mean wind direction in the wake of a turbine does not vary considerably as the downstream distance increases. It is important to note that this observation can only be made for a turbine operating inside a numerical wind tunnel model; since, in actual operating conditions, wake meandering might result in large scale movements of the entire wake [5]. The results presented here still provide an insight in the overall movement of the wake without the influence of external disturbances. They indicate that wake meandering is not an inherent property of the wind turbine wake and that the process is essentially caused by large scale atmospheric structures, as originally proposed by Sanderse [5].

On the other hand, the turbulent fluctuations in the wind direction are quite significant when compared with the mean wind direction. It is interesting to note that the turbulent character of wind direction, to some extent, bears a relationship with the average turbulence intensity behaviour in the wake. It can be observed that the effects of the helical vortex structures in the near-wake and the tunnel walls in the far-wake are apparent on the wind direction fluctuations as well. Unfortunately, the trends for wind direction variation in the wake cannot be compared with any experimental or empirical model, since such measurements have not been performed before.

3.3. Occurrence of dynamic stall on downstream wind turbine blades

The effects of rapidly varying wind conditions on downstream wind turbines can be illustrated by an analytical model [11] that uses the operating conditions of the turbine as inputs and determines the occurrence of dynamic stall on wind turbine blades as a percentage of the blade span. Dynamic stall can be considered as one of the major causes of unsteady loads on wind turbine blades and is caused when the local angle of attack at any section of the blade exceeds the critical static-stall angle of attack [33]. In wind turbines, dynamic stall can be caused by unsteady inflow, yaw misalignment, tower shadow and wind gusts [34]. All these factors contribute in the rapid variations of the turbine blade angle of attack, which in turn results in the occurrence of the unsteady phenomenon.

The model uses the ambient wind conditions as input and determines the distribution of reduced frequency along the turbine blade at different azimuth angles. The distribution is, then, compared with the limiting reduced frequency of the airfoil. The limiting reduced frequency is defined as the smallest rate of change of angle of attack at which the most salient features of dynamic stall are

observed on a 2D airfoil. The regions where the calculated reduced frequency is larger than the limiting reduced frequency are the dynamic-stall-affected regions of the turbine blade. The percentage of the blade span under the influence of dynamic stall is termed as the threshold radius at the particular azimuth angle. For further details, including the derivation and validation of the model, along with its limitations, readers are referred to the article by Choudhry *et al*. [11].

In the following analysis, the distribution of the threshold radius with azimuth angle for the upstream and the downstream wind turbine, at selected locations (y/d = 2, 5, 10, 15), is presented as polar plots in Figure 10 where the blade azimuth angle is the polar-axis and percentage of the blade span is the vertical-axis. The turbines considered in the present study are similar, with a rotor diameter of 10.1 m and operating at a constant rotational speed of 71.6 rpm. Furthermore, the vertical wind shear is assumed to be zero for both the upstream and the tandem wind turbine and hence the mean velocity is constant along the entire rotor section. The blade is composed of the S809 airfoil for which the limiting reduced frequency is 0.026, based on 2D dynamic stall experiments [35]. The rotor of the upstream wind turbine is aligned with the oncoming freestream wind and therefore the yaw angle is zero degrees. On the other hand, the rotor for the downstream turbine is aligned with the rotational axis of the upstream turbine and, therefore, the downstream wind turbine experiences the wind directions as indicated in Figure 9. Similarly, the remaining model inputs, such as the mean wind speed and turbulence intensity, have also been extracted from the LES, using Figure 7 and Figure 8 respectively.

The occurrence of dynamic stall on the upstream and the downstream wind turbine, as a function of spacing between the turbines,is shown in Figure 10. It can be observed that due to the negligible incoming turbulence intensity, zero yaw angle and uniform inflow, the upstream wind turbine is free of dynamic stall. On the other hand, for the downstream wind turbine, a completely asymmetrical, twin-lobe distribution of threshold radius is observed at all downstream stations. At y/d = 2, due to the increased turbulence and the large rate of change of wind direction, an increased occurrence of

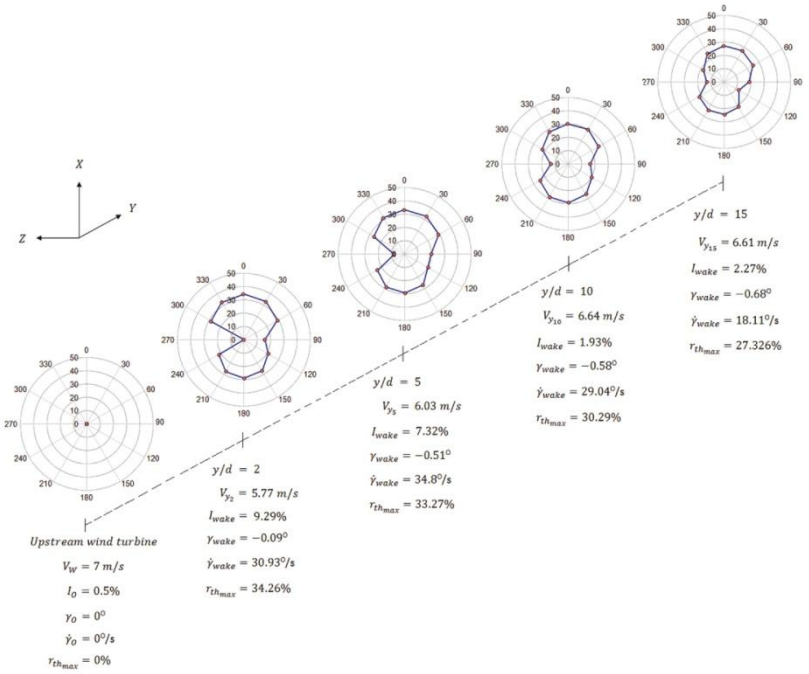

Figure 10. Threshold radius distribution for an upstream and tandem wind turbine based on wake characteristics determined by LES, illustrating the regions of a downstream wind turbine affected by dynamic stall

WIND ENGINEERING Volume 38, No. 5, 2014 PP 535–548 545

dynamic stall is apparent. As indicated in Figure 10, a little over 34% of the turbine blade will be affected by dynamic stall at one point in the rotation cycle ($\gamma_{th_{max}} = 34.26\%$). As the distance between the turbines is increased to five rotor diameters ($y/d = 5$), the occurrence of dynamic stall is slightly reduced on the downstream wind turbine blades. Further increase in the spacing between the turbines ($y/d = 10, 15$), only results in a slight decrease of the affected zones as shown in Figure 10. This is primarily due to the large turbulence intensity and the large rate of change of wind direction in the far-wake.

It is worth repeating here that the distributions presented in Figure 10, for both the upstream and the downstream wind turbines, are based on the LES results. In actual conditions, however, the effects of vertical wind shear, larger ambient turbulence intensity and the sporadic behaviour of wind direction will result in the upstream wind turbines experiencing dynamic stall as well. Similarly, a larger occurrence on downstream wind turbine can also be observed due to added turbulence in the wake. Therefore, the analysis presented here should only be considered a conservative estimate of the occurrence of dynamic stall on downstream wind turbines.

4. SUMMARY

The present article revisits the wind turbine wake studies performed at the University of Adelaide. The wake behind the NREL Phase VI wind turbine, operating inside a numerical wind tunnel with test section dimensions similar to the NASA Ames wind tunnel, was determined using Large Eddy Simulation. It was shown through instantaneous contours of vorticity that immediately behind the turbine, a tightly-wound helical vortex structure emanating from the tips is formed. Due to wake instability and mutual interaction with the root vortices, this structure becomes unstable and ultimately breaks down resulting in the formation of two pairs of counter-rotating streamwise vortices. Comparison of the flow structures with the contours of dimensionless velocity and turbulence intensity indicated that the regions of velocity deficits and high turbulence intensities were restricted to the regions of high vorticity. It was surmised by the authors that the reduced power output, larger unsteady loads and impulsive noise observed in commercial wind farms are directly related to the downstream wind turbine blades passing through these vortex structures.

Furthermore, a comparison of mean flow quantities computed using the LES and those predicted using the conventionally-employed empirical models is presented. The study assisted in discerning the behaviour of the mean flow parameters inside the numerical wind tunnel model that was used in the simulation. It was observed that in the near-wake the LES predictions were superior since the empirical models do not take into account the formation and the eventual breakdown of the vortex structures. Conversely, it was observed that in the far-wake, the predictions from the LES were influenced by the tunnel walls.

Finally, in order to explicitly understand the effects of wake on a downstream turbine, a study was undertaken to determine the regions of a downstream turbine blade affected by dynamic stall as a consequence of operating in the wake. The model employed for this purpose used the mean parameters extracted from the LES as inputs. It was observed that the increase in turbulence intensity and the large rate of change of wind direction are the primary causes of increased occurrence of dynamic stall on downstream wind turbines. The conservative estimate showed that unsteady fluctuations in the blade angle of attack near the root regions is prominent even at large downstream distances.

REFERENCES

[1] Manwell JF, McGowan JG and Rogers AL. *Wind energy explained*. Wiley Online Library, 2002.

[2] Snel H. Review of the present status of rotor aerodynamics. *Wind Energy*. 1998; 1: 46–69.

[3] Crespo A, Hernandez J and Frandsen S. Survey of modelling methods for wind turbine wakes and wind farms. *Wind Energy*. 1999; 2: 1–24.

[4] Vermeer L, Sørensen JN and Crespo A. Wind turbine wake aerodynamics. *Progress in Aerospace Sciences*. 2003; 39: 467–510.

[5] Sanderse B. Aerodynamics of wind turbine wakes. *Energy research Centre of the Netherlands, ECN-E-09-016*. 2009.

[6] Mo J-O, Choudhry A, Arjomandi M and Lee Y-H. Large eddy simulation of the wind turbine wake characteristics in the numerical wind tunnel model. *Journal of Wind Engineering and Industrial Aerodynamics*. 2013; 112: 11–24.

[7] Calaf M, Meneveau C and Meyers J. Large eddy simulation study of fully developed wind-turbine array boundary layers. *Physics of Fluids*. 2010; 22: 015–110.

[8] Troldborg N, Sorensen JN and Mikkelsen R. Numerical simulations of wake characteristics of a wind turbine in uniform inflow. *Wind Energy*. 2010; 13: 86–99.

[9] Wu Y-T and Porté-Agel F. Large-eddy simulation of wind-turbine wakes: evaluation of turbine parametrisations. *Boundary-Layer Meteorology*. 2011; 138: 345–66.

[10] Sørensen NN, Michelsen J and Schreck S. Navier–Stokes predictions of the NREL phase VI rotor in the NASA Ames 80 ft × 120 ft wind tunnel. *Wind Energy*. 2002; 5: 151–69.

[11] Choudhry A, Arjomandi M and Kelso R. Horizontal axis wind turbine dynamic stall predictions based on wind speed and direction variability. *Proceedings of the Institution of Mechanical Engineers, Part A: Journal of Power and Energy*. 2013; 227: 338–51.

[12] Mo J-O, Choudhry A, Arjomandi M, Kelso R and Lee Y-H. Effects of wind speed changes on wake instability of a wind turbine in a virtual wind tunnel using large eddy simulation. *Journal of Wind Engineering and Industrial Aerodynamics*. 2013; 117: 38–56.

[13] Simms DA. *NREL unsteady aerodynamics experiment in the NASA-Ames wind tunnel: A comparison of predictions to measurements*. National Renewable Energy Laboratory, 2001.

[14] Hand M and Simms D. Unsteady Aerodynamics Experiment. *2001*. 2001.

[15] Kraichnan RH. Diffusion by a random velocity field. *Physics of Fluids*. 1970; 13: 22–31.

[16] Smirnov A, Shi S and Celik I. Random flow generation technique for large eddy simulations and particle-dynamics modeling. *Transactions of the ASME-I-Journal of Fluids Engineering*. 2001; 123: 359–71.

[17] Yang Z, Sarkar P and Hu H. An experimental investigation on the wake characteristics of a wind turbine in an atmospheric boundary layer wind. *29th AIAA Applied Aerodynamics Conference*. 2011, p. 1–18.

[18] Wagner S, Bareiss R, Guidati G and Wagner-Bareiß-Guidati. Wind turbine noise. 1996.

[19] Hubbard HH and Shepherd KP. Aeroacoustics of large wind turbines. *The Journal of the Acoustical Society of America*. 1991; 89: 2495.

[20] Van den Berg G. Effects of the wind profile at night on wind turbine sound.*Journal of Sound and Vibration*. 2004; 277: 955–70.

[21] Bowdler D. Amplitude modulation of wind turbine noise: a review of the evidence. *Institute of Acoustics Bulletin*. 2008; 33: 31–41.

[22] Doolan C, Moreau DJ and Brooks LA. Wind turbine noise mechanisms and some concepts for its control. *Acoustics Australia*. 2012; 40: 7–13.

[23] Mortensen N, Landberg L, Troen I and Petersen E. Getting started. Vol. 1, Wind Analysis and Application Program (WASP), User's Guide. Risø-I-666 (EN), *Risø National Laboratory*, Roskilde, Denmark, 1993.

[24] Mortensen NG, Heathfield DN, Myllerup L, et al. Getting Started With WAsP8. *Risø National Laboratory*. 2003.

[25] Troen I and Petersen EL. European wind atlas. *Roskilde: Risø National Laboratory, 1989*. 1989; 1.

[26] Jensen NO. *A note on wind generator interaction*. 1983.

[27] Katic I, Højstrup J and Jensen N. A simple model for cluster efficiency. 1986.

[28] Barthelmie R, Larsen G, Frandsen S, et al. Comparison of wake model simulations with offshore wind turbine wake profiles measured by sodar.*Journal of Atmospheric and Oceanic Technology*. 2006; 23: 888–901.

[29] Hansen MOL. *Aerodynamics of wind turbines*. Earthscan/James & James, 2008.

WIND ENGINEERING Volume 38, No. 5, 2014 PP 535–548 547

[30] Hassan U. A wind tunnel investigation of the wake structure within small wind turbine farms. 1993.

[31] Vermeulen P. An experimental analysis of wind turbine wakes. 1980, p. 431–50.

[32] Melbourne W. Criteria for environmental wind conditions. *Journal of Wind Engineering and Industrial Aerodynamics*. 1978; 3: 241–9.

[33] Carr LW and Chandrasekhara M. Compressibility effects on dynamic stall. *Progress in Aerospace Sciences*. 1996; 32: 523–73.

[34] Schreck SJ, Robinson, M.C., Hand, M.M. and Simms, D.A. Blade dynamic stall vortex kinematics for a horizontal axis wind turbine in yawed conditions. *Journal of Solar Energy Engineering*. 2001; 123: 272.

[35] Ramsay R R, Hoffmann M J and Gregorek G M. Effects of Grit Roughness and Pitch Oscillations on the S809 Airfoil. NREL/TP-442-7817, *National Renewable Energy Laboratory,* Golden, CO, 1995.

CHAPTER 5

EFFECTS OF SEPARATION BUBBLE ON STEADY-STATE LIFT

5.1 Chapter Overview

This chapter presents a detailed numerical analysis of the transition process on a thick NACA 0021 airfoil at low freestream turbulence levels and low Reynolds numbers. Under these conditions several unique aerodynamic characteristics have been observed on the thick foil. These include a lift-curve slope that exceeds the theoretical maximum and an abrupt stall behavior, which is not typical of such airfoils. In the article, which constitutes this chapter, a comparative analysis of two recently-developed transition models has been presented. During this analysis, it has been observed that a long separation bubble on the upper surface of

the airfoil is primarily responsible for the unique aerodynamic features observed on the airfoil. The significance of this study is two-fold:

1) The study demonstrates that distinct flow features in the vicinity of the airfoil can induce global changes in the behavior of the airfoil. This can be extended to explain the non-linear lift behavior observed for the airfoil undergoing dynamic stall. This concept is further discussed in Chapter 6 of the thesis.
2) The study provides a useful insight into the steady-state behavior of the thick airfoil at low freestream Reynolds numbers and turbulence levels that are typical of conventional wind tunnels. The knowledge is useful in analyzing the effects of different flow control methods at steady-state conditions presented in Chapter 7 of the thesis.

The numerical analysis presented in this chapter and the discussions are included as an article published in the International Journal of Heat and Fluid Flow.

5.2 Numerical Study of Long Separation Bubbles

Statement of Authorship

Title of Paper	A study of long separation bubble on thick airfoils and its consequent effects
Publication Status	◉ Published, ○ Accepted for Publication, ○ Submitted for Publication, ○ Publication style
Publication Details	Choudhry, Amanullah, Maziar Arjomandi, and Richard Kelso. "A study of long separation bubble on thick airfoils and its consequent effects." International Journal of Heat and Fluid Flow 52 (2015): 84-96.

Author Contributions

By signing the Statement of Authorship, each author certifies that their stated contribution to the publication is accurate and that permission is granted for the publication to be included in the candidate's thesis.

Name of Principal Author (Candidate)	Amanullah Choudhry		
Contribution to the Paper	Developed ideas, performed the numerical analysis, interpreted the date, wrote the manuscript, acted as the corresponding author, wrote the rebuttal		
Signature		Date	

Name of Co-Author	Maziar Arjomandi		
Contribution to the Paper	Supervised the work, helped in developing ideas, manuscript evaluation and feedback		
Signature		Date	

Name of Co-Author	Richard Kelso		
Contribution to the Paper	Supervised the work, helped in developing ideas, manuscript evaluation and feedback		
Signature		Date	

Name of Co-Author			
Contribution to the Paper			
Signature		Date	

International Journal of Heat and Fluid Flow 52 (2015) 84–96

Contents lists available at ScienceDirect

International Journal of Heat and Fluid Flow

journal homepage: www.elsevier.com/locate/ijhff

A study of long separation bubble on thick airfoils and its consequent effects

Amanullah Choudhry *, Maziar Arjomandi, Richard Kelso

School of Mechanical Engineering, The University of Adelaide, South Australia 5005, Australia

ARTICLE INFO

Article history:
Received 5 April 2014
Received in revised form 7 October 2014
Accepted 1 December 2014

Keywords:
Low Reynolds number
Camber effect
Airfoil transition modelling
Separation induced transition
Separation bubble
MAV

ABSTRACT

A parametric study has been performed to analyse the flow around the thick-symmetric NACA 0021 airfoil in order to better understand the characteristics and effects of long separation bubbles (LoSBs) that exist on such airfoils at low Reynolds numbers and turbulence intensities. In the article, the prediction capabilities of two recently-developed transition models, the correlation-based γ–Re_θ model and the laminar-kinetic-energy-based κ–κ_L–ω model are assessed. Two-dimensional steady-state simulations indicated that the κ–κ_L–ω model predicted the separation and reattachment process accurately when compared with published experimental work. The model was then used to study the attributes and the effects of LoSBs as a function of the angle of attack, freestream turbulence intensity and Reynolds number. It was observed that LoSBs considerably degrade the aerodynamic performance of airfoils and lead to abrupt stall behaviour. It is, furthermore, illustrated that the presence of the LoSB leads to an induced camber effect on the airfoil that increases as the airfoil angle of attack increases due to the upstream migration of the bubble. An increase in the Reynolds number or turbulence levels leads to a reduction in the bubble extent, considerably improving the airfoil performance and leading to a progressive trailing-edge stall.

1. Introduction

Separation bubbles are generated primarily in applications involving low Reynolds number flows with large pressure gradients such as compressor blades in turbo-machines, high-altitude unmanned-air-vehicles, micro-air-vehicles and wind turbines (Lin and Pauley, 1996). The presence of the separation bubble is generally considered undesirable since it can impact the aerodynamic efficiency and stall behaviour of airfoils (Nakano et al., 2007; Zhang et al., 2008). The bubble can alter the flow at low Reynolds numbers and can consequently have adverse effects on the performance of the machine. Difficulties can also arise during airfoil testing in wind tunnels for applications involving high Reynolds number flows due to undesirable scale effects since most experimental wind tunnels operate in low Reynolds number regimes (Lissaman, 1983; Ol et al., 2005). The traditional methods to avoid these scale effects such as the addition of roughness strips and trip wires on airfoils or the addition of freestream turbulence also add a degree of complication and uncertainty to the process. Therefore, the characteristics of the separation bubble and its effects need to be understood well to improve the design methodology of airfoils.

The most prevalent type of transition observed on airfoils and wings at low Reynolds numbers is the separation-induced transition. Separation-induced transition primarily occurs when a laminar boundary layer is exposed to large adverse pressure gradients, such as those near the leading edge of airfoils, resulting in its separation. The separated shear layer then undergoes transition due to amplification of velocity disturbances in the flow (Alam and Sandham, 2000a). The resulting turbulent shear layer reattaches some distance downstream resulting in the formation of an enclosed region commonly referred to as a separation bubble. The primary aspects of separation-induced transition, adapted from Horton (Horton, 1968), are illustrated in Fig. 1.

The location and size of the separation bubble is a function of the airfoil profile, freestream Reynolds number, turbulence intensity and the angle of attack (Tani, 1969; Swift, 2009). Separation bubbles can be classified either as short or long based on their chordwise extent and consequent effects on an airfoil pressure and velocity distributions. A short separation bubble (SSB) encompasses a chordwise extent of less than one percent and therefore does not influence the pressure distribution around the airfoil to a large degree (Tani, 1961). After transition occurs in the separated

* Corresponding author at: School of Mechanical Engineering, The University of Adelaide, Adelaide, South Australia 5005, Australia. Tel.: +61 413032885.
E-mail address: amanullah.choudhry@adelaide.edu.au (A. Choudhry).

http://dx.doi.org/10.1016/j.ijheatfluidflow.2014.12.001
0142-727X/

shear layer, the pressures start to return to the inviscid distribution that would exist if there was no bubble present (Katz and Plotkin, 1991). On the other hand, a long separation bubble (LoSB) can cover several percent of the airfoil chord and, therefore, severely affects the pressure distribution and the forces generated by the airfoil. Due to increased interaction with the exterior flow, the pressure distribution may be modified to such a large extent that it may be substantially different compared to the inviscid values (Gaster, 1966). The effects of both types can clearly be seen in Fig. 2 where it can be observed that the presence of the separation bubble results in a zero pressure gradient region due to flow stagnation inside the bubble (Gaster, 1969). Therefore, once the flow separates, the pressure barely changes due to the very low flow velocities and the relatively low streamline curvature in the free-stream flow. As shown by Bursnall and Loftin (1951), the flow is fully turbulent prior to reattachment, indicating that it is likely the transition process aids in the shear layer reattachment.

SSBs are commonly observed on thin airfoil sections near the leading edge where large pressure gradients exist and have been studied extensively (Crabtree, 1959; Von Doenhoff, 1938; Tani, 1939; Owen and Klanfer, 1953). It has been shown that an increase in the angle of attack or a reduction in the Reynolds number can lead to the 'bursting' of the bubble resulting in the formation of a LoSB or an unattached free shear layer (Gaster, 1969). Therefore, the LoSBs are considered as the precursor of thin airfoil stall (Bak et al., 1998). On the other hand, the effects of LoSBs have not been studied in much detail since it is believed that these exist only due to the bursting of SSBs. However, literature survey and experiments have revealed that long bubbles can exist on the suction side of thick airfoils at low Reynolds number and their presence dictates the aerodynamic efficiency and stall behaviour of thick airfoil sections (Jacobs, 1932; Raghunathan et al., 1988; Swalwell et al., 2001; Hansen et al., 2011). Therefore, it is important to understand the global characteristics of a long separation bubble in order to improve the understanding of its consequent effects on the performance of an airfoil at low Reynolds numbers. Such a study will aid in the selection of appropriate control techniques to avoid the possible losses incurred by the presence of LoSBs.

In aerospace applications, parametric studies are most conveniently performed using numerical modelling techniques. Efforts have been made by several researchers to understand the characteristics of laminar separation bubbles. Marxen et al. (2004) performed Direct Numerical Simulation (DNS) of flow over a flat plate in order to observe the basic characteristics of separation-induced transition. Galbraith and Visbal (2008) conducted Large Eddy Simulation (LES) in order to determine characteristics of the separation bubble on the SD7003 airfoil. However, the use of DNS and LES for wall-bounded flows requires prohibitively long runtimes and, therefore, these methods are not currently being used

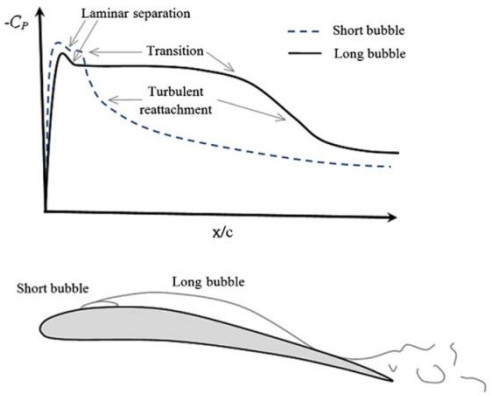

Fig. 2. The resultant pressure distribution on an airfoil due to presence of a short and long separation bubble.

for purposes other than research. On the other hand, RANS-based approaches coupled with linear-stability theory, offer an attractive alternative for prediction of separation-induced transition (Windte et al., 2006; Radespiel et al., 2007; Lian and Shyy, 2007). In the present article, two recently-developed RANS-based transition models, the γ–Re_θ model (Menter et al., 2006) and the κ–κ_L–ω model (Walters and Cokljat, 2008) have been tested and compared. Both models have been studied extensively against standard test cases and have been shown to predict the transition onset and extent with reasonable accuracy (Walters and Cokljat, 2008; Langtry et al., 2006; Menter, 2011). However, these RANS-based models have not been compared with each other before. The γ–Re_θ model has been shown to have superior prediction capabilities compared to other correlation-based models (Suluksna and Juntasaro, 2008). On the other hand, the κ–κ_L–ω model focuses on the theory behind the model, instead of the results; however, there is little proof of the models' general applicability (Turner, 2012). Therefore, the two transition models have been assessed and compared in the current paper for the flow around NACA 0021 airfoil, based on the criteria established by Zingg and Godin (2009) for turbulence model assessment. In addition to this, a detailed analysis has been performed to study the characteristics of the LoSB and its effects on the performance of the NACA 0021 airfoil as a function of Reynolds number, freestream turbulence intensity and angle of attack. A peculiar effect of the LoSB has been noted in the present work and is discussed in detail in the article.

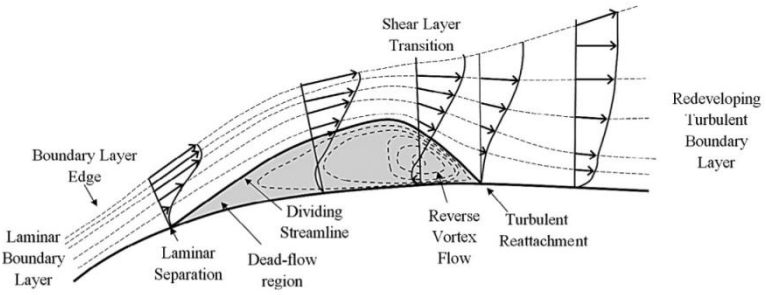

Fig. 1. Separation-induced transition, reproduced from Horton (1968).

2. Transition modelling

2.1. Correlation based intermittency model

The correlation-based intermittency model employing local variables, γ–Re_θ model, was first proposed in 2002 by Menter et al. (2002). Instead of using correlation-based functions to determine the transition onset, such as those proposed by Narasimha (1985) and Abu-Ghannam and Shaw (1980) the γ–Re_θ model was based on vorticity Reynolds number (Re_υ) which is dependent solely on local variables as shown:

$$Re_\upsilon = \frac{\rho y^2}{\mu}\frac{\partial u}{\partial y} = \frac{\rho y^2}{\mu}\Omega$$

Here Ω is the vorticity and y is the wall normal distance. The maximum value of Re_υ is dependent on the momentum thickness Reynolds number. The transport equation for intermittency is used to trigger the transition process and is given by Menter et al. (2006):

$$\frac{\partial \rho\gamma}{\partial t} + \frac{\partial \rho u_j \gamma}{\partial x_j} = P_{\gamma 1} - E_{\gamma 1} + P_{\gamma 2} - E_{\gamma 2} + \frac{\partial}{\partial x_j}\left[\left(\mu + \frac{\mu_t}{\sigma_f}\right)\frac{\partial \gamma}{\partial x_j}\right]$$

The intermittency transport equation includes two proprietary functions: F_{length}, which controls the transition extent and $Re_{\Theta c}$ which determines the onset of transition. Furthermore, the transport equation for momentum thickness Reynolds number at the transition onset is given as:

$$\frac{\partial \rho Re_{\Theta t}}{\partial t} + \frac{\partial \rho u_j Re_{\Theta t}}{\partial x_j} = P_{\Theta t} + \frac{\partial}{\partial x_j}\left[\sigma_{\Theta t}(\mu + \mu_t)\frac{\partial Re_{\Theta t}}{\partial x_j}\right]$$

When the boundary layer separates, the transition model follows the following modification that allows the intermittency to exceed unity:

$$\gamma_{sep} = \min\left\{8\max\left[\left(\frac{Re_\upsilon}{2.193 Re_{\Theta c}}\right) - 1, 0\right]e^{-\left(\frac{R_T}{15}\right)^4}, 5\right\}F_{\Theta t}$$

Here, $F_{\Theta t}$ is the blending function that confines the modification to boundary layer type flows. The modification allows for larger production of turbulent kinetic energy at separation as well in order to hasten the reattachment. The artificial production of turbulence allows accurate modelling of turbomachinery applications for which the model was designed. The transition model has been coupled with Menter's κ–ω SST model (Menter, 1994) where the production and destruction terms from the original SST model have been modified using the intermittency, making the γ–Re_θ model a four equation turbulence model. A complete description of the model is available in the article by Menter et al. (2006).

2.2. Laminar-kinetic-energy Model

The laminar-kinetic-energy model employed in the current article is the one proposed by Walters and Cokljat (2008) and is based on observations of the phenomena associated with laminar kinetic energy. Klebanoff (1971), while studying the effects of freestream turbulence on laminar boundary layers, discovered 'streaky structures' that lead to fluctuations in pressure and streamwise velocities. The fluctuation energy was termed as laminar kinetic energy. The laminar kinetic energy modelling can be coupled with existing turbulence models in order to improve the predictions of the transition process.

The (Walters and Cokljat, 2008) κ–κ_L–ω model solves three additional transport equations for laminar and turbulent kinetic energy as well as the specific dissipation rate along with the basic RANS equations. The additional transport equations are:

$$\frac{D\kappa_T}{Dt} = P_{\kappa_T} + R_{BP} + R_{NAT} - \omega\kappa_T - D_T + \frac{\partial}{\partial x_j}\left[\left(\upsilon + \frac{\alpha_T}{\sigma_\kappa}\right)\frac{\partial \kappa_T}{\partial x_j}\right]$$

$$\frac{D\kappa_L}{Dt} = P_{\kappa_L} - R_{BP} - R_{NAT} - D_L + \frac{\partial}{\partial x_j}\left[\upsilon\frac{\partial \kappa_L}{\partial x_j}\right]$$

$$\frac{D\omega}{Dt} = C_{\omega 1}\frac{\omega}{\kappa_T}P_{\kappa_T} + \left(\frac{C_{\omega R}}{f_W} - 1\right)\frac{\omega}{\kappa_T}(R_{BP} + R_{NAT}) - C_{\omega 2}\omega^2 + C_{\omega 3} f_\omega \alpha_T f_W^2 \frac{\kappa_T^{1/2}}{d^3} + \frac{\partial}{\partial x_j}\left[\left(\upsilon + \frac{\alpha_T}{\sigma_\omega}\right)\frac{\partial \omega}{\partial x_j}\right]$$

The terms in the model equations represent production, destruction and transport mechanisms. It should be noted that the model is ω-based rather than being ε-based like the original version (Walters and Leylek, 2004) since it was observed that the ω-based approach yields superior results in the transition onset predictions (Walters and Leylek, 2005).

The effects of the laminar and turbulent kinetic energy on the Reynolds stress terms was included through the total eddy viscosity concept (Volino, 1998), defined as:

$$-\overline{u_i' u_j'} = \upsilon_{TOT}\left(\frac{\partial u_i}{\partial x_j} + \frac{\partial u_j}{\partial x_i}\right) - \frac{2}{3}\kappa_{TOT}\delta_{ij}$$

Here, υ_{TOT} is the sum of the small-scale eddy viscosity and the large scale eddy viscosity and κ_{TOT} is the sum of the turbulent and laminar kinetic energies. The laminar kinetic energy was used to describe the low frequency, high amplitude fluctuations in the pre-transitional laminar boundary layer. The fluctuations occur at a single scale and nearly all energy is contained in a single streamwise component. This implies that the process is largely two-dimensional and does not require a three-dimensional analysis. However, it is important to understand that these two-dimensional mechanisms are not equivalent to the instabilities caused by the 2D Tollmien–Schlichting (T–S) waves. Separation-induced transition can be considered as a type of bypass transition where the primary modes of natural transition, including the production of T–S waves, are 'by-passed' (Alam and Sandham, 2000b).

A complete description of the model equations and constants can be found in the articles by Walters and Leylek (2004) and Walters and Cokljat (2008).

3. Numerical method

3.1. Numerical scheme

The flow governing equations were solved using a cell-centred control volume space discretization approach for the fluid domain. The partial differential equations based on Reynolds Averaged Navier Stokes (RANS) equations are as follows:

$$\frac{\partial \rho}{\partial t} + \frac{\partial}{\partial x_i}(\rho u_i) = 0$$

$$\frac{\partial}{\partial t}(\rho u_i) + \frac{\partial}{\partial x_j}(\rho u_i u_j) = -\frac{\partial p}{\partial x_i} + \frac{\partial}{\partial x_j}\left[\mu\left(\frac{\partial u_j}{\partial x_i} + \frac{\partial u_i}{\partial x_j} - \frac{2}{3}\delta_{ij}\frac{\partial u_i}{\partial x_j}\right)\right] + \frac{\partial}{\partial x_j}(\rho\overline{u_i' u_j'})$$

The Reynolds stress term ($\rho\overline{u_i' u_j'}$) is resolved using the turbulence model of choice to close the system of equations. In the present work, pressure–velocity coupling was handled using the implicit pressure-based algorithm SIMPLE. Steady-state simulations were performed which simplifies the above equations by eliminating the time marching. The choice of steady-state simulations was motivated by the seminal work of Pauley et al. (1990) who showed that LoSBs are steady separation bubbles without any vortex shedding. Simulations were initialized based on the

inlet boundary conditions. The equations were solved iteratively using second-order upwind scheme for spatial discretization of variables to improve the solution accuracy and numerical stability. The models were applied using the commercial software ANSYS® Fluent, *Release* 14.5. The lift and drag coefficients as well as the normalized residuals of all variables were monitored to ensure adequate convergence of the steady-state simulation.

The turbulence models were evaluated based on the criteria presented by Zingg and Godin (2009). The criteria and the relevant steps taken to ensure numerical accuracy are summarized as follows:

1. *Experimental flow conditions must be reproduced in the numerical work*: The experimental conditions of chord Reynolds number and freestream turbulence intensity were matched through a study conducted to determine the boundary conditions. The airfoil trailing edge was truncated at 0.99c since zero thickness at the trailing edge is both practically unrealistic and problematic during grid-generation.
2. *Numerical error must be considerably smaller than the turbulence modelling errors*: This has been addressed by conducting a grid independence study to ensure adequate mesh resolution was achieved for the simulations.
3. *Experimental errors should be minimal*: Care was taken while selecting the appropriate experimental data sets based on accuracy. The data selected were the low Reynolds number experiments conducted on the NACA 0021 airfoil at the University of Adelaide KC wind tunnel (Hansen, 2012). Uncertainty analysis was performed to ensure that experimental predictions of forces and pressures were accurate. Further details can be found in the reference (Hansen, 2012).
4. *The location of laminar-turbulent transition must be known a priori and defined in the simulations*: The location of laminar separation and turbulent reattachment were deduced from the experimental pressure distributions. However, it is important to note that the location of transition was not defined in the present simulations in advance since this parameter was specifically being assessed.

3.2. Computational mesh

The computational grid employed in the present study for the simulation of flow around the NACA 0021 airfoil was constructed using POINTWISE® and is illustrated in Fig. 3. The mesh was constructed using an O-type grid topology, centred on the airfoil, in order to reduce the overall skewness of the near-wall elements as the mesh density is increased for the subsequent grid independence study. Structured quadrilateral elements were used in the current work since they provide the added advantage of a higher degree of control and accuracy, lower memory consumption and a faster convergence rate due to flow alignment with the grid elements (Sanders, 2009). A total of 250,000 elements were used to model the flow with 880 grid points along the airfoil surface and 284 in the wall-normal direction. The grid density was increased significantly as the mesh approached the airfoil from the boundaries to capture the salient flow features in the vicinity of the airfoil and to decrease the interpolation errors. The boundaries of the domain were placed at a distance of 20 chord lengths from the airfoil in order to ensure that the boundary location did not influence the flow (Fig. 3a). A total of 30 inflation layers were used in the vicinity of the airfoil to accurately model the boundary layer flow (Fig. 3b). The airfoil trailing edge was truncated in order to match the experiments (Fig. 3c). The height of the first cell was based on the required minimum value of y^+ ($\leqslant 1$) for the low-Re turbulent

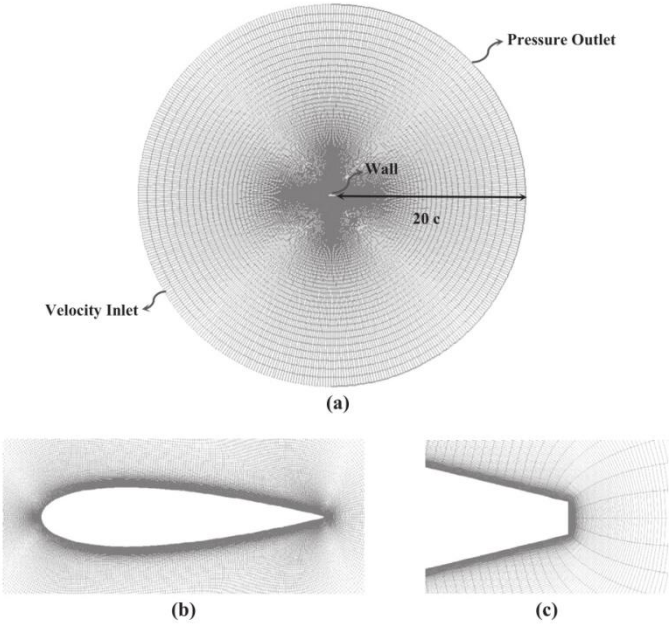

Fig. 3. (a) Typical grid topology used in the current study showing the overall grid resolution and boundary conditions. (b) Close-up view of the mesh in the vicinity of the airfoil. (c) Truncated trailing edge mesh.

models used in the current work in order to accurately model the boundary layer. Furthermore, the y^+ was also checked as part of the routine post-processing for all simulations conducted in the present work and it was made certain to be less than one.

3.3. Boundary conditions

As can be observed in Fig. 3, the domain boundary was split into two regions, the velocity inlet and the pressure outlet, to implement the appropriate boundary conditions. The freestream velocity was specified at the inlet such that the chord Reynolds number of 120,000 was attained in the simulation to match the experiments. The angle of attack was also varied at the velocity inlet using the respective velocity components. The gauge pressure at the pressure outlet was specified to be zero. Furthermore, wall-condition ($U = 0$) was specified for the airfoil surface so that the no-slip boundary condition was enforced and no turbulence was produced from the wall itself for both models. The freestream turbulence specification method chosen for the current work was to define the turbulence intensity and turbulence length scale at the inlet boundary. The inlet turbulence length scale and the inlet turbulence intensity are used in the Fluent CFD software to set the inlet specific dissipation rate and the turbulence kinetic energy respectively. These quantities are then calculated in the domain based on the transport equations presented earlier in Section 2. As suggested by Langtry and Menter (2005) for the γ–Re_θ model and by Walters and Cokljat (2008) for the κ–κ_L–ω model, the turbulent parameters at the inlet need to be specified such that the turbulence intensity in the vicinity of the body is similar to the experimental conditions. The turbulence intensity measured near the leading edge of the airfoil (TI_{LE}) in the experiment was 0.6% (Hansen et al., 2011). Therefore, simulations were first conducted at an angle of attack of zero degrees in order to observe the effects of inlet turbulence length scale, the decay of turbulence intensity in the domain and to establish the appropriate turbulent parameters for the inlet boundary conditions. Since turbulence is a dissipative phenomenon, an arbitrarily large value of turbulence intensity of 7.5% was selected at the inlet and was kept constant while the inlet turbulence length scale was varied. As soon as the flow enters the domain, the turbulence is dissipated and the value of turbulence intensity rapidly falls as the flow progresses towards the leading edge of the airfoil. The final value of the turbulence intensity at the leading edge of the airfoil (TI_{LE}) as a function of the inlet length scale at a Reynolds number of 120,000 is shown in Fig. 4 for both transition models. It can be observed that for similar turbulence length scales, the decay in turbulence intensities is more severe for the κ–κ_L–ω model. As stated earlier, the decay is governed by the transport equations of specific dissipation rate and turbulence kinetic energy. Furthermore, note that the increase in the length scales associated with the turbulent structures results is a smaller decay rate of turbulence intensity. This makes intuitive sense since smaller structures are more prone to dissipation compared to larger eddies. Also indicated in the plot is the required turbulence intensity of the experiment (0.6%). Using this method, the appropriate boundary conditions for both transition models were obtained in order to satisfy the criterion set by Zingg and Godin (2009).

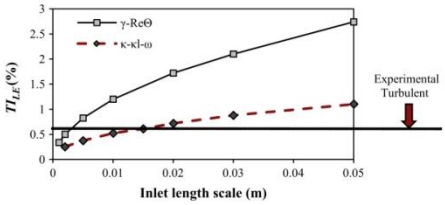

Fig. 4. Variation of turbulence intensity at the leading edge of the airfoil as a function of the specified inlet turbulence length scale for the two transition models. Note that the turbulence intensity specified at the inlet was kept constant at the arbitrary value of 7.5%. Therefore, the plot further indicates the decay rate of turbulence intensity as a function of the inlet length scales. The required turbulence intensity measured at the leading edge of the experiment is also indicated.

It should be noted here that the turbulence length scale does not play a significant role for this particular type of transition process. Here, the laminar boundary layer is expected to detach under the influence of adverse pressure gradients and then reattach after transitioning from laminar to turbulent flow. As shown by Butler et al. (2001) for a turbine blade cascade case where a similar transition process is observed, the process is not affected by the length scale of turbulent structures and is primarily dependent on the freestream turbulence intensity, Reynolds number and the pressure distribution. Similarly, experimental work by Cao (2010) demonstrated that the turbulence length scale had minimal effect on the performance of an airfoil at low freestream turbulence intensities and Reynolds numbers. The authors believe that the transition process is affected only when the length scales are comparable with the boundary layer thickness of the airfoil. However, in the present case and the works cited above, the length scales specified are at least order of magnitude smaller than the typical boundary layer thickness. Consequently, it is believed that the length scales, in this particular case, do not affect the transition process.

3.4. Grid independence study

A grid sensitivity analysis was performed to ascertain whether the selected grid density was of sufficient resolution and that the spatial discretization errors were minimal. The total number of elements of the original mesh was halved and doubled to generate two additional meshes for this study. The study was conducted at the angle of attack of zero and 4°, a Reynolds number of 120,000 and a TI_{LE} of 0.6%. The airfoil drag coefficient was monitored as the dependent variable for the study conducted at an angle of zero degrees whereas surface pressure distributions have been compared for the angle of attack of 4°. The dual check was performed in order to ensure that the mesh influence was locally small in the critical transitional flow region.

The results of the gird independence study are summarized in Table 1 where it can be observed that the mesh with 125,000 elements is sufficient, at a first glance. This is because doubling the mesh results in a little over 0.5% change in the predicted drag coefficient. However, comparison of the surface pressure distributions for the different mesh densities revealed instabilities in the predicted pressures on the airfoil suction side for the smaller mesh density of 125,000 elements. It is important to note that the instabilities were observed only for the κ–κ_L–ω model, as shown in Fig. 5(a), indicating that the chordwise resolution is not sufficient to capture the transition process. The instabilities disappeared as

Table 1
Grid independence study.

Mesh size (distribution)	Farfield location	γ–Re_θ	κ–κ_L–ω
		Drag coefficient (0°)	
125 k (440 × 284)	20*c*	0.01992496	0.026036741
250 k (880 × 284)	20*c*	0.019799614	0.026192013
500 k (1108 × 451)	20*c*	0.019696975	0.026138515
		Drag coefficient (5°)	
250 k (880 × 284)	20*c*	0.026083962	0.032757482
344 k (880 × 391)	40*c*	0.026184851	0.032984562

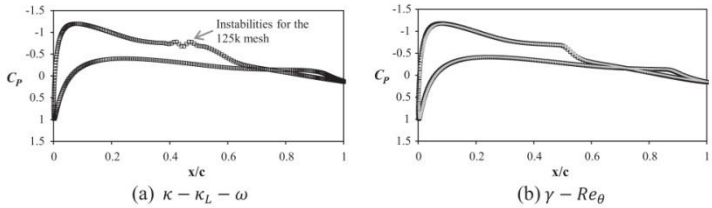

Fig. 5. Comparison of surface pressure distributions for two different mesh densities at an angle of attack of 4°. The smaller density mesh of 125,000 elements (□) exhibits instabilities in the surface pressure when compared with the larger mesh density of 250,000 elements (–) for the κ–κ_L–ω model in (a). On the other hand, the pressure distribution is similar for the γ–Re_θ model (b).

the mesh density was increased. On the other hand, for the γ–Re_θ model, no such fluctuations in the surface pressures were observed for either mesh density, as shown in Fig. 5(b). A similar pressure distribution was observed for the largest mesh density of 500,000 elements for both models. Therefore, in order to ensure that the LoSB features were accurately modelled, the mesh size of 250,000 elements was found sufficient and hence used in subsequent studies.

A further study was conducted to ensure that the boundary location had a minimal effect on the airfoil performance. For this purpose, an additional mesh was generated with the same O-type grid topology centred on the airfoil. However, for this case, the farfield boundary was located at a distance of 40 chord lengths from the airfoil surface. A similar near-surface grid distribution was maintained in order to ensure that the solution was only sensitive to the farfield boundary location. Furthermore, the inlet boundary conditions were modified to ensure that the turbulence intensity was 0.6% near the airfoil leading edge. For this study, the drag coefficients were compared at a moderate angle of attack of 5°. The results have been summarized in Table 1 where it can be observed that the variation in drag coefficient as a result of the boundary location is negligible. Furthermore, apart from a slight increase in $C_{p_{min}}$, the pressure distribution was also observed to be similar for both cases. Therefore, for the subsequent analysis, boundary location of 20c was considered sufficient.

3.5. Comparison of the transition models

The comparison of experimental and computed lift and drag coefficients is shown in Fig. 6. Simulations were conducted at a Reynolds number of 120,000 using the two transitional models over a range of angles to establish the accuracy of both models.

It can be observed that the γ–Re_θ model under-predicts both lift and drag coefficients for most of the range of angles considered in the present study. The divergence of the coefficients increases considerably as the angle of attack is increased. Even at the smaller angles, where complete flow separation is not observed, the values are under-predicted showing the inability of the γ–Re_θ scheme to accurately model the aerodynamic characteristics influenced by the presence of the separation bubble. Furthermore, the γ–Re_θ model, predicts a gradual stall behaviour more commonly observed on thick airfoil sections at high Reynolds number flows.

On the other hand, the κ–κ_L–ω model shows a much better agreement with the experimental lift coefficient, specifically in the attached-flow regime. The deviation in the lift is still observed at the higher angles but to a lesser extent as compared to the γ–Re_θ model. The drag coefficients, on the other hand, are exceedingly well-predicted by the κ–κ_L–ω model, especially considering the two-dimensional nature of the simulations. Furthermore, the stall behaviour of the airfoil is modelled comparatively well through the κ–κ_L–ω model. As can be observed, at such low Reynolds numbers the airfoil undergoes an abrupt stall, similar to thin airfoil sections, due the bursting of the separation bubble.

A comparison of the measured and computed pressure coefficients at selected angles is shown in Fig. 7. In general, both models under-predict the suction pressures on the airfoil consistently, with the degree of discrepancy growing as the angle of attack is increased. The peak suction pressures on the airfoil upper surface are constantly under-predicted, as compared to the experiments, regardless of the angle of attack. On the other hand, the pressures on the lower side have been computed reasonably well, illustrating that the models can perform realistically for attached flows with negligible adverse pressure gradients.

It is interesting to note that both models tend to accurately capture the point of separation and transition to some extent for the cases where the flow is largely attached (Fig. 7a–d). These are the locations where the pressure distribution first levels off and where the pressure distribution starts to follow the 'inviscid' distribution, respectively as explained earlier. However, the γ–Re_θ model predicts an earlier reattachment as compared to the κ–κ_L–ω model

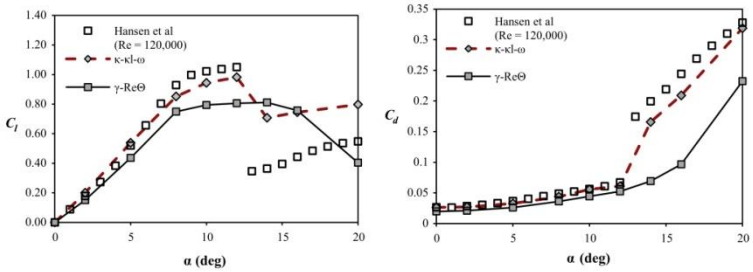

Fig. 6. Comparison of experimental and predicted force coefficients for the NACA 0021 airfoil at transitional Reynolds number of 120,000 using the two transition models.

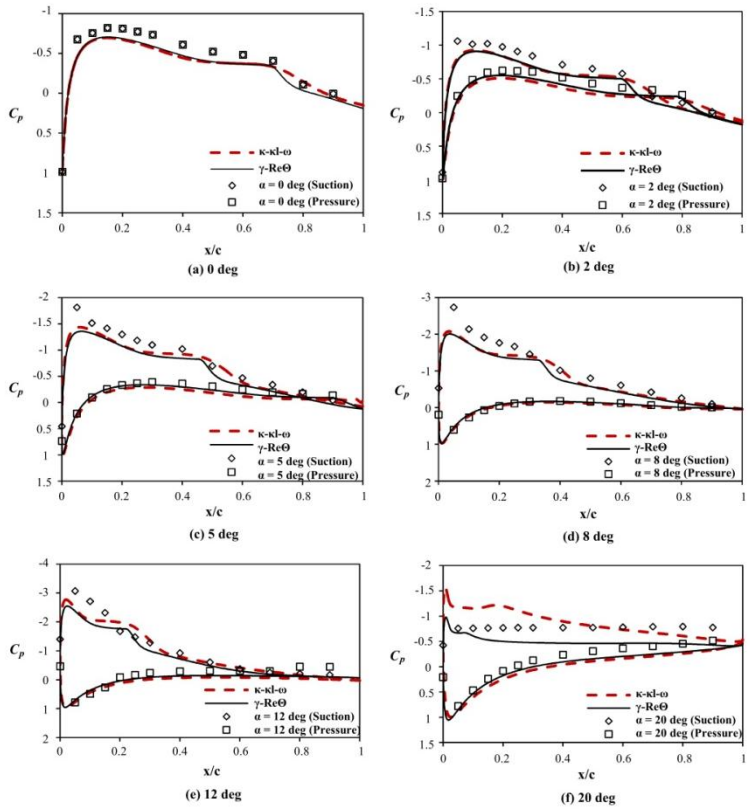

Fig. 7. Comparison of pressure coefficient distribution at selected angles of attack for the NACA 0021 airfoil at transitional Reynolds number of 120,000.

and the experiments. The inability to accurately predict the point of reattachment stems from the inherent empiricism employed in the model that allows additional turbulence to be generated as soon as the flow starts to transition (Menter et al., 2002; Langtry and Menter, 2005). This results in earlier reattachment of the flow as can be deduced from the pressure distributions presented in Fig. 7. On the other hand, the κ–κ_L–ω model quite closely follows the experimental pressure distribution and accurately models the bubble behaviour, especially at the smaller angles. Furthermore, note that the minimum pressure coefficients as predicted by the two models are approximately similar, especially at the lower angles (Fig. 7a–d). Therefore, it is expected that the lift prediction should be at least comparable between the two models. However, as seen in Fig. 6, the lift predicted by the γ–Re_θ model is smaller as compared to that predicted by the κ–κ_L–ω model, even at lower angles of attack. The difference in the prediction of lift stems from the dissimilar pressure distributions computed by the two models associated with the separation bubble as shown in Fig. 7. The authors believe that the larger bubble predicted by the κ–κ_L–ω model results in an induced camber effect on the airfoil due to alteration of the external flow. This induced camber effect due to the LoSB results in the increased and more accurate lift predictions by the κ–κ_L–ω model.

The skin friction coefficient on the airfoil upper surface is illustrated in Fig. 8. Here, the predictions from the two models are compared at two representative angles. The distribution clearly depicts the location of laminar separation, turbulence onset, turbulent reattachment and turbulent separation, as predicted by the two models. The κ–κ_L–ω model predicts a slightly earlier laminar separation and transition onset compared to the γ–Re_θ model. However, notice that the 'strength' of the transition, the gradient of C_f curve after the transition onset, is more subtle for the κ–κ_L–ω model. This leads to a delayed reattachment compared to that predicted by the γ–Re_θ model and, therefore, a larger bubble is observed in this case. Note that the as the angle of attack increases, the bubble starts to migrate upstream due to an earlier laminar separation caused by increased adverse pressure gradients.

The upstream migration of the LoSB on the airfoil surface as a function of increasing angle of attack is presented in Fig. 9. Here the velocity vectors of the mean-flow about the airfoil at selected angles of attack, calculated using the two turbulent models, are illustrated. Furthermore, the locations of laminar separation (LS), turbulent reattachment (TR) and the subsequent turbulent separation at higher angles are also illustrated. For the κ–κ_L–ω model, it can be observed from Fig. 9 that at zero degrees, after laminar separation, the boundary layer does not reattach. On the other hand,

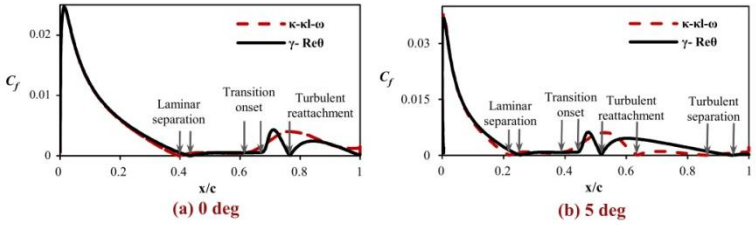

Fig. 8. Comparison of skin friction coefficient at the upper surface of the airfoil as predicted by the two transition models.

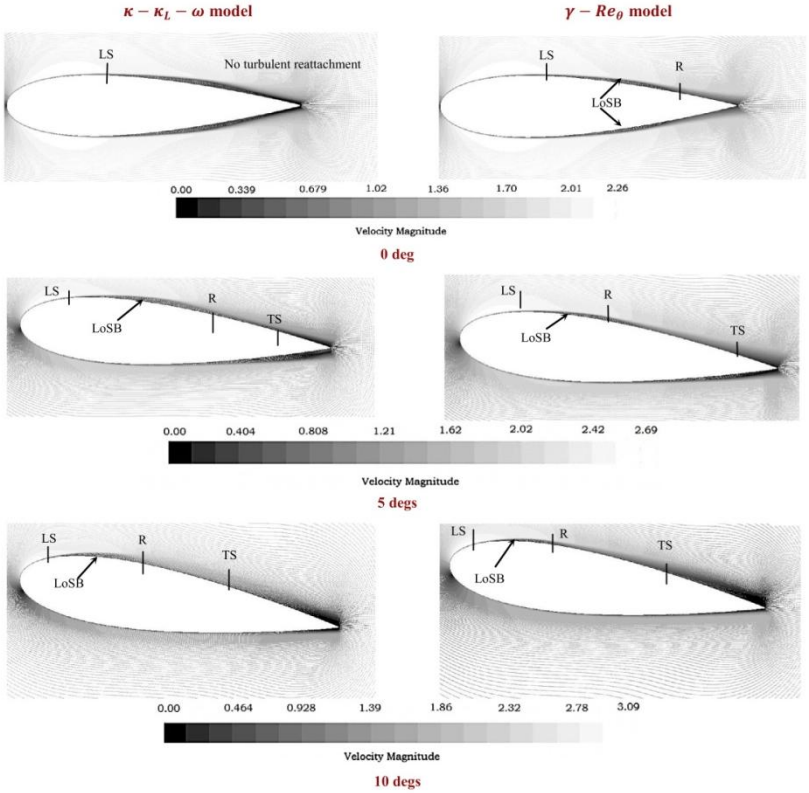

Fig. 9. Velocity vectors at selected incidences illustrating the LoSB on the NACA 0021 airfoil. The left column shows the vectors for the κ–κ_L–ω model and the right column shows the same for the γ–Re_θ model. The locations of laminar separation (LS) followed by turbulent reattachment (R) and the subsequent turbulent separation (TS) at higher angles are also marked for the upper surface of the airfoil.

for the γ–Re_θ model, the separated shear layer reattaches near the trailing edge of the airfoil resulting in the formation of the LoSB even at the zero angle of incidence. This is primarily due to the artificial turbulence generated at the onset of turbulence, as stated earlier. As the angle of attack increases, the adverse pressure gradients increase near the leading edge of the airfoil causing earlier separation of the laminar boundary layer. The increased levels of turbulence at the higher angles aid in boundary layer transition, which leads to an earlier reattachment. Therefore, the bubble length decreases as the bubble migrates upstream with the increase in the angle of attack.

A close-up view of the LoSB at an angle of attack of 10°, computed by the two models, is presented in Fig. 10 where the velocity vectors have been overlapped with the contours of turbulence intensity. Here, it can be observed quite clearly that the κ–κ_L–ω model predicts a gradual increase in turbulence levels as the transition process begins, compared to the abrupt increase in the turbulence intensity predicted by γ–Re_θ model. This abrupt increase

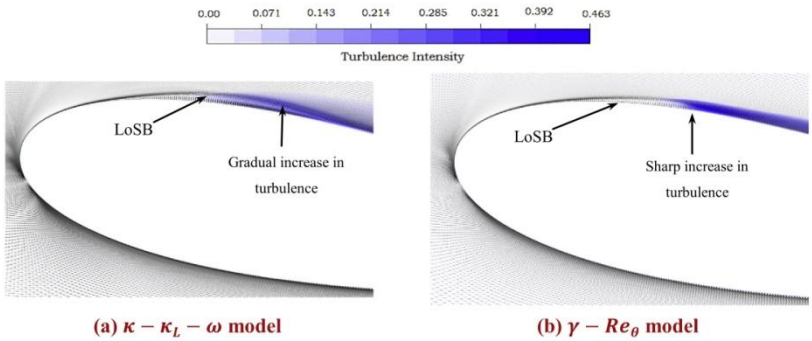

Fig. 10. A close-up view of the LoSB as computed by the two models on the NACA 0021 airfoil at an angle of attack of 10°. The height of the separated shear layer enclosing the LoSB can directly be observed here as being greater for the κ–κ_L–ω model compared to the γ–Re_θ model. Furthermore, the sharp rise in turbulence intensity is responsible for the rapid transition observed for the γ–Re_θ model.

in the turbulence levels allows faster transition of the separated shear layer and hence leads to the earlier reattachment predicted by the γ–Re_θ model, as explained before. Furthermore, due to the earlier reattachment, the height of the separated shear layer is visibly smaller as compared to height predicted by the κ–κ_L–ω model. Therefore, the bubble thickness, computed by the κ–κ_L–ω model, is also larger, leading to greater influence on the airfoil performance.

The separation of the laminar boundary layer, turbulent reattachment and the subsequent separation of the turbulent boundary layer have been determined using the wall shear stress, and reaffirmed using the surface pressure distributions on the airfoil. These are illustrated in Fig. 11 as a function of the angle of attack for both models. Here, it can clearly be observed that the γ–Re_θ model predicts an earlier reattachment of the detached shear layer as compared to the κ–κ_L–ω model leading to a smaller bubble extent. Furthermore, the γ–Re_θ model predicts turbulent separation for an extended range of angles as compared to the κ–κ_L–ω model. The artificial production of turbulence in the γ–Re_θ, after laminar separation, results in a stronger turbulent boundary layer at reattachment. The outcome is higher mixing and exchange of momentum that leads to the prediction of a turbulent boundary layer that is comparatively less prone to re-separation, in comparison with the κ–κ_L–ω model. This behaviour also causes the gradual stall prediction of the γ–Re_θ model as compared to the κ–κ_L–ω model which calculates, a more accurate, abrupt stall behaviour of the airfoil at such conditions.

A direct visual to gauge the extent of the bubble predicted by the two models is illustrated in Fig. 12 where the length of the LoSB

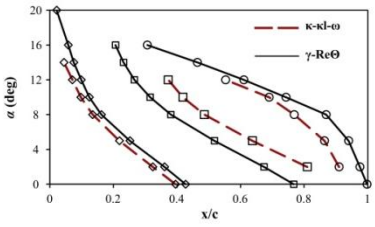

Fig. 11. Location of the laminar separation (◇), turbulent reattachment (□) and turbulent separation (○) points on the NACA 0021 airfoil at a Reynolds number of 120,000 and Tl_{LE} of 0.6% as a function of angle of attack.

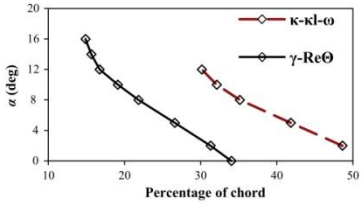

Fig. 12. Extent of the separation bubble predicted by the two models at a Reynolds number of 120,000 and Tl_{LE} of 0.6% as a function of the angle of attack.

is presented as a function of angle of attack. It can be observed that the γ–Re_θ model predicts the separation bubble extent to be an average of 15% shorter compared to the κ–κ_L–ω model. The bubble, therefore, does not affect the flow to such a high degree.

Based on these discussions, it can be inferred that the κ–κ_L–ω model is superior in its predictions of the LoSB as compared to the γ–Re_θ model. Therefore, in the subsequent analysis of the LoSB on a two-dimensional thick airfoil section, the κ–κ_L–ω model is employed.

4. The long separation bubble

4.1. General characteristics

The general flow structure of a long separation bubble is similar to that of a short one apart from a few dissimilarities as shown in Fig. 13. The most prominent of these is that when, due to adverse pressure gradient, the laminar boundary layer separates, it spans a considerably larger distance prior to complete transition. The low entrainment rate of the dominantly laminar shear layer results in an extended region of trapped slow-moving or 'dead' flow. The extended dead flow region causes the zero pressure gradients observed in the pressure distributions around thick airfoils such as those shown in Fig. 7. As the downstream distance increases, the transition is initiated in the detached shear layer which results in increased entrainment and larger mixing. Further downstream, as the transition process completes, the detached shear layer starts to converge towards the airfoil surface resulting in a region of weak flow recirculation. The recirculating zone immediately after the dead air region is also of significant length compared to the ones observed in short bubbles. The detached shear layer is now effectively turbulent and leads to higher entrainment, larger Reynolds

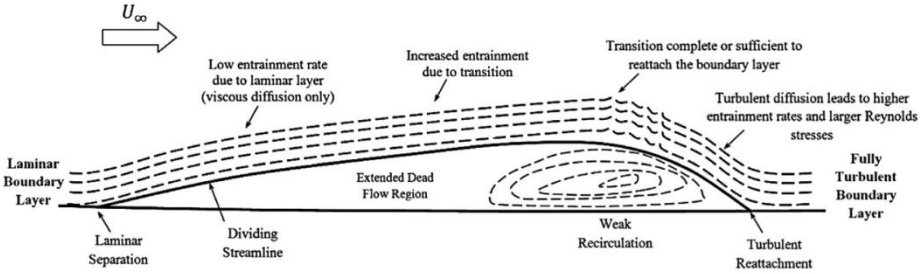

Fig. 13. General characteristics of a long separation bubble on a thick airfoil section.

stresses and streamline curvature as shown by Kelso et al. (1993). Finally, the detached shear layer attaches to the airfoil surface as a fully turbulent boundary layer resulting in the formation of the long separation bubble.

The long bubble, therefore, interacts with the external flow for a considerable length and alters the aerodynamic behaviour of the airfoil, primarily inducing a camber effect. A similar camber effect has been observed by the present authors in the works of Mueller and Batil (1982), Bastedo and Mueller (1986) and by Laitone (1997) for other thick airfoils operating at low Reynolds numbers. It can be observed from Fig. 11 that as the angle of attack increases, the bubble moves upstream due to earlier separation caused by the increased pressure gradients near the leading edge and earlier reattachment caused by the increased levels of disturbance at higher angles. As postulated by Von Doenhoff (1938), the separated flow proceeds tangent to the surface at the point of separation. Therefore, an increase in the angle of attack results in the increase in the separation angle of the shear layer resulting in the increase in the bubble thickness O'Meara and Mueller (1987) and hence the associated camber effect. Therefore, as the bubble moves towards the leading edge of the airfoil, the associated lift benefit increases since an airfoil with maximum camber point close to the leading edge produces higher lift (Hansen, 2012). However, it is important to note that the associated lift benefits are accompanied by drag penalties such that the overall lift-to-drag ratio is degraded due to the presence of the bubble. This is discussed further in the following sections.

4.2. Effects of Reynolds number

Simulations were conducted to understand the global bubble behaviour as a function of the Reynolds number. The Reynolds number was varied while TI_{LE} was kept constant at approximately 0.6%. As before, the separation of the laminar boundary layer, turbulent reattachment and the separation of the turbulent boundary layer were extracted using the wall shear stresses and pressure distributions on the airfoil. These are represented as the dotted, full and dashed lines respectively in Fig. 14. It can be observed that an increase in the Reynolds number results in significant changes in the overall bubble extent and the behaviour of the turbulent separation point. The following salient features can be observed:

- *Laminar separation*: As the Reynolds number increases, there is a delay in the laminar separation and the airfoil, therefore, experiences a larger laminar zone of reduced skin friction. However, at higher angles there is no noticeable influence of the Reynolds number on the laminar separation point.
- *Turbulent reattachment*: The increase in Reynolds number results in an accelerated transition process that causes earlier reattachment of the turbulent shear layer. Therefore, the turbulent reattachment point moves upstream as the Reynolds number is increased. This leads to a considerable reduction in the length of the separation bubble as the Reynolds number is increased.
- *Turbulent separation*: The increase in Reynolds number also tends to delay the separation of the turbulent boundary layer. This implies that the bubble itself has a little influence on the stall behaviour of the airfoil at larger Reynolds numbers.

Therefore, an increase in the Reynolds number substantially improves the airfoil performance in terms of a delay in stall and an increase in the maximum lift attainable.

A direct comparison of the lift-to-drag ratios and the extent of the bubble as a function of Reynolds number can be seen in Fig. 15. It can be observed that an increase in Reynolds number results in a significant decline in the extent of the separation bubble. As expected, an increase in the angle of attack further shrinks

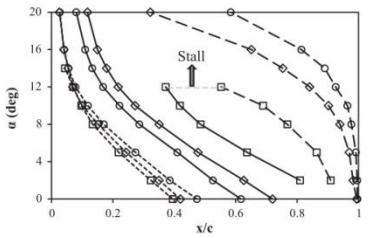

Fig. 14. Locations of the laminar separation (dotted), turbulent reattachment (solid) and turbulent separation (dashed) points at a constant TI_{LE} of 0.61% as a function of Reynolds number (□ – 120,000, ◇ – 250,000, ○ – 500,000).

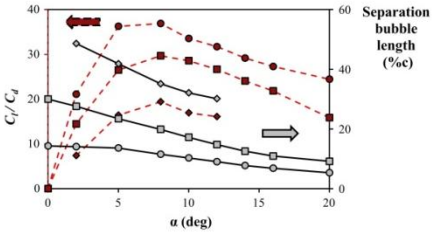

Fig. 15. Extent of the long separation bubble represented as a percentage of the chord length (solid lines) and consequent effect on the airfoil lift-to-drag ratio (dashed lines) as a function of Reynolds number (◇ – 120,000, □ – 250,000, ○ – 500,000).

the bubble. At the highest Reynolds number of 500,000, there is an abrupt change in the length of the separation bubble observed from 5° to 8°. The increase in Reynolds number, therefore, leads to a substantial reduction in the bubble size and limits it negative influences on the airfoil. It is important to note however that it is not possible in the current case to isolate the effects of the bubble on the airfoil performance from the effects of the increasing Reynolds number. Therefore, a direct estimate of the effects of the bubble is only possible with a study of influence of turbulence intensity on the bubble as presented in the following section.

4.3. Effects of turbulence intensity

Simulations were conducted at selected angles of attack from 0° to 20° in order to understand the effects of turbulence intensity on the global characteristics of the large separation bubble on the NACA 0021 airfoil at a Reynolds number of 120,000. The sensitivity of the bubble on the suction side of the airfoil as a function of Tl_{LE} are summarized in Fig. 16 where the laminar separation, turbulent reattachment and turbulent separation are shown as dotted, full and dashed lines respectively. The following salient features can be observed:

- *Laminar separation*: A delay in laminar separation occurs as the turbulence intensity is increased, resulting in a larger laminar zone. On the other hand, as the angle of attack increases, the laminar separation point moves upstream as expected for all cases. However, there is negligible effect of turbulence intensity on the laminar separation point location at high angles of attack.
- *Turbulent reattachment*: The turbulent reattachment point moves upstream as the turbulence intensity is increased, indicating that the transition process is considerably hastened due to the increase in the ambient turbulence intensity. This results in a comparatively smaller bubble on the suction side of the airfoil.
- *Turbulent separation*: The turbulent separation point moves downstream as the turbulence levels are increased resulting in delayed separation. On the other hand, as the angle of attack is increased, the turbulent separation point moves upstream under the influence of larger adverse pressure gradients.

The extent of the bubble and the consequent effects on the airfoil lift-to-drag ratio are illustrated in Fig. 17. It can be observed here that as the angle of attack increases, the size of the separation bubble decreases following an approximately similar pattern for all cases of Tl_{LE}. For the largest Tl_{LE} case, however, a slight abruption in the extent of the separation bubble is observed, showing similar behaviour to the study of Bastedo and Mueller for the Wortmann

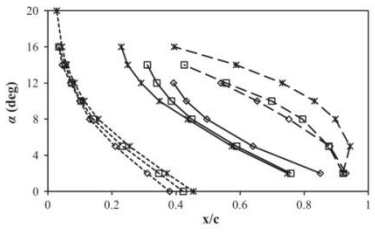

Fig. 16. Locations of laminar separation (dotted), turbulent reattachment (solid) and turbulent separation (dashed) points on the NACA 0021 airfoil at a Reynolds number of 120,000 as a function of Tl_{LE} (◇ – 0.375%, □ – 1.1%, ✱ – 2.75%).

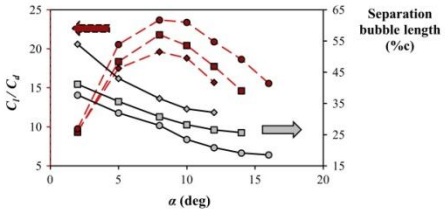

Fig. 17. Extent of the long separation bubble represented as a percentage of the chord length (solid lines) and consequent effect on the airfoil lift-to-drag ratio (dashed lines) as a function of Tl_{LE} (◇ – 0.375%, □ – 1.1%, ○ – 2.75%).

FX63-137 airfoil (Bastedo and Mueller, 1986). The abrupt change in the extent occurs primarily due to the upstream movement of the turbulent reattachment point due to an increase in the accumulated ambient disturbances. However, unlike Bastedo and Mueller, we do not classify the bubble as a short separation bubble since it still encompasses a considerable portion of the airfoil chord.

The lift-to-drag ratio (C_l/C_d) of the airfoil as a function of turbulence intensity is also presented in Fig. 17 in order to directly compare the effects of the bubble extent on the airfoil performance. It can be observed from the plot that the angle of maximum C_l/C_d is not influenced by the increase in the turbulence levels. However, a considerable improvement in the magnitude of maximum C_l/C_d can be observed as the extent of the bubble decreases. An approximate decrease in the bubble extent of 9% leads to an improvement of around 17% in the maximum C_l/C_d. The increase in ambient turbulence also results in an increase in the airfoil stall angle of attack. This primarily results from the greater mixing in the turbulent boundary layer which can then withstand the adverse pressures for larger extents.

A supplementary study was conducted at a Reynolds number of 120,000 in order to observe the airfoil performance without the presence of a separation bubble. In experiments, this can be accomplished by tripping the flow over the airfoil or by adding leading-edge roughness to make the boundary layer turbulent. However, in a numerical analysis, this would require significant re-meshing and re-modelling of the flow. Alternatively, the γ–Re_θ model can be used to add roughness on the airfoil using user-defined-functions in the software. But, since the model has been deemed unsatisfactory for the simulating the bubble behaviour, it has not been employed at this stage. Therefore, the κ–κ_L–ω model was applied to simulate the flow at a sufficiently large turbulence intensity, in order to achieve a similar effect. The large increase in turbulence intensity at the leading edge of the airfoil aids in rapid transition of the attached flow, similar to the effects of distributed roughness strips. However, the drag in this case is expected to be higher compared to the imposed by-pass transition observed with roughness elements. For the supplementary study, a Tl_{LE} of 15% was found adequate to mitigate the presence of the bubble at all angles of attack.

Simulations at these conditions were conducted at the selected angles and the variation of lift-to-drag ratio as a function of angle of attack is presented in the Fig. 18. It can be noticed that, although the overall lift-to-drag ratio of the airfoil is reduced due to an increase in the turbulence intensity, there is a considerable improvement in the stall angle of attack. The lift-to-drag ratio is slightly degraded due to a large increase in the drag of the airfoil at such high turbulence levels. Furthermore, the camber effect associated with the bubble, described earlier, also disappears in this case due to the absence of the bubble. The increase in the airfoil stall angle of attack also occurs due to the turbulent boundary layer being more resistant to separation. Consequently, the airfoil

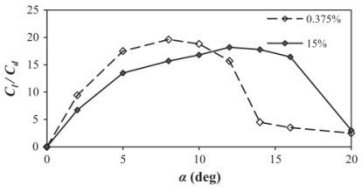

Fig. 18. Comparison of the airfoil performance at different Tl_{LE}.

does not undergo an abrupt stall due to the bursting of the bubble and instead experiences a progressive trailing edge stall. It can be observed that the mitigation of the bubble leads to an approximately 33% increase in the stall angle of attack.

Therefore, the decrease in the bubble extent considerably improves the performance of the airfoil by increasing the laminar zone, thus reducing the drag, and improving the overall lift-to-drag ratio due to a smaller bubble. The most practical benefit of a reduced bubble extent is the increase in the stall angle of attack. Therefore, for application involving low Reynolds numbers and turbulence intensities flows, such as MAVs and small wind turbines, the use of appropriate tripping techniques or the addition of roughness strips near the leading edge of thick airfoils would improve the performance, stability and operation of the device by diminishing the effects of the LoSB.

5. Conclusion

The flow around a two-dimensional NACA 0021 airfoil was calculated at low Reynolds numbers and turbulence intensities to study the long separation bubble and its effects on the airfoil performance. In the present article, two transition models, the correlation-based intermittency model developed by Menter et al. (2006) and the laminar-kinetic-energy model proposed by Walters and Cokljat (2008), were first evaluated based on the criteria established by Zingg and Godin (2009) for turbulence model assessment in order to ensure the accuracy and validity of the study presented in the article. Steady-state simulations of the airfoil were conducted in order to obtain the mean behaviour of the separation bubble and its effects on the airfoil performance. It was observed that both the γ–Re_θ model and the κ–κ_L–ω model were able to predict the laminar boundary layer separation and the point of transition to some extent. However, due to the generation of additional turbulence, the γ–Re_θ model predicted earlier reattachment as compared to the κ–κ_L–ω model and the experiments. This is primarily because the model has been calibrated for small separation bubbles observed in turbomachinery environments. The γ–Re_θ model relies heavily on empiricism and therefore suffers from a lack of universality. Therefore, the κ–κ_L–ω model was deemed more suitable for studies related to the separation bubble on thick airfoil sections operating at low Reynolds numbers and small turbulence intensities.

Simulations were conducted using the κ–κ_L–ω model at several turbulence levels and Reynolds numbers to study the characteristics of the long separation bubble and its effects on the NACA 0021 airfoil over a range of angles. The global features of the long separation bubble were studied by evaluating the locations of the points of laminar separation and turbulent reattachment. It was observed that the extent of the bubble decreases as the angle of attack, Reynolds number or freestream turbulence levels are increased. The bubble, due to its significant extent, had a profound impact on the performance of the airfoil. Of particular note is the induced camber effect on the airfoil that leads to a higher lift generation, but with the cost of increased drag. The overall lift-to-drag ratio of the airfoil, therefore, was degraded due to the presence of the bubble. An increase in the Reynolds number or the turbulence intensity resulted in the decrease of the bubble extent, thereby considerably improving the performance of the airfoil. The presence of the bubble and alteration of flow in the immediate vicinity of the airfoil can also be translated to similar effects observed on pitching airfoils undergoing dynamic stall. In this case, the large-scale vorticity can lead to changes in the camber and thickness of airfoils and, therefore, cause the non-linearity observed in the airfoil lift during the pitching cycle (Choudhry et al., 2014).

The present study demonstrates that large separation bubbles degrade the performance of airfoils to a significant extent by decreasing the overall lift-to-drag ratio and incurring abrupt stall. It was observed that an approximate decrease in the bubble extent of 9% leads to an improvement in the lift-to-drag ratio of about 17%. Furthermore, the complete mitigation of the bubble, due to increase of turbulence levels, resulted in the increase of the stall angle of attack by approximately 33%. This confirms the need for the addition of roughness elements or tripping devices near the leading edges of thick airfoil sections for application involving low Reynolds numbers and turbulence intensities flows such as those encountered in MAVs and small wind turbines. Such a measure will improve the performance and stability of the airfoil by reducing the effects of the LoSB on the thick airfoil and significantly improve the operation of the device.

References

Abu-Ghannam, B., Shaw, R., 1980. Natural transition of boundary layers—the effects of turbulence, pressure gradient, and flow history. J. Mech. Eng. Sci. 22, 213–228.
Alam, M., Sandham, N., 2000a. Direct numerical simulation of 'short'laminar separation bubbles with turbulent reattachment. J. Fluid Mech. 410, 1–28.
Alam, M., Sandham, N.D., 2000b. Direct numerical simulation of 'short'laminar separation bubbles with turbulent reattachment. J. Fluid Mech. 403, 223–250.
Bak, C., Aagaard Madsen, H., Fuglsang, P., Rasmussen, F., 1998. Double stall.
Bastedo, W.G., Mueller, T., 1986. Spanwise variation of laminar separation bubbles on wings at low Reynolds number. J. Aircraft. 23, 687–694.
Bursnall, W.J., Loftin, L.K., 1951. Experimental investigation of localized regions of laminar-boundary-layer separation. National Advisory Committee for Aeronautics.
Butler, R.J., Byerley, A.R., VanTreuren, K., Baughn, J.W., 2001. The effect of turbulence intensity and length scale on low-pressure turbine blade aerodynamics. Int. J. Heat Fluid Flow 22, 123–133.
Cao, N., 2010. Effects of turbulence intensity and integral length scale on an asymmetric airfoil at low Reynolds numbers.
Choudhry, A., Leknys, R., Arjomandi, M., Kelso, R., 2014. An insight into the dynamic stall lift characteristics. Exp. Thermal Fluid Sci. 58, 188–208.
Crabtree, L., 1959. The Formation of Regions of Separated Flow on Wing Surfaces. HM Stationery Office.
Galbraith, M., Visbal, M., 2008. Implicit large eddy simulation of low Reynolds number flow past the SD7003 airfoil. AIAA Paper 225, 2008.
Gaster, M., 1966. Structure and behavior of laminar separation bubbles. AGARD CP 4, 813–854.
Gaster, M., 1969. The Structure and Behaviour of Laminar Separation Bubbles. HM Stationery Office.
Hansen, KL., 2012. Effect of leading edge tubercles on airfoil performance.
Hansen, K.L., Kelso, R.M., Dally, B.B., 2011. Performance variations of leading-edge tubercles for distinct airfoil profiles. AIAA J. 49, 185–194.
Horton HP. Laminar separation bubbles in two and three dimensional incompressible flow, 1968.
Jacobs, E.N., 1932. The Aerodynamic Characteristics of Eight Very Thick Airfoils from Tests in the Variable Density Wind Tunnel. National Advisory Committee for Aeronautics.
Katz, J., Plotkin, A., 1991. Low-Speed Aerodynamics: from Wing Theory to Panel Methods. McGraw-Hill, Singapore.
Kelso, R., Lim, T., Perry, A., 1993. The effect of forcing on the time-averaged structure of the flow past a surface-mounted bluff plate. J. Wind Eng. Ind. Aerodyn. 49, 217–226.
Klebanoff, P., 1971. Effect of free-stream turbulence on the laminar boundary layer. Bull. Am. Phys. Soc. 10, 1323.
Laitone, E., 1997. Wind tunnel tests of wings at Reynolds numbers below 70 000. Exp. Fluids 23, 405–409.
Langtry, R., Menter, F., 2005. Transition modeling for general CFD applications in aeronautics. AIAA Paper 522, 2005.
Langtry, R.B., Menter, F., Likki, S., Suzen, Y., Huang, P., Völker, S., 2006. A correlation-based transition model using local variables-Part II: test cases and industrial applications. J. Turbomach. 128, 423–434.

Lian, Y., Shyy, W., 2007. Laminar-turbulent transition of a low Reynolds number rigid or flexible airfoil. AIAA J. 45, 1501–1513.
Lin, J.M., Pauley, L.L., 1996. Low-Reynolds-number separation on an airfoil. AIAA J. 34, 1570–1577.
Lissaman, P., 1983. Low-Reynolds-number airfoils. Annu. Rev. Fluid Mech. 15, 223–239.
Marxen, O., Rist, U., Wagner, S., 2004. Effect of spanwise-modulated disturbances on transition in a separated boundary layer. AIAA J. 42, 937–944.
Menter, F.R., 1994. Two-equation eddy-viscosity turbulence models for engineering applications. AIAA J. 32, 1598–1605.
Menter, F.R., 2011. Turbulence Modeling for Engineering Flows. ANSYS Inc.
Menter, F., Esch, T., Kubacki, S. Transition modelling based on local variables. In: Proceedings of the 5th International Symposium on Engineering Turbulence Modeling and Measurements, 2002.
Menter, F., Langtry, R., Likki, S., Suzen, Y., Huang, P., Völker, S., 2006. A correlation-based transition model using local variables-Part I: model formulation. J. Turbomach. 128, 413–422.
Mueller, T.J., Batil, S.M., 1982. Experimental studies of separation on a two-dimensional airfoil at low Reynolds numbers. AIAA J. 20, 457–463.
Nakano, T., Fujisawa, N., Oguma, Y., Takagi, Y., Lee, S., 2007. Experimental study on flow and noise characteristics of NACA0018 airfoil. J. Wind Eng. Ind. Aerodyn. 95, 511–531.
Narasimha, R., 1985. The laminar-turbulent transition zone in the boundary layer. Prog. Aerosp. Sci. 22, 29–80.
Ol, M.V., McAuliffe, B.R., Hanff, E.S., Scholz, U., Kähler, C., 2005. Comparison of laminar separation bubble measurements on a low Reynolds number airfoil in three facilities. AIAA Paper 5149, 2005.
O'Meara, M., Mueller, T., 1987. Laminar separation bubble characteristics on an airfoil at low Reynolds numbers. AIAA J. 25, 1033–1041.
Owen, P., Klanfer, L., 1953. On the laminar boundary layer separation from the leading edge of a thin aerofoil. Defense Tech. Inform. Center.
Pauley, L.L., Moin, P., Reynolds, W.C., 1990. The structure of two-dimensional separation. J. Fluid Mech. 220, 397–411.
Radespiel, R.E., Windte, J., Scholz, U., 2007. Numerical and experimental flow analysis of moving airfoils with laminar separation bubbles. AIAA J. 45, 1346–1356.
Raghunathan, S., Harrison, J., Hawkins, B., 1988. Thick airfoil at low Reynolds number and high incidence. J. Aircraft. 25, 669–671.
Sanders, DD., 2009. CFD Modeling of Separation and Transitional Flow in Low Pressure Turbine Blades at Low Reynolds Numbers. Virginia Polytechnic Institute and State University.
Suluksna, K., Juntasaro, E., 2008. Assessment of intermittency transport equations for modeling transition in boundary layers subjected to freestream turbulence. Int. J. Heat Fluid Flow 29, 48–61.
Swalwell, K., Sheridan, J., Melbourne, W., 2001. The effect of turbulence intensity on stall of the NACA 0021 aerofoil. In: Proceedings 14th Australasian Fluids Mechanics Conference. Adelaide, Adelaide University, p. 941–944.
Swift, KM., 2009. An Experimental Analysis of the Laminar Separation Bubble at Low Reynolds Numbers.
Tani, I., 1939. Note on the interplay between the laminar separation and the transition from laminar to turbulent of the boundary layer (In Japanese). J. Soc. Aero. Sci. Japan 6, 122–134.
Tani, I., 1961. Critical Survey of Published Theories on the Mechanism of Leading-Edge Stall. Aeronautical Research Institute.
Tani, I., 1969. Boundary-layer transition. Annu. Rev. Fluid Mech. 1, 169–196.
Turner, C., 2012. Laminar Kinetic Energy Modelling for Improved Laminar-Turbulent Transition Prediction. The University of Manchester.
Volino, R., 1998. A new model for free-stream turbulence effects on boundary layers. J. Turbomach. 120, 613–620.
Von Doenhoff, A.E., 1938. A Preliminary Investigation of Boundary-Layer Transition Along a Flat Plate With Adverse Pressure Gradient. National Advisory Committee for Aeronautics.
Walters, D.K., Cokljat, D., 2008. A three-equation eddy-viscosity model for Reynolds-averaged Navier-Stokes simulations of transitional flow. J. Fluids Eng. 130, 121401.
Walters, D.K., Leylek, J.H., 2004. A new model for boundary layer transition using a single-point RANS approach. Trans. ASME-T-J. Turbomachinery 126, 193–202.
Walters, D.K., Leylek, J.H., 2005. Computational fluid dynamics study of wake-induced transition on a compressor-like flat plate. J. Turbomach. 127, 52–63.
Windte, J., Scholz, U., Radespiel, R., 2006. Validation of the RANS-simulation of laminar separation bubbles on airfoils. Aerosp. Sci. Technol. 10, 484–494.
Zhang, W., Hain, R., Kähler, C.J., 2008. Scanning PIV investigation of the laminar separation bubble on a SD7003 airfoil. Exp. Fluids 45, 725–743.
Zingg, D., Godin, P., 2009. A perspective on turbulence models for aerodynamic flows. Int. J. Comput. Fluid Dynam. 23, 327–335.

CHAPTER 6

INSIGHT INTO THE DYNAMIC STALL PROCESS

6.1 Chapter Overview

The present chapter provides a detailed discussion of the lift behavior of a thick NACA 0021 airfoil undergoing constant pitch-rate dynamic stall. The discussion is based on a combination of experimental results, both pressure measurements and flow visualization, and the review of some of the most seminal works performed in the subject. Initially, the effects of different flow conditions on the dynamic stall process are investigated. In this study, the precursor to dynamic stall is defined, based on experimental observations. Moreover, the effects of reduced frequency on the maximum lift, the effects of Reynolds number on the process, and the effects of airfoil profile have been explored. Furthermore, a detailed

insight into the lifting behavior of airfoils undergoing unsteady separation has been presented. This is accomplished by a sub-categorization of the lift-curve into smaller segments and an analysis of each segment separately. Based on this study, it is shown that the primary dynamic stall vortex causes the severe stall that is observed on an airfoil during unsteady separation. It is, furthermore, concluded that the intensity of this stall increases as the reduced frequency or Reynolds number increase.

The article that constitutes this chapter has been published in the Experimental Thermal and Fluid Sciences and is presented in the next section.

6.2 Dynamic Stall Lift

Statement of Authorship

Title of Paper	An Insight into the Dynamic Stall Lift Characteristics
Publication Status	⦿ Published, ○ Accepted for Publication, ○ Submitted for Publication, ○ Publication style
Publication Details	Choudhry, A., Leknys, R., Arjomandi, M., & Kelso, R. An Insight into the Dynamic Stall Lift Characteristics. Experimental Thermal and Fluid Science, DOI: http://dx.doi.org/10.1016/j.expthermflusci.2012.07.006.

Author Contributions

By signing the Statement of Authorship, each author certifies that their stated contribution to the publication is accurate and that permission is granted for the publication to be included in the candidate's thesis.

Name of Principal Author (Candidate)	Amanullah Choudhry		
Contribution to the Paper	Designed and carried out the experiment, interpreted data, developed ideas, wrote the manuscript, wrote the rebuttal, acted as the corresponding author		
Signature		Date	

Name of Co-Author	Ryan Leknys		
Contribution to the Paper	Assisted in experiment, extracted flow visualization images, developed ideas		
Signature		Date	

Name of Co-Author	Maziar Arjomandi		
Contribution to the Paper	Supervised the work, helped in developing ideas, manuscript evaluation		
Signature		Date	

Name of Co-Author	Richard Kelso		
Contribution to the Paper	Supervised the work, helped in developing ideas, manuscript evaluation		
Signature		Date	

Experimental Thermal and Fluid Science 58 (2014) 188–208

Contents lists available at ScienceDirect

Experimental Thermal and Fluid Science

journal homepage: www.elsevier.com/locate/etfs

An insight into the dynamic stall lift characteristics

Amanullah Choudhry *, Ryan Leknys, Maziar Arjomandi, Richard Kelso

School of Mechanical Engineering, The University of Adelaide, Adelaide, South Australia 5005, Australia

ARTICLE INFO

Article history:
Received 12 April 2014
Received in revised form 15 July 2014
Accepted 15 July 2014
Available online 24 July 2014

Keywords:
Dynamic stall
Stall intensity
Unsteady lift
Constant pitch
Thick airfoil

ABSTRACT

The article presents an insight into the dynamic stall lift characteristics through experimental work and a detailed survey of the seminal articles related to the phenomenon. Of particular interest is the dynamic stall observed on lifting surfaces as they undergo high-rate pitching motions at constant speeds up to a predetermined maximum angle of attack. The effects of several contributing parameters, such as the reduced frequency, Mach and Reynolds numbers of operation and the airfoil geometry, have been investigated. In addition, the behavior of the lift curve slope for an airfoil undergoing constant pitch dynamic stall has been analyzed in detail to gain a better understanding of the mechanism for the unsteady case. The unsteady lift-curve has been broken down into stages and each stage has been analyzed separately. The aim is to obtain a deeper insight into the lift generation mechanism involved in unsteady motion of the airfoil in order to improve the design of flow control techniques to exploit the dynamic stall process for a large range of applications.

1. Introduction

Dynamic stall and its associated effects are one of the most critical factors that limit the design and operation of aerodynamics-related applications such as helicopters, flapping-wing micro-air-vehicles and wind turbines. Dynamic stall can be considered as the delay of conventional flow separation on wings and airfoils caused by rapid variations in the angle of attack beyond the critical static stall angle due to virtually any kind of unsteady motion [8]. The unsteady motion, including pitching, plunging, heaving or a combination of these, results in the generation of intense vorticity on the suction side of the airfoil which is accompanied by large excursions in lift, drag and pitching moments, well beyond those observed during steady-state operation [9,17].

The unsteady effects associated with the rapid variations of the angle of attack of an airfoil were first observed by Kramer [41]. However, after this initial study, due to its limited perceived applicability at the time, little attention was given to the problem till it was identified on retreating blades of helicopters in the 1960s [28,31]. Due to the abrupt pitching moment excursions, the phenomenon has posed severe restrictions on the flight envelopes and attainable performance of the vehicle as well as imposing high demands on the material selection for the blade. Dynamic stall has also been observed on wind turbine blades [13,21,75], where it limits the performance of the turbines and negatively affects the fatigue life of the blades [80], thereby increasing the operation and maintenance costs. In wind turbines, dynamic stall has been observed to be caused by unsteady inflow, gusts, rapid changes in wind direction and yawed operation [13,76,81]. Furthermore, for conventional fixed-winged aircraft, vertical convections of large-scale air-masses can also induce dynamic stall on the wings during operation in the lower atmosphere resulting in turbulence, large fatigue loads and passenger discomfort. One aspect of dynamic stall research has, therefore, been motivated to principally avoid or suppress, to some extent, the coupled unsteady effects of the phenomenon [8,17,40,42,46,55,58].

In contrast to the above, research is also being directed towards efficient control of dynamic stall to take advantage of the increased lift. This new-found interest primarily stems from the study of bird and insect flight. Flapping motion is the major mode of locomotion for the flying insects and birds, and the swimming of fish [50,93]. It has been observed that the wing area and aspect ratio of birds and insects is generally too small in comparison to their body mass to sustain any reasonable steady-state flight [82]. Therefore, it is believed that birds and insects take advantage of the dynamic stall effects such as the high magnitude of unsteady lift to sustain their flights [49]. The high manoeuvrability of flying animals has also piqued interest in improving the manoeuvrability of fighter jets through exploiting the unsteady aerodynamic effects of dynamic stall. However, unlike the previous cases where sinusoidal oscillations are commonly encountered and studied, focus on aircraft manoeuvrability enhancements [43,64] has directed the research attention towards airfoil pitching at constant rates to high angles

* Corresponding author. Tel.: +61 413032885.
E-mail address: amanullah.choudhry@adelaide.edu.au (A. Choudhry).

http://dx.doi.org/10.1016/j.expthermflusci.2014.07.006
0894-1777/

of attack [89]. Furthermore, recent interest in the development of micro-air-vehicles, motivated by military needs of aerial reconnaissance in confined spaces, has also increased the need in understanding of the unsteady phenomenon to exploit the high magnitudes of the lift force produced.

However, regardless of the significant progress made towards the understanding of unsteady separation in recent years, dynamic stall still remains one of the major unsolved problems in aerodynamics. A detailed understanding of the complex flow phenomenon is required for its efficient control and possible application. Therefore, the primary focus of the current article is to decipher the trends in the lift curve of an airfoil pitching at constant rates to predetermined maximum angles of attack. The choice of constant pitch rates as the principal unsteady motion inducing dynamic stall, instead of the more conventionally studied sinusoidally-pitching motions, is primarily due to the limited insight available for the former type. Consequently, an attempt has been made to highlight the fundamental aspects of dynamic stall lift using literature, theories and supplementary experimental and flow visualization studies.

2. Experimental setup

2.1. Pressure measurements

Pressure measurements were carried out on a pitching airfoil in the closed-loop KC Wind Tunnel at the University of Adelaide. The working section of the tunnel has a cross section of 0.5 m × 0.5 m as shown in Fig. 1a. The turbulence intensity of the working section was measured to be approximately 0.6%. The test Reynolds number based on the airfoil chord length was varied between 50,000 and 150,000 for the experiment.

The model selected for the study was the thick, symmetric NACA 0021 airfoil, constructed from acrylic. The airfoil was manufactured in two parts, with a total of 17 pressure taps along the mid-span based on a similar distribution to that of Jumper et al. [39]. The pressure taps were concentrated near the leading edge of the airfoil, as shown in Fig. 1b, since the largest pressure variations were expected in this region. For both the suction and pressure sides, a total of nine pressure taps were drilled in the foil surface. The chord length of the airfoil was 100 mm and the span was 495 mm, leading to an aspect ratio of 4.95 and a maximum blockage of approximately 12% at an angle of attack of 40 deg. The aspect ratio of the airfoil was considered adequate since in previous experiments [6,32,54,59], aspect ratios of generally less than 4 have been used to determine the dynamic effects on pitching airfoils. Furthermore, as indicated by Leishman [47], dynamic stall characteristics of finite-span wings are qualitatively similar to those of two-dimensional airfoils. Therefore, no corrections were applied to the results presented in the article. On the other hand, as shown by Granlund et al. [26], dynamic blockage is more benign compared to static blockage and does not influence the results to a large extent. Moreover, since at present no viable methods are available to determine wall corrections for the dynamic case, the results presented here are as measured without any corrections applied.

The airfoil was mounted vertically in the center of the working section as indicated in Fig. 1a. The bottom of the foil was connected to a heavy steel pedestal and the top was pinned to the ceiling of the working section to mitigate vibrations. The gap between the ceiling of the working section of the tunnel and the airfoil top was less than 5 mm in order to minimize three-dimensional effects due to tip vortices. This is in accord with the prescribed standards for the gap in two-dimensional studies [7] and is similar to earlier experiments performed in the tunnel [30]. The airfoil was instrumented with *TruStability*® differential pressure sensors that were board-mounted, self-calibrated and placed inside the airfoil as shown in Fig. 1b. The maximum deviation of the sensors is 0.25% from the best-fit-straight-line fitted to the output measured over the pressure range of ±1 psi. The sensors provided analogue outputs and their frequency response was defined by the sampling rate of the data acquisition system. The positive port of the differential pressure sensors were connected to the pressure taps using copper tubing and flexible plastic hoses. The length of the hoses was kept as small as possible in order to minimize any damping and phase delays in the pressure response of the system following the recommendation of Irwin et al. [33]. Even then, a slight delay of 0.05 s in the pressure response of the system was observed during initial testing, which was corrected. On the other hand, as shown by Yoshida et al. [98], the bends in the hoses have a negligible effect on the pressure measurements and were, therefore, untreated. The negative ports were connected to a reference plenum that was in turn left open to the ambient conditions to provide the freestream static pressures. The differential measurements were recorded digitally at a rate of 5000 samples per second using the *National Instruments*® USB-6210 Data Acquisition System (NI-DAQ). The differential pressures were non-dimensionalized using the dynamic pressure of the freestream, which was measured using a Pitot-static tube and the Fluke 922 Airflow meter. The airfoil was rotated about its mid-chord using a 22 mm diameter *Maxon*® brushed DC electric motor coupled with a 157:1 reduction gearbox to provide the suitable moment for the experiment. The motor reached the set rotational speed in approximately 0.03 s which was considerably smaller than the run-time for experiment. The motor was placed inside a steel frame, shown in Fig. 1c, which in turn was mounted on the heavy steel pedestal to inhibit vibrations. An electronic position encoder was connected to the motor to monitor the position and velocity. The encoder was connected to a computer-based control system which was used to provide the position and velocity information for the experiment through an in-house code developed using *NI-LabVIEW*®.

The chord-normal (C_N) and chord-axial (C_A) aerodynamic force coefficients were obtained through integration of the area between the pressure distribution curves using the following expressions:

$$C_N = -\oint C_p d\left(\frac{x}{c}\right)$$

$$C_A = \oint C_p d\left(\frac{y}{c}\right)$$

The numerical integration was performed using the trapezoidal rule for non-uniform spacing between the pressure taps following Hansen [29] as follows:

$$\int_a^b f(x)dx \approx \frac{1}{2}\sum_{k=1}^{N}(x_{k+1} - x_k)(f(x_{k+1}) + f(x_k))$$

Here, $f(x)$ is the pressure coefficient as a function of chordwise position, N is the total number of pressure taps on both the suction and pressure sides, x is the chordwise position and a, b are the stagnation pressure taps. The numerical integration was carried out in the anticlockwise direction starting from the leading edge of the airfoil forming a closed loop around the foil. Finally, the lift (C_L) and pressure drag (C_D) coefficients were determined using the coordinates transformation.

Each test case was repeated ten times in order to obtain the averaged results that are presented in this article.

2.2. Hydrogen-bubble flow visualizations

Additional investigations were carried out in this series of experiments to understand the dominant flow features during

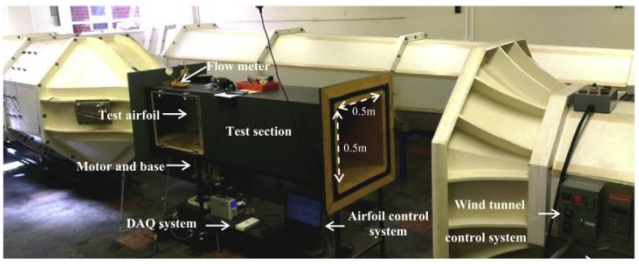

(a) The KC Wind Tunnel used for the dynamic stall experiments in the current study.

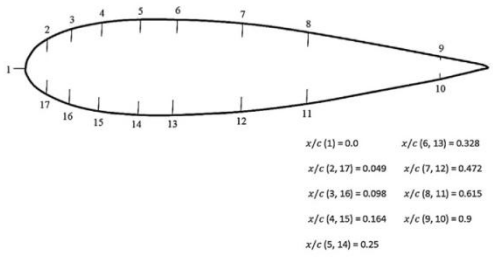

(b) Pressure tap location for the NACA 0021 airfoil used in the current experiments.

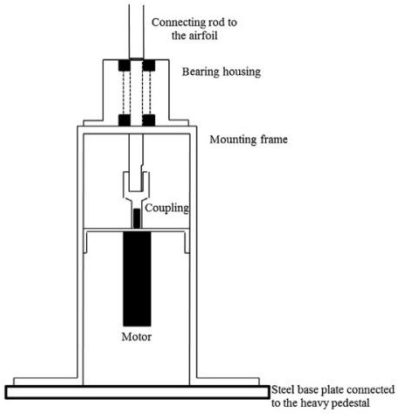

(c) Schematic diagram of the motor and base configuration used in the current experiment

Fig. 1. Experimental setup for pressure measurement on the pitching NACA 0021 airfoil.

the dynamic stall process using flow visualization with hydrogen-bubble wire. The flow visualization experiments were carried out in the 0.25 m^2 working section of a closed-return water channel at the University of Adelaide. The test Reynolds numbers, based on airfoil chord length, for the flow visualization experiments varied between 6700 and 21,000. Three different airfoil sections, the thin symmetrical NACA 0012 with small leading edge radius, the NACA 4418 which incorporated camber and increased thickness resulting in an increased leading edge radius, and finally the NREL S809 airfoil which is used predominantly in the wind turbine industry, were considered in this study. The airfoils were pitched at the quarter-chord using a similar setup to that described in the

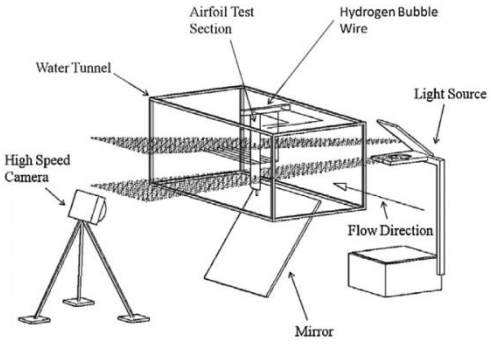

Fig. 2. Sketch of the experimental setup used for the flow visualization study.

previous section. A sketch of the experimental setup used for the flow visualization study is shown in Fig. 2. Images were acquired using a Kodak ES 1.0 digital camera that relayed the images directly to a PC. The flow was illuminated using a thin sheet of light generated by an overhead projector. The flow was visualized close to the mid-span location using a mirror positioned below the water tunnel as shown in Fig. 2.

It is important to note that, even though the attainable chord Reynolds number is significantly lower compared to the wind tunnel experiments, the large scale vortical structures produced by the pitching airfoil are largely similar for both cases. This has been shown by Erm [20] and Thompson [86] in their respective studies where flow behaviors were found to be comparable even when the Reynolds numbers were dissimilar.

3. Primary parameters

Dynamic stall is an unsteady phenomenon that occurs due to the rapid motion of an airfoil resulting in operation beyond the critical stall angle of attack of the airfoil. During dynamic stall, an increase in the lift generated by the airfoil is observed during the airfoil pitch-up and is often associated with the formation of a large vortex structure on the suction side of the airfoil, conventionally referred as the dynamic stall vortex (DSV). However, the extent to which the vortex structure contributes to the generated lift of an airfoil is not well understood. As the vortex convects downstream, the lift generated by the airfoil suddenly drops and the airfoil goes into a state of deep stall. One of the primary reasons that dynamic stall is more difficult to analyse and model, as compared to its steady-state counterpart, is its dependence on a much larger range of parameters. For the steady-state case, the parameters influencing the stall behavior are the airfoil geometry and surface finish, freestream turbulence, chord Reynolds number (R_{e_c}) and the Mach number [5]. On the other hand, even for the simpler case of forced motion of the airfoil at a constant pitch rate, understanding of dynamic stall is obscured due to dependence on many, and often interrelated [8,58], flow parameters such as compressibility and chord Reynolds number effects, the reduced frequency of oscillation and the location of pitch axis, three-dimensionality and tunnel effects as well as the geometry of the airfoil [55]. For sinusoidally-pitching airfoils, the mean and the maximum angle of attack of the oscillation cycle are also significant factors [45]. An attempt is made in the present section to summarize the current state of knowledge regarding the effects of the contributing parameters on dynamic stall.

3.1. Reduced frequency

The reduced frequency is used to describe the unsteadiness of flows over airfoils and wings [27]. It is defined as the ratio of convective time scales (c/U) and the time scale of forced oscillation ($1/\dot{\alpha}$) [16]. For an airfoil of chord length of c, pitching about the mid-chord at a constant pitch rate of $\dot{\alpha}$ (rad/s), the reduced frequency is defined as [39]:

$$\kappa = \frac{\dot{\alpha}c}{2U} \tag{1}$$

From Eq. (1), when $\kappa = 1.0$, the convective time scales and the unsteady time scales are of the same order and the flow is unsteady. However, significant differences compared to the static stall characteristics have been observed for reduced frequency values as low as 0.05 [69]. Leishman [47] reported that reduced frequency values larger than 0.05 are more critical since the unsteady aerodynamics can cause large fluctuations in the surface pressures on airfoils and wings leading to increased loads. Below this reduced frequency, the flow can be treated as quasi-steady.

However, according to Digavalli [16], the ratio of the viscous-diffusion length-scale to the airfoil-motion length-scale ($\kappa\sqrt{R_{e_c}}$) is the primary cause of the unsteady effects at such low reduced frequencies. Hence, even when $\kappa = 0.01$, this ratio may exceed 1.0 depending on the chord Reynolds number of the flow, rendering the flow as primarily unsteady from a viscous perspective. Experiments conducted by the present authors also illustrate that unsteady effects manifest at reduced frequencies as low as 0.005 ($\kappa\sqrt{R_{e_c}} > 1$) as shown in Fig. 3. However, at such low reduced frequencies, no clear peaks in lift, associated with the DSV, were observed. It can, however, be seen that there is a clear increase in the stall angle of attack and the lift produced by the airfoil. Furthermore, as shown in Fig. 3, clear presence of the dynamic stall vortex, in the form of the lift peak in lift, is observed when the reduced frequency is increased to 0.0095 or when $\kappa\sqrt{R_{e_c}} > 2$. Similar observation was made for the other Reynolds numbers in the current experiment.

It is important to emphasize here that the factor $\kappa\sqrt{R_{e_c}}$ would in most cases be greater than unity due to large Reynolds numbers of today's aerospace applications. Therefore, even small disturbances can manifest as significant unsteadiness on wings and blades. However, for experimental work, this is generally not the case due to the low freestream velocities and restriction on the chord lengths. Therefore, care must be taken to ensure that at least this condition is met during experiments to note any salient unsteady effects.

Considerable research has been conducted to understand the effects of reduced frequencies on the dynamic stall characteristics of different airfoils. It has been observed that an increase in the reduced frequency results in the delay of dynamic stall onset to larger angles of attack and a significant increase in the lift force produced by the airfoil [39,73,77]. This can be observed in the

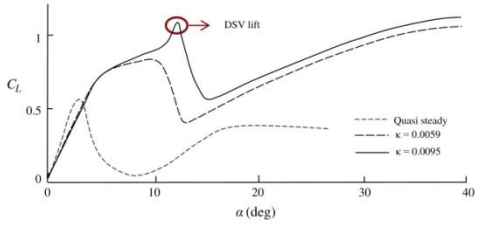

Fig. 3. Threshold reduced frequency at a Reynolds number of 50,000.

plots, shown in Fig. 4a and b, of lift coefficient vs. angle of attack for the NACA 0015 and 0021 airfoils respectively pitching at constant rates about the mid-chord.

Comparison with the steady-state case indicates that the airfoil can generate increasing lift forces beyond the critical stall angle of attack with increasing reduced frequency. The onset of dynamic stall is delayed to higher angles of attack as well, thereby increasing the lifting potential of the wing. It is interesting to note that, based on the current experiments, an indefinite increase in the reduced frequency does not seem to result in a similar increase in the maximum lift coefficient. This is illustrated in Fig. 5a using a simple plot of the percentage increase in maximum lift due to dynamic stall as a function of reduced frequency for the NACA 0021 airfoil. It can be observed that after a certain reduced frequency, the lift produced by the airfoil appears to level off. The limit of this reduced frequency depends upon the chord Reynolds number and decreases with the increase in the Reynolds number. The authors acknowledge that the test reduced frequencies are too limited in order to draw a general conclusion, but such behavior warrants further investigations.

Sheng et al. [79] showed that the dynamic stall onset angle of attack varies linearly with the reduced frequency. The authors also observed a somewhat comparable trend in the current experiments, as shown in Fig. 5b for the smallest Reynolds number. However, for the larger Reynolds numbers, there seems to be parabolic trend in the dynamic stall onset angle of attack. A similar parabolic trend can be observed at the outset for the smallest Reynolds number as well. However, afterwards, the stall angle of attack varied linearly with the reduced frequency.

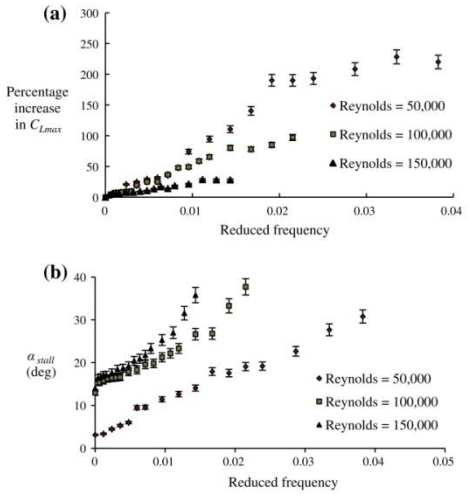

Fig. 5. (a) Percentage increase in maximum lift as a function of reduced frequency and Reynolds number and (b) change in the dynamic stall onset angle of attack as a function of reduced frequency for different Reynolds number for NACA 0021 airfoil. The error bars shown relate to one standard deviation of the data.

3.2. Reynolds number

Using the Reynolds number to characterize the flows around airfoils undergoing dynamic stall is a difficult task, especially when considering the unsteadiness generated by the motion of the airfoil itself. The primary effects on the forces and pressure distributions have been studied in detail by several research groups [14,58,74,99] and it has generally been concluded that the Reynolds number of the flow plays a minor role in the dynamic stall process. Through direct surface pressure measurements, Robinson and Wissler [74] concluded that the increase in the Reynolds number has a minimal effect on the stall process as a whole. However, they indicated that as the Reynolds number increases, the low-pressure peaks near the leading edge were observed to increase. Similarly, Choudhuri and Knight [14] showed that increasing the Reynolds number from 10^4 to 10^5 resulted in the decrease of the length scales associated with the flow structures. However, the overall effects were still deemed insignificant. In the same way, Ol et al. [66] observed that for an airfoil undergoing pitch and plunge motion, the effects of Reynolds number variations from 10,000 to 60,000 were minimal. These studies, therefore, indicate that the Reynolds number does not play a significant role during the dynamic stall process. It can be argued, however, that the range of Reynolds numbers that has been tested is limited. For Reynolds numbers applicable to industrial flows (order of 10^6), the National Renewable Energy Laboratories (NREL) conducted a series of experiments to understand the unsteady aerodynamics of sinusoidally-pitching foils [70,71,72]. Test results for two such airfoils, the S809 and the S813, operating at different Reynolds numbers are illustrated in Fig. 6. The test airfoils had smooth surface finish and were tested at different combinations of the mean and maximum angles of attack. The cases presented in Fig. 6 are for the airfoils pitching at pre- and post-stall states, as is evident from the angles of attack. It can be observed from the plots that for the two airfoils, the general trend and the hysteresis in the lift force remain approximately similar, especially during pre-stall conditions. On the other hand, for the post-stall conditions, a slightly larger hysteresis and larger values of the peak lift coefficients are observed for the smaller Reynolds number. Therefore, in general it has been concluded that the Reynolds number plays an insignificant role in the dynamic stall process.

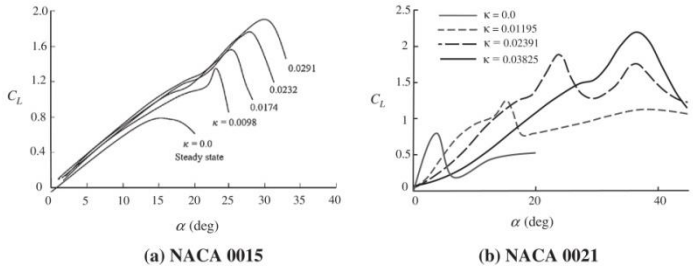

Fig. 4. Effects of increasing reduced frequency on the lift characteristics of (a) NACA 0015 airfoil (reproduced from Jumper et al. [39]) and (b) NACA 0021 airfoil (Re = 50,000).

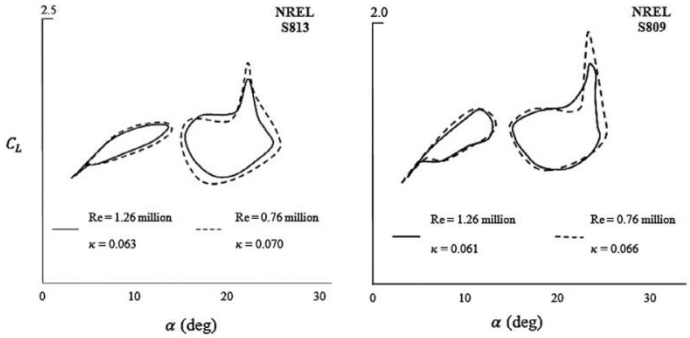

Fig. 6. Similarities in the lift curves of NREL S809 and S813 airfoils undergoing sinusoidal oscillations at different Reynolds numbers. The plots have been reproduced from Refs. [69,71]). The slight differences are primarily due to the slightly varying reduced frequencies.

On the other hand, referring to Fig. 5, it can be observed that the Reynolds number indeed plays a considerable role in the forces produced by the airfoil. This has been further elaborated in the plot of C_L vs. α presented in Fig. 7 for the NACA 0021 airfoil operating at two different Reynolds numbers and constant reduced frequency of 0.012. As can be observed, the maximum lift generated by the airfoil and the dynamic stall angle of attack both increase significantly due to the increase in the Reynolds number. Similar observations have been made by other researchers as well. Zhang and Schlüter [99], for example, recently conducted a Large Eddy Simulation of a flat plate pitching about mid-chord over a range of Reynolds numbers between 440 and 21,000. They showed that for very small Reynolds numbers, typically less than 10,000, the maximum lift coefficient of the flat plate exhibits a non-linear behavior. A similar non-linear behavior in the lift force for a harmonically pitching 0012 airfoil was observed by Amiralaei et al. [4].

The authors' conjecture is that the dynamic stall process is greatly influenced by the state of the boundary layer prior to any unsteadiness. At the Reynolds number of 120,000, the boundary layer around the NACA 0021 airfoil undergoes transition from laminar to turbulent on the suction side of the airfoil [29]. Therefore, it can be argued that the boundary layer is predominantly laminar at a Reynolds number of 50,000 and, therefore, more prone to be affected by adverse pressure gradients during the pitch-up motion. Consequently, the boundary layer in this case is expected to readily separate and the dynamic stall angle of attack is likely to be considerably smaller compared to the case of the higher Reynolds number, as evidenced in Fig. 7. Therefore, the turbulent boundary layer, being less susceptible to the influence of adverse pressure gradients during pitch-up, remains attached for a larger range of angles. This leads to the larger dynamic stall angle of attack and the larger generated lift force. For the studies cited in the present section, the range of the Reynolds number is restricted in the sense that the boundary layer is substantially turbulent in all cases. Therefore, no significant effects of the Reynolds number on the dynamic stall process were observed in those studies.

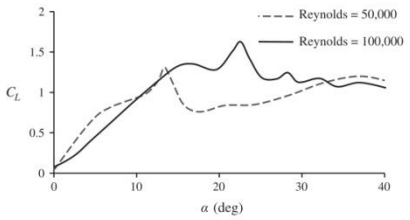

Fig. 7. The lift characteristics of a NACA 0021 airfoil at similar reduced frequency (κ = 0.012) as a function of Reynolds number from the wind tunnel experiments.

It is interesting to note that as the Reynolds number increases, the vortex structures observed are more compact. This can be observed in the flow visualizations of the NACA 0012 airfoil shown in Fig. 8. The airfoil was pitched at a reduced frequency of 0.2 and the changes in the flow patterns were observed. It is noted that although the vortex structures are largely similar, they are slightly more compact at the higher Reynolds number. An increase in the vortex strength due to a compact core can result in the increase of suction pressures. Furthermore, a small increase in the circulation is also plausible due to the resultant changes in the flow patterns. These can lead to the higher lift generated by the airfoil at the larger Reynolds numbers.

3.3. Mach number

The effects of compressibility on rapidly pitching airfoils are quite significant, even at low Mach numbers, primarily due to the unsteadiness caused by the airfoil motion. McCroskey et al. [57] indicated that for airfoils undergoing sinusoidal pitch, sonic conditions were observed near the leading edge for $M_\infty \geqslant 0.2$. Therefore, even for relatively low freestream Mach numbers, the pitching of the airfoil can induce high local Mach numbers near the leading edges of the airfoils resulting in shock formation. This results in an additional complexity to the overall dynamic stall process that needs to be understood and investigated for applications such as helicopters and highly manoeuvrable aircraft.

It is important to note that supersonic conditions can be encountered even under steady state conditions due to flow acceleration over the suction side. On the other hand, during unsteady conditions, the problem is aggravated since a comparatively small freestream Mach number can induce supersonic conditions. However, despite its relative importance, comparatively few studies have been conducted to understand the effects of Mach number changes on the dynamic stall process. Visbal [89] performed numerical studies on NACA 0015 airfoil using the unsteady, compressible, mass-averaged Navier–Stokes equations and an algebraic eddy viscosity turbulence model, observing that for $M_\infty \geqslant 0.5$, the flow field on the upper surface of the airfoil was supersonic due to the pitching of the airfoil. He found that as the angle of attack of the airfoil increased, a well-defined supersonic

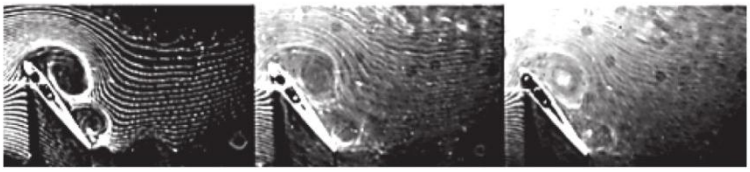

Fig. 8. Flow structures around NACA 0012 airfoil at an angle of attack of 50 deg, undergoing dynamic stall at similar reduced frequencies of 0.2 but at different Reynolds number. The flow structures, albeit more compact, are largely similar.

region, observed near the leading edge, started to grow as indicated in Fig. 9. In this figure, the airfoil is operating at a freestream Mach number of 0.6, a Reynolds number of 10^6 and a reduced frequency of 0.0225 (according to Eq. (1)). Due to the severe shock-boundary-layer interaction, the separation near the foot of the shock starts to spread both upstream and downstream. As the separation region reaches the leading edge, the pressures drop causing moment stall and subsequently massive flow separations.

For $M_\infty < 0.5$, the supersonic region is still observed near the leading edge, however, to a much smaller spatial extent. It was shown that for a freestream Mach number of 0.3, the chordwise extent of the supersonic bubble was approximately 3.0%, indicating that for even the small freestream Mach numbers, the effects of compressibility cannot be ignored. It was observed by Visbal [89] that for such cases ($M_\infty < 0.5$), DSV was still formed but was initiated through a leading edge stall instead of the conventional trailing edge stall observed for unsteady airfoils at incompressible conditions.

In terms of the lift behavior of the airfoil, an increase in the maximum lift coefficient was observed as the pitch rate was increased while keeping the Mach number constant, similar to the behavior at lower Mach numbers. Visbal [89] showed that increasing the reduced frequency at a Mach number of 0.6 resulted in not only an increase of the maximum lift coefficient but also a jump in the entire lift curve, analogous to the effect of added camber. These trends have been reproduced and presented in Fig. 10(a) where the reduced frequencies have been redefined according to Eq. (1).

By contrast with the above, decrease in the stall delay and the maximum lift coefficient were observed as the Mach number was sequentially increased while keeping the reduced frequency and the Reynolds number constant, as indicated in Fig. 10(b). A similar decrease in the $C_{l_{max}}$ was also observed by McCroskey et al. [57] and Chandrasekhara and Carr [12]. However, this argument needs further investigations, since Choudhuri and Knight [14] showed to the contrary that as the freestream Mach number is increased from 0.2 to 0.5, the formation of DSV is delayed and that there is a delay in the stall onset as well.

Visbal [89] did not observe the formation of the DSV at high freestream Mach numbers, similar to the early studies performed by Liiva [48]. Liiva [48] showed that increasing the Mach number results in the formation of shocks that somehow inhibit the process of vortex shedding. However, using Stroboscopic-Schlieren images, Chandrasekhara and Carr [12] observed that the DSV is present at all Mach numbers ($0.15 \leqslant M_\infty \leqslant 0.45$) and reduced frequencies that were tested. Furthermore, the presence of shocks near the leading edge of the airfoil at high subsonic Mach numbers during pitching also appears to be a disputed observation. The discussions provided here warrant further investigations to understand the effects of freestream Mach number on the dynamic stall process in detail, especially at supersonic freestream Mach numbers. Such studies are essential for the design of the high-speed and highly-manoeuvrable aircraft and applications such as wind turbines and helicopters which operate in subsonic flow regimes but may undergo supersonic conditions during the dynamic stall process, severely limiting their performance.

3.4. Airfoil geometry

The effects of airfoil shape on the dynamic stall process have been studied by McCroskey et al. [57] and Wilby [95]. In general, it has been believed that the airfoils with better steady-state stall characteristics presented better dynamic stall behavior in terms of maximum lift coefficients and stall delays [47,57]. Dynamic stall tests on eight airfoil sections, primarily used in the helicopter industry, with thickness-to-chord ratios varying between 9.5% and 16.6% and camber varying between 0% and 2% of the chord length were performed by McCroskey et al. [57]. The tested airfoil profiles are shown in Fig. 11.

McCroskey et al. [57] defined the regimes of operation for dynamically oscillating airfoils as either light or deep, depending on the difference between the maximum angle of attack of the oscillation and the critical stall angle of attack of the airfoil. The light dynamic stall behavior of airfoils encompasses the distinct formation of the DSV near the leading edge and the observation of hysteresis in the airloads. More precisely, according to Mulleners

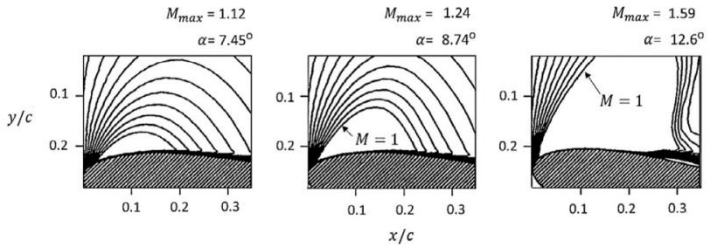

Fig. 9. Growth of the supersonic region near the leading edge of the 0015 airfoil operating at a freestream Mach number of 0.6, Reynolds number of 10^6 and a reduced frequency of 0.0225 [89].

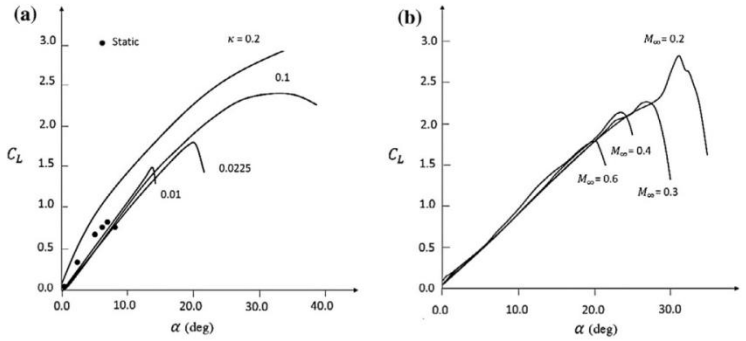

Fig. 10. (a) Effects of increasing the reduced frequency and keeping the Mach number constant (0.6) on the lift characteristics of NACA 0015 airfoil. (b) Effects of increasing the Mach number while keeping reduced frequency constant (0.0225) on the lift characteristics of NACA 0015 airfoil [89].

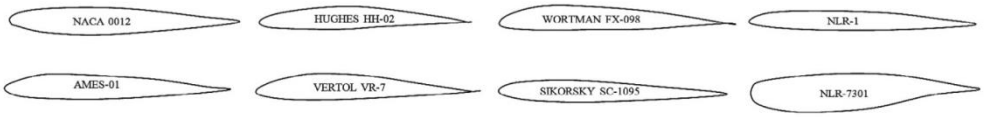

Fig. 11. Airfoils tested by McCroskey et al. [57].

and Raffel [63], the light stall is experienced when the downstroke motion begins before the stall is fully developed. On the other hand, the deep dynamic stall regime is identified by a large hysteresis in the forces and moments as well as formation of a distinct DSV. Mulleners and Raffel [63] identified this regime when the stall onset occurs during the upstroke part of the motion.

Dynamic stall lift characteristics of four representative airfoils at light stall conditions are shown in Fig. 12. For all tested airfoils, dynamic overshoot in the maximum lift coefficient was observed to occur. The distinct differences observed in the hysteresis loops of lift coefficient can be considered to be primarily due to the airfoil geometry, since the rest of the operating parameters are similar. For example, it was observed that both NACA 0012 and AMES-01 airfoil underwent similar types of trailing edge separations during the dynamic stall process; however, the lift behavior of the two airfoils is significantly different. It can further be observed that for the NACA 0012, the hysteresis loop in the lift is considerably larger than that observed for the AMES-01 airfoil. On the other hand, the FX-098 airfoil experiences a very sudden drop in the lift coefficient as compared to NACA 0012 airfoil at the end of the oscillation. Similar comparisons reveal that cambered airfoils with rounder leading edges tend to exhibit smaller hysteresis loops.

On the other hand, McCroskey et al. [57] stated that during the deep dynamic stall regime, the effects of airfoil geometry are not significant. An overlay of the lift curves for four representative airfoils undergoing deep dynamic stall, however, clearly illustrates the contrary and indicates the dominant effects of airfoil shape on the process (Fig. 13). It is interesting to note that the VR-7 and the NLR-7301 airfoils tend to have similar lift characteristics during the upstroke; however, the maximum lift coefficients and the angle of dynamic stall are different. The NLR-7301 airfoil indicates more resilience towards unsteady separation as compared to the other airfoil sections that were tested at similar conditions. In fact, according to the classification of Mulleners and Raffel [63], the airfoil still seems to be operating in the light stall regime. A primary indication of the deep dynamic stall is the formation of secondary vortex structures after the convection of the primary DSV. For the other airfoils, this is apparent from the plot presented in Fig. 13 where the secondary peaks in the lift just prior to the downstroke result from the secondary vortex structures. On the other

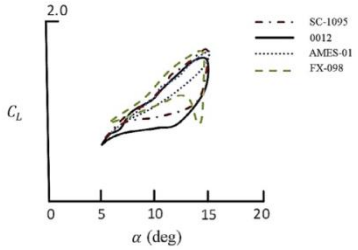

Fig. 12. Light dynamic stall for selected airfoil sections tested by McCroskey et al. [57] operating at similar conditions (M_∞ = 0.30, $\alpha = 10° + 5° \sin \omega t$ and κ = 0.10). The figure clearly indicates the effects of airfoil profiles on the lift characteristics during light dynamic stall.

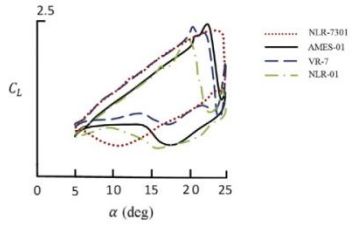

Fig. 13. Deep dynamic stall for selected airfoils tested by McCroskey et al. [57] at similar operating conditions (M_∞ = 0.25, $\alpha = 15° + 10° \sin \omega t$ and κ = 0.10) indicating the clear effects of airfoil shape.

hand, no such observation can be made for the NLR-7301 airfoil indicating that the DSV is formed when the airfoil starts its return journey. This implies that the NLR-7301 airfoil will sustain lift for a larger range of angles for the same conditions as compared to the other airfoil sections. Furthermore, significant variations can be observed in the magnitude of the hysteresis in the lift curve of different airfoils that were tested, indicating the apparent distinction in post-stall behavior of the airfoils. Hence, the profile of an airfoil is of primary importance and significantly affects the surrounding flow field and, in consequence, the forces produced during the dynamic stall process.

The cases presented in Figs. 12 and 13 are for airfoils pitching in a sinusoidal fashion. However, similar observations can be made regarding airfoils pitching at constant angular velocities through the flow visualization studies performed, presented in Fig. 14. The airfoils in this case are operating at what can be considered

Fig. 14. Flow structures around the NACA 0012, NACA 4418 and NREL S809 airfoil undergoing constant pitch dynamic stall to a maximum angle of attack of 50° at a Reynolds number of 10,000 and a reduced frequency of 0.1. Each subsequent sequence represents an increment of 5° starting from an angle of attack of zero degrees.

as analogous to the deep stall regime. It can be observed that under similar operating conditions, the flow structures around the airfoils are notably different and, therefore, the expected forces would also vary quite significantly. For the symmetric NACA 0012 airfoil, it can be observed that the dynamic stall vortex is formed much earlier in the cycle, near the leading edge as compared to the other airfoils. This leads to an earlier onset of unsteady separation for this particular airfoil. On the other hand, for the NACA 4418 airfoil and the S809 airfoil, the vortex formation is delayed to higher angles. Similarly, comparison of the vortex structures for the NACA 4418 and S809 airfoils illustrates that the vortex is more compact for the S809 airfoil. This indicates that the vortex core is stronger and will produce larger, and more local, effects on the airfoil suction pressures compared to the NACA 4418 airfoil. Therefore, it can be concluded that the airfoil geometry plays a considerable role during the dynamic stall process and needs to be further investigated.

From the above discussions, it might have become apparent to the reader that there exists a lack of quantifiable parameters that can be used to evaluate the performance of an airfoil for dynamic stall cases. For example, from Fig. 12, it can be observed that the AMES-01 airfoil has significantly better dynamic stall characteristics during the light stall regime due to the visibly smaller hysteresis in the lift force as compared to the other airfoils. However, such an observation is difficult to make when dealing with the deep stall cases as those presented in Fig. 13. Therefore, the authors of the current article have suggested a few parameters that can be used to compare the aerodynamic performance of airfoils undergoing dynamic stall, such as the stall intensity factor and the limiting reduced frequencies. The details of these parameters are presented later in this article.

3.5. Other parameters

Several other parameters directly influence the dynamic stall phenomenon as well as its predictions for engineering applications. Some of these include the associated three-dimensional effects of oscillating a finite wing and the effects of the type of unsteady motion on the dynamic stall.

Three-dimensional effects on the dynamic stall process have been investigated experimentally by Lorber et al. [52] and Piziali [68] and numerically by Spentzos et al. [83] and Visbal et al. [88], while flow visualizations have been performed by Gad-el-Hak and Ho [24]. The unsteady separated flows around three-dimensional wings have been observed to be dominated by large-scale vortical structures with spatial extents of approximately a unit chord length [24]. However, the effects of three-dimensionality are primarily restricted to the regions near the wing tips where the flow can be distinguished as three distinct zones: the wing tip vortex, the DSV and the intermediate zone where the tip vortex interacts with the DSV [1]. The interaction between the two vortex structures is presented in Fig. 15 for the NACA 0012 wing [83]. It can be observed that the core of the DSV is severely affected by the wing tip vortex in the intermediate zone and remains near the leading edge regardless of the instantaneous angle of attack. It can further be observed that the spatial extent of the intermediate zone steadily increases towards the root of the wing as the angle of attack increases. Due to these interactions, it has generally been concluded that the two-dimensional semi-empirical models for dynamic stall are suitable for large aspect ratio wings [47,85]. In engineering applications, such as helicopters and wind turbines, the flow field will also be affected by the centrifugal flow caused by the rotation of the blades. This adds further to the complexity of three-dimensional dynamic stall problem.

Similarly, the type of unsteady motion that causes dynamic stall, such as pitching and heaving at constant rates or sinusoidally, has significant effects on the dynamic stall process. The primary motivation for looking into different types of unsteady motion is related to the particular application of interest. For example, studies on simple ramp-type motions or dynamic stall at constant pitch rates are particularly useful for aerobatic aircraft undergoing tight turns [89], whereas studies of dynamic stall due to sinusoidal motion are particularly important when dealing with helicopter blades during the retreating phase 1960s [28,31]. Similarly, the heave-type motions can be related to bird and insect flight or fixed wing aircraft experiencing turbulence in the lower atmosphere

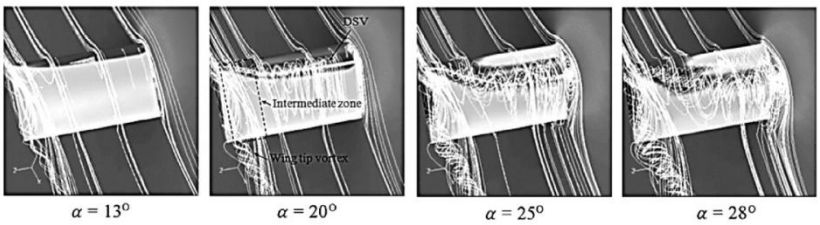

Fig. 15. Streamlines around the NACA 0012 wing pitching at a constant reduced frequency of 0.1, a Reynolds number of 6.9×10^4 and a Mach number of 0.2, indicating the spanwise evolution of the DSV and its interaction with the wing tip vortex [83].

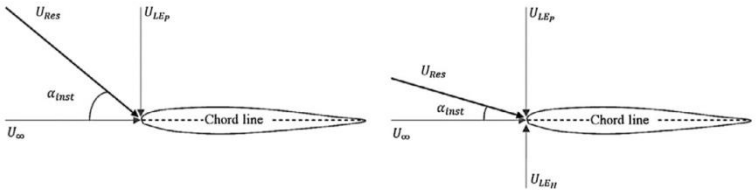

Fig. 16. Velocity vectors and the instantaneous angle of attack at the start of a simple ramp type motion (left) and a combined heave-ramp-type motion (right).

[44]. However, the authors of the present article propose that regardless of the type of motion, the primary effect can be considered to be on the angle of attack histories experienced by the airfoil due to the particular type of motion that is experienced. This is because, unlike the simple steady-state case, the instantaneous angle of attack for the unsteady case is dependent on several velocity vectors that form the resultant velocity experienced by the airfoil. Note that the instantaneous angle of attack, illustrated in Fig. 16, is not the same as the conventionally-defined angle of attack, between the freestream velocity and the airfoil chord. The velocity vectors involved in two different types of motions are indicated in Fig. 16. For the simple ramp-type motion, it can be observed that the freestream velocity (U_∞) and the velocity of the leading edge due to pitching (U_{LE_P}) constitute the resultant velocity (U_{Res}) experienced by the airfoil. On the other hand, for an airfoil undergoing heaving motion as well, an additional component of heave velocity (U_{LE_H}) also factors in the determination of the resultant velocity. Hence, for similar magnitudes of U_∞ and U_{LE_P}, the instantaneous angle of attack (α_{inst}) differs for the two cases due to the additional heave velocity component. The figure, therefore, simply illustrates that it is the angle of attack histories (α_{inst}) that are important rather than the type of motion itself. This inference can be drawn due to the key similarities observed between all dynamic stall cases caused by different types of unsteady motions. These similarities include, but are not limited to, the large overshoots in lift and the formation of the DSV [51]. This leads to the conclusion that a universal parameter can be defined for all types of unsteady motions using the freestream velocity and the resultant velocity experienced by the airfoil.

4. Dynamic stall lift characteristics

Due to the complexity of the dynamic stall process, several discrepancies exist in the present literature as to the actual cause of lift during dynamic stall. Early research [19,57] has indicated that the primary cause of the large increase in lift is due to the presence of the concentrated vortex structure on the suction side of the airfoil. Similarly, Walker et al. [91] also proposed, through the use of direct flow visualizations and surface hot wires, that the primary DSV structure was responsible for the increased lift as long as it stays in the vicinity of the airfoil. However, this concept was opposed by Albertson et al. [2] when they proposed that the DSV was not responsible for the sustenance of lift in the unsteady case. The lack of consensus regarding the sustenance of lift during unsteady motions indicates that a unified theory of lift generation during dynamic stall is lacking. In the present section, the authors have attempted to present some theories explaining the generation lift by an airfoil pitching at constant pitch rates (ramp-type motion). An insight into the lift characteristics of an airfoil during such unsteady motions can help in the fundamental understanding of the phenomenon.

For the ramp-type motion, the airfoil is allowed to be pitched at constant angular rates to a pre-determined maximum angle of attack, generally starting at an angle of zero degrees. Unlike the sinusoidal-case, where the airfoil returns to the minimum angle of the cycle, in the ramp-case, the airfoil is allowed to maintain the maximum angle of attack of the cycle for several chord lengths of flow travel. During the later stages of the pitch-up, the formation of the DSV is observed, depending primarily on the reduced frequency of pitching. A comparison of the lift curves for both the steady and unsteady case for the NACA 0015 airfoil has been presented earlier in Fig. 4. From the figure, several interesting characteristics of the lift curve for a symmetric airfoil can be extracted. These are presented in Fig. 17, with slight exaggeration, to highlight some of the more interesting characteristics.

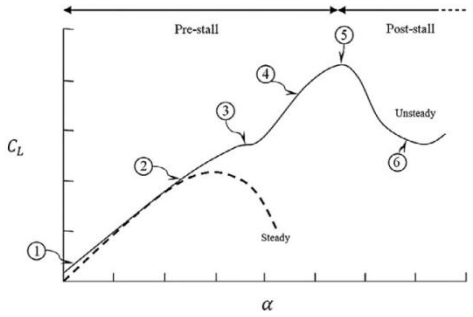

Fig. 17. Comparison of the primary lift curve characteristics of the unsteady ramp-type dynamic stall with steady-state behavior.

The unsteady lift curve can conventionally be divided into the pre- and post-stall regimes. From Fig. 17, the primary lift curve characteristics are:

1. At the onset of rotation, the lift produced at zero angle of attack for the unsteady case is slightly larger as compared to that produced by the simple symmetric airfoil during steady state operation.
2. As the angle of attack increases, the lift curve slope starts to decrease to some extent and a slight curvature is observed in the so-called linear region of the lift curve. As the steady-state stall angle of attack is exceeded, the airfoil continues to generate lift.
3. A slight kink or plateau is observed in the lift curve.
4. With further increase in the angle of attack, the lift curve slope is observed to increase. This is the stage at which the primary DSV is observed.
5. The airfoil experiences complete flow separation and there is a sudden decrease in the lift indicating the occurrence of dynamic stall.
6. The airfoil continues to generate lift beyond dynamic stall if pitching is continued. The post-stall lift characteristics during the foil rotation are still superior compared to the steady-state lift characters.

4.1. Pre-stall regime

For an airfoil undergoing constant pitch motions, the lift coefficient in the so-called 'linear' regime experiences some peculiar effects such as increased lift at the onset of motion and a decreased lift curve slope [36,38,39]. These effects have also been observed using conformal mapping techniques that model the inviscid, unsteady flow around an airfoil pitching at constant rates [3,87]. A further effect, observed by the present authors, is the slight curvature in the lift coefficient curve (Section 4.1.2) before the formation of the DSV. Afterwards, a slight kink is observed in the lift curve just prior to the formation of the DSV. Subsequently, the lift curve slope increases due to the presence of the vortex. These effects have been discussed in further detail in the following sections.

4.1.1. The onset

The step increase in lift at the onset of rotation was illustrated by Jumper et al. [39] experimentally by fitting a straight line through the so-called linear region of the lift curve for the dynamic stall cases. It was observed that increasing the reduced frequency resulted in an increase in the lift at the onset of rotation. The

increase in lift can be explained using the Wagner's function, a quasi-steady model used to determine the lift acting at the quarter-chord ($c/4$) of the airfoil following a step change in the angle of attack. The airfoil at the onset of rotation experiences a step change in the angle of attack due to the action of induced velocities at the leading edge (illustrated in Fig. 16). However, the lift increase due to the step change is not instantaneous and a considerable delay is observed for the airfoil to reach the new quasi-steady lift value. The delay is primarily due to the time taken for the circulation to adjust to the new steady state and also for the wake to reach a steady state. The quasi-steady assumption of the Wagner's function is attractive primarily due to its simplicity; however, it ignores the dependency of forces and moments on the frequency content of the motion. Therefore, in order to enforce the quasi-steady assumption, the motion of the airfoil needs to be modeled as a series of step changes, each occurring over a small time step.

The lift increase is achieved by obtaining the velocity component normal to the flow (downwash) at $3c/4$. The increase in lift per unit span following a step-change in the angle of attack is given by:

$$\Delta L = \frac{1}{2}\rho V^2 c a_1 \Delta\alpha \varphi(\tau) = \frac{1}{2}\rho V c a_1 \omega \varphi(\tau)$$

Here ρ is air density, c is chord length, a_1 is the lift slope before stall for the steady-case, Δa is step change in angle of attack, $\varphi(\tau)$ is Wagner's function, τ is non-dimensional time ($\tau = 2Vt/c$) and ω is the downwash ($\omega = V\sin(\Delta\alpha) = V\Delta\alpha$). For the incompressible case, according to Fung [23], Wagner's function is given by:

$$\varphi(\tau) = 0, \quad \tau < 0 \quad \text{and} \quad \varphi(\tau) = \frac{\tau+2}{\tau+4}, \quad \tau \geqslant 0$$

The effect of the step change in the angle of attack on the unsteady lift and comparison with quasi-steady behavior, according to Wagner's function, is illustrated in Fig. 18. Due to the step change in the angle of attack, the unsteady lift (represented by the dotted curve) instantaneously jumps to half of the final steady-state lift value. This can be translated as the slight increase in the lift observed at the onset.

Physically speaking, impulsively rotating an airfoil, results in the formation of a strong vorticity near the leading edge, known as the starting vortex [22,65,67]. The starting vortex induces a significant amount of local velocity around the airfoil near the leading edge. However, as the vortex convects downstream, due to diffusion of its vorticity, the lift starts to decrease rapidly [60]. Due to this, the unsteady lift asymptotes towards the final steady state value, reaching approximately 90% of it after 7.5 chord lengths of travel, as illustrated in Fig. 18. Wagner's function, therefore, models the effects of the starting vortex by stating that the instantaneous increase in lift at the start of the motion is half of the final steady state value ($\varphi(\tau) = \frac{1}{2}$ at $\tau = 0$) and afterwards it tends to increase gradually to the final steady state value.

The effects of the starting vortex have also been observed by Tupper [87] and Panda and Zaman [67] in their corresponding studies related to the wakes behind constant pitching and sinusoidally oscillating airfoils, respectively. For an airfoil pitching at constant rates, Tupper [87] proposes that the step change in lift at the onset of rotation can be determined using the wake behind the airfoil and is dependent only on the reduced frequency and the thickness-to-chord ratio of the airfoil [3,87]:

$$\Delta C_L = \pi\kappa\left[1 + \frac{2}{3}(t/c)\right]$$

It can be observed from Fig. 19 that the empirical approximation provides a good estimate of the step change in lift coefficient at the onset of rotation when compared with experimental observations for the NACA 0021 airfoil at a Reynolds number of 50,000. It can be observed that, for a particular airfoil, increasing the reduced frequency results in an approximate linear increase in the lift step at onset.

4.1.2. The 'linear' regime

After the step change in lift due to the onset of the airfoil rotation, a continuous decrease in the lift curve slope is observed for the unsteady case as the angle of attack increases. This steady decrease eventually appears as a slight curvature in the lift slope.

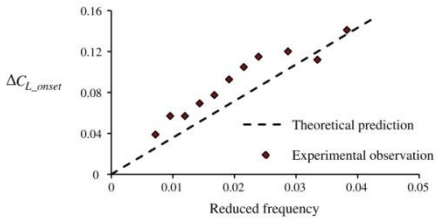

Fig. 19. Comparison of theoretical prediction of lift increase at the onset and experimental observations for the 0021 airfoil at a Reynolds number of 50,000.

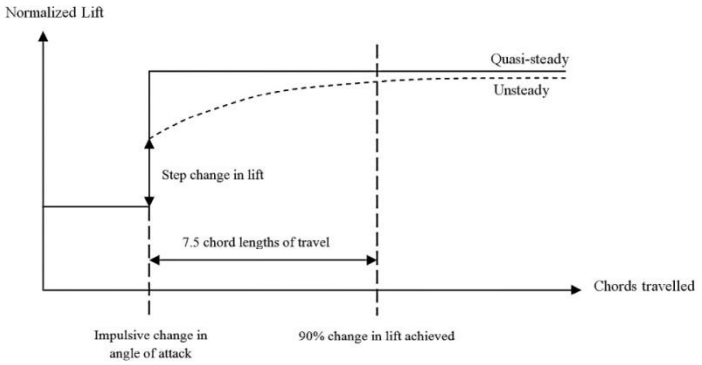

Fig. 18. Comparison of quasi-steady and unsteady lift generated by a body as explained by Wagner's function.

These changes in the lift can be attributed to the downwash caused by the pitching and can be consequently related to and predicted by the Wagner's function. In this case, a constant pitching airfoil can, therefore, be assumed to pitch in a series of steps as indicated in Fig. 20 where a comparison of the lift curves during steady and unsteady conditions is shown in slight exaggeration for clarity. The zoomed-in view of the so-called linear portion of the lift coefficient for the unsteady case is presented as well. As seen in Fig. 20, the constant-pitch motion of the airfoil can be interpreted as a series of step changes in the angle of attack (represented by the dotted-quasi-steady step changes in lift). The unsteady increase in lift, therefore, caused by the apparent downwash of the pitching motion, tends to asymptotically approach the quasi-steady value as predicted by the Wagner's function. This results in the slight curvature that is observed in the lift force curve. The decreased lift slope observed for the unsteady case during the pre-stall regime was also discussed by Wright and Cooper [96] based on the same principles that the effect of the induced downwash at the leading edge is responsible for the reducing the effective angle of attack experienced by the airfoil. Since Wagner's function also uses the downwash component of velocity to estimate the delay in fluid response to unsteady motion, the decrease in the lift curve slope can be explained using the same theory.

From a physical perspective, these phenomena can also be explained in terms of increased apparent thickness and apparent camber of the airfoil. It is well known that increasing the thickness of an airfoil results in the decrease of the lift slope, whereas, increasing the camber results in a shift of the entire lift curve upward. As observed by Jumper et al. [39], up until the quarter-chord separation (i.e. the onset of DSV formation), the general flow pattern follows the contours of the airfoil. As the airfoil pitches, a thickening of the boundary layer is observed due to flow reversal inside the boundary layer. Since the mean flow still follows the contours of the airfoil, this leads to the apparent increase in the thickness and camber as observed by the oncoming flow. The thickening of the boundary layer and the resultant change in the airfoil profile is indicated for the NACA0012 airfoil in Fig. 21. The airfoil is pitching at a reduced frequency of 0.1 and a freestream Reynolds number of 6700.

The sudden jump in lift at the onset of rotation and the decrease in the lift slope can, therefore, be explained due to the combined effects of increased camber and thickness. However, from the plots (Fig. 4), it can be observed that the lift slope continually decreases with increasing angle of attack. Therefore, as the angle of attack increases, the rate of apparent increase in camber decreases as compared to the rate of increase of apparent thickness. This results in the decrease of the lift curve slope as the angle of attack increases and, therefore, in the curvature that is observed in the pre-stall regime prior to the formation of the DSV. This can also be inferred, to some extent, by the flow visualization performed by Walker et al. [91].

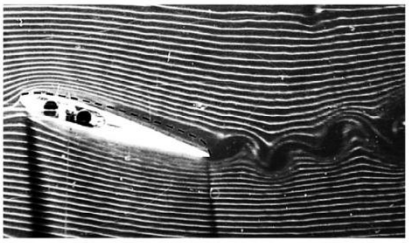

Fig. 21. The apparent change in airfoil profile, indicated by the dotted line, due to unsteady operation at a reduced frequency of 0.1 and a Reynolds number of 6700.

It is interesting to note that for the unsteady case, as the angle of attack increases beyond the steady-state stall angle of attack, the airfoil still sustains the lift prior to the formation of the DSV near the leading edge. This observation was also made by Albertson et al. [2], where they noted that much of the lift was produced prior to the formation of the DSV. This regime of lift generation is primarily of significant interest since it can be considered as the 'useable' lift prior to the formation of the catastrophic DSV and subsequent and inevitable deep stall.

The persistence of lift can be physically attributed to the creation of a counter-clockwise vortex near the trailing edge of the airfoil due to the pitching. The vortex induces a suction pressure on the separated shear layer at the trailing edge, in turn keeping the flow attached for longer periods of time. This can be observed in Fig. 22 where the NACA 4418 airfoil pitched at a very high reduced frequency of 2.04 is at the maximum angle of attack (40°) of its pitching cycle. The roll-up of the separated shear layer at the trailing edge can also be observed in the figure as the large trailing edge vortex. The starting vortex has also merged with the trailing edge vortex and is not distinguishable, much like in earlier studies [65]. Furthermore, a bubble region can be seen near the leading edge of the airfoil which will eventually evolve into the DSV.

Other theories regarding the sustenance of lift prior to the formation of the DSV can include the leading edge jet effect [19,61]. As the airfoil pitches up, the boundary layer resistance to separation is increased due to momentum addition caused by the large tangential wall velocity difference between the stagnation point and the upper airfoil surface. A rolling leading edge analogy can be used to highlight this effect further (Fig. 23(a)). The rolling leading edge induces favorable momentum transfer into the weakened

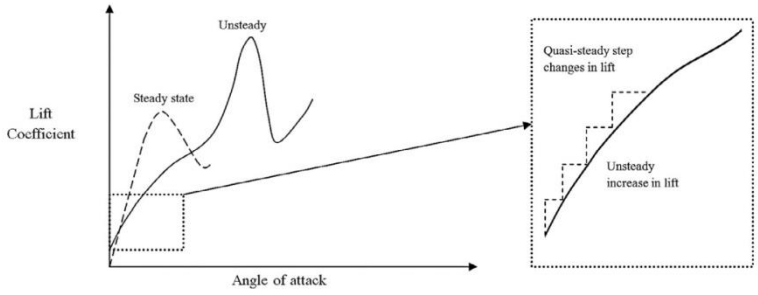

Fig. 20. The behavior of the so-called linear regime explained using the Wagner's function by assuming the constant pitch motion as a series of small steps.

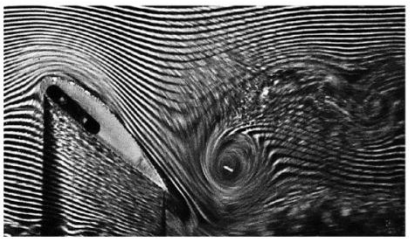

Fig. 22. A counter-clockwise trailing edge vortex created due to rapid pitching of the 4418 airfoil at a high reduced frequency of 2.04. The starting vortex is engulfed by this large trailing edge vortex.

boundary layer at high angles of operation similar to a leading edge jet [62]. The effects can be observed from Fig. 23(b) where an increase in the rotational speed of the leading edge cylinder results in the increase of the maximum lift coefficient. The rotational speed is shown as the ratio of surface velocity of the cylinder and the freestream velocity ($(U_C/U)_{LE}$). This is similar to the effect of increased reduced frequency on the lift coefficient of a pitching airfoil. A lager reduced frequency implies a larger velocity differential between the stagnation point and the upper surface. Therefore, it can be argued that as the airfoil pitches up, the boundary layer is strengthened due to the effects analogous to those of a rolling leading edge, resulting in a fuller boundary layer profile and attached flow for longer intervals.

4.1.3. The plateau

The convection of the starting vortex over the airfoil induces large-scale disturbances in the attached boundary layer near the surface. The merging of the starting vortex with the trailing edge vortex is, therefore, accompanied by regions of reversed flow inside the boundary layer. Reversed flow in the boundary layer is typically indicative of flow separation for the steady-state case. However, the classical criterion of zero skin friction coefficient at the wall is not indicative of flow separation for the unsteady case as proposed by Sears and Telionis [78] who state that unsteady separation should not be based on the flow reversal in general, but instead on the observation of global flow changes such as shedding of large scale vorticity in the wake. The region of flow reversal can also be seen on the suction side of the airfoil in Fig. 22 as the slight void just above the airfoil. A similar void has been observed in the PIV experiments reported by Wernert et al. [94].

It can be argued that the kink in the lift curve is simply a continuation of the decreasing lift curve slope. However, the 'plateau-effect' in the lift curve is too sudden to be considered simply as the decreasing lift slope. The present authors propose that the convection of the starting vortex and resultant flow reversal causes the plateau in the lift curve of an airfoil undergoing unsteady motion. At the instant in time just prior to the formation of the DSV, the region of flow reversal can be considered to contain a series of positive and negative concentration of vorticity in the boundary layer. McAlister and Carr [53] were able to show that the region of reversed flow consisted of several shear-layer vortices and speculated that these were of no obvious consequence. These concentrated vorticity regions are hardly distinguishable but due to their polarity, end up cancelling the effects of one another. The resultant effect is largely comparable to flow separation. This can be observed in Fig. 24 where the surface pressure distribution around the airfoil is shown. As can be seen, the pressures near the leading edge level out, indicating that flow separation has indeed occurred. As the airfoil continues to pitch, there is a slight increase in the suction pressures around the quarter-chord region, indicating the formation of the DSV.

4.1.4. The dynamic stall vortex

According to the classical description by Carr et al. [10], the thin reverse flow region rapidly transits from the trailing edge towards the leading edge of a sinusoidally-pitching airfoil. This event is considered to be the most fundamental precursor to the formation of the DSV. This can also be observed for airfoils pitching at constant pitch rates as shown in Fig. 14. The forward motion of the separation point from the trailing edge towards the leading edge, as explained in the previous section, results in the kink in the lift forces. As the region of reverse flow moves upstream and reaches approximately the quarter-chord station of the airfoil, catastrophic breakdown of the separation bubble near the leading edge results

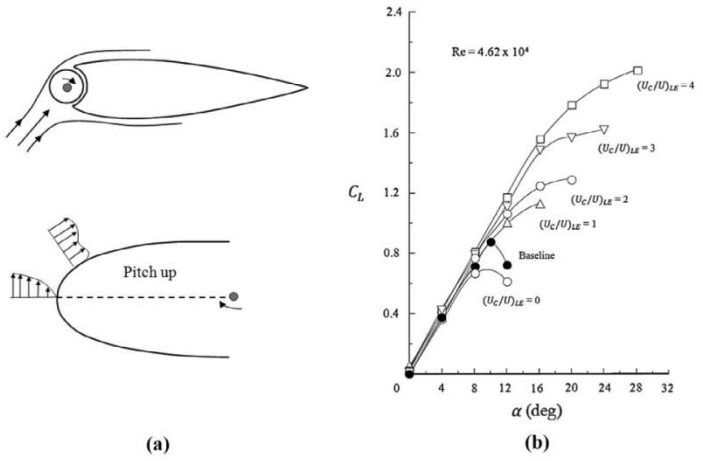

(a) (b)

Fig. 23. (a) Moving wall analogy to explain the leading edge jet effect for a pitching airfoil. (b) Effects of leading edge cylinder rotation on the lift and stall characteristics of an airfoil [61].

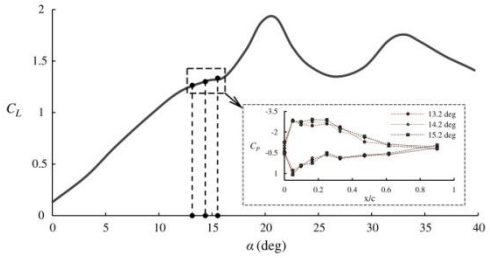

Fig. 24. The pressure distribution on the NACA 0021 airfoil as the lift curve levels off. The airfoil is operating at a Reynolds number of 50,000 and pitching at a reduced frequency of 0.024.

in the formation of the DSV [39,54,56]. The DSV induces large-scale changes in the flow field around the airfoil. It results in the increase of suction pressures over the airfoil [89,90] as well as inducing large-scale reverse-flow near the airfoil surface due to its clockwise sense [91]. The increase in the suction pressures results in an instantaneous increase in the lift slope. The variation of surface pressures of the NACA 0021 airfoil as the angle of attack of the airfoil increases, as well as the development and convection of the DSV, can be seen in the plots presented in Fig. 25. The plots indicate that the DSV is formed just after the plateau in the lift curve is observed. The presence of the DSV results in an increase of the suction pressures on the airfoil and causes the airfoil lift to increase. It can be inferred that the vortex has a low pressure core and, therefore, effects the overall lift generation during the later stages of the pitching cycle. Numerical simulations performed by Wang et al. [92] and Gharali and Johnson [25] for a sinusoidally-pitching airfoils also illustrate the low pressure core of the vortex.

As the airfoil continues to pitch, a secondary vortex structure is also observed to form near the leading edge of the airfoil. As the DSV convects further downstream, and reaches the mid-chord of the airfoil, the lift coefficient reaches its maximum value. Other researchers have also observed similar effects for the maximum lift generated by the airfoil [11,28].

It has been observed that the global vortex kinematics and properties are largely dependent on parameters such as the reduced frequency and the maximum angle of attack. The angle at which the vortex is observed and the strength of the vortex structure, and therefore the lift generated, are directly related to the reduced frequency. Furthermore, the strength of the vortex is related to the amount of circulation it induces and therefore can be approximated using the rotational velocity of the vortex. However, no direct experimental or numerical measurements or estimations of the strength of the DSV have been reported, although an indirect inference can be made from the work of Walker et al. [91]. Through the use of hot-wires, near-surface velocity measurements were conducted on the upper surface of an airfoil. According to the reported results, an increase in the reduced frequency resulted in the increase of the reverse flow velocities at the airfoil surface. Therefore, it can be inferred that as the reduced frequency increases, it results in the increase of rotational velocities of the vortex that induce the reverse flow at the airfoil surface. Furthermore, since circulation is directly related to the rotational velocities of the system, it results in a distinct increase in the maximum lift as the reduced frequency increases. Numerical work by Visbal [89] also indicates that the increase in the reduced frequency directly results in the increase of the suction pressures due to the DSV.

Similarly it is interesting to note that the maximum angle of attack also plays a significant role in the development of the DSV. It has been observed that if the maximum angle of attack is sufficiently high, the process of vortex shedding is well organized and the vortices are visibly distinct [55]. This is primarily because

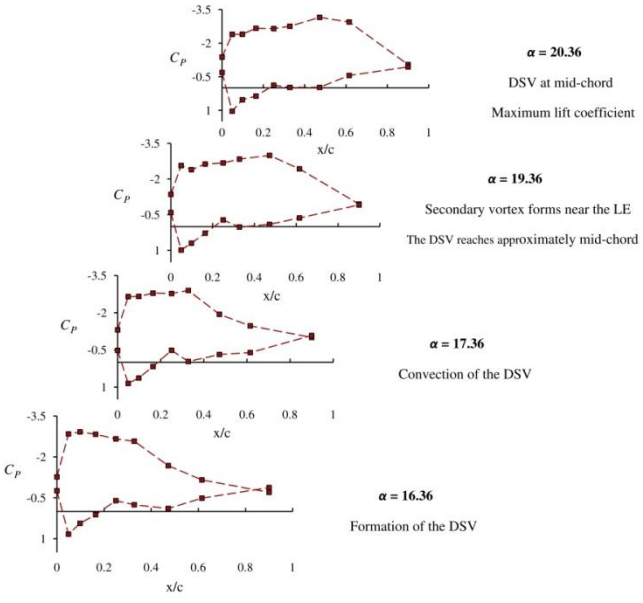

Fig. 25. Series of surface pressure distributions for $\kappa = 0.024$ and a Reynolds number of 50,000.

the DSV, after its inception, is largely affected by the freestream flow. However, a larger final angle of attack of the airfoil serves to 'shield' the vortex for longer intervals, hence permitting it to stay in close proximity to the airfoil for longer times. The effects are shown in Fig. 26 where the evolution of the DSV is presented as a function of the maximum angle of attack of the pitching cycle. In one instance, the airfoil was allowed to pitch to a maximum angle of attack of 30° and then stopped, whereas in the other case, the airfoil was allowed to continue its pitching motion until a maximum angle of attack of 60°. The effects of the freestream flow on the evolution of the vortex structures are clearly visible. It can be observed that for the case where the maximum angle of attack is

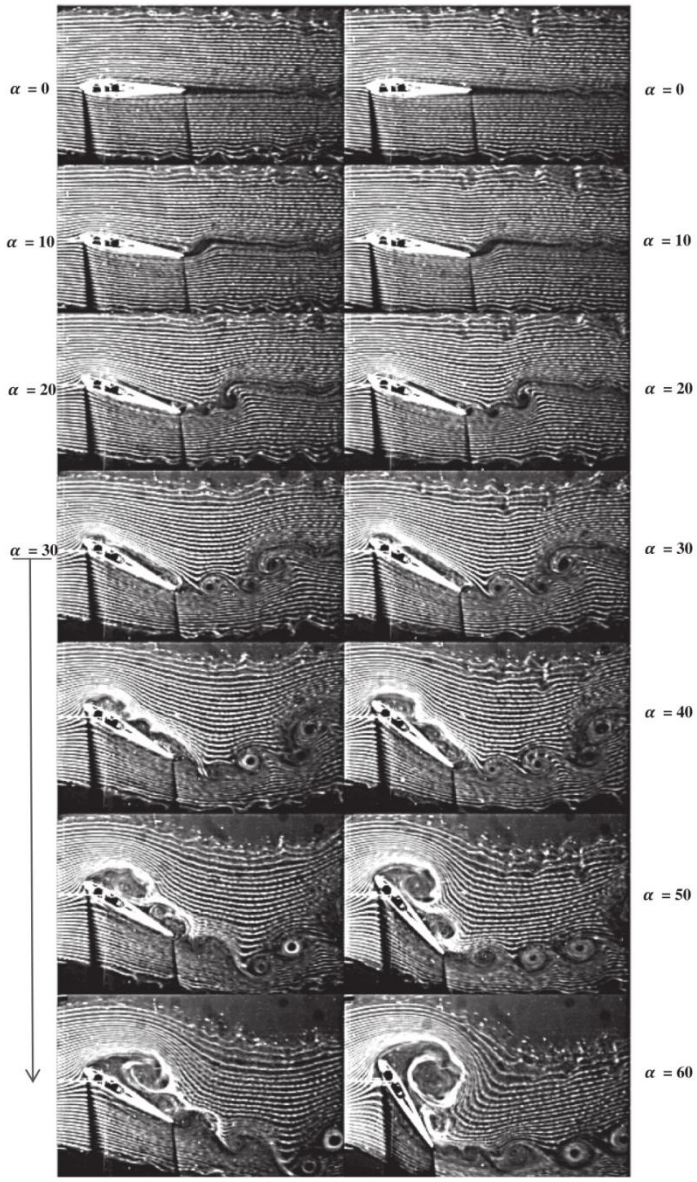

Fig. 26. The effects of maximum angle of attack on the primary DSV during the pitching cycle ($\kappa = 0.2$, $Re = 6700$). A larger maximum angle serves to shield the vortex structure allowing comparatively uninhibited growth.

30°, the primary DSV suffers from streamwise stretching and an elongated vortex is observed. In comparison, for the 60° case, the vortex structure is shielded by the airfoil and continues to develop with less interference from the freestream. This allows the vortex structure to remain in the vicinity of the airfoil for longer time intervals.

It might be of some note to revisit the idea of induced camber that was discussed in Section 3.1.2. It is easily deducible from Fig. 26 that the lift histories of airfoil for the two cases will vary due to the difference in the prominent flow structures. The vortices developed around the airfoil can be considered to impart an apparent camber effect, as illustrated in Fig. 27. The figure presents the final instances from Fig. 26 and indicates the vortex structures for the two cases along with an approximate apparent camber induced by these vortices. For the case where the DSV is shielded by the airfoil to some extent, the induced camber is apparently larger compared to the other case. This results in larger lift slopes due to the formation and unhindered evolution of the DSV.

Similarly, a probable explanation for the high lift produced by the vortex can be the Magnus effect, induced by the vortex itself. It can be recalled that the Magnus effect is related to the generation of lift on rotating bodies and is particularly of interest when accurate predictions of ballistic missile trajectories and rifle shell inaccuracies are of concern [84]. For the case of an airfoil undergoing unsteady separation, the DSV itself can be considered as a rotating circular cylinder, adding additional circulation to the airfoil-system. It has been observed that a spinning cylinder produces much larger lift forces as compared to airfoils of the same planform area, with a penalty of larger drag [5]. This is analogous to the effects of the DSV which considerably increases the lift force produced by an airfoil with a comparative increase in drag.

4.2. Post-stall regime

The post-stall regime of the lift curve occurs when the DSV has departed and the flow is completely separated from the airfoil. The airfoil goes into a state of deep stall and flow is only recovered when the angle of attack is brought down to sufficiently lower values compared to the steady-state stall angle of attack. However, if the airfoil is still allowed to rotate beyond the point of flow separation, a secondary peak in lift is observed. The post stall regime is one of the most investigated features of dynamic stall, primarily due to its large influence on the fatigue life of helicopter and wind turbine blades.

4.2.1. The stall

After its inception, the DSV, under the influence of the freestream flow, convects over the surface of the airfoil inducing a complex, non-linear pressure field. The convection of the vortex is also associated with a discontinuous change in circulation over the airfoil. As the vortex moves downstream, the forces and moments generated by the airfoil reach their respective maximum values, albeit not exactly simultaneously. Secondary and sometimes tertiary vortices are also observed occasionally and produce additional fluctuations in the aerodynamic loads, although to a greatly reduced extent as compared to the effects of the primary DSV [55]. Finally, the DSV departs the vicinity of the airfoil, leading to large scale flow separation. According to the definition of Sears and Telionis [78], the airfoil is now under a state of complete unsteady stall. The convection of the DSV from the airfoil surface causes a rapid decrease in the lift of the airfoil.

As discussed earlier, it is difficult to estimate the intensity of stall from simple visual inspection of the flow or the lift curves (for example those presented in Fig. 4). Therefore, at present there is a lack of a quantifiable parameter that can be used to compare the stalling characteristics of different airfoils under steady-state or unsteady operation. For this reason, the authors of the current article present a new parameter termed the stall intensity factor. The stall intensity factor for the steady-state case and the ramp-type unsteady case can be defined using the lift slope ($\Delta C_l/\Delta\alpha$) after separation and the overall decrease in lift after the first peak (ΔC_l) and prior to the secondary peak as:

$$SI = \left(\frac{\Delta C_l}{\Delta\alpha}\right)(\Delta C_l)$$

The parameters involved in the above definition of the stall intensity factor are illustrated graphically in Fig. 28 for the simple ramp-type unsteady case. Note that $\Delta\alpha$ is measured in radians. The same equation as above can be used for the steady-state case to compare the stalling characteristics of different airfoils. On the other hand, for the sinusoidally oscillating airfoils, the stall intensity factor can be defined as the area of hysteresis loop observed in the lift coefficient and therefore represents the loss of energy experienced during the cycle.

Using the definition of stall intensity factor, we can now examine and systematically evaluate the stall behavior of airfoils operating at both steady and unsteady conditions. For the simple

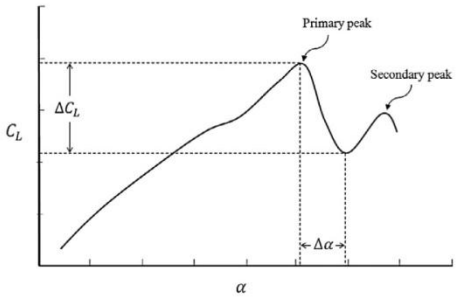

Fig. 28. Parameters involved in the definition of stall intensity factor.

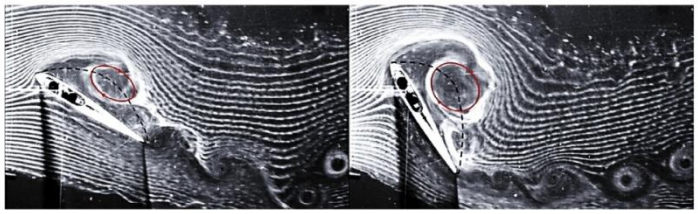

Fig. 27. The apparent camber effect due to the presence of the vortex structure at the maximum angle of the cycles presented in Fig. 18.

ramp-type dynamic stall case, the effects of increasing the reduced frequency on the stall intensity have been presented in Fig. 29. The NACA 0021 airfoil from the current experiments and the NACA 0015 airfoil from Jumper et al. [39] are compared with each other. Note that a reduced frequency of zero implies the steady-state case. It can be observed that an increase in the reduced frequency results in the increase of the stall intensity factor in an approximate linear fashion for both the airfoils. This indicates that increasing the reduced frequency, while keeping the other parameters of operation constant, results in an increase in the severity of stall experienced by the airfoil. Furthermore, the severity of stall is larger for the thicker airfoil at the smaller reduced frequencies. However, an increase in the reduced frequency does not worsen the conditions as quickly as it does for the thinner airfoil. Similarly, the effects of Reynolds number can also be seen from the plot. It can be observed that an increase in the Reynolds number exacerbates the stall condition of the airfoil operating at unsteady conditions.

Similarly, a simple comparison of Figs. 12 and 13 show that operation in the deep-stall regime results in a much more significant loss of energy as compared to operation in the light-stall regime. Comparison of the post-stall behavior of different airfoils is also possible. For example, a simple visual comparison of the different airfoils shown in Fig. 12 indicates that the area of hysteresis loop formed is significantly smaller for the AMES-01 airfoil and therefore this airfoil has significantly better post-stall characteristics as compared to the other airfoils.

Another parameter that can be used to quantify the resistance of a particular airfoil to the initiation of dynamic stall is the limiting reduced frequency [13]. The limiting reduced frequency can be defined as the non-dimensional pitch rate at which the most salient features of dynamic stall become apparent. The parameter was used to predict the occurrence of dynamic stall on wind turbine blades. The limiting reduced frequency can be considered to define the boundary between quasi-steady and unsteady behavior. It indicates the inherent resistance of the airfoil towards the occurrence of dynamic stall due to an unsteady motion and is primarily dependent on the airfoil geometry. An airfoil with a larger limiting reduced frequency will inherently be more appropriate for applications where dynamic stall needs to be avoided.

4.2.2. The flat plate behavior

Interestingly, a clear trend follows through the general post-stall behavior of an airfoil pitching at a constant pitch rate as presented in Fig. 30. The post-stall characteristics of a pitching airfoil [37] closely resembles the post-stall characteristics of a rotating flat plate [15]. As can be observed, the aerodynamic lifting characteristics of a translating and rotating flat plate clearly exhibit a parabolic trend. It is interesting to note that post-stall characteristics of the pitching airfoil, with the exception of the lift-peaks, display a similar parabolic trend. Therefore, after dynamic stall, the airfoil starts to behave similar to a rotating flat plate, much like an airfoil

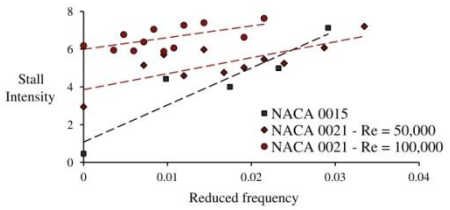

Fig. 29. Effects of increasing reduced frequency on the stall intensity factor of two different airfoils (NACA 0015 from Jumper et al. [39] and the NACA 0021 from current experiments). Also shown is the effect of increased Reynolds number on the stall intensity factor for the NACA 0021 airfoil.

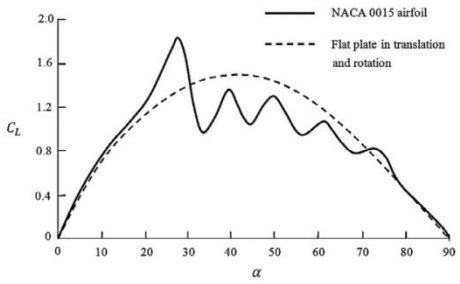

Fig. 30. Lift coefficient for a pitching 0015 airfoil [37] and a flat plate undergoing both rotation and translation [15] indicating the dominant parabolic trend in the lift curves for both cases.

acting as a flat plate after simple steady-state stall. Note that here the general trend in the behavior of the lift curve is of particular importance in this case since a direct comparison of both the cases is not reasonable due to the dissimilar operating conditions and the imposed unsteadiness.

The flat plate lifting characteristics have been thoroughly investigated by several researchers due to particular interest in insect flight [15,34,35,97]. Iversen et al. [35] observed an increase in the lift generated by a rotating flat plate as the relative tip speed was increased. The relative tip speed is the ratio of leading edge tip speed to the freestream velocity and can, therefore, be considered equivalent to the reduced frequency parameter used for airfoils. This observation clearly illustrates that a rotating flat plate can generate significant lift even though the effects of geometry are clearly not present in this case. It furthermore shows that the rotation of the plate induces some form of circulation that contributes to the overall lift generated [18]. The comparison presented in Fig. 30 prompts the conjecture that majority of the lift generated on the pitching airfoil, with the exception of the lift-peaks, is generated due to the motion of the airfoil and not as much on the geometry of the profile. However, significant amount of research is still required to concretely correlate the lift generated by an airfoil and a flat plate and, therefore, understand the underlying principles of the flow.

5. Summary

The article presents an insight into the dynamic stall lift characteristics of a pitching airfoil. The purpose of the article is to improve our understanding of the unsteady process and to encourage a more systematic approach towards dynamic stall research. It has been indicated that the dynamic stall process is dependent on several parameters such as the reduced frequency of motion, the Reynolds and Mach numbers of operation and the airfoil geometry. Furthermore, three-dimensional effects due to pitching of small aspect ratio wings and different types of motion inducing dynamic stall further add to the complexity of the problem. The authors have emphasized in the article a need for systematic studies that can help in better understanding the effects of all these parameters on the unsteady process. These are summarized as follows:

(1) An increase in the reduced frequency has been observed to increase the maximum lift generated by the airfoils undergoing dynamic stall. However, it has been shown that the maximum lift generated during dynamic stall process approaches a certain limit as a function of reduced frequency. A larger range of reduced frequencies needs to be investigated to conclusively show this effect.

(2) The effects of Reynolds number on the dynamic stall process have generally been declared as minimal. However, as shown in the current work, the Reynolds number and the state of the boundary layer prior to unsteady excitation plays a significant role in the forces produced by the airfoil. A larger range of Reynolds numbers needs to be investigated to understand this effect.
(3) The effects of Mach number on the dynamic stall process are generally disputed. It has been argued that an increase in Mach number results in the reduction of the unsteady effects associated with the dynamic stall process. It is, however, disputed whether or not a DSV is observed during operation at compressible conditions. Furthermore, the authors were not able to find any studies related to dynamic stall at supersonic freestream conditions.
(4) The effects of airfoil profile on the dynamic stall process have been largely ignored. This is primarily due to a lack of quantifiable parameters that can be used to compare airfoil performance during unsteady operation. It has been shown in the present article that the airfoil profile tends to significantly affect the flow features in its vicinity and, therefore, alters the lift and stall characteristics of the airfoil. Hence, there is a need for organized study towards understanding the effects of airfoil leading edge radius, camber and thickness-to-chord ratio on the dynamic stall process.
(5) Three dimensional effects, such as finite-span wings and spanwise flow due to helicopter or wind turbine blade rotation, also affect the global flow features during the dynamic stall process. However, a detailed analysis of the effects of these flow features on the lift curve characteristics is still lacking.

In addition, the causes of lift sustenance for an airfoil pitching at constant pitch rates undergoing dynamic stall have been investigated in the article. The research has been based on the prevalent theories found in literature and authors' conjectures based on surface pressure measurements and flow visualizations of the dynamic stall process. The unsteady lift curve can be divided into pre- and post-stall states much like the conventional steady state situation. The lift curve characteristics of an airfoil pitching at constant rates, in conjunction with Fig. 31, can be summarized as follows:

(1) At the onset of rotation, the lift produced at zero angle of attack for the unsteady case is found to be slightly larger

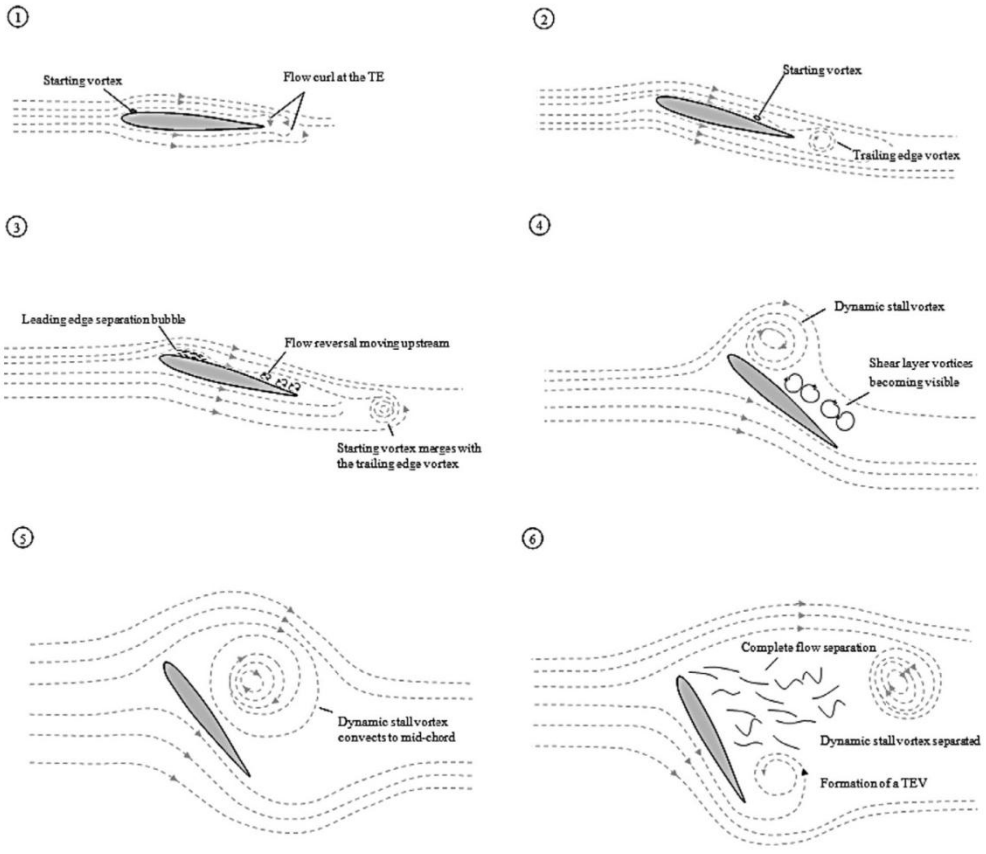

Fig. 31. Authors' conjecture of the flow topologies around an airfoil undergoing constant pitch dynamic stall.

as compared to that produced by the simple symmetric airfoil during steady state operation. This is primarily due to the effects of a starting vortex that induces additional circulation near the airfoil leading edge. The effects of the starting vortex can be modeled using the Wagner's function. Furthermore, it has been shown that Tupper's [87] equation fits the data well regardless of the Reynolds number. This also illustrates that the strength of the starting vortex is related only to the profile of the airfoil section and the reduced frequency.

(2) As the angle of attack increases, the lift curve slope of the airfoil starts to decrease continually and a slight curvature is observed in the so-called linear regime of the lift curve. This behavior can be explained due to the apparent thickening of the boundary layer on the suction side of the airfoil. The thickening results from the passage of the starting vortex that leaves a region of reversed flow in its wake. However, due to the inertia of the fluid and low pressure zones, created by the motion of the airfoil, near the trailing edge, the mean flow still follows the contours of the airfoil. Hence, the thickening of the boundary layer results in the increase of apparent camber and apparent thickness of the airfoil. The combined effect results in the slight curvature of the lift curve. These effects can also be modeled using the Wagner's function by dividing the constant pitch motion into a series of small steps. The sustenance of lift during the linear regime, on the other hand, can be attributed to the formation of a trailing edge vortex that induces suction pressures on the separated shear layer, leading to its incessant attachment.

(3) A sudden plateau is observed in the lift curve that, to some extent, can be considered as partial flow separation. The plateau occurs after the starting vortex has merged with the trailing edge vortex. Due to the expanse between the trailing edge vortex and the airfoil, the regions of reversed flow near the trailing edge start to grow swiftly and the separation point steadily moves towards the leading edge of the airfoil. At the same time, a bubble region is formed near the leading edge. Instantaneously, much of the flow is separated from the airfoil surface and, therefore, the slight kink is observed. The slight plateau can therefore be considered as a precursor to the DSV formation.

(4) After the plateau, an evident increase in the lift slope occurs for a pitching airfoil. The increase in the lift slope is principally due to the formation of the DSV which appears when the reverse flow accumulation from the trailing edge finally forces the shear layer at the leading edge to be pushed away from the airfoil surface. The roll-up of the shear layer results in the formation of the DSV which leads to the large increase of suction pressures on the surface of the airfoil.

(5) Finally the maximum lift is achieved as the DSV convects to approximately the mid-chord of the airfoil. The maximum lift during the dynamic stall process is large compared to the steady-state maximum lift coefficient. However, this large increase is also accompanied by an equivalent increase in the drag presumably due to the large angle. The behavior of the vortex and its effects can be considered synonymous to the rotating circular cylinder and associated lift as described by the Magnus effect.

(6) Afterwards, a sudden drop in lift coefficient is observed and the airfoil goes into a state of deep stall. The resultant flow separation occurs due to the detachment of the DSV and was found to be more severe compared to the steady state case. It was also observed, through the use of a newly-defined stall intensity factor, that the increase in the pitch rate results not only in the increase of the maximum lift coefficient but also causes the stall intensity to increase. Furthermore, it was shown that the increase in the Reynolds number results in the increase of the stall intensity factor for a particular airfoil.

The airfoil continues to generate lift beyond dynamic stall if the pitching is continued. The post-stall lift characteristics during unsteady case were still found to be superior as compared to the steady-state lift characters and were similar to those of a rotating flat plate. Therefore, much like the steady state case, a pitching airfoil during post stall behaves like a pitching flat plate that exhibits a clear parabolic trend in the lift curve.

Therefore, the present article provides a detailed analysis of the lift characteristics of an airfoil undergoing dynamic stall due to constant pitch motion beyond the steady state stall angle of attack. A better understanding of the lifting characteristics of an airfoil during dynamic stall can aid in the design of flow control techniques to reduce the negative effects of the process or to improve the lifting characteristics of wings for a large range of applications.

References

[1] J. Adler, M. Luttges, Three-dimensionality in unsteady flow about a wing, 23rd Aerospace Sciences Meeting, American Institute of Aeronautics and Astronautics, Reno, NV, 1985.
[2] J. Albertson, T. Troutt, W. Siuru, J. Walker, Dynamic Stall Vortex Development and The Surface Pressure Field of a Pitching Airfoil, DTIC Document, 1987.
[3] A. Allaire, Investigation of potential and viscous flow effects contributing to dynamic stall, Air Force Interim Rep. 1 (1984).
[4] M. Amiralaei, H. Alighanbari, S. Hashemi, An investigation into the effects of unsteady parameters on the aerodynamics of a low Reynolds number pitching airfoil, J. Fluids Struct. 26 (2010) 979–993.
[5] J.D. Anderson, Fundamentals of Aerodynamics, McGraw-Hill, New York, 2001.
[6] P.L. Ardonceau, Unsteady pressure distribution over a pitching airfoil, AIAA J. 27 (1989) 660–662.
[7] B. Barlow, W.H. Rae, A. Pope, Low-Speed Wind Tunnel Testing, John Wiley & Sons, Canada, 1999.
[8] L.W. Carr, Progress in analysis and prediction of dynamic stall, J. Aircr. 25 (1988) 6–17.
[9] L.W. Carr, M. Chandrasekhara, Compressibility effects on dynamic stall, Prog. Aerosp. Sci. 32 (1996) 523–573.
[10] L.W. Carr, K.W. McAlister, W.J. McCroskey, Analysis of The Development of Dynamic Stall Based on Oscillating Airfoil Experiments, NASA TN D-8382, 1977.
[11] F.O. Carta, An analysis of the stall flutter instability of helicopter rotor blades, J. Am. Helicopter Soc. 12 (1967) 1–18.
[12] M. Chandrasekhara, L. Carr, Flow visualization studies of the Mach number effects on dynamic stall of an oscillating airfoil, J. Aircr. 27 (1990) 516–522.
[13] A. Choudhry, M. Arjomandi, R. Kelso, Horizontal axis wind turbine dynamic stall predictions based on wind speed and direction variability, Proc. Inst. Mech. Eng., Part A: J. Power Energy 227 (2013) 338–351.
[14] P.G. Choudhuri, D. Knight, Effects of compressibility, pitch rate, and Reynolds number on unsteady incipient leading-edge boundary layer separation over a pitching airfoil, J. Fluid Mech. 308 (1996) 195–218.
[15] M.H. Dickinson, K.G. Gotz, Unsteady aerodynamic performance of model wings at low Reynolds numbers, J. Exp. Biol. 174 (1993) 45–64.
[16] S.K. Digavalli, Dynamic Stall of a NACA 0012 Airfoil in Laminar Flow, PhD Thesis, Massachusetts Institute of Technology, 1994.
[17] J.A. Ekaterinaris, M.F. Platzer, Computational prediction of airfoil dynamic stall, Prog. Aerosp. Sci. 33 (1998) 759–846.
[18] C. Ellington, The aerodynamics of hovering insect flight. I. The quasi-steady analysis, Philos. Trans. R. Soc. Lond., B 305 (1984) 1–15.
[19] L. Ericsson, J. Reding, Fluid mechanics of dynamic stall Part I. Unsteady flow concepts+, J. Fluids Struct. 2 (1988) 1–33.
[20] L. Erm, Measurement of flow-induced pressures on the surface of a model in a flow visualization water tunnel, Exp. Fluids 35 (2003) 533–540.
[21] C.S. Ferreira, G. van Kuik, G. van Bussel, F. Scarano, Visualization by PIV of dynamic stall on a vertical axis wind turbine, Exp. Fluids 46 (2009) 97–108.
[22] P. Freymuth, The vortex patterns of dynamic separation: a parametric and comparative study, Prog. Aerosp. Sci. 22 (1985) 161–208.
[23] Y. Fung, An Introduction to the Theory of Aeroelasticity, Dover Pubns, 2002.
[24] M. Gad-el-Hak, C. Ho, Unsteady vortical flow around three-dimensional lifting surfaces, AIAA J. 24 (1986) 713–721.
[25] K. Gharali, D.A. Johnson, Dynamic stall simulation of a pitching airfoil under unsteady freestream velocity, J. Fluids Struct. (2013).
[26] K. Granlund, M. OL, D. Garmann, M. Visbal, Experiments and Computations on Abstractions of Perching, in: Proceedings of the 28th AIAA Applied Aerodynamics Conference, 2010.

[27] S. Gupta, J.G. Leishman, Dynamic stall modelling of the S809 aerofoil and comparison with experiments, Wind Energy 9 (2006) 521–547.
[28] N.D. Ham, M.S. Garelick, Dynamic stall considerations in helicopter rotors, J. Am. Helicopter Soc. 13 (1968) 49–55.
[29] K.L. Hansen, Effect of leading edge tubercles on airfoil performance, PhD Thesis, University of Adelaide, 2012.
[30] K.L. Hansen, R.M. Kelso, B.B. Dally, Performance variations of leading-edge tubercles for distinct airfoil profiles, AIAA J. 49 (2011) 185–194.
[31] F.D. Harris, R.R. Pruyn, Blade Stall Half Fact, Half Fiction, J. Am. Helicopter Soc. 13 (1968) 27–48.
[32] H.E. Helin, J.M. Walker, Interrelated Effects of Pitch Rate and Pivot Point on Airfoil Dynamic Stall, DTIC Document, 1985.
[33] H. Irwin, K. Cooper, R. Girard, Correction of distortion effects caused by tubing systems in measurements of fluctuating pressures, J. Wind Eng. Ind. Aerodyn. 5 (1979) 93–107.
[34] K. Isaac, A. Colozza, J. Rolwes, Force measurements on a flapping and pitching wing at low Reynolds numbers, 44th AIAA Aerospace Sciences Meeting and Exhibit, Reno, Nevada, 2006.
[35] J. Iversen, Autorotating flat-plate wings – the effect of the moment of inertia, geometry and Reynolds number, J. Fluid Mech. 92 (1979) 327–348.
[36] E. Jumper, R. Dimmick, A. Allaire, The effect of pitch location on dynamic stall, J. Fluids Eng. 111 (1989) 256.
[37] E. Jumper, J. Hitchcock, R. Docken, Investigating dynamic stall using a modified momentum-integral method, AIAA, 25th Aerospace Sciences Meeting, Reno, NV, 1987.
[38] E. Jumper, R. Hugo, Simple theories of dynamic stall that are helpful in interpreting computational results, Comput. Phys. Commun. 65 (1991) 158–163.
[39] E. Jumper, S. Schreck, R. Dimmick, Lift-curve characteristics for an airfoil pitching at constant rate, J. Aircr. 24 (1987) 680–687.
[40] M.F. Kerho, Adaptive airfoil dynamic stall control, J. Aircr. 44 (2007) 1350–1360.
[41] M. Kramer, Increase in the maximum lift of an airfoil due to a sudden increase in its effective angle of attack resulting from a gust, NASA TM-678, 1932.
[42] A. Krzysiak, Improvement of helicopter performance using self-supplying air jet vortex generators, J. KONES Powertrain Transp. (2013) 20.
[43] J.D. Lang, M.S. Francis, Unsteady Aerodynamics and Dynamic Aircraft Maneuverability, DTIC Document, 1985.
[44] K. Lee, J. Kim, Numerical analysis of the unsteady subsonic flow around a plunging airfoil, Int. J. Aeronaut. Space Sci. 14 (2013) 201–209.
[45] J. Leishman, Dynamic stall experiments on the NACA 23012 aerofoil, Exp. Fluids 9 (1990) 49–58.
[46] J. Leishman, T. Beddoes, A semi-empirical model for dynamic stall, J. Am. Helicopter Soc. 34 (1989) 3–17.
[47] J.G. Leishman, Principles of Helicopter Aerodynamics, Cambridge University Press, 2006.
[48] J. Liiva, Unsteady aerodynamic and stall effects on helicopter rotor blade airfoil sections (dynamic stall data for helicopter rotor blade analyses obtained by oscillatory tests in pitch and in vertical translation at full scale Reynolds number), J. Aircr. 6 (1968) 46–51.
[49] U.M. Lindhe Norberg, Structure, form, and function of flight in engineering and the living world, J. Morphol. 252 (2002) 52–81.
[50] H. Liu, K. Kawachi, A numerical study of insect flight, J. Comput. Phys. 146 (1998) 124–156.
[51] P.F. Lorber, F.O. Carta, Airfoil dynamic stall at constant pitch rate and high Reynolds number, J. Aircr. 25 (1988) 548–556.
[52] P.F. Lorber, F.O. Carta, A.F. Covino Jr., An Oscillating Three-Dimensional Wing Experiment: Compressibility, Sweep, Rate, Waveform, and Geometry Effects on Unsteady Separation and Dynamic Stall, DTIC Document, 1992.
[53] K. McAlister, L. Carr, Water tunnel visualizations of dynamic stall, J. Fluids Eng. 101 (1979) 376.
[54] K.W. McAlister, L.W. Carr, W.J. McCroskey, Dynamic Stall Experiments on The NACA 0012 Airfoil, Technical Paper 1100, NASA, 1978.
[55] W. McCroskey, The Phenomenon of Dynamic Stall, DTIC Document, 1981.
[56] W. McCroskey, L. Carr, K. McAlister, Dynamic stall experiments on oscillating airfoils, AIAA J. 14 (1976) 57–63.
[57] W. McCroskey, K. McAlister, L. Carr, S. Pucci, O. Lambert, R. Indergrand, Dynamic stall on advanced airfoil sections, J. Am. Helicopter Soc. 26 (1981) 40–50.
[58] W.J. McCroskey, Unsteady airfoils, Annu. Rev. Fluid Mech. 14 (1982) 285–311.
[59] W.J. McCroskey, L.W. Carr, K.W. McAlister, Dynamic stall experiments on oscillating airfoils, AIAA J. 14 (1976) 57–63.
[60] U.B. Mehta, Z. Lavan, Starting vortex, separation bubbles and stall: a numerical study of laminar unsteady flow around an airfoil, J. Fluid Mech. 67 (1975) 227–256.
[61] V. Modi, Moving surface boundary-layer control: a review, J. Fluids Struct. 11 (1997) 627–663.
[62] V. Modi, F. Mokhtarian, JOUKOWSKY AIRFOIL WITH CIRCULATION CONTROLt, in: A collection of technical papers: AIAA 12th Atmospheric Flight Mechanics Conference, August 19–21, 1985, American Institute of Aeronautics and Astronautics Snowmass, Colorado, 1985. 85-1772, p. 50.
[63] K. Mulleners, M. Raffel, The onset of dynamic stall revisited, Exp. Fluids 52 (2012) 779–793.
[64] Y.-Y. Niu, C.-C. Chang, How do aerodynamic forces of the pitching rigid and flexible airfoils evolve?, AIAA J (2013) 1–7.
[65] K. Ohmi, M. Coutanceau, T.P. Loc, A. Dulieu, Vortex formation around an oscillating and translating airfoil at large incidences, J. Fluid Mech. 211 (1990) 37–60.
[66] M.V. Oi, L. Bernal, C.K. Kang, W. Shyy, Shallow and deep dynamic stall for flapping low Reynolds number airfoils, Exp. Fluids 46 (2009) 883–901.
[67] J. Panda, K. Zaman, Experimental investigation of the flow field of an oscillating airfoil and estimation of lift from wake surveys, J. Fluid Mech. 265 (1994) 65–96.
[68] R. Piziali, An Experimental Investigation of 2-D and 3-D Oscillating Wing Aerodynamics for A Range of Angles of Attack Including Stall, NASA Technical Memorandum 4632, 1993.
[69] R.R. Ramsay, M.J. Hoffmann, G.M. Gregorek, Effects of Grit Roughness and Pitch Oscillations on the S809 Airfoil, NREL/TP-442-7817, National Renewable Energy Laboratory, Golden CO, 1995.
[70] R.R. Ramsay, M.J. Hoffman, G.M. Gregorek, Effects of Grit Roughness and Pitch Oscillations on the S809 Airfoil, NREL/TP-442-7817, National Renewable Energy Laboratory, Golden CO, 1995.
[71] R.R. Ramsay, G.M. Gregorek, Effects of Grit Roughness and Pitch Oscillations on the S813 Airfoil: Airfoil Performance Report, 1999.
[72] R.R. Ramsay, M.J. Hoffmann, G.M. Gregorek, Effects of Grit Roughness and Pitch Oscillations on the S801 Airfoil: Airfoil Performance Report, 1999.
[73] D. Rival, C. Tropea, Characteristics of pitching and plunging airfoils under dynamic-stall conditions, J. Aircr. 47 (2010) 80–86.
[74] M. Robinson, J. Wissler, Pitch rate and Reynolds number effects on a pitching rectangular wing, in: Proceedings of the 6th Applied Aerodynamics Conference, AIAA, 1988, pp. 428–440.
[75] S. Schreck, M. Robinson, Blade three-dimensional dynamic stall response to wind turbine operating condition, J. Sol. Energy Eng. 127 (2005) 488.
[76] S. Schreck, M. Robinson, M. Hand, D. Simms, HAWT dynamic stall response asymmetries under yawed flow conditions, Wind Energy 3 (2000) 215–232.
[77] S.J. Schreck, Unsteady Vortex Dynamics and Surface Pressure Topologies on a Finite Pitching Wing, DTIC Document, 1994.
[78] W. Sears, D. Telionis, Boundary-layer separation in unsteady flow, SIAM J. Appl. Math. 28 (1975) 215–235.
[79] W. Sheng, R.M. Galbraith, F. Coton, A modified dynamic stall model for low Mach numbers, J. Sol. Energy Eng. 130 (2008) 31013.
[80] D.E. Shipley, M. Miller, M. Robinson, M. Luttges, D. Simms, Evidence that aerodynamic effects, including dynamic stall, dictate HAWT structural loads and power generation in highly transient time frames, National Renewable Energy Lab, Golden, CO (United States), 1994.
[81] D.E. Shipley, M.S. Miller, M.C. Robinson, Dynamic stall occurrence on a horizontal axis wind turbine blade, National Renewable Energy Lab, Golden, CO (United States), 1995.
[82] W. Shyy, Y. Lian, J. Tang, D. Viieru, H. Liu, Aerodynamics of Low Reynolds Number Flyers, Cambridge University Press, 2007.
[83] A. Spentzos, G. Barakos, K. Badcock, B. Richards, P. Wernert, S. Schreck, M. Raffel, Investigation of three-dimensional dynamic stall using computational fluid dynamics, AIAA J. 43 (2005) 1023–1033.
[84] W. Swanson, The Magnus effect: a summary of investigations to date, J. Basic Eng. 83 (1961) 461.
[85] C.M. Tan and L. W. Carr, The AFDD International Dynamic Stall Workshop on Correction of Dynamic Stall Models with 3-D Dynamic Stall Data, NASA TM 110375, U.S. Army Aviation and Troop Command TR 96-A-009, 1996.
[86] D. Thompson, Water Tunnel Flow Visualisation of Vortex Breakdown Over the F/A-18, DTIC Document, 1990.
[87] K. Tupper, The Effect of Trailing Vortices on the Production of Lift on an Airfoil Undergoing a Constant Rate of Change of Angle of Attack, DTIC Document, 1983.
[88] M. Visbal, T.O. Yilmaz, D. Rockwell, Three-dimensional vortex formation on a heaving low-aspect-ratio wing: computations and experiments, J. Fluids Struct. (2013).
[89] M.R. Visbal, Dynamic stall of a constant-rate pitching airfoil, J. Aircr. 27 (1990) 400–407.
[90] J. Walker, H. Helin, D. Chou, Unsteady Surface Pressure Measurements on a Pitching Airfoil, DTIC Document, 1985.
[91] J. Walker, H. Helin, J. Strickland, An experimental investigation of an airfoil undergoing large-amplitude pitching motions, AIAA J. 23 (1985) 1141–1142.
[92] S. Wang, D.B. Ingham, L. Ma, M. Pourkashanian, Z. Tao, Turbulence modeling of deep dynamic stall at relatively low Reynolds number, J. Fluids Struct. 33 (2012) 191–209.
[93] Z.J. Wang, Vortex shedding and frequency selection in flapping flight, J. Fluid Mech. 410 (2000) 323–341.
[94] P. Wernert, W. Geissler, M. Raffel, J. Kompenhans, Experimental and numerical investigations of dynamic stall on a pitching airfoil, AIAA J. 34 (1996) 982–989.
[95] P. Wilby, An experimental investigation of the influence of a range of aerofoil design features on dynamic stall onset, in: 10th European Rotorcraft Forum, 1984.
[96] J.R. Wright, J.E. Cooper, Introduction to Aircraft Aeroelasticity and Loads, Wiley, 2008.
[97] J. Wu, A. Vakili, J. Wu, Review of the physics of enhancing vortex lift by unsteady excitation, Prog. Aerosp. Sci. 28 (1991) 73–131.
[98] A. Yoshida, Y. Tamura, T. Kurita, Effects of bends in a tubing system for pressure measurement, J. Wind Eng. Ind. Aerodyn. 89 (2001) 1701–1716.
[99] X. Zhang, J.U. Schlüter, Numerical study of the influence of the Reynolds-number on the lift created by a leading edge vortex, Phys. Fluids 24 (2012) 065102.

CHAPTER 7

DYNAMIC STALL CONTROL

7.1 Chapter Overview

The present chapter primarily investigates the different passive flow control methods that have been used to negate the effects of dynamic stall on wind turbine blades. The article presented in this chapter describes the control objectives of dynamic stall for wind turbine applications and highlights the control requirements necessary for the mitigation of unsteady effects. The experimental investigation of three difference control methods is reported in the article. These methods include: (1) Streamwise vortices created using leading edge delta vortex generators (2) Spanwise vortices produced using a novel concept of a rigid elevated wire, affixed permanently in front of the leading edge and

(3) a cavity at the quarter-chord location. These methods were selected based on an in-depth understanding of the unsteady separation process and a detailed literature survey of the different methods used in the past to control the process. It has been observed that control techniques that enhance mixing and improve the resistance of the boundary layer to separation are suitable options for dynamic stall control on wind turbine blade. The experiments provide the required evidence that these methods lead to a delay in the dynamic stall onset as well as improve the post-stall lift conditions of the airfoil. Therefore, the application of these control methodologies is expected to lead to post-stall load alleviation as well as improvement in the performance of the turbine during steady-state operation.

7.2 Methods to Control Dynamic Stall for Turbines

Statement of Authorship

Title of Paper	Methods to control dynamic stall for wind turbine applications
Publication Status	○ Published, ○ Accepted for Publication, ◉ Submitted for Publication, ○ Publication style
Publication Details	Choudhry, Amanullah, Maziar Arjomandi, and Richard Kelso. Methods to control dynamic stall for wind turbine applications. Renewable Energy

Author Contributions

By signing the Statement of Authorship, each author certifies that their stated contribution to the publication is accurate and that permission is granted for the publication to be included in the candidate's thesis.

Name of Principal Author (Candidate)	Amanullah Choudhry		
Contribution to the Paper	Designed and performed the experiment, interpreted the data, developed ideas, wrote the manuscript, acted as the corresponding author.		
Signature		Date	

Name of Co-Author	Maziar Arjomandi		
Contribution to the Paper	Supervised the work, helped in developing ideas, manuscript evaluation and feedback		
Signature		Date	

Name of Co-Author	Richard Kelso		
Contribution to the Paper	Supervised the work, helped in developing ideas, manuscript evaluation and feedback		
Signature		Date	

Name of Co-Author			
Contribution to the Paper			
Signature		Date	

Methods to Control Dynamic Stall for Wind Turbine Applications

Amanullah Choudhry [a§], Maziar Arjomandi [a†], Richard Kelso [a‡]

[a] School of Mechanical Engineering, The University of Adelaide, South Australia 5005, Australia

[§] Position: PhD Student (corresponding author)

Mailing address: Amanullah Choudhry, School of Mechanical Engineering, The University of Adelaide, SA 5005, Adelaide

Email address: amanullah.choudhry@adelaide.edu.au

Phone number: +61413032885

[†]Position: Senior Lecturer

[‡]Position: Associate Professor

Abstract

Dynamic stall (DS) is encountered when the sectional angles of attack of a wind turbine blade rapidly exceeds the steady-state stall angle of attack, due to inflow turbulence, gusts and yaw-misalignment. The process is considered as a primary source of unsteady loads on wind turbine blades and negatively influences the performance and fatigue life of a turbine. In the present article, the control requirements for DS have been outlined for wind turbines based on an in-depth analysis of the process. Three passive control methodologies have been investigated for dynamic stall control: (1) streamwise vortices generated using vortex generators (VGs), (2) spanwise vortices generated using a novel concept of an elevated wire (EW), and (3) a cavity to act as a reservoir for the reverse flow accumulation. The methods were observed to delay the onset of DS by several degrees as well as reduce the increased lift and drag forces that are associated with the DSV. However, only the VG and the EW were observed to improve the post-stall characteristics of the airfoil.

Keywords

Dynamic stall control; vortex generators; cavity; elevated wire; streamwise vortices; spanwise vortices;

1. Introduction and Background

Dynamic stall is the process of delayed flow separation on airfoils caused by rapid excursions in the angle of attack beyond the steady-state stall angle [1]. The delay in flow separation results in increased lift, well beyond the steady-state maximum value, as well as in the formation of a coherent vortex near the leading edge (LE) of the airfoil [2, 3]. This vortex, known as the dynamic stall vortex (DSV), results in further increase in the lift force generated by the airfoil. Once the vortex sheds, the airfoil goes into a state of deep stall. The overall loss of lift due to dynamic stall has been observed to be far more severe than that observed during steady-state operation [4]. After the initial study by Kramer [5], due to its limited perceived applicability at the time, little attention was given to the problem of dynamic stall, until it was found to occur on the retreating blades of helicopters during forward flight [6, 7]. The periodic increases in lift and pitching moments, due to the DSV formation, severely limits the flight envelopes and attainable performance of the vehicle as well as imposing high demands on the material selection for the blade. Furthermore, a large hysteresis in the lift force is observed when the angles of the blade section reduce, indicating a delay in flow and lift recovery during the process. On the other hand, dynamic stall has also been observed on wind turbine blades [8, 9], where it leads to increased fatigue damage accumulation at the rotor-hub joint due to large excursion in lift [10] as well as increased noise generation due to blade-vortex interaction [11]. In wind turbines, dynamic stall is caused by rapid variations of wind speed and direction [8, 12, 13] and is, therefore, more unpredictable compared to the rotor blades of helicopters. Furthermore, due to operation in the wake of other turbines, which consists of large-scale vortical structures of high turbulence intensity and velocity deficits [9, 14, 15], the problem of dynamic stall is considerably aggravated for downstream wind turbines [9].

Therefore, the primary motivation towards the research into the unsteady separation is to principally avoid or suppress the process to some extent. However, the control requirements are basically application-driven. For example, as shown in Figure 1a, the primary requirement of dynamic stall control in helicopters is to reduce the overall hysteresis in the lift force, while maintaining an average lift during the process. It is, furthermore, desirable to delay the process to higher angles of attack and to reduce the aerodynamic damping, due to the DSV formation. Dynamic stall due to sinusoidal oscillations is generally classified as either light- or deep-stall [16]. The light-stall regime is defined when the downstroke motion of the airfoil begins prior to the formation of the dynamic stall vortex, whereas deep-stall occurs when the dynamic stall vortex, and the consequent lift overshoot, are observed prior to the downstroke [17]. Therefore, in Figure 1a, the uncontrolled case (solid line) is representative of a deep-stall condition on the airfoil. Here, the lift overshoot is principally due to the formation of the DSV and the subsequent stall occurs when the DSV departs from the airfoil surface. A secondary peak can also be observed in the uncontrolled case just prior to the downstroke motion. Note that the large hysteresis in this case is caused by the flow separation that follows the DSV departure. On the other hand, the controlled case (dashed line) in Figure 1a is representative of the light-stall conditions. In this case, the formation of the DSV is delayed to higher angles due to the control. Furthermore, the DSV formed should be of a reduced strength and therefore would result in a smaller lift rise. This is advantageous because, once the vortex convects, the resultant hysteresis in the lift will be significantly smaller. Furthermore, due to the formation of a DSV of reduced strength, an added benefit is that the peak negative pitching moment excursions will also be reduced considerably, compared to the uncontrolled case.

For wind turbines, the primary control objectives are similar to the helicopter case. However, in this case, due to gusts of significant length scales or prolonged yaw-misalignment, the angles of attack might not reduce to small enough values to allow flow reattachment. Therefore, the blade would operate in unsteady separated flow condition for extended periods of time. Hence, the primary control objective here, as shown in Figure 1b, is not only to reduce the increased vortex lift, but also to decrease the lift decay after the vortex departs. This control objective would lead to improved post-stall behaviour of the turbine and reduced vibrations in the blade. Furthermore, it is desirable to reduce the fluctuations in the lift, after primary DSV separation.

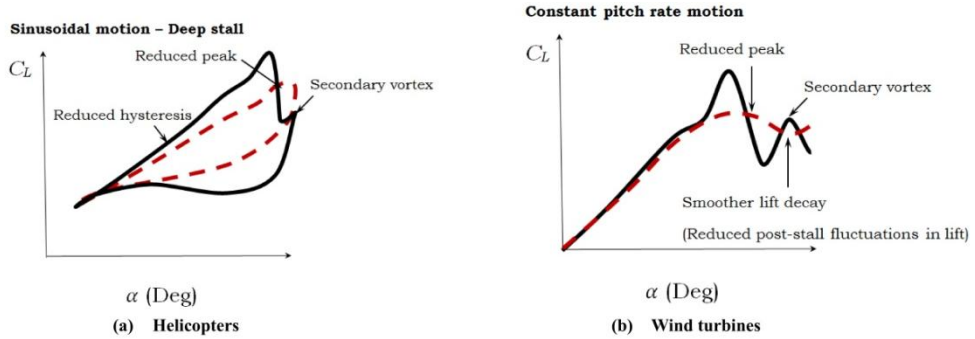

Figure 1 - Control objectives for dynamic stall for different applications. The dashed curves are the desired controlled cases.

It is interesting to note that the lift behaviour of the airfoil for the constant pitch rate case and the sinusoidal case are largely similar. The only difference in that for the sinusoidal case the airfoil is allowed to return to the initial angles of the cycle. On the other hand, for the constant pitch rate case, the airfoil pitches at a constant pitch rate to a maximum angle of attack and holds the maximum angle for extended periods of time. Therefore, for the sinusoidal case, a control technique is required to assist in the flow and lift recovery process during downstroke motion. This is synonymous, to some extent, for the control requirement of smoother lift decay during the constant pitch rate case. The purpose of mentioning the similarity for both cases is to illustrate that the effects of control are transferrable from one case to the other.

Several attempts have been made to control dynamic stall, particularly for applications in helicopter rotors. An extensive literature review was performed to understand the feasibility and effectiveness of different methods that have been used to control dynamic stall, particularly the lift associated with the DSV. Gardner *et al.* [18] studied the influence of fluid injection into the flow through different jet configurations and noted a considerable reduction in the vortex lift. Karim and Acharya [19] used flow removal as a means to reduce the vortex strength. Similarly, periodic excitation has been shown to reduce the hysteresis in the lift considerably [20, 21]. However, this method was confined to light dynamic stall conditions. However, the methods involving flow addition or removal require complex plumbing and reservoirs of compressed air or vacuum tanks to influence the flow field and therefore are not feasible for practical applications. On the other hand, passive flow-control methods, such as vortex generator (VG), have recently been investigated as a means to control dynamic stall. These methods have a zero net-mass flux and, therefore, are easier to implement. It has generally been observed that an increase in the VG height can results in a decrease of the lift hysteresis [22]. Furthermore, VG configurations producing counter-rotating streamwise vortices have been observed to be more beneficial for reducing the lift hysteresis compared to the configurations that produce co-rotating streamwise vortices [23]. However, these studies have also been limited to the light dynamic stall cases and, therefore, no indications can be made regarding the method's potency to reduce the DSV strength. A unique arrangement of VGs on the underside of the airfoil was proposed by Mai *et al.* [24]. This arrangement was found to be beneficial in reducing the influence of the VGs during steady-state operation at lower angles. At higher angles, the VGs were observed to delay the steady-state flow separation from the airfoils. However, testing at dynamic conditions indicated that the VGs were unable to influence the formation of the primary DSV and, therefore, did not decrease the vortex lift or improve the ensuing severe flow separation. Although, similar to other studies, the lift hysteresis was significantly reduced due to the streamwise-vortices created by the VGs. In addition to streamwise vortices, spanwise-oriented vortices, produced through unsteady actuation of plasma actuators, result in a reduced DSV lift and the subsequent hysteresis [25]. However, the vortices generated in this case are co-rotating and significantly weaker compared to the vortices generated by VGs. Furthermore, the actuation of plasma actuators would require energy to influence the flow. More conventional methods, such as LE slats, have also been shown to reduce the hysteresis in the lift and slightly delay the onset of vortex formation [26, 27]. However, the increase in drag, due to a slat deployment, reduces the applicability of this method. Other LE modifications, such as the Variable Droop Leading-Edge (VDLE) concept [28] and the Dynamically Deforming Leading-Edge (DDLE) concept [29], have been used to reduce the strength of the DSV. During VDLE, the

airfoil LE is drooped such that the overall camber of the foil changes. On the other hand, the DDLE concept changes the LE radius as the airfoil undergoes the pitching motion. Both methods, though difficult to implement on actual blades, illustrate the significant impact of airfoil geometry on the dynamic stall process. Similarly, several hybrid schemes have been used to improve the unsteady lift characteristics of an airfoil during pitching motions. These include combinations of plasma actuators/gurney flaps [30], trailing-edge flaps/gurney flaps [31] and even hybrid schemes involving three separate control methods (VGs, VDLE and gurney flap) [32]. However, it is generally difficult to implement such schemes. Therefore

From this literature review, the primary attributes of the control technique required for dynamic stall mitigation can be highlighted as follows:

- It is necessary for the control technique to be implemented prior to the formation of the dynamic stall vortex in order to influence the vortex lift and the severe stall conditions that follow the vortex departure [18, 19, 24, 27, 33].
- The control strategy needs to be implemented near the airfoil LE [19, 34, 35]. Trailing edge devices have been observed to have a minimalistic effect on the dynamic stall process unless the control area is very large [36-38]. This is primarily because the DSV originates near the LE.
- Severe restrictions of active control for dynamic stall mitigation on wind turbine blades are caused by issues pertaining to sensor selection and location, determination of suitable precursors to unsteady separation, the control algorithm, stability of the system and rapid deployment rates. Therefore, passive flow control methods are more suitable for dynamic stall control on wind turbine blades. Passive flow-control techniques, generally, have the added benefit of easier implementation compared to active methods and require no energy for operation.

The selection of the control methodologies, furthermore, should be based on an in-depth understanding of the dynamic stall process. In recent research, through literature survey and recent experiments including surface pressure measurements and flow visualization [4], the authors of the present article were able to observe that the DSV is formed primarily due to flow reversal that originates near the trailing edge and travels upstream towards the leading edge of the airfoil during the pitch-up. This flow reversal, when it reaches the airfoil LE, causes the shear layer detachment that ultimately rolls-up to form the dynamic stall vortex. Therefore, the primary hypothesis of the current work is that in order to delay the vortex formation and to reduce the strength of the vortex, it is pertinent that the control methodology should deter reverse flow migration towards the leading edge during the pitch-up. Hence, in the present article, dynamic stall control primarily in relation to wind turbine applications has been achieved using flow-control methods that would enhance the mixing of flow and inhibit the upstream migration of reverse flow. The three control methods that have been tested are:

1) Streamwise-oriented counter-rotating vortices generated by LE vortex generators (VG).
2) Spanwise-oriented counter-rotating vortices using a novel technique of a LE circular wire elevated above the airfoil (EW).
3) A circular cavity at the quarter chord location (C) to act as a reservoir for the reverse flow.

2. Experimental method

2.1 Baseline airfoil

In the present work, the thick symmetric NACA 0021 airfoil was selected as the baseline model. Pressure measurements were carried out on the pitching airfoil in the closed-loop KC Wind Tunnel at the University of Adelaide. The working section of the tunnel had a length of 2.4m and a cross-sectional area of $0.25m^2$ as shown in Figure 2a. The turbulence intensity in the working section was measured to be approximately 0.6%. The test Reynolds numbers based on the airfoil chord length of 0.1m was $0.5x10^5$ and $1x10^5$. The test airfoil was constructed from acrylic in two parts, with a total of 17 pressure taps along the mid-span. The pressure taps were concentrated near the leading edge of the airfoil since the largest pressure variations were expected in this region. The distribution of the pressure taps along the upper and lower surface of the airfoil are shown in Figure

2b. The test airfoil was mounted vertically inside the wind tunnel and spanned the cross section of the tunnel with a small gap of 5mm at the top to allow unhindered rotation. The bottom of the foil was attached to a heavy base pedestal and the top was pinned to the ceiling of the working section to mitigate vibrations in the foil.

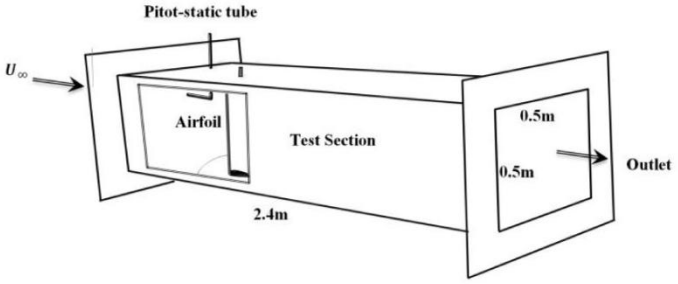

(a) A schematic illustration of the KC Wind Tunnel test section used in the experiment.

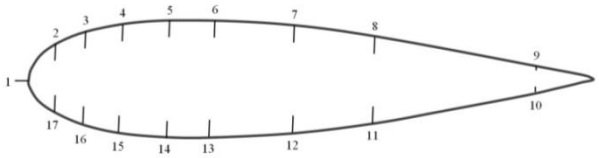

x/c (1) = 0.0 x/c (6, 13) = 0.328

x/c (2, 17) = 0.049 x/c (7, 12) = 0.472

x/c (3, 16) = 0.098 x/c (8, 11) = 0.615

x/c (4, 15) = 0.164 x/c (9, 10) = 0.9

x/c (5, 14) = 0.25

(b) Location of pressure taps for the NACA 0021 airfoil used in the current experiment.

Figure 2 – Experimental setup for pressure measurements on the pitching airfoil.

The airfoil was instrumented with *TruStability*® differential pressure sensors that were board-mounted and placed inside the airfoil. The sensors were connected to the pressure taps using copper tubes and plastic hoses. The length of the hoses was kept small to minimize any damping and phase delays in the pressure response of the system. However, a slight delay of 0.052s was still observed in the pressure response of the system, which was corrected. The measurements were recorded digitally at a rate of 5000 samples per second using the *National Instruments*® USB-6210 Data Acquisition System for the dynamic runs. The airfoil was rotated at constant rates about its mid-chord using a 22mm diameter *Maxon*® brushed DC electric motor coupled with a 157:1 reduction gearbox to provide the suitable moment for the experiment. A computer-based control system was used to provide the position and velocity information for the experiment using an in-house code. The freestream dynamic pressure was acquired using a Pitot-static tube and the Fluke 922 Airflow meter.

The chord-normal (C_N) and chord-axial (C_A) aerodynamic force coefficients were obtained through integration of the area between the pressure distribution curves using the following expressions:

$$C_N = -\oint C_p \, d\left(\frac{x}{c}\right)$$

$$C_A = \oint C_p \, d\left(\frac{y}{c}\right)$$

Finally, the lift (C_L) and pressure-drag (C_D) coefficients were determined using coordinate transformation. Further details of the experimental arrangement and details regarding the lift behaviour during constant pitch rate dynamic stall on the thick airfoil can be found in reference [4].

2.2 Vortex generators:

The VGs used in the present research were constructed using a rigid aluminium foil and adhered to the surface of the airfoil at the LE covering the entire span. Counter-rotating VGs [39], shown in Figure 3, were used in the current research due to the higher entrainment compared to the other types [40, 41]. The delta configuration selected for the VGs in the experiment is known to produce stronger streamwise vortices and has been shown to be the optimum shape for VGs [42]. The VGs were sized based on an optimization study from previous research for the steady-state case since no such optimization work is available for unsteady case. The height of the VGs (h) was selected to be 3% of the chord length for the current experiments. The height was deliberately chosen larger since severe adverse pressure gradients are expected during the pitch-up process. As shown by Lin [39], larger VGs create stronger streamwise vortices as compared to the submerged-VGs and are expected to withstand the large adverse pressures during the dynamic stall process. The distance between pairs of VGs was selected to be $3.3h$ ($\approx 0.1c$), as suggested by Heine *et al.* [23]. No specific guidelines are available for the length of individual vane and the distance between each individual vane of the VGs. Therefore, these were selected based on the conventional estimates from previous experiments [43]. Similarly, the angle of the vanes with respect to the freestream was also selected to be 20^{O} based on earlier studies [43].

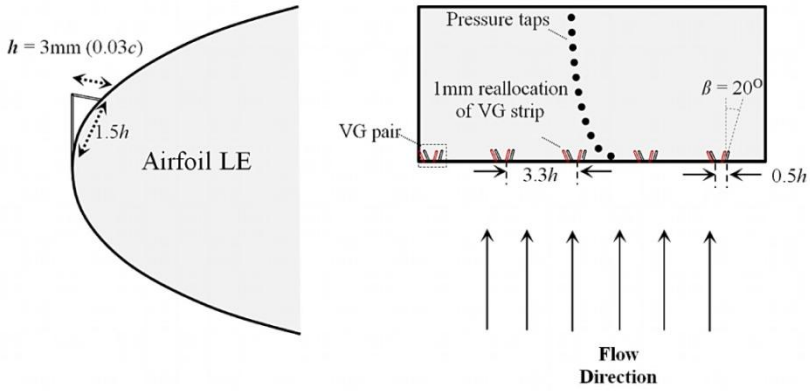

Figure 3 – Schematic illustration of the vortex generators used in the current experiment.

It is known that the vortex generators constitute a local effect in the immediate vicinity of the vanes and downstream where the streamwise vortices exist. Hence, pressure measurements are prone to error when measured at a single location. Generally, three or more rows of pressure tapings have been used to obtain the averaged pressure response of the VG-affected-flow. However, due to the limited space inside the airfoil, this method could not be utilized in the present study. Therefore, instead of having multiple rows of pressure tappings, in the present work the VG-strip was moved one mm in the spanwise direction for each consecutive pressure measurement. This is also illustrated in the top view presented in Figure 3. The pressure coefficients were then measured again for the new position and process was repeated. It was observed that three such re-allocations of the VG strip were sufficient to obtain the averaged pressure distribution on the airfoil.

2.3 Elevated wire:

Similar to counter-rotating streamwise vortices produced using vortex generators, a novel concept of utilizing counter-rotating spanwise-oriented vortices has been proposed in the present research. Such vortices will also enable high mixing between the external and boundary layer flow and will aid to hinder the upstream migration of reverse flow during pitch-up. For this purpose, an elevated circular wire of 0.95mm (0.95%c) diameter was used to generate the spanwise vortices, as illustrated schematically in Figure 4. The wire used was of sufficient rigidity and did not fluctuate under the influence of the flow. The wire was located in front of the airfoil LE and was elevated using shims placed underneath the wire at different locations along the span. The position of the shims was deliberately kept far from the row of pressure taps, in order to minimize any flow alterations caused

by the shims. The distance between the wire and the airfoil leading edge was also varied between 1 and 3%*c* for the current experiment.

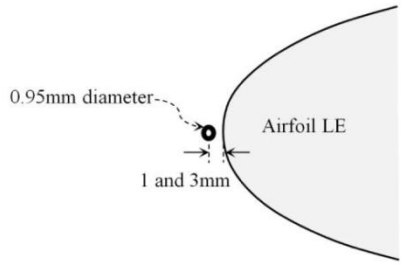

Figure 4 – Schematic illustration of the elevated wire concept used in the current experiment to create a train of spanwise-oriented counter-rotating vortices on the upper surface of the airfoil.

2.4 Circular cavity:

The final control methodology explored in the article is the use of a circular cavity on the upper surface of the airfoil. The principle hypothesis behind this particular flow control methodology was to allow a 'reservoir' for reverse flow accumulation during pitch-up. Even though, the concept is difficult to implement on real turbine blades, the notion here was to demonstrate that reverse flow accumulation can lead to a significant delay in dynamic stall onset. Furthermore, it was believed that the vortex trapped inside the cavity would lead to a smoother lift-decay after the primary DSV detaches from the airfoil surface. Lasagna *et al*.[44] had already shown that a circular cavity when placed aft of the point of maximum thickness is ineffective without the use of continuous suction to sustain the vortex inside the cavity. However, works of Olsman and Colonius [45] indicated that the cavity placed prior to the point of maximum thickness, where flow separation for thick airfoils is generally encountered, would yield appreciable improvements in the lift-to-drag ratio of the airfoil, particularly due to a decrease in the overall drag. Therefore, in the present study, a circular cavity of diameter 0.08*c* was milled from the upper surface of the airfoil at the quarter-chord location, as shown in Figure 5. The cavity configuration used in the experiment is different from those proposed by earlier researcher such as Chernyshenko[46], in that no special attention was diverted to optimizing the cavity flow. The vortex inside the cavity is known to be unstable [47] and therefore most research has been focussed on efficient trapping of the vortex inside the cavity cell. To this end, a simple ideology is proposed in the article that the gap length of the cavity should be smaller than the diameter of the cavity. This would allow vortex deformation prior to its departure from the cavity cell thereby increasing the time it stays in the vicinity of the foil. Furthermore, as proposed by Olsman and Colonius [45], the cavity edges were kept sharp in order to promote the receptivity and interaction with the detached shear layer. The circular cavity would therefore act as a trapped-vortex-cell for enhanced performance during steady state operation. For the dynamic stall case, it is hypothesized that the cavity will act as a reservoir for the reverse flow and will lead to a delay in DSV formation. It is also theorized that the trapped vortex inside the cavity will lead to improvements in the post-stall characteristics of the airfoil.

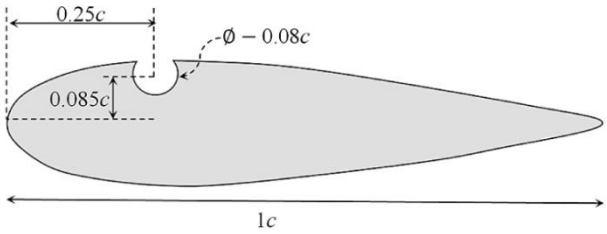

Figure 5 – A schematic illustration of the cavity configuration used in the current experiment to allow reverse-flow accumulation during pitch-up.

3. The dynamic stall process

Prior to the analysis of the different control methodologies it is important to understand the dynamic stall process in detail. A recent experimental campaign to gain a deeper insight into the process was conducted by the authors [4]. A brief description of the dynamic stall process at constant pitch rates is outlined as follows and illustrated in Figure 6.

1. At the onset of rotation, the lift produced by the airfoil at an angle of attack of zero degrees is slightly larger compared to that of the same airfoil at steady-state conditions. The lift increment is caused by a starting vortex that induces additional circulation to the rotating wing. Further to this, the drag produced by the airfoil is also slightly larger at the onset.
2. As the airfoil pitches, the displaced flow at the trailing edge results in the formation of a trailing edge (TE) vortex structure that impinges the separated shear layer onto the airfoil surface at the TE. This allows the flow to remain attached during pitch-up and results in the sustained lift even beyond the steady-state stall angle of attack. The drag of the pitching airfoil also continues to increase, albeit not at the same rate. Non-linear lift curve behaviour is observed here due to apparent changes in camber and thickness of the airfoil during the pitch-up.
3. After the departure of the TE vortex, the shear layer near the TE elevates from the airfoil surface. The reverse-flow regions start to move upstream as the angle of attack further increases. Furthermore, a region of concentrated vorticity, bound by a shear layer, develops near the leading edge (LE) of the airfoil. The effect is a sudden levelling of the lift force due to an apparent flow separation. No notable effects are observed on the drag force during this.
4. As the airfoil continues to pitch, the reverse flow from the TE starts to move towards the LE of the airfoil, steadily increasing the shear layer lift-up at the LE. Finally, due to the large adverse gradients, the shear layer rolls up and results in the formation of DSV. As the vortex grows in strength due to accumulation of vorticity from the shear layer, a rapid increase in both lift and drag forces is observed.
5. The peaks in the lift and drag forces are observed when the DSV convects to approximately the mid-chord of the airfoil.
6. After the departure of DSV, large-scale flow separation occurs on the airfoil resulting in an abrupt loss of lift. The drag at this point also decreases slightly, due to the departure of the DSV, before recommencing. Post stall fluctuations in the forces are observed due to secondary and tertiary vortices that are produced after the convection of the primary DSV.

Based on this brief overview of the dynamic stall process, the control strategy of the present research can now be stated as suppression of the DSV by reducing the upstream migration of the reverse flow towards the airfoil LE. In the present work, this is accomplished by either re-energizing the boundary layer through mixing and preventing the flow reversal for prolonged intervals or by accumulating the reverse flow at locations other than the LE.

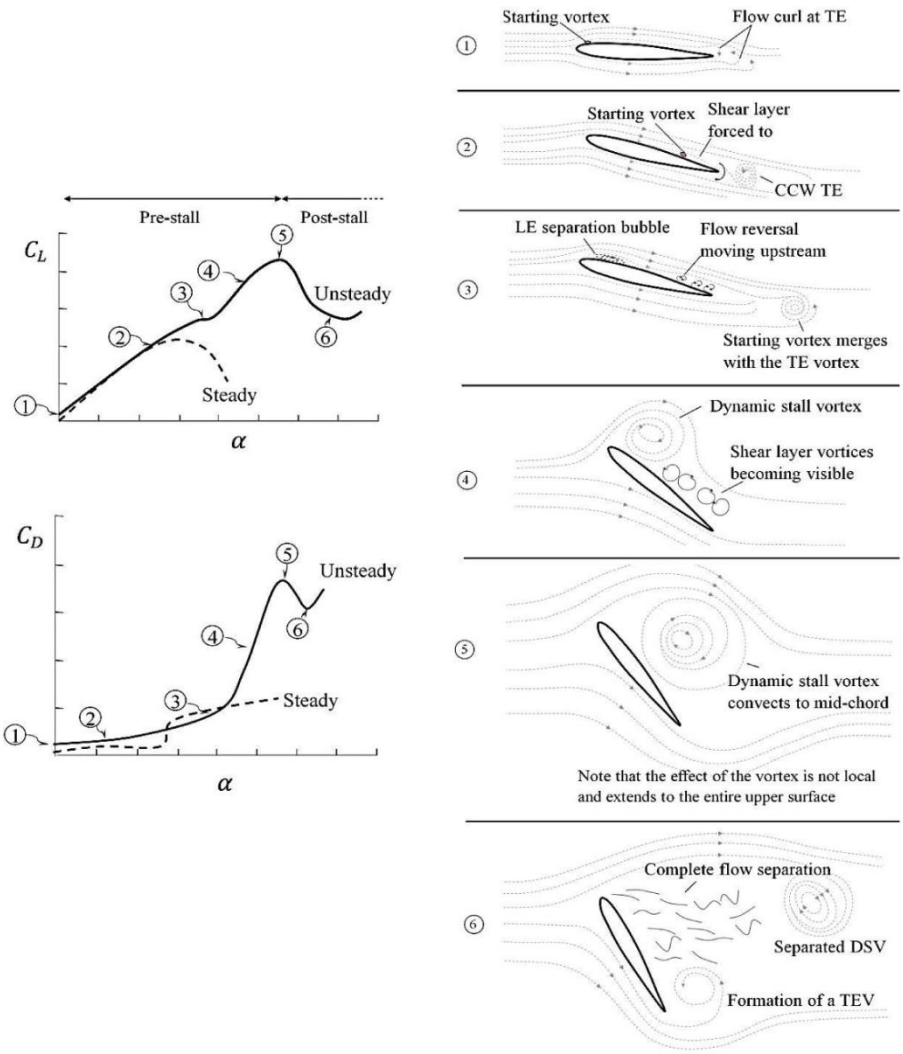

Figure 6 - The dynamic stall process during constant pitch rate motion.

4. Steady-state stall control

4.1 Vortex generators (VGs)

The use of vortex generators (VGs) to suppress flow separation was first observed by Taylor [48] for diffuser applications. Since then, considerable research has been conducted in order to optimize the VGs for ideal separation control with minimal drag penalties [39]. It is known that the VGs induce streamwise vortices that energize the boundary layer by enabling mixing with the external flow. A similar effect was observed in the current experiments. As shown in Figure 7, the use of VGs leads to a significant increase in the stall angle of attack. In fact, for the angles examined in the current experiment, lift stall is not observed on the airfoil with VGs (Figure 7a). Furthermore, the pressure-drag after separation of the airfoil with VGs is significantly smaller compared to that of the simple airfoil, as can be observed in Figure 7b. However, the overall lift-to-drag ratio of the airfoil with VGs is smaller compared to the clean airfoil, primarily due to the smaller lift and larger drag at pre-stall conditions as shown in Figure 7c. Despite the initial larger values of lift at zero degrees, the lift-curve slope suddenly declines for the airfoil with VGs. This is believed to be caused by the elimination of a long

separation bubble that exists on the clean airfoil surface at small Reynolds numbers and turbulence intensities [49]. The bubble has been observed to induce a camber effect on the airfoil that increases with increasing angle of attack, due to the upstream relocation of the bubble. Therefore, the lift of the clean airfoil is considerably larger compared to that of the airfoil with the VGs. The streamwise vortices that are produced using the VGs reinforce the boundary layer and results in the negation of the camber effect associated with the long separation bubble. This leads to the smaller lift-slope, decreased maximum lift value and a smaller lift-to-drag ratio at pre-stall conditions.

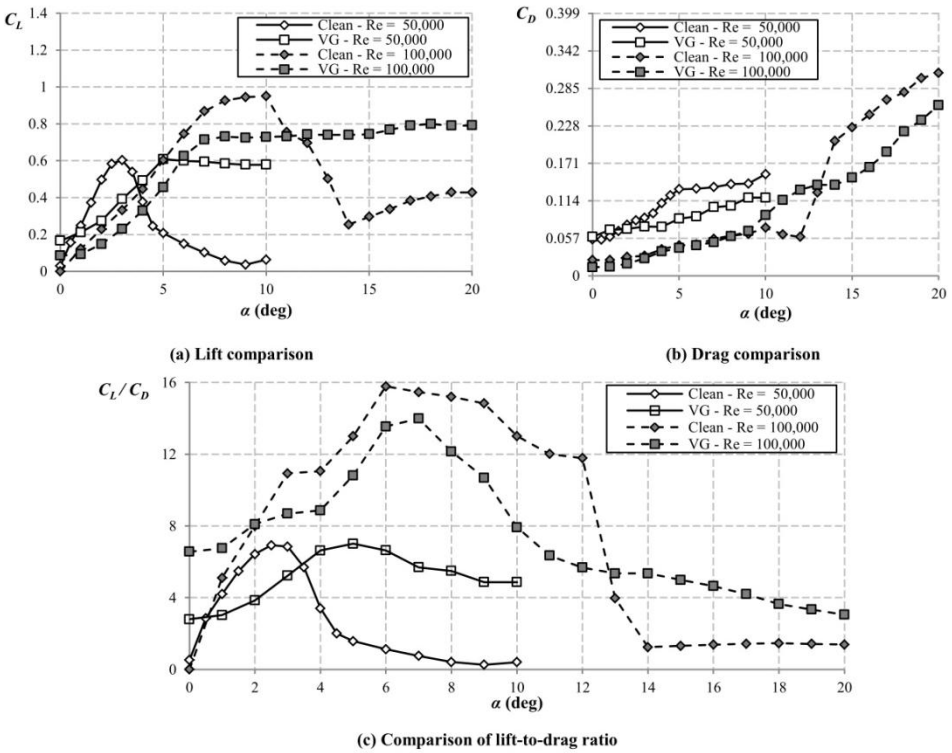

Figure 7 – Comparison of the performance of clean NACA 0021 airfoil and the NACA 0021 airfoil installed with leading-edge VGs.

4.2 Elevated wire (EW)

The concept of an elevated wire to improve airfoil performance is novel in this work and the improvements are illustrated in Figure 8 for both heights and the Reynolds numbers studied in the experiment. As can be observed, the use of an elevated wire leads to a considerable delay in the steady-state stall for both heights. Increasing the distance between the wire and the airfoil further improves the post-stall lift characteristics of the airfoil. The post-stall lift and drag characteristics are of particular importance for wind turbines since the inboard stations of a turbine blade seldom operate at fully attached conditions. An improved post-stall behaviour will, therefore, significantly increase the performance of the turbine and improve the load distribution along the blade, resulting in reduced torsional and bending loads. The comparatively better post-stall lift characteristics for the larger elevation can be attributed to the creation of coherent counter-rotating spanwise vortices that entrain the external flow in a more efficient manner compared to the smaller elevation. As a spanwise vortex convects over the surface of an airfoil, a viscous response is initiated in near-wall flow. This response is directly related to the circulation bound in the spanwise vortex originating from the cylinder [50]. The spanwise vortex interacts with the vorticity-field in the boundary layer on the surface of the airfoil resulting in its rapid rise into a thin spire that then strongly interacts with the external flow. Therefore, as the distance between the airfoil and the wire is increased, coherent vortex structures of increased circulation traverse the airfoil surface. This improves the

performance of the airfoil in terms of separation delay due to improved mixing as seen in Figure 8. Note that here as well the lift-curve slope is considerably smaller compared to that of the clean airfoil. The long separation bubble observed on the upper surface of the clean airfoil is also mitigated here due the traversing of the spanwise vortices over the airfoil surface. Since the camber effect, associated with the long separation bubble is negated, the maximum lift observed is also significantly smaller.

Nevertheless, unlike the VGs, the use of an elevated wire leads to a significant reduction of pressure drag. It can be argued that the pressure-drag is not representative of the entire wire/airfoil system, since the drag produced by the wire itself has not been included in the plots presented in Figure 8. However, since the drag contributions due to a control device, such as VGs or any other method, are generally not added to the system, it is reassuring that the pressure-drag and, hence, the wake size of the airfoil are considerably smaller in this case. Further studies are planned using a load cell to fully incorporate the drag penalties associated with the wire. It is interesting to note that at the Reynolds number of 1 x 10^5, at the smaller angles, a 'drag-bucket' is observed for the airfoil with an elevated wire at the height of 3%c, similar to that observed on laminar airfoils [51, 52]. However, here the minimum drag is not observed at an angle of attack of zero degrees. In fact, the drag curve seems to be shifted toward slight larger angles, with the minimum drag occurring at an angle of attack of 2 degs. The 'drag-bucket' is known to be caused when the majority of the flow on the airfoil is laminar and when the momentum thickness boundary layer is smaller at the point of separation. The consequence is that the wake is narrower compared to that of the clean airfoil. A similar 'drag-bucket' has been observed for the cavity case, discussed next.

The comparison of the lift-to-drag ratio of the clean airfoil and the different wire heights is illustrated in Figure 8c. As can be observed, due to the decrease in the pressure-drag for the controlled case, the overall lift-to-drag ratio is considerably improved compared to the clean airfoil. The improved post-stall characteristics of the controlled case are clearly evident here as the significantly larger lift-to-drag ratio.

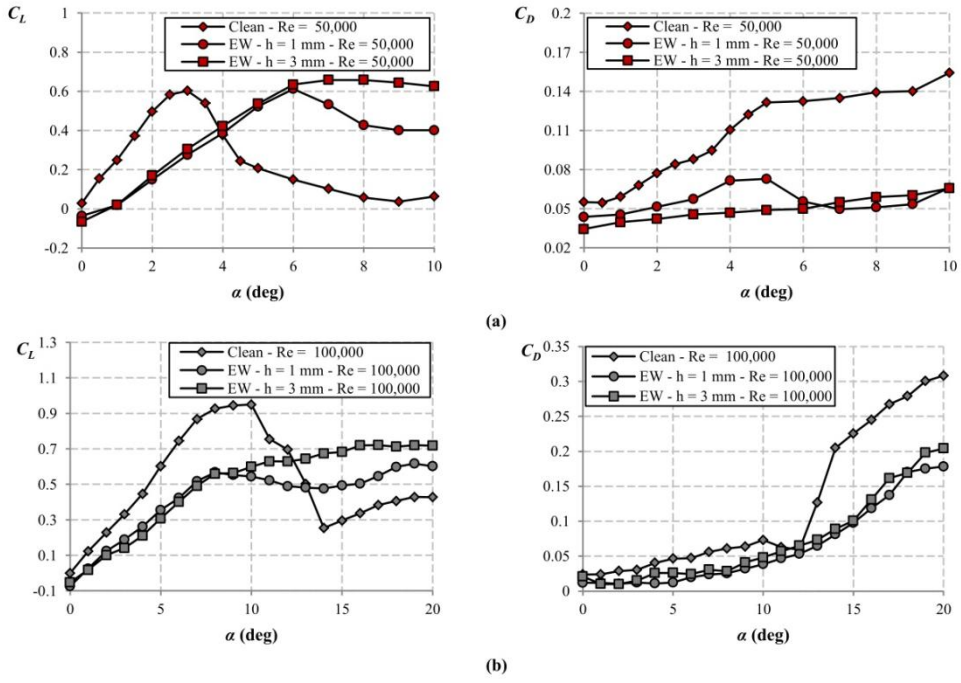

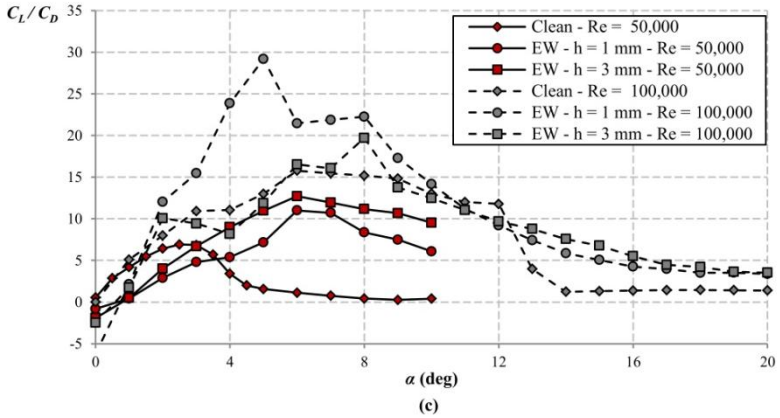

(c)

Figure 8 – Effects of an elevated wire (EW) on the steady-state performance of NACA 0021 airfoil at (a) Reynolds number = 50,000 and (b) Reynolds number = 100,000. The comparison of lift-to-drag ratio is illustrated in (c).

4.3 Cavity (C)

The final control methodology explored in this article is the incorporation of a circular cavity on the airfoil upper surface at the quarter-chord location. The comparison of lift and drag coefficients of the airfoil with a cavity and the clean airfoil for the two Reynolds number tested in the present study are shown in Figure 9a and 9b. As can be observed, the use of a cavity on the suction side of the airfoil is highly beneficial for the steady-state case. For both Reynolds number, there is a marked increase in the steady-state stall angle of attack. Furthermore, it can be observed that at the higher Reynolds number, the lift produced by the airfoil with the cavity is approximately similar to the clean airfoil, prior to flow separation at higher angles of attacks. However, the lift produced by the airfoil with a cavity is slightly smaller compared to the clean airfoil at lower angles (0–5 degs). This is primarily because up to an angle of attack of 4 degs, the laminar separation leading to a bubble formation on the upper surface of the clean airfoil is aft of the cavity location [49]. Therefore, at the smaller angles, the long separation bubble is not formed as a result of the flow energizing due to the shear layer oscillations over the cavity. However, as the angle of attack increases, the laminar separation point moves upstream of the cavity location. Therefore, the cavity does not influence the lift-curve slope to a large extent beyond 5 degs. At the critical angle of attack for the clean airfoil, the turbulent reattachment point of the long separation bubble lies inside the cavity and, therefore, the cavity here acts as a turbulator, resulting in the attached flow. At the smaller Reynolds number, the cavity on the airfoil simply acts as a turbulator. Therefore, a marked decrease in the lift-curve slope and an increase in the drag at smaller angles are observed for this case.

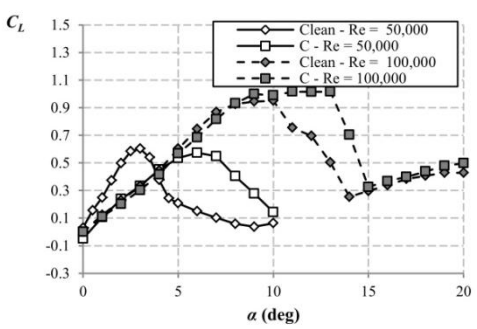

(a) Lift comparison

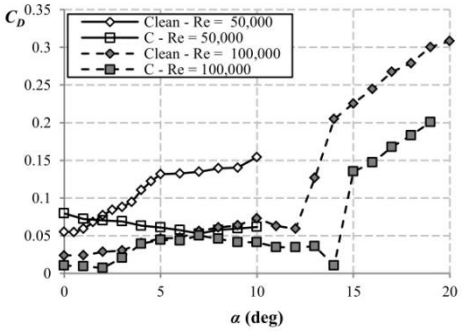

(b) Drag comparison

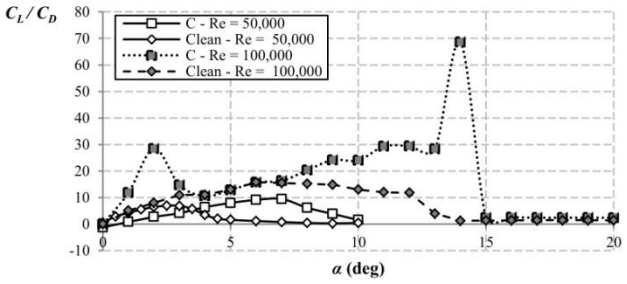

(c) Comparison of lift-to-drag ratio

Figure 9 - Comparison of the performance of clean NACA 0021 airfoil and the NACA 0021 airfoil installed with a circular cavity at the quarter-chord location.

The large reduction in drag, especially at the lower angles at a Reynolds number of 1 x 10^5, can be explained using the 'moving-wall' effect proposed by Donelli *et al.*[53]. It was suggested that the vortex flow constitutes a moving surface and replaces the solid wall of the baseline airfoil, thus improving the drag behaviour of the airfoil. On the other hand, as evidenced by Olsman and Colonius [45], the wake behind the airfoil with a cavity is considerably smaller compared to the clean airfoil. The smaller wake produced by the airfoil with a cavity results in the smaller pressure drag as seen in the above plots. These results further indicate that the location of the cavity on the airfoil surface is of significance. As shown by Lasagna *et al*. [44], a cavity placed aft of the point of maximum thickness is relatively benign and may in fact deteriorate the airfoil performance to an extent. However, the present work shows that if the cavity is placed upstream of the point of separation, the flow acceleration at the leading edge, due to favourable pressure gradients at this location, will sustain the vortex structure leading to a decrease in the drag. Note that the vortex inside the cavity is driven and supported by the shear layer over the cavity gap [54] and therefore the decrease in drag is only observed for the larger Reynolds number case when the detached shear layer has a sufficient velocity to sustain the vortex. These results, therefore, also justify the use of a smaller gap length compared to overall diameter of the cavity. The smaller gap allows the cavity to sustain the vortex for improved airfoil performance.

5. Dynamic stall control

The primary topic of the current article is the control of unsteady separation, specifically for wind turbine applications. In the following, the three control methodologies, investigated for steady-state cases earlier, are examined for the dynamic stall case. The airfoil was equipped with the individual control and pressure measurements were acquired at a sampling rate of 5000Hz. The foil was rotated about the mid-chord at a constant pitch rate from an angle of attack of zero degs up to a maximum angle of attack of 40 degs. The pressure distribution around the airfoil was acquired during the pitch-up and after the airfoil stopped. For all cases, the pressure distribution was used to obtain the lift and drag forces generated by the airfoil. Note that the results presented in the following section are for the Reynolds number of 0.5 x 10^5 since the most salient features of the unsteady process were clearly visible for this Reynolds number.

5.1 Vortex generators

The effect of the passively-deployed delta-type VGs on the dynamic stall process is illustrated in Figure 10. Here, the lift and drag coefficients for two different pitch rates are presented for the clean NACA 0021 airfoil and foil with VGs installed at the airfoil LE. At the onset of rotation, the lift produced is considerably larger for the case with VGs. However, afterwards, the lift-slope is smaller compared to the clean airfoil. The use of VGs also eliminates the plateau in the lift-curve, caused by apparent separation and a LE bubble, observed for the clean airfoil section. Furthermore, the streamwise counter-rotating vortices result in a substantial reduction of the DSV strength as can be seen by the reduction of the maximum lift and drag associated with the DSV. This behaviour is believed to be caused by the segmentation of the large DSV formed on the clean airfoil into smaller vortices of reduced effect. These smaller vortices will exist between each VG pair and, therefore, it can be

argued that the effect can be further minimized by reducing the gap between the VG pairs. A study of sinusoidal leading-edge serrations [55], that also produce streamwise-oriented counter-rotating vortices, illustrated a similar effect. It was shown that reducing the distance between the peaks of the LE serrations resulted in reduced lift hysteresis and peak lift during sinusoidal oscillations. Furthermore, an approximate 10% delay in the angle of unsteady flow separation is observed in the plots, though the effectiveness in stall-delay slightly reduces as the pitch rate increases. The stall delay here illustrates the effectiveness of the VGs to hinder the upstream march of the reverse flow. Note that the drag force prior to the formation of the DSV is similar to that of the clean airfoil. This is primarily caused by the larger size of the vortex generators used in the experiment. The VGs tend to create vortices that are of at least similar scale as the size of the VGs and, therefore, the pressure drag associated with these vortices is similar to the drag increase caused by apparent thickness increase during pitch-up of the clean airfoil. The post-stall characteristics however are considerably improved due to the use of VGs. It can be observed that airfoil now undergoes smoother lift decay due to the flow entrainment caused by the vortex generators. The post-stall variations in lift are completely suppressed through the use of VGs.

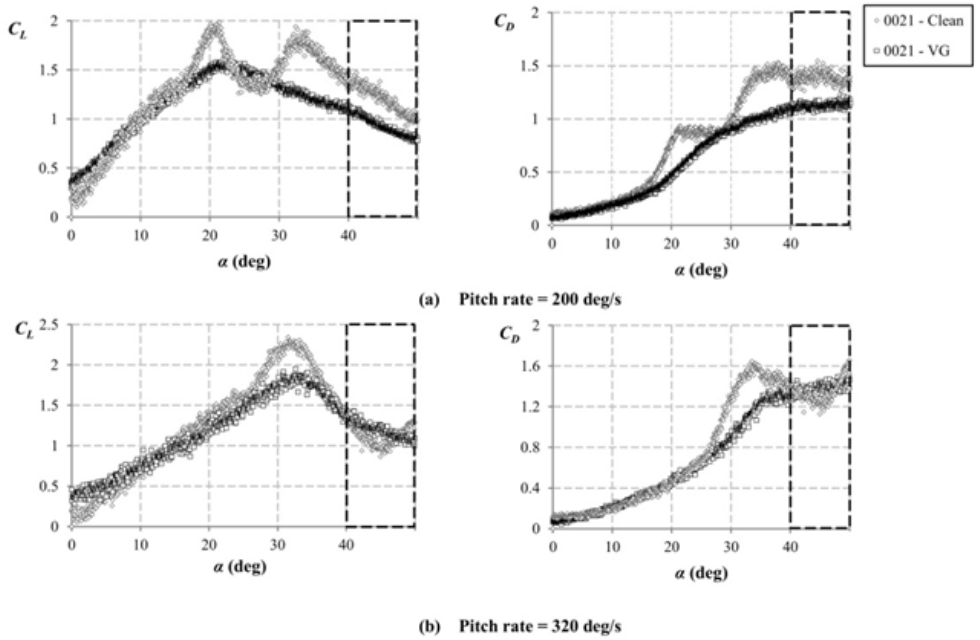

Figure 10 – The effect of counter-rotating VGs at the leading edge on the dynamic stall process for the NACA 0021 airfoil at a Reynolds number of 0.5 x 10^5. The dark grid, after the angle of attack of 40 degs, illustrates the lift and drag behaviour of the airfoil after the pitching process has stopped.

5.2 Elevated wire

The concept of an elevated wire to suppress flow separation through small-scale spanwise-oriented counter-rotating vortices, to enhance mixing, is novel in this work. The concept at first might appear similar to Vortex-Induced-Vibration (VIV) of elastically mounted cylinders [56, 57]. However, the size of the upstream cylindrical wire in the current case is less than 1%c and therefore the shed vorticity is approximately of similar scale as the boundary layer thickness during dynamic stall pitch-up [58]. Such an arrangement will, therefore, not induce the large-scale vibrations that are conventionally observed during the VIV process.

The effects of counter-rotating spanwise vortices produced by an elevated wire at different heights on the dynamic stall process for the NACA 0021 airfoil are illustrated in Figure 11 for two different pitch rates. As can be observed the increase in the height of the wire results in overall improvements of the performance of the airfoil during the unsteady separation process. For the smaller height of 1%c, it can be observed that the stall process is actually hastened for both pitch rates. This premature stall might be caused by a thickening effect of

the boundary layer, similar to that observed for large trip heights [59]. In this case, it appears that the DSV is not formed at all and the airfoil seems to sustain a constant lift during the pitch-up process. Only when the foil rotation is stopped, the airfoil lift starts to degrade. Such a post-stall behaviour is useful for wind turbines, especially near the root regions. This behaviour might be caused by the under-developed vortices that are shed from the wire at this elevation. Coherent vortices have been observed behind circular cylinders at an approximate distance of $3d$ at a Reynolds number of the order of 10^3, based on the cylinder diameter (d) [60]. Therefore, the under-developed vortices, in this case, simply perturb the boundary layer flow in the immediate vicinity of the airfoil during the pitch-up and lead to an earlier separation. On the other hand, when the wire height is maintained at 3%c, coherent counter-rotating spanwise vortices are produced that enable rapid mixing of the boundary layer and the external flow. This results in the delay of the dynamic separation, due to resistance of the energized boundary layer to reverse-flow. However, similar to the previous case of vortex generators, the increase in the pitch rate accelerates the dynamic stall onset. For the pitch rate of 200deg/s, it can be observed that stall is delayed by approximately 25%, whereas for the pitch rate of 320deg/s the unsteady flow separation is delayed by only 5%. However, the lift associated with the dynamic stall vortex is significantly reduced for all cases. Further to this, the post stall characteristics are also improved compared to the clean airfoil due to smaller fluctuations in lift after separation. The drag characteristics of the airfoil with the elevated wire at the airfoil LE are notable. As can be observed from Figure 11, the pressure drag produced by the airfoil is significantly reduced due to the spanwise vortices that originate from the wire at both heights. However, due to earlier separation at the smaller elevation, the drag of the airfoil quickly rises. As described earlier, the increase in drag during the dynamic stall process is particularly due to the apparent increase in thickness of the airfoil during the unsteady motion. It is believed that the use of coherent spanwise vortices mitigates this effect considerably and results in the smaller drag observed in Figure 11.

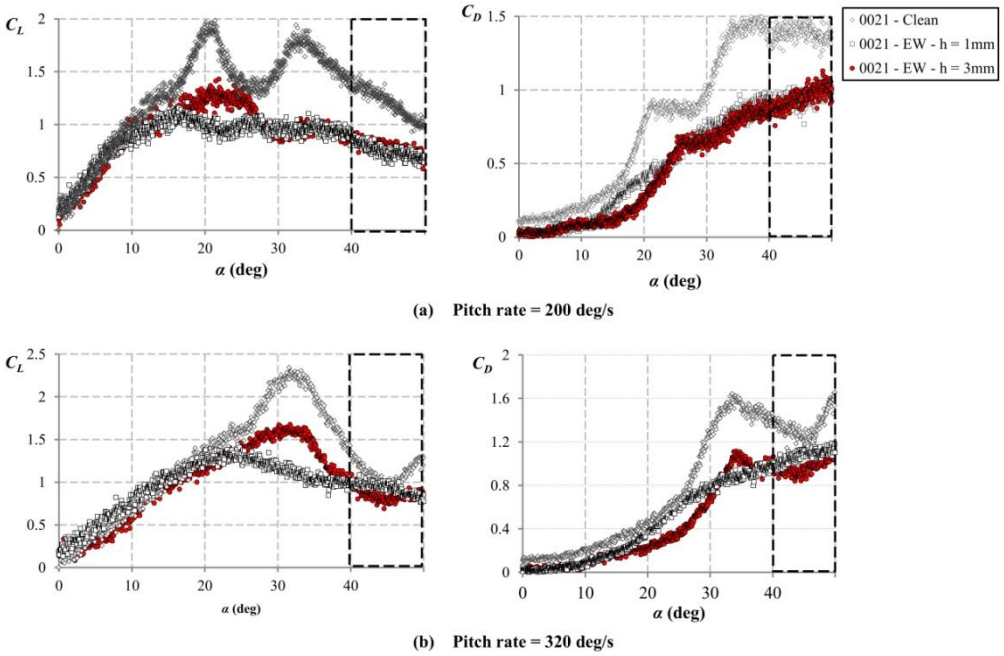

Figure 11 – The effects of counter-rotating spanwise vortices from an elevated wire (EW) on the dynamic stall process for the NACA 0021 airfoil at a Reynolds number of 0.5 x 10^5. The effects of varying the height of the wire are also included in the plots. The dark grid, after an angle of attack of 40 degs, illustrates the lift and drag behaviour of the airfoil after the pitching process has stopped.

5.3 Cavity

The effects of a cavity located at the quarter-chord of the thick NACA 0021 airfoil is shown in Figure 12 for the two different pitch rates. It can be observed that for the smaller pitch rate, the maximum lift is reduced by

approximately 18% whereas for the larger pitch rate, the reduction is only 9%. This indicates that as the pitch rate increases, the effects of the cavity on the dynamic stall vortex also reduce to some extent. Furthermore, as can be observed from the plots, the use of a cavity leads to an approximate increase in the dynamic stall onset angle of attack by over 18% for both cases. Unlike the previous cases, here the dynamic stall delay is caused by reverse flow accumulation inside the cavity and therefore an approximately similar delay is observed regardless of the pitch rate. However, for larger reduced frequencies, the accumulation rate of the reverse flow increase [19] leading to a larger lift peak at the higher pitch rate. On the other hand, the loss of lift after the vortex convection is approximately similar to the clean airfoil. This illustrates that once the flow has separated, the cavity displays no favourable role in flow reattachment, primarily due to operation in separated region.

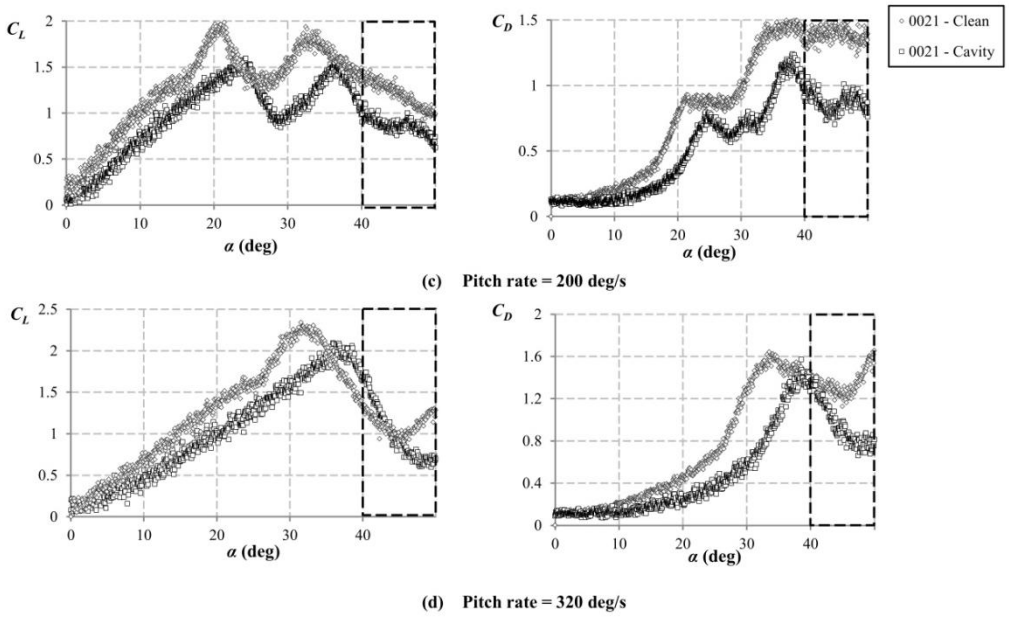

Figure 12 – The effects of a suction-side cavity on the process of the dynamic stall for the NACA 0021 airfoil at a Reynolds number of 0.5x10^5. The dark grid, after an angle of attack of 40 degs, illustrates the lift and drag behaviour of the airfoil after the pitching process has stopped.

The resultant pressure drag on the airfoil is considerably reduced during the pitch-up and the DSVformation. The cavity, in this case initially acts as a turbulator due to shed vorticity from the cavity cell and shear layer oscillations which lessen the flow reversal during the pitch-up, decreasing the pressure drag to some extent. As the angle of attack approaches the critical value, the reverse flow starts to accumulate inside the cavity. This leads to a decrease in the shear layer lift-up that leads to the formation of the dynamic stall vortex on the clean airfoil. The resulting effect is a considerable delay in the vortex formation and the pressure drag associated with the DSV. However, once the adverse pressure gradients increase due to the increase in the angle of attack, the shear layer rolls up to form the primary DSV, albeit of considerably lesser extent and strength. Therefore, the decrease in the drag for the airfoil with a cavity is associated with the smaller DSV at the higher angles.

6. Comparison of the Methods

The three methods investigated in the present research for dynamic stall control are compared in Figure 13 for the pitch rate of 200deg/s and a Reynolds number of 50,000. Note that this particular case is representative of the entire experimental campaign and the results summarized here are applicable for all cases. In the plot, the four primary control objectives for dynamic stall lift are also highlighted. Note that the lift peak is representative of the DSV strength and, therefore, a larger lift peak would also imply increased drag and negative pitching moment peaks. Furthermore, a delay in the onset of vortex formation is also desirable. In addition, the rate of lift-decay after the primary DSV convects governs the fatigue load of the turbine blades, as does the post-stall

variation in the lift force. As can be observed from Figure 13, all three methods result in significant reduction of dynamic stall lift. This indicates that the DSV strength is reduced due to the applied controls. Similarly, all three methods cause a delay in the stall onset. However, it was observed, during the course of this research, that an increase in the pitch rate reduces the effects of the all three control methods to some extent. However, no case was observed where the methods did not yield significant benefits compared to the clean airfoil. It can, furthermore, be observed that the post-stall lift characteristics are also significantly improved. The vortex generators, in this case, yield the most benefits in terms of less abrupt lift-decay after separation and fewer post-stall lift oscillations. On the other hand, the cavity does not yield any significant benefits for the post-stall regime. The lift decay is similar to that of the clean airfoil, as are the post-stall fluctuations in lift.

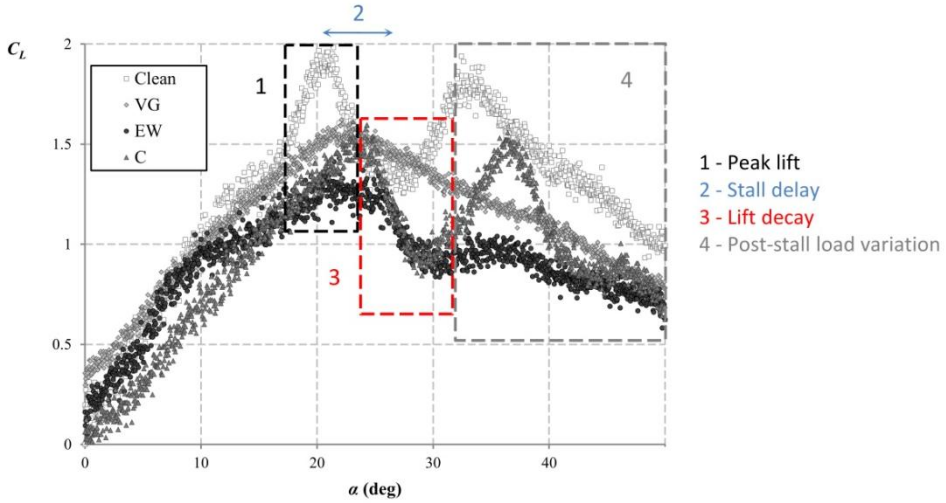

Figure 13 - Comparison of the three methods investigated in the study for dynamic stall control at a pitch rate of 200degs/s and a Reynolds number of 0.5×10^5. The required control objectives are also highlighted in the plot.

A summary of the control methods is presented in Table 1. Here, each control method has been assigned a rank, in comparison with the other methods investigated during this research for each of the individual control requirements illustrated in Figure 13. The total of these rank numbers represents the efficacy of each method for dynamic stall control, with the smallest number illustrating the best method. Based on this research, it can be concluded that the vortex generators and the elevated wire concept are of equally effective. It should be noted here that the height of the elevated wire used in the following comparison is 3%c, since the smaller height leads to an earlier occurrence. It can be observed from Table 1 that the spanwise vortices, produced using an elevated wire, lead to significant improvements in the pre-stall lift behaviour during unsteady separation. On the other hand, the streamwise vortices, produced using the vortex generators, considerably improve the post-stall lift behaviour of the airfoil. It should be noted here that the streamwise vortices from the vortex generators would be significantly larger compared to the spanwise vortices produced from the elevated wire. It is anticipated that if the size of the spanwise vortices is increased, either by increasing the distance between the wire and the airfoil LE or by increasing the wire diameter, the post-stall lift behaviour can be improved, considerably.

Table 1 – Summary and comparison of the three methods investigated in the present research for dynamic stall control. The ranks are determined based on the effects on the lift produced during the dynamic stall process and are assigned in comparison.

		Rank			
Method	**Effect**	**Peak lift**	**Stall delay**	**Lift decay**	**Post-stall**
Vortex Generators	Produces streamwise-oriented counter-rotating vortices that entrain the flow hindering upstream migration of reverse flow. The DSV is segmented resulting in smaller vortices of reduced strength and impact.	**2**	**2**	**1**	**1**
Elevated Wire	Produces spanwise-oriented counter-rotating vortices that entrain the flow hindering upstream migration of reverse flow. The DSV strength is significantly reduced. The over-all pressure drag associated with the wake is also reduced.	**1**	**1**	**2**	**2**
Cavity	Acts as a turbulator at smaller angles and a reservoir, for reverse flow accumulation, at higher angles. A consistent delay in dynamic stall is observed. However, at higher pitch rates, the vortex strength remains largely unaffected.	**2**	**2**	**3**	**3**

7. Conclusion

In the present article, three different passive control methodologies have been explored for dynamic stall control specifically for wind turbine applications. The passive control methods investigated in the article were selected based on an in-depth understanding of the dynamic stall process. It was observed that dynamic stall vortex and the pertinent flow features become apparent when reverse flow from the trailing edge starts to travel upstream towards the leading edge of the airfoil. Due to this, the shear layer at the leading edge lifts up resulting in the formation of the dynamic stall vortex. Therefore, the control methodologies investigated in the article were centred on the hypothesis that the control application should deter the upstream migration of reverse flow during pitch-up. The three control methods investigated in this research include:

1) Leading edge vortex generators to produce counter-rotating streamwise-oriented vortices.
2) A novel concept of elevated wire to produce counter-rotating spanwise-oriented vortices.
3) A cavity at the quarter-chord of the airfoil to act as a reservoir.

Experiments have shown that all three methods have a considerable impact on the dynamic stall process of the thick NACA 0021 airfoil. The methods were observed to delay the onset of flow separation with varying degrees of success. The use of spanwise- and streamwise-oriented vortices reduced the reverse flow migration towards the leading edge and resulted in the delayed onset of dynamic stall. It was observed that the effectiveness of the methods decreased with the increase in the pitch rate. On the other hand, the cavity acted as a reservoir to store the reverse flow and therefore an approximate constant delay in the onset of flow separation was observed. Furthermore, it was observed that all three methods lead to a decrease in the strength of the dynamic stall vortex through different mechanisms. Furthermore, streamwise- and spanwise-oriented vortices resulted in a considerable improvement in the post-stall behaviour of the airfoil. The loss in lift observed for the clean airfoil was considerably lessened using these control methods. On the other hand, the cavity leads to a consistent delay in the dynamic stall onset but no beneficial effects were observed during the post-stall.

Based on this research, it can be inferred that the methods that are applied at the leading edge of an airfoil and result in a higher flow mixing can be used for dynamic stall control on wind turbine blades. An added benefit is that these methods can be implemented very conveniently on currently operational turbines to improve the

unsteady loading conditions of these turbines. In terms of wind turbines, an increase in the dynamic stall onset implies that the turbine would now be able to withstand larger turbulence in both wind speed and direction. This indicates that the turbines can be packed closer together, with lesser effect of the wake of one turbine on the other. Similarly, the decrease in the dynamic stall vortex strength and improvements in the post-stall characteristics would reduce the bending and torsional loads associated with the vortex as well as considerably lessen the vibrations in the turbine blades. Therefore, the maintenance costs associated with the turbine operation and performance of the turbines can be improved considerably. The effects of these devices on the dynamic stall process are encouraging and further research is warranted for full-scale deployment.

8. References

1. Carr, L.W., *Progress in analysis and prediction of dynamic stall.* Journal of Aircraft, 1988. **25**: p. 6-17.
2. Carr, L.W. and M. Chandrasekhara, *Compressibility effects on dynamic stall.* Progress in Aerospace Sciences, 1996. **32**(6): p. 523-573.
3. Ekaterinaris, J.A. and M.F. Platzer, *Computational prediction of airfoil dynamic stall.* Progress in Aerospace Sciences, 1998. **33**(11-12): p. 759-846.
4. A. Choudhry, et al., *An Insight into the Dynamic Stall Lift Characteristics.* Experimental Thermal and Fluid Science doi: http://dx.doi.org/10.1016/j.expthermflusci.2014.07.006, 2014.
5. Kramer, M., *Increase in the maximum lift of an airfoil due to a sudden increase in its effective angle of attack resulting from a gust.* NASA TM-678, 1932.
6. Harris, F.D. and R.R. Pruyn, *Blade StallHalf Fact, Half Fiction.* Journal of the american helicopter society, 1968. **13**(2): p. 27-48.
7. Ham, N.D. and M.S. Garelick, *Dynamic stall considerations in helicopter rotors.* Journal of the american helicopter society, 1968. **13**(2): p. 49-55.
8. Choudhry, A., M. Arjomandi, and R. Kelso, *Horizontal axis wind turbine dynamic stall predictions based on wind speed and direction variability.* Proceedings of the Institution of Mechanical Engineers, Part A: Journal of Power and Energy, 2013. **227**(3): p. 338-351.
9. Choudhry, A., M. Arjomandi, and R. Kelso, *Effects of wake interaction on downstream wind Turbines.* Wind Engineering (In-press), 2014.
10. Shipley, D.E., et al., *Evidence that aerodynamic effects, including dynamic stall, dictate HAWT structural loads and power generation in highly transient time frames*. 1994, National Renewable Energy Lab., Golden, CO (United States).
11. Laratro, A., et al., *A discussion of wind turbine interaction and stall contributions to wind farm noise.* Journal of Wind Engineering and Industrial Aerodynamics, 2014. **127**: p. 1-10.
12. Schreck, S., et al., *HAWT dynamic stall response asymmetries under yawed flow conditions.* Wind Energy, 2000. **3**(4): p. 215-232.
13. Shipley, D.E., M.S. Miller, and M.C. Robinson, *Dynamic stall occurrence on a horizontal axis wind turbine blade*. 1995, National Renewable Energy Lab., Golden, CO (United States).
14. Mo, J.-O., et al., *Effects of wind speed changes on wake instability of a wind turbine in a virtual wind tunnel using large eddy simulation.* Journal of Wind Engineering and Industrial Aerodynamics, 2013. **117**: p. 38-56.
15. Mo, J.-O., et al., *Large eddy simulation of the wind turbine wake characteristics in the numerical wind tunnel model.* Journal of Wind Engineering and Industrial Aerodynamics, 2013. **112**: p. 11-24.
16. McCroskey, W., et al., *Dynamic stall on advanced airfoil sections.* Journal of the american helicopter society, 1981. **26**(3): p. 40-50.
17. Mulleners, K. and M. Raffel, *The onset of dynamic stall revisited.* Experiments in fluids, 2012. **52**(3): p. 779-793.
18. Gardner, A., K. Richter, and H. Rosemann, *Numerical investigation of air jets for dynamic stall control on the OA209 airfoil.* CEAS Aeronautical Journal, 2011. **1**(1-4): p. 69-82.
19. Karim, M. and M. Acharya, *Suppression of dynamic-stall vortices over pitching airfoils by leading-edge suction.* AIAA journal, 1994. **32**(8): p. 1647-1655.
20. Greenblatt, D. and I. Wygnanski, *Dynamic stall control by periodic excitation, Part 1: NACA 0015 parametric study.* Journal of Aircraft, 2001. **38**(3): p. 430-438.
21. Greenblatt, D., et al., *Dynamic stall control by periodic excitation, part 2: Mechanisms.* Journal of Aircraft, 2001. **38**(3): p. 439-447.
22. Pape, A.L., et al., *Dynamic Stall Control Using Deployable Leading-Edge Vortex Generators.* AIAA journal, 2012. **50**(10): p. 2135-2145.
23. Heine, B., et al., *Dynamic stall control by passive disturbance generators.* AIAA journal, 2013. **51**(9): p. 2086-2097.

24. Mai, H., et al., *Dynamic stall control by leading edge vortex generators.* Journal of the American Helicopter Society, 2008. **53**(1): p. 26-36.
25. Post, M.L. and T.C. Corke, *Separation control using plasma actuators: dynamic stall vortex control on oscillating airfoil.* AIAA journal, 2006. **44**(12): p. 3125-3135.
26. Carr, L. and K. McAlister, *The effect of a leading-edge slat on the dynamic stall of an oscillating airfoil.* AIAA paper, 1983. **2533**: p. 1983.
27. Yu, Y.H., et al., *Dynamic stall control for advanced rotorcraft application.* AIAA journal, 1995. **33**(2): p. 289-295.
28. Chandrasekhara, M., P.B. Martin, and C. Tung, *Compressible dynamic stall control using a variable droop leading edge airfoil.* Journal of aircraft, 2004. **41**(4): p. 862-869.
29. Chandrasekhara, M., M. Wilder, and L. Carr, *Unsteady stall control using dynamically deforming airfoils.* AIAA journal, 1998. **36**(10): p. 1792-1800.
30. Feng, L.-H., et al., *Flow control over a NACA 0012 airfoil using dielectric-barrier-discharge plasma actuator with a Gurney flap.* Experiments in fluids, 2012. **52**(6): p. 1533-1546.
31. Lee, T. and Y. Su, *Pitching Airfoil with Combined Gurney Flap and Unsteady Trailing-Edge Flap Deflection.* AIAA journal, 2012. **50**(2): p. 503-507.
32. Mumtaz, M., et al. *Dynamic Stall Control through Passive Devices in Hybrid Configuration*. in *51st Aerospace Sciences Meeting, Grapevine, Texas*. 2013.
33. Mishra, A., *A Coupled CFD/CSD Investigation of the Effects of Leading Edge Slat on Rotor Performance.* 2012.
34. Greenblatt, D. and I.J. Wygnanski, *The control of flow separation by periodic excitation.* Progress in Aerospace Sciences, 2000. **36**(7): p. 487-545.
35. Greenblatt, D. and I. Wygnanski, *Effect of leading-edge curvature and slot geometry on dynamic stall control.* AIAA Paper, 2002. **3271**: p. 2002.
36. Davis, G., D. Feszty, and F. Nitzsche. *Trailing edge flow control for the mitigation of dynamic stall effects*. in *31st European Rotorcraft Forum, European Rotorcraft Forum, Florence, Italy*. 2005.
37. Lee, T. and P. Gerontakos, *Dynamic stall flow control via a trailing-edge flap.* AIAA journal, 2006. **44**(3): p. 469-480.
38. Rennie, R. and E.J. Jumper, *Experimental measurements of dynamic control surface effectiveness.* Journal of aircraft, 1996. **33**(5): p. 880-887.
39. Lin, J.C., *Control of turbulent boundary-layer separation using micro-vortex generators.* AIAA paper, 1999(99-3404).
40. Velte, C.M., M.O.L. Hansen, and D. Cavar, *Flow analysis of vortex generators on wing sections by stereoscopic particle image velocimetry measurements.* Environmental Research Letters, 2008. **3**(1): p. 015006.
41. Angele, K., *Experimental studies of turbulent boundary layer separation and control.* 2003.
42. Godard, G. and M. Stanislas, *Control of a decelerating boundary layer. Part 1: Optimization of passive vortex generators.* Aerospace Science and Technology, 2006. **10**(3): p. 181-191.
43. Lin, J.C., *Review of research on low-profile vortex generators to control boundary-layer separation.* Progress in Aerospace Sciences, 2002. **38**(4): p. 389-420.
44. Lasagna, D., et al., *Effects of a trapped vortex cell on a thick wing airfoil.* Experiments in fluids, 2011. **51**(5): p. 1369-1384.
45. Olsman, W. and T. Colonius, *Numerical Simulation of Flow over an Airfoil with a Cavity.* AIAA journal, 2011. **49**(1).
46. Chernyshenko, S., *VortexCell2050: fundamentals of actively controlled flows with trapped vortices. EU Executive summary report for contract no*. 2009, AST4-CT-2005-012139, http://cordis. europa. eu/documents/documentlibrary/120142501EN6. pdf.
47. Zannetti, L., *Vortex equilibrium in flows past bluff bodies.* Journal of Fluid Mechanics, 2006. **562**: p. 151-171.
48. Taylor, H., *The elimination of diffuser separation by vortex generators.* United Aircraft Corp, 1947.
49. Choudhry, A., M. Arjomandi, and R. Kelso, *A Study of long separation bubble on thick airfoils and its consequent effects (Under-revision).* International Journal of Heat and Fluid flow, 2014.
50. Doligalski, T., C. Smith, and J. Walker, *Vortex interactions with walls.* Annual Review of Fluid Mechanics, 1994. **26**(1): p. 573-616.
51. Selig, M.S., M.D. Maughmer, and D.M. Somers, *Natural-laminar-flow airfoil for general-aviation applications.* Journal of aircraft, 1995. **32**(4): p. 710-715.
52. Dole, C.E. and J.E. Lewis, *Flight theory and aerodynamics: a practical guide for operational safety*. 2000: John Wiley & Sons.
53. Donelli, R., et al., *Flow models for a vortex cell.* AIAA journal, 2009. **47**(2): p. 451-467.

54. Tutty, O., R. Savelsberg, and I.P. Castro, *Three-dimensional flow in circular cavities of large spanwise aspect ratio.* Journal of Fluid Mechanics, 2012. **707**: p. 551-574.
55. Borg, J., *The effect of leading edge serrations on dynamic stall*. 2012, University of Southampton.
56. Guilmineau, E. and P. Queutey, *Numerical simulation of vortex-induced vibration of a circular cylinder with low mass-damping in a turbulent flow.* Journal of Fluids and Structures, 2004. **19**(4): p. 449-466.
57. Derakhshandeh, J.F., et al., *Effect of a rigid wall on the vortex induced vibration of two staggered circular cylinders.* Journal of Renewable and Sustainable Energy, 2014. **6**(3): p. 033114.
58. Geissler, W. and H. Haselmeyer, *Investigation of dynamic stall onset.* Aerospace science and technology, 2006. **10**(7): p. 590-600.
59. Chandrasekhara, M., M. Wilder, and L. Carr, *Boundary-layer-tripping studies of compressible dynamic stall flow.* AIAA journal, 1996. **34**(1): p. 96-103.
60. Derakhshandeh, J.F., et al., *The effect of arrangements of two circular cylinders on the maximum efficiency of vortex-induced vibration power using a scale-adaptive simulation model.* J. Fluids Struct.(unpublished).

CHAPTER 8

CONCLUSION AND FUTURE WORK

Dynamic stall is one of the most prominent flow separation problems encountered on wind turbine blades. The process begins with a rapid change in the blade sectional angle of attack, caused by turbulent inflow, gusts, tower-shadow effects, and yaw misalignment. During dynamic stall, the angle of attack quickly exceeds the steady-state stall angle of attack of the airfoil. Generally, for wind turbines the inboard stations of the turbine blades are often already operating at fully separated conditions. This further exacerbates the dynamic conditions that could occur due to changes in the sectional angle of attack. The process results in an increased lift production, beyond the steady-state maximum value and the design loads of the turbine. The process is characterized by an intense leading edge vortex, commonly referred to as

the dynamic stall vortex. The dynamic stall vortex, due to a low pressure core, results in a rapid increase in the lift-curve slope, drag and negative moment that damage the wind turbine blades. The convection of the vortex structure results in an abrupt loss in lift that can cause vibrations in the blade and influence the fatigue life of the turbine. After the primary vortex, secondary and often tertiary vortices are observed that can further degrade the fatigue life of the turbine. Furthermore, the process also negatively influences the performance of the turbine due to delayed flow reattachment. Due to the occurrence of dynamic stall, therefore, the performance of the turbine is affected and maintenance costs of wind turbine blades are exceedingly large. Hence, in the current thesis, detailed investigations into the causes of dynamic stall on wind turbine blades, the lift-characteristics during unsteady separation, and methods that can be used to mitigate its effects are presented and discussed.

8.1 Significance of Present Work

Much research into dynamic stall has been focused on controlling the problem of unsteady separation on retreating helicopter blades. Simple actuation of the designed control method is required in this case since dynamic stall occurrence is limited to the retreating blade of the rotor. This allows for the use of active control methods for dynamic stall. However, in wind turbines the occurrence of dynamic stall is highly unpredictable due to an ensemble of influencing parameters such as turbulence in the inflow, gusts and large variations in wind direction. Therefore, in this case, passive flow control methods need to be utilized to minimize the effects of dynamic stall. However, most passive flow control methods influence the steady-state performance in some manner. Therefore, it is also desirable to use these methods only in

regions where the control is necessary. Focusing on these aspects, the significance of the current work can be described as follows:

1) An analytical model was formulated and validated to predict the occurrence of dynamic stall on wind turbine blades. The model can be used during the design phase of wind turbines to predict the regions of the blades where passive control will be necessary for dynamic stall control. It was observed that these regions are located at the inboard section of the blade. Generally, these regions are already operating at steady-state stall. Therefore, a control methodology applied in these regions would not negatively influence the performance of the turbine. However, it will aid in reducing the impact of dynamic stall on the turbine blades.
2) The causes of unsteady separation on downstream wind turbines have been discussed. It has been observed that turbulent variations in wind direction are the primary cause of unsteady separation on downstream wind turbines. Therefore, a staggered wind turbine farm arrangement is more suitable for optimized operation. The distance between the rows will also be greater, compared to aligned turbines, and will help reduce the velocity deficit and turbulence intensity.
3) Lift and separation characteristics of thick airfoil sections have been understood in detail for both steady and unsteady conditions. Thick airfoils are of particular interest in this case since they constitute the inboard stations of wind turbine blades where unsteady separation is prevalent. The following are the significant findings related to lift and stall characteristics of thick airfoil sections:
    a. At steady-state conditions, it has been observed that long separation bubbles can exist on the suction sides of the airfoils at low freestream turbulence levels and/or Reynolds numbers. These bubbles can erupt at high angles of attack when the

separated shear-layer is unable to reattach downstream of the point of separation, due to adverse pressure gradients. This leads to an abrupt stall on thick airfoil sections leading to higher stall intensity. This type of stall characteristic is more representative of thin-airfoil stall. Of particular note, however, is the lift behavior of the airfoil as it is affected by the separation bubble. The bubble was observed to impart a camber effect on the airfoil surface, resulting in more lift than would be available for the case without any separation bubble. This effect was observed to increase as the angle of attack of the airfoil increased due to the upstream migration of the bubble. The changes to the lift curve due to the presence of the bubble can improve our understanding of the lift produced during dynamic stall where significant changes in the vicinity of the airfoil during an upstroke motion can lead to changes in the lift behavior of the foil.

b. The lift behavior of an airfoil undergoing unsteady separation has been investigated in detail. Based on pressure measurements and flow visualization, the lift characteristics of a thick NACA 0021 airfoil have been investigated in detail. The non-linear lift behavior during the process of dynamic stall, prior to the formation of the vortex, can be attributed to the thickening of the boundary layer that causes apparent changes in the camber and thickness of the foil. Afterwards, the formation of the dynamic stall vortex causes a sudden increase in the lift-curve slope. It was observed that the strength of this vortex increases with the increase in the reduced frequency and Reynolds number. Furthermore, the stalling characteristics of the airfoil during unsteady separation are also governed by the primary dynamic stall vortex. A parameter was formulated to

evaluate the intensity of stall during steady- and ramp-type separation. This method was used to quantify the abrupt loss in lift during separation and can be used to compare the stalling performance of different airfoils under different conditions. The method clearly illustrates that the unsteady separation is more intense compared to steady-state separation of the same airfoil. It was also observed that an increase in reduced frequency and Reynolds number further increases the stall intensity of the airfoil. This is primarily due to an increase in the vortex strength and its eventual detachment, leaving a large-scale flow separation above the airfoil.

c. A precursor for the unsteady separation on the thick NACA 0021 airfoil was proposed based on the product of reduced frequency and the square root of chord Reynolds number ($\kappa\sqrt{Re_c}$). It was illustrated through experimental work that when $\kappa\sqrt{Re_c} > 2$, the dynamic stall vortex is observed on the airfoil. This precursor can be used for active flow control of dynamic stall by determining the real-time variation of sectional angles of attack using the analytical model developed earlier in this research. Based on this precursor, flow control can be activated when the local $\kappa\sqrt{Re_c}$ of a blade section exceeds the value of two.

4) Passive flow control methodologies have been investigated in the research, based on an in-depth understanding of the dynamic stall lifting characteristics of an airfoil as well as the flow control requirements for wind turbine applications. The methods are selected based on the notion that the impact of unsteady separation can be reduced by decreasing the upstream migration of reversed flow towards the leading edge of the airfoil thereby delaying the formation of the vortex and reducing its strength. For this purpose, the methods

investigated in the present research are: (1) Streamwise vortices created using leading edge delta vortex generators, (2) Spanwise vortices produced using a novel concept of elevated wire affixed permanently in front of the leading edge, and (3) cavity at the quarter-chord location. The first two methods are based on the idea of creating strong streamwise and spanwise vortices that would enhance mixing, improve the boundary layer ability to withstand adverse pressure gradients and reduce the upstream migration of the reversed flow during airfoil pitch-up. The final method is investigated based on the concept that the reversed flow be accumulated in a 'reservoir', in the form of the cavity, to delay the onset of dynamic stall. It was, furthermore, anticipated that the vortex trapped by the cavity would lead to improved post-stall lift behavior for the airfoil undergoing dynamic stall. All three methods were observed to influence the dynamic stall process to different extents. However, the effects were less pronounced at higher reduced frequencies. Therefore, the figures provided in the following summary are an average of the cases examined during this research. The influence of the flow control methodologies is summarized as follows:

a. Of all three, the least successful and probably the least practical method was the cavity. It was observed that an airfoil with a cavity, though significantly influencing the DSV lift, did not show any beneficial effect on the post-stall behavior of the airfoil. This was primarily because the cavity was inside the separated zone after the dynamic stall vortex convected downstream. A decrease of approximately 12%, on average, was observed in the maximum lift associated with the primary DSV. Furthermore, it was observed that the cavity acted as a reservoir, allowing reverse-flow accumulation and leading to an approximately 18% delay in the dynamic stall angle of attack.

b. The counter-rotating streamwise vortices generated using delta vortex generators were observed to reduce the primary DSV lift by approximately 18% on average. A slight delay in the dynamic stall process of approximately 5% was also observed using delta-type vortex generators. However, the most significant effect of the streamwise vortices produced by the vortex generators was a considerable reduction in the intensity of stall after separation. This, furthermore, illustrates that the vortex generators at the leading edge of the airfoil can help in the process of lift recovery after the primary DSV separates.

c. The final method employed to control the dynamic stall process was novel in this work. It was noted during the literature review that, similar to streamwise vortices, spanwise vortices can also enhance mixing and improve separation characteristics. However, no feasible method existed that could produce counter-rotating spanwise-oriented vortices for increased fluid entrainment. Therefore, in this research, an elevated wire of diameter less than 1% chord length was used to create small coherent spanwise vortices that would traverse the airfoil surface. It was observed that these spanwise vortices interfered significantly with the formation of the primary DSV during pitch-up and resulted in an approximate reduction of 24% in the vortex lift. This was followed by a considerably improved post-stall behavior where no secondary or tertiary vortices were observed to influence the lift force. It was observed that after flow separation, the lift force consistently persisted at a constant value during the upstroke. Furthermore, depending on the height of the elevated wire, delays in the dynamic stall process were also observed. For a wire height of 1% chord length, the process was advanced and resulted in an earlier separation.

However, increasing the wire height to 3% of chord length resulted in an approximately 17% delay in the stall angle of attack. Perhaps, the most beneficial aspect of this method is the reduced profile drag that is observed on the airfoil during both steady and unsteady operation.

8.2 Further Research Avenues

Several avenues of future research are available that can be used to further the understanding of dynamic stall control on wind turbine blades. These are:

1) The proposed analytical model for dynamic stall predictions on wind turbine blades is based on geometric variations in wind speed and direction. However, it is widely understood that as the flow approaches the turbine blades, the wind speed decreases slightly. Also, a skewed wake could influence the oncoming wind speeds and direction. These effects can be included in the model using available empirical approximations for improved predictions of dynamic stall.
2) Further testing should be conducted to verify whether the precursor established for dynamic stall onset is valid for other airfoils. It is anticipated that the precursor would be largely different based on the profile of the airfoil. Therefore, a database should be established to provide the precursor for different airfoil profiles and link the onset of dynamic stall, under similar operating conditions, to the airfoil geometrical properties.
3) As shown in Chapter 2 of the thesis, an increased camber and rounded leading edge can delay the dynamic stall process significantly. It was, furthermore, shown in Chapter 4 that the stall intensity for a thicker airfoil is significantly higher compared to a thinner member of the same airfoil family. Therefore, systematic

research should be conducted to understand the effects of geometry on dynamic stall lift and stall. Such a study will be helpful in selection of appropriate profiles during the design phase of wind turbines.

4) The precursor to dynamic stall ($\kappa_{lim} = \sqrt{Re_c}/2$ for NACA 0021 airfoil) can be used with the analytical model to devise an active control routine for dynamic stall control on wind turbine blades. The control technique will require active monitoring of wind conditions and the turbine orientation. Using this data and the limiting reduced frequency, the routine can predict the occurrence of dynamic stall on wind turbine blades prior to its initiation.
5) Further investigations need to be conducted into the mechanisms involved for the elevated-wire concept presented in the study. Furthermore, optimization studies based on wire diameter, position along the chord, and elevation need to be performed.
6) Since counter-rotating spanwise-oriented vortices have been observed to be most successful at improving post-stall conditions, new techniques should be developed to generate this structure more efficiently.
7) The proposed control methodologies can be implemented on small-scale wind turbines to document their effects on the performance of the wind turbines. Furthermore, field tests can also be performed for this purpose. Further testing for large-scale wind turbines to understand the effects of higher Reynolds number is also recommended.
8) It is also important to note that the studies presented in this thesis have been limited to small levels of turbulence. Further work, therefore, can be proposed to test these hypothesis at substantially larger and realistic values of turbulence intensity.

APPENDIX A

The numerical study of the wind turbine wake carried out at the University of Adelaide was presented at the 7th Australasian Congress on Applied Mechanics, organized by the Engineers Australia. The conference article that resulted from this submission has been included here for quick referral of the simulation setup and validation of the wake data used in Chapter 4 of the thesis.

Choudhry, A., Mo, J. O., Arjomandi, M., & Lee, Y. H. (2012). Turbulent wake study of NREL phase VI wind turbine in a virtual wind tunnel using Large Eddy Simulation. In *Proceedings: the 7th Australasian Congress on Applied Mechanics (ACAM 7)*, 9-12 December 2012, the University of Adelaide, North Terrace Campus/National Committee on Applied Mechanics of Engineers Australia (p. 837). Engineers Australia.